Characterization of Epitaxial Silicene on the Ag(111) Surface with Synchrotron-Based Soft X-Ray Spectroscopy

A Thesis Submitted to the
College of Graduate Studies and Research
in Partial Fulfillment of the Requirements
for the degree of Doctor of Philosophy
in the Department of Physics and Engineering Physics
University of Saskatchewan
Saskatoon

By
Neil W. Johnson

Permission to Use

In presenting this thesis in partial fulfilment of the requirements for a Postgraduate degree from the University of Saskatchewan, I agree that the Libraries of this University may make it freely available for inspection. I further agree that permission for copying of this thesis in any manner, in whole or in part, for scholarly purposes may be granted by the professor or professors who supervised my thesis work or, in their absence, by the Head of the Department or the Dean of the College in which my thesis work was done. It is understood that any copying or publication or use of this thesis or parts thereof for financial gain shall not be allowed without my written permission. It is also understood that due recognition shall be given to me and to the University of Saskatchewan in any scholarly use which may be made of any material in my thesis.

Requests for permission to copy or to make other use of material in this thesis in whole or part should be addressed to:

Head of the Department of Physics and Engineering Physics
163 Physics Building
116 Science Place
University of Saskatchewan
Saskatoon, Saskatchewan
Canada
S7N 5E2

Abstract

The eventual incorporation of two-dimensional materials into electronic devices will require an intimate understanding of their electronic properties, as well as how these properties are affected by the material's local environment. The specific focus of this thesis is on silicene, the silicon-based analogue to the prototypical 2D material graphene. In particular, the studies contained within this thesis aim to elucidate the electronic properties of silicene monolayers and multilayers grown on the Ag(111) surface through combination of *ab initio* density functional theory calculations and synchrotron-based soft X-ray spectroscopy.

The first study explores the electronic interaction between epitaxial silicene monolayers and their Ag(111) substrate, finding evidence for significant hybridization between them that confers a metallic electronic structure upon the silicene. The second examines the effects of oxidation on the electronic and structural characteristics of epitaxial silicene monolayers on Ag(111), refuting the notion of a bandgap opening at low oxygen coverage and showing that the structure is inherently unstable at high oxygen coverage. Finally, silicene growth beyond a monolayer is studied, and strong evidence for the instability of multilayer silicene on Ag(111) is presented.

In addition, this thesis contains a review of the history, properties and potential applications of a variety of two-dimensional materials, focusing on the qualities that will impact their application to electronic devices. It also discusses the techniques involved in producing, structurally characterizing, and predicting and measuring the electronic properties of epitaxial silicene on Ag(111).

Acknowledgements

First and foremost, I would like to thank my supervisor Professor Alexander Moewes for his support, advice and encouragement throughout my graduate studies and the process of writing this thesis. It has been a privilege to have had a supervisor with his level of dedication to his students and his research.

I would like to thank the former members of the Beamteam for their guidance and patience at the outset of my graduate studies. In particular, David Muir, John McLeod and Teak Boyko were instrumental in helping me to develop my experimental and theoretical skills. In addition, I would like to thank all of the members of the Beamteam, past and present, for their lively and informative discussions both on- and off-topic over the last five years. It was certainly educational.

I gratefully acknowledge the financial support that I received throughout my graduate studies from the Department of Physics and Engineering Physics, the College of Graduate Studies and Research, the University of Saskatchewan, the Province of Saskatchewan and the Natural Sciences and Engineering Research Council's Postgraduate Scholarship program.

My research would not have been possible without the hard work and dedication of the Canadian Light Source and Advanced Light Source staff, the WestGrid development team and the support staff of the Department of Physics and Engineering Physics at the University of Saskatchewan.

Further acknowledgements specific to each project I have undertaken are included at the end of the manuscripts in Chapters 6–9.

Finally, I would like to acknowledge the love and support of my family and my amazing fiancée, Sarah Stewart. This thesis is dedicated to them.

Contents

List of Tables

List of Figures

List of Abbreviations

0D, 1D, 2D, 3D	Zero-, One-,Two-, and Three-Dimensional
ALS	Advanced Light Source
ARPES	Angle-Resolved Photoemission Spectroscopy
BL8	Beamline 8.0.1
CB	Conduction Band
CLS	Canadian Light Source
CH	Core Hole
CMOS	Complementary Metal-Oxide Semiconductor
CVD	Chemical Vapour Deposition
DFT	Density Functional Theory
DOS (pDOS, tw-DOS)	Density of States (Partial, Transition-Weighted)
EDXR	Energy-Dispersive X-ray Reflectivity
EPU	Elliptically Polarizing Undulator
ESML	Epitaxial Silicene Monolayer
FET	Field-Effect Transistor
FSML	Freestanding Silicene Monolayer
GGA	Generalized Gradient Approximation
HB	High-Buckled
HCT	Honeycomb-Chained-Triangle
IET	Inequivalent-Triangle
IPFY	Inverse Partial Fluorescence Yield
LAPW	Linearized Augmented Plane Wave
LB	Low-Buckled
LDA	Local Density Approximation
LEED	Low-Energy Electron Diffraction
LEEM	Low-Energy Electron Microscopy
LSDA	Local Spin Density Approximation
mBJ	Modified Becke-Johnson
ML, BL, TL	Monolayer, Bilayer, Trilayer
nc-AFM	Non-Contact Atomic Force Microscopy
$(n)nn$	(Next-)Nearest Neighbour
NXES	Non-Resonant X-Ray Emission Spectroscopy
PBE-GGA	Perdew-Burke-Ernzerhof Generalized Gradient Approximation
PFY	Partial Fluorescence Yield
PVD	Physical Vapour Deposition
REIXS	Resonant Elastic and Inelastic X-ray Scattering (Beamline)
RXES	Resonant X-Ray Emission Spectroscopy
SEM	Scanning Electron Microscopy
SOC	Spin-Orbit Coupling
SPM	Scanning Probe Microscopy

STM	Scanning Tunnelling Microscopy
STS	Scanning Tunnelling Spectroscopy
SXF	Soft X-Ray Fluorescence (Endstation)
TB	Tight-Binding (Approximation)
TEM	Transmission Electron Microscopy
TEY	Total Electron Yield
TFET	Tunnelling Field-Effect Transistor
TFY	Total Fluorescence Yield
TMDC	Transition Metal Dichalcogenide
UHV	Ultra-High Vacuum
UV	Ultraviolet
VB	Valence Band
vdW	van der Waals
VUV	Vacuum Ultraviolet
XAS	X-Ray Absorption Spectroscopy
XEOL	X-Ray Excited Optical Luminescence
XES	X-Ray Emission Spectroscopy
XRD	X-Ray Diffraction

Chapter 1

Introduction

Sustaining Moore's Law requires that, with each new generation of electronic devices, the individual components that comprise them decrease exponentially in size. Some practical problems associated with small and densely packed integrated circuit components include efficient power delivery and heat dissipation, and such concerns have recently led to the announcement that Moore's Law will no longer be targeted as an industry benchmark [1]. In addition, there are more fundamental hurdles looming on the not-too-distant horizon as miniaturization continues apace. Currently, the minimum feature size on modern integrated circuits is on the order of a few tens of nm, typically patterned on to the chip with visible or ultraviolet (UV) photolithography. With the advent of extreme-UV photolithography and free-electron lasers, the spatial resolution of the lithographic sources will improve and the minimum feature size could be pushed down to the order of a few nm. This is where the first of the fundamental hurdles occurs, one that has already been witnessed in the smallest complementary metal-oxide semiconductor (CMOS) devices: quantum tunnelling.

The CMOS layout requires electrical insulation between the gate and the depletion region, which in bulk Si based devices is accomplished by growing a thin layer of the native surface oxide, SiO_2. However, as the lateral dimensions of the transistor decrease, the thickness of the surface oxide must decrease proportionally. With this narrowing of the potential barrier between gate and conduction channel comes an exponential increase in tunnelling probability, resulting in a gate current that can cause significant issues with heat generation and degradation of logic signals [2]. Tunnelling can therefore be deleterious to the functioning of traditionally-designed transistors, but the process can also be taken advantage of by appropriately re-designing the device. Tunneling field-effect transistors (TFETs) – which use tunnelling injection instead of thermionic injection of carriers – are expected to improve

significantly on the switching characteristics of certain devices [3].

Another effect that will come into play at slightly smaller scales is that of material *dimensionality*. Above a certain material-dependent threshold, typically on the order a few tens of nm, electronic properties such as bandgap and conductivity are fixed at their "bulk" or "macroscopic" values. However, when one or more dimensions of the material are reduced below this threshold into the "mesoscopic" scale, the majority of charge carrier wavefunctions feel the effects of the boundary conditions at the material's surface, significantly altering its net electronic structure. This can be seen (quite literally) in the zero-dimensional (0D) class of materials referred to as "quantum dots", in which the radius of the particle is smaller than the effective radius of its excitons. This compression of the excitonic wavefunction modulates the electronic bandgap (and therefore the dot's primary fluorescence wavelength), resulting in fluorescence that can be tuned across the visible spectrum and beyond. Much like quantum tunnelling, while dimensionality effects could cause unexpected and often deleterious behaviour in small-scale devices, they could also be intentionally implemented in the design of new mesoscopic devices to drastically improve their capabilities. In order to accomplish this feat, a better understanding of the electronic characteristics of these relatively new mesoscopic materials is required.

Perhaps the most famous mesoscopic material is the two-dimensional (2D) carbon allotrope graphene, which is composed of an atom-thick sheet of π-bonded hexagonal carbon rings. Its unique electronic, mechanical and optical properties have led to it being named a candidate material for electronics, optoelectronics, photovoltaics, nanofiltration, and a whole host of other potential applications. In the decade since its was first isolated in the laboratory in 2004 [4], novel methods for producing large area, low-cost and consistently high-quality graphene sheets have been developed. This material is almost poised to overtake three-dimensional (3D) Si as the basis of modern electronics, but there remain a few significant practical and fundamental challenges that graphene researchers must overcome before full-scale implementation is feasible.

One practical challenge is the industrial retooling that would be associated with switching from Si- to C-based devices, which would by no means be a trivial process. In this respect, silicene – graphene's Si-based analogue – has a distinct advantage. Further, silicene has been

shown to inherently avoid some of graphene's critical shortcomings, suggesting that this novel mesoscopic material might be a more appropriate basis for future low-dimensional electronic devices. However, producing and characterizing silicene is associated with its own list of unique challenges, and research into this novel material is still in its infancy.

In this manuscript, I will detail my research into the electronic and structural properties of epitaxial silicene monolayers and multilayers grown on the Ag(111) surface. In Chapter 2, I will begin by briefly outlining the development of 2D materials, from their first appearance in the literature some 70 years ago to the rapid period of development that has occurred in the last decade following the first successful isolation of monolayer graphene. I will then compare and contrast the electronic properties of graphene and silicene, outlining the advantages and disadvantages of each in terms of their potential application to electronic devices. In Chapter 3, I will describe the process of producing epitaxial silicene monolayers and multilayers on Ag(111) substrates, as well as some methods for determining their atomic structure. Chapter 4 will contain an overview of density functional theory (DFT) using the WIEN2k software suite, with an eye toward calculating the electronic structures of 2D materials. Chapter 5 will focus on synchrotron-based soft X-ray spectroscopy, including the generation of synchrotron radiation, beamline design, the complementary techniques of soft X-ray absorption and emission spectroscopy (XAS and XES, respectively) and special considerations for 2D materials in soft X-ray spectroscopy experiments. Chapter 6 will contain the first of my studies on the epitaxial silicene/Ag(111) system; a characterization of the electronic structure of the various monolayer silicene sheets that can be grown on this particular Ag face. In Chapter 7, I will discuss the results of a related study that examined the mechanism and effects of the oxidation of epitaxial silicene monolayers. Chapter 8 will review my work with epitaxial silicene bilayers and multilayers on the Ag(111) face. Chapter 9 will deviate from silicene to discuss my research into $LiGaO_2$, and Chapter 10 will conclude this manuscript with a brief discussion on the current state and future prospects of silicene research.

Chapter 2

2D Materials

Graphene is the prototypical 2D material; it was the first member of the 2D family to be explored theoretically and the first freestanding atom-thick material to be successfully produced and characterized. It consists of a macroscopic, atomically thin plane of sp^2-hybridized hexagonal carbon rings, and can be thought of as a single sheet of the layered 3D carbon allotrope graphite (see Figure 2.1) or as an essentially infinite polycyclic aromatic carbon molecule. It is sometimes referred to as the "mother of all graphitic forms" [5] as cutting or curling a sheet of graphene can generate the one-dimensional (1D) carbon nanotubes, nanoribbons or nanowires and the 0D fullerenes, and stacking multiple graphene sheets yields 3D graphite. Over the last decade, research into graphene, its lower-dimensional derivatives and analogous 2D materials has arguably been more active than any other field in condensed matter physics, with about 40 publications appearing per day in 2014 for 2D graphene alone [6]. This intense interest stems from the combination of unique mechanical, thermal, electronic, magnetic, quantum mechanical and relativistic effects that graphene and its counterparts regularly exhibit. In this chapter, I will briefly trace the history of 2D materials and explore their unique characteristics, with an eye toward how these materials may be used to improve the capabilities of modern electronic devices.

2.1 Atomically Thin Graphite

Graphene's first appearance in the literature occurred in 1947 [7], decades before the material would be formally named. This study was not specifically intended to be an investigation into the characteristics of a 2D system. Instead, P.R. Wallace considered the graphene structure as a first-order approximation in his tight-binding (TB) calculations of the electronic structure of

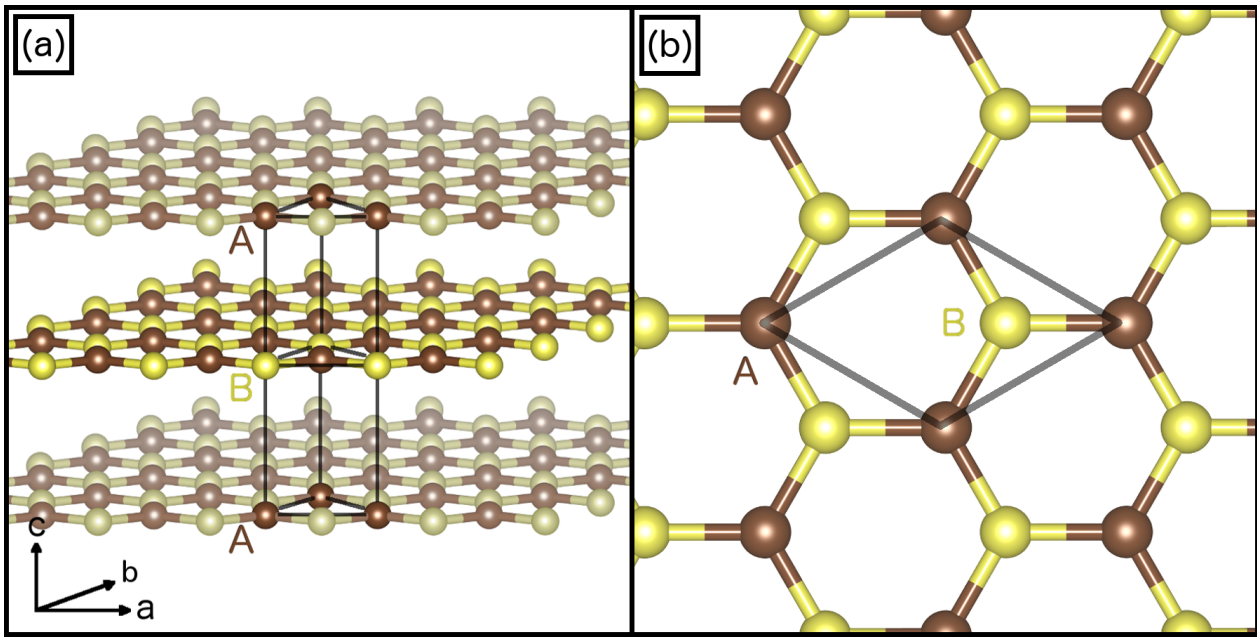

Figure 2.1: (a) The crystal structure of graphite, showing its "AB" or "Bernal"-type stacking configuration. (b) Top-view of the crystal structure of graphene, a single plane removed from the graphite structure. The A and B sites (brown and yellow, respectively) each contribute to a separate but equivalent triangular sublattice. The black lines show the borders of a single graphene unit cell. Structural visualization provided by VESTA [8].

graphite. The 2D model reduced the number of dimensions required in the TB approximation as it neglected the c crystal axis, which in graphite contains a van der Waals interaction that is much weaker than the covalent bonds in the ab plane. Wallace briefly noted some unusual results in the bandstructure of the atom-thick graphitic sheet, including an isotropic linear crossing of the valence and conduction bands with a degenerate point located at the intersection of the Fermi energy and the corners of the hexagonal Brillouin zone (Figure 2.2; see Appendix A for a similar TB derivation). While it was made clear in Wallace's analysis that this peculiar bandstructure would result in a very high in-plane conductivity, the more fundamental implications of graphene's bandstructure were not immediately realized, partly owing to the fact that it was widely believed that such 2D sheets were inherently unstable and therefore would never exist.

About a decade earlier, Peierls and Landau made compelling arguments against the stability of infinite 2D crystalline order. Peierls used the harmonic approximation of lattice dynamics to show that the mean out-of-plane displacement of atoms in a 1D lattice embed-

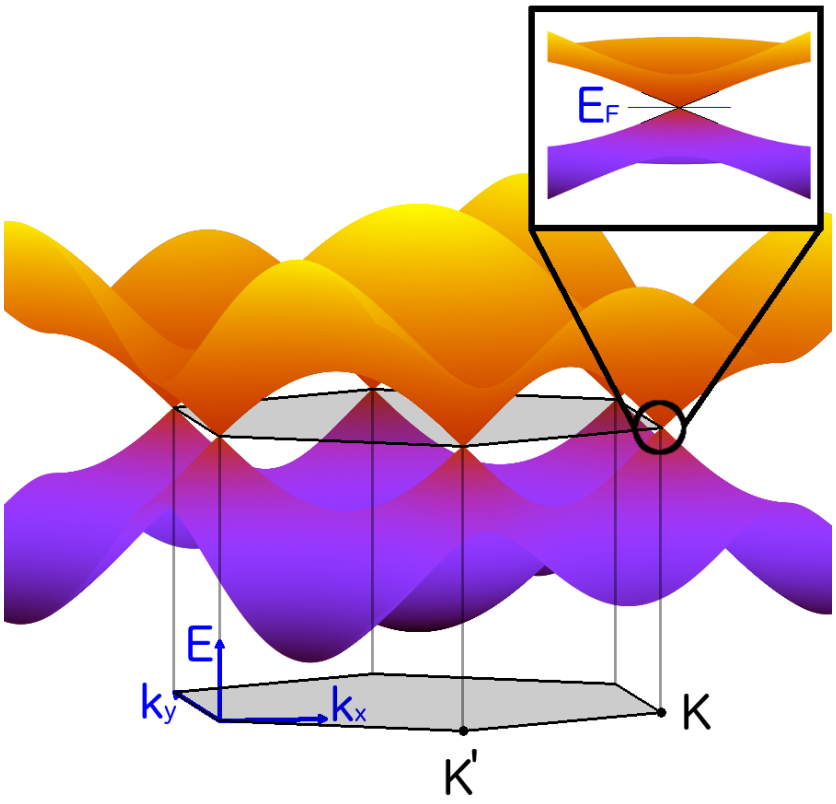

Figure 2.2: A plot of the TB-derived bandstructure of graphene in 3D energy-momentum space. The shaded hexagon indicates the first Brillouin zone with the important K and K' corners indicated. The inset shows a close-up of the conical dispersion in the vicinity of the K or K' points and the Fermi level.

ded in 2D space would diverge logarithmically with increasing lattice length, an argument which could be extended to a 2D lattice embedded in 3D space [9]. The logarithmic divergence has been shown to be inevitable at any finite temperature, and is the product of the unrestricted growth of transverse phonons [10]. Where the out-of-plane displacement approaches the same scale as the interatomic distance (1.42 Å for graphene) the dislocation of the atoms would likely result in the rolling or crumpling of the 2D sheet into lower-energy 1D or 3D structures. Landau and Lifshitz independently arrived at the same conclusion using an argument based on the free energy in a 2D crystalline system with infinite area [11], and Mermin would later extend a method that he and Wagner had used to argue against 2D magnetic order [12] to find that it could also be applied to 2D crystalline order in general [10, 13].

While none of these calculations expressly forbade the existence of relatively small planar molecules like the polycyclic aromatic hydrocarbons, they did impose a limit on the lateral

extent and viable temperature range for large planar sheets – though it was not clear at the time precisely what these limits would be. In addition, none of these arguments excluded the possibility of a 2D sheet stabilized by a 3D crystal, such as atomically thin monolayers on a crystalline or amorphous substrate, or quasi-freestanding 2D substructures embedded in a supporting 3D matrix. Nevertheless, they seemed to cast serious doubt on whether completely freestanding, large-area 2D materials like the graphitic sheets Wallace described could ever be manufactured. Before I recount the efforts made toward realizing freestanding graphene, it is helpful to motivate this search by further exploring the physical implications of graphene's conical bandstructure and the unique electronic characteristics that are expected as a result.

2.2 The Physics of Dirac Cone Systems

Conventional semiconductors exhibit a parabolic band dispersion near the valence band (VB) maximum and the conduction band (CB) minimum, which is identical to the dispersion of a free particle up to a multiplicative constant. Absorbing this factor into the inertial mass of the carriers allows them to be modelled as free electrons and holes with an effective mass (m^*) that can vary with material, direction of carrier motion and carrier identity (i.e., electrons versus holes). Assuming an isotropic band structure for simplicity, and with $|\vec{q}|$ describing a small displacement in momentum space from the band extremum, the dispersion is given by

$$E(\vec{k}) = \frac{\hbar^2 |\vec{q}|^2}{2m^*}, \tag{2.1}$$

so that

$$\frac{1}{m^*} \propto \frac{\partial^2 E}{\partial q^2}. \tag{2.2}$$

In practice, the band dispersion is often not isotropic and the effective mass becomes a tensor with the same dimensionality as the material. Additionally, the VB maximum and CB minimum often have different curvatures, such that the effective mass tensor is dependent on whether the carrier is a hole in the VB or an electron in the CB.

As derived in Appendix A, for small momenta $\vec{q}$ measured relative to the three K Brillouin zone corners, the graphene Hamiltonian has the form:

$$\hat{H}(\vec{q}) = \hbar v_F \begin{pmatrix} 0 & q_x - iq_y \\ q_x + iq_y & 0 \end{pmatrix}, \tag{2.3}$$

and near the K' corners:

$$\hat{H}(\vec{q}) = \hbar v_F \begin{pmatrix} 0 & -q_x - iq_y \\ -q_x + iq_y & 0 \end{pmatrix}. \tag{2.4}$$

This Hamiltonian produces a linear dispersion relation:

$$E(\vec{q}) = \hbar v_F \left|\vec{q}\right|, \tag{2.5}$$

which is decidedly different from the parabolic dispersion in classical semiconductors, so much so that the free particle approximation is no longer a valid way to describe carrier motion. Were it applied, the linear relationship between E and $|\vec{q}|$ would indicate an infinite effective carrier mass near the Fermi level where the bands are linear, and zero mass at the degenerate point where the curvature is infinite.

Instead, by using the Pauli matrices

$$\sigma_x = \begin{pmatrix} 0 & 1 \\ 1 & 0 \end{pmatrix} \qquad \sigma_y = \begin{pmatrix} 0 & -i \\ i & 0 \end{pmatrix}, \tag{2.6}$$

one can recast the low-energy Hamiltonian into the following form:

$$\hat{H}(\vec{q}) = \hbar v_F \vec{\sigma} \cdot \vec{k}. \tag{2.7}$$

As was first pointed out by Semenoff in 1984 [14], this formalism is equivalent to the relativistic Dirac equation for a spin-1/2 particle with zero rest mass (also known as the Weyl equation). Because of this similarity, the linear region of the dispersion relation is often referred to as the Dirac cone, and the degenerate neutrality point as its Dirac point. Conduction in graphene can therefore be accurately modelled as charge-carrying quasiparticles behaving like massless Dirac fermions in a medium with a constant "speed of light" $v_F \sim 10^6$

m s^{-1}. However, this should not be taken to mean that the electrons and holes themselves are massless. Indeed, a finite cyclotron effective mass can be derived by examining how the area A of a closed, isoenergetic loop in k-space changes with energy at the Fermi level [15]:

$$m_c^* = \frac{\hbar^2}{2\pi} \left| \frac{\partial A}{\partial E} \right|_{E=E_F}. \tag{2.8}$$

Neglecting the trigonal warping and the inequivalence between electron and hole states that arises from next-nearest neighbour (nnn) considerations (see Appendix A), the closed loops are circular with a radius of $|\vec{k_F}| = E_F/\hbar v_F$, and therefore have an area of $\pi|\vec{k_F}|^2 = \pi(E_F/\hbar v_F)^2$. As such, the cyclotron mass for both electrons and holes becomes

$$m_c^* = \frac{E_F}{v_F^2} = \frac{|\vec{k_F}|}{v_F}. \tag{2.9}$$

This quantity is non-zero whenever the Fermi level is shifted away from the Dirac point, and its relationship to the Fermi energy closely resembles Einstein's famous relativistic relationship $E = mc^2$, again with the Fermi velocity taking the place of the speed of light. It might be tempting to substitute this expression for the cyclotron effective mass into the usual equations for semiconductors, but this would be inappropriate. Conduction in graphene is described by fundamentally different physics, better approximated by the equations governing massless particles in quantum electrodynamics than the kinematic equations for massive free particles.

However, the electron and hole cyclotron masses are useful in that, together with the free carrier concentration n, they can serve as a relatively straightforward way of differentiating between a conventional semiconductor and a Dirac cone system. The free carrier concentration in a material can be calculated by examining its Fermi surface, which in the case of 2D materials with isotropic dispersion is simply a circle with area $A_F = \pi k_F^2$. The number of filled states per unit cell in the CB (or empty states per unit cell in the VB, if the Fermi energy is below the Dirac points) is given by:

$$N = g_s g_v \frac{A_F}{A_{BZ}}, \tag{2.10}$$

where g_s and g_v are both 2 for the spin and valley degeneracies of graphene and A_{BZ} is the

area of the Brillouin zone shown in Appendix A. Dividing this value by the area of graphene's unit cell A_{UC} gives the carrier concentration n per unit area of graphene,

$$n = 4\frac{A_F}{A_{BZ}A_{UC}} = \frac{4\pi k_F^2}{(2\pi)^2} = \frac{k_F^2}{\pi}, \tag{2.11}$$

where I have used the relation $A_{BZ}A_{UC} = (2\pi)^N$, with N being the dimensionality of the system. Inserting this equation into Equation 2.9 yields:

$$m_c^* = \frac{\sqrt{\pi}}{v_F}\sqrt{n} \tag{2.12}$$

The carrier density can be indirectly measured through the Shubnikov-de Haas oscillations and the cyclotron mass inferred from absorption experiments (e.g. see References 16, 17). Observing a square-root relationship between these two parameters is not only an indication that one is working with a Dirac cone system, but it affords researchers the ability to experimentally confirm the Fermi velocity predicted by TB and DFT calculations.

Another relatively easy-to-measure hallmark of 2D materials like graphene is that they exhibit unusual Landau quantization. In the quantum mechanical description of cyclotron motion, free particles are restricted to quantized cyclotron radii with quantized energy levels given by:

$$E_N = \pm h\omega_c \left(N + \frac{1}{2}\right). \tag{2.13}$$

These energies are similar to the energy levels of a quantum harmonic oscillator, with $\omega_c = eB/m_c^* v_F$ being determined by the strength of the applied field as well as the Fermi velocity and the cyclotron effective mass of the carriers. The resulting Landau levels, shown in Figure 2.3(a), are evenly spaced in energy and occur at minimum energy $|E_0| = \frac{1}{2}h\omega_c$. The factor $\left(N + \frac{1}{2}\right)$ can be seen as the result of Bohr-Sommerfeld quantization [18], which describes the allowable values for a particle's momentum when integrated over a closed loop in free space.

However, this derivation does not apply to the electrons and holes in graphene since they cannot be treated as free particles. As first pointed out by Pancharatnam [19] and later developed by Berry [20], a particle travelling adiabatically on a closed path can undergo a phase shift (in addition to the expected dynamical phase shift) that is dependent on the

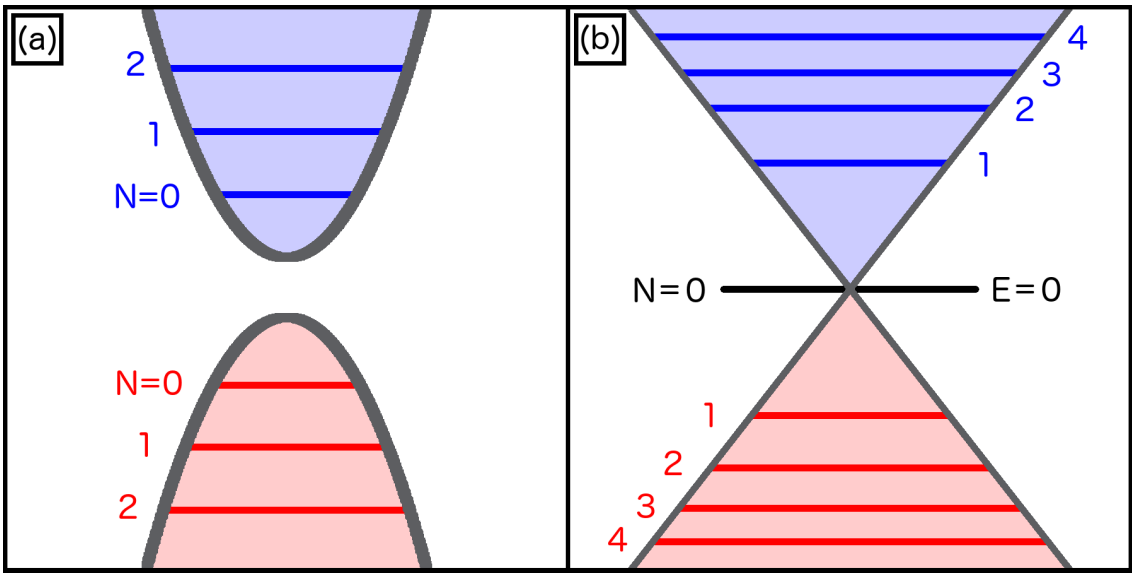

Figure 2.3: An illustration of the difference between the Landau levels in (a) a conventional semiconductor and (b) graphene. In a conventional semiconductor, the energies of the Landau levels are proportional to N, so they are evenly spaced from each other. In graphene and other 2D Dirac cone hosts, the energy levels are proportional to $\sqrt{N}$ and the level with index 0 occurs at $E = 0$.

geometry of the Hamiltonian. Called the Berry phase, this quantity is a gauge-invariant observable that would have significant effects on the motion of particles within a system. For the graphene Hamiltonian, the presence of degenerate points at K and K' causes the system to have a non-trivial Berry phase of π [20], so an adiabatic evolution in a closed loop encircling these degeneracies will flip the sign of the wavefunction. One immediate implication of the non-trivial Berry phase in graphene is the topological protection of the Dirac cone against small perturbations, meaning that low concentrations of defects will not result in the loss of the Dirac point or the conical bandstructure [21]. With respect to the Landau levels in graphene, the Berry phase adds an additional term to the Bohr-Sommerfeld quantization conditions, so that the energy levels are instead dependent on

$$E_N \propto \left(N + \frac{1}{2} \pm \frac{1}{2} \right). \tag{2.14}$$

Further, the orbital energy in a Dirac cone system scales with $\sqrt{N}$ instead of N [22–24], so the Landau levels are not evenly spaced in energy (see Figure 2.3(b)). These levels can be inferred through plots of the quantum Hall conductivity versus the applied field, as shown in

References 16, 17.

Together, the square root dependence of carrier cyclotron mass on carrier density, the uneven spacing of the Landau energies and the existence of a Landau level at $E = 0$ indicate that the physical processes describing carriers in Dirac cone systems are fundamentally different from those of conventional 3D materials. Further, they provide relatively straightforward ways to verify the presence of a Dirac cone and test the dimensionality of any given sample.

2.3 Graphene's Electronic Properties

Given the fundamental differences between the physics of charge transport in classical semiconductors and 2D Dirac cone hosts like graphene, it is perhaps no surprise that the latter should exhibit a host of unique electronic properties, or that these differences can have significant implications toward their implementation into electronic devices.

One of the most well-known of graphene's electronic properties is its strong ambipolar field effect (see Figure 2.4). When isolated and in the absence of an external field, the Fermi level in a graphene sheet lies directly at the Dirac points. It will therefore have an equal amount of free electrons and holes at finite temperature, and at zero temperature there should theoretically be no free carriers. Application of a gate voltage to the sheet or doping it with charged atoms will move the Fermi level into either the conduction or valence band sections of the Dirac cone, resulting in an excess of electrons or holes, respectively. Therefore the production of n- or p-type graphene can be accomplished through an external gate voltage, and the carrier type and concentration can be widely tuned by varying the strength of the applied field. The conductivity of the sheet should also be tuneable in the same manner, and should vanish completely at zero temperature and zero applied field owing to the lack of free carriers. While the ambipolar field effect has previously been observed in metallic films, the magnitude of the change in carrier concentration is typically only a few percent [25], while for graphene it would theoretically be much more dramatic. For example, using the dispersion relation $E_F = v_F|\vec{k}_F|$ and from the carrier concentration given in Equation 2.11,

$$n = \frac{E_F^2}{\pi\hbar^2 v_F^2}, \tag{2.15}$$

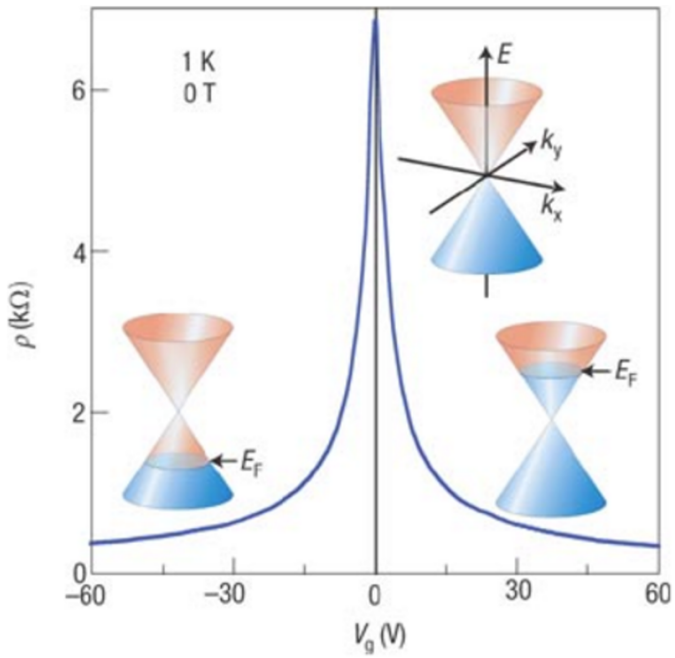

Figure 2.4: An illustration of the ambipolar field effect in graphene. Depending on the polarity and magnitude of the gate voltage V_g, the majority carrier identity and concentration can be tuned, nearly decreasing to zero at $V_g = 0$. As a result, the resistivity of graphene (ρ, vertical axis) varies significantly with the gate voltage. Reprinted by permission from Macmillan Publishers Ltd: A. Geim and K. Novoselov, *Nature Materials*, **6**, 183 (2007) [5]. Copyright 2007.

which gives an increase in carrier concentration from 0 to 7×10^{11} cm^{-2} when the Fermi level is moved from 0 eV to ± 0.1 eV, and up to 7×10^{13} cm^{-2} when the Fermi level is near the edge of the linear regime at ± 1 eV.

Another characteristic relevant to graphene's inclusion in devices is its fast charge propagation. In classical semiconductors such as Si and GaAs, charge carriers attain a maximum saturation velocity only under the influence of high internal fields, and the magnitude of this maximum velocity depends heavily on the material's defect concentration and its temperature. The same is not true for charge propagation in graphene, as the massless Dirac fermions all have identical speeds regardless of the applied voltage, and at $\sim 10^6$ m s^{-1} it is about an order of magnitude higher than the saturation velocities of room-temperature Si or GaAs [26]. One of the most important measures of field-effect transistor (FET) performance is the switching rate, which is related to the carrier velocity in the material the FET is con-

structed from. A graphene-based FET could in theory provide significantly faster transistor switching with a lower power consumption than a comparable device made from a traditional semiconductor.

For a Dirac fermion, the sign of the quantity $\vec{\sigma} \cdot \vec{k}$ in Equation 2.7 describes the helicity of the particle; the spin projection of the fermion on its direction of motion. It commutes with the Dirac Hamiltonian, and is therefore a good quantum number that is subject to conservation. In graphene, the same term describes a pseudospin projection (called the chirality) that is determined by the particular sublattice the quasiparticles reside on. Again, it commutes with the Hamiltonian, which translates to a conservation of pseudospin projection in graphene's quasiparticles. Rather than this value being positive for particles and negative for antiparticles as it is in quantum electrodynamics, it is positive for electrons and negative for holes in graphene at the K point, and the opposite at the K' point.

Another implication of the non-trivial Berry phase shift in graphene is that its carriers are predicted to be immune to backscattering, since the wavefunctions corresponding to a rotation in the clockwise and counterclockwise direction will pick up opposite phase shifts and therefore destructively interfere [27]. This can also be seen as a conservation of chirality, as the backscattering of a quasiparticle incident on a scattering centre corresponds to an intra-valley transition that flips the sign of $\vec{\sigma} \cdot \vec{k}$, a conserved quantity. As such, the mean free path of charge carriers in graphene is expected to be large, perhaps even larger the physical extent of some small device components, opening up the possibility of purely ballistic transport in graphene-based devices [28].

The lack of backscattering is closely related to the paradoxical phenomenon called Klein tunnelling, in which a relativistic Dirac fermion normally incident on a potential barrier (of arbitrary thickness) with an amplitude on the order of the rest mass of that particle will have a tunnelling probability that approaches unity with increasing barrier height [29,30] (Figure 2.5(a)). Since the rest mass of graphene's quasiparticles is zero, any sharp barrier should then qualify as a candidate for Klein tunnelling. Additionally, perfect transmission can occur at multiple oblique angles of incidence depending on the barrier geometry [30](Figure 2.5(b)). Klein tunnelling therefore hinders the construction of graphene-based devices that implement *p-n* or *p-n-p* junctions as a switching mechanism, since the junctions would be transparent

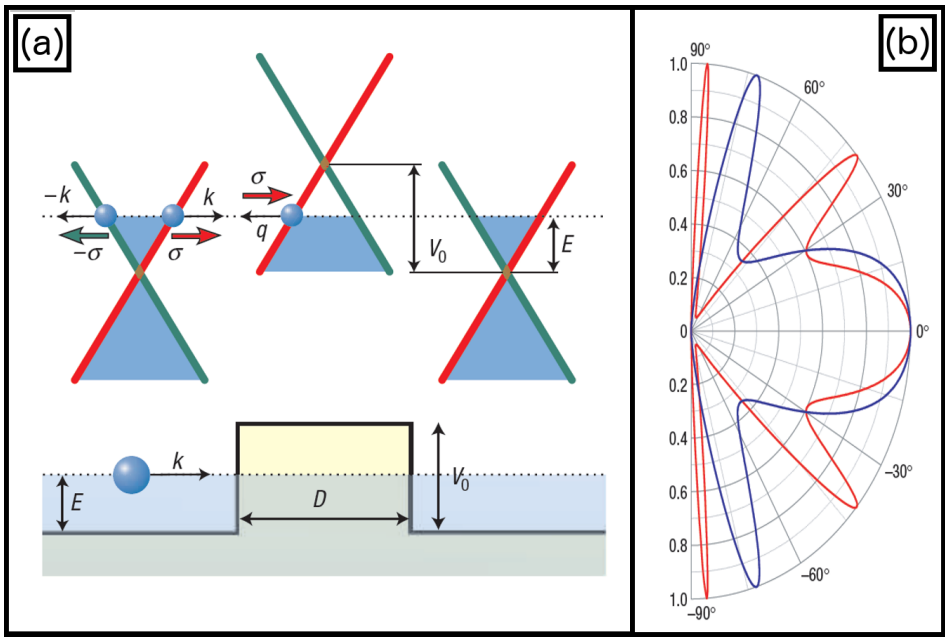

Figure 2.5: An illustration of the Klein tunnelling effect in graphene, adapted from reference 30. In (a), the relationship between Klein tunnelling and the conservation of chirality σ is shown. A right-moving electron normally incident on the barrier can only be scattered into a left-moving hole if chirality is to be conserved, resulting in complete charge transmission through the barrier. In (b), the transmission coefficient is plotted as a function of incident angle for single-layer graphene with two different barrier heights. Reprinted by permission from Macmillan Publishers Ltd: Nature Physics M. Katsnelson *et al.*, *Nature Physics*, **2**, 620 (2006) [30]. Copyright 2006.

to a significant number of carriers. Given that such units are almost ubiquitous in electronic devices, being the major components of FETs, bipolar junction transistors and diodes, this effect complicates a transition to graphene-based electronics.

There are a multitude of other properties that have made graphene a material of intense interest in a wide variety of fields, ranging from basic physics research to specific industrial applications. At very low temperatures, graphene exhibits the fractional quantum Hall effect, meaning that the Hall conductance of the material is quantized in fractional rather than integer units of e^2/h [31]. This phenomenon is related to the topological order that causes the degenerate point in the Dirac cone to be protected, and allows for the study of anyonic quasiparticles that demonstrate fractional charge and fractional statistics [32]. Graphene's high in-plane conductivity and, as a monolayer, high optical transparency (though it absorbs more visible light than expected for an atom-thick material [33]) make it an ideal transparent

conductor for photovoltaic cells and touch screens. The extreme strength of the sp^2 bonds lead to graphene and its derivatives having some of the highest tensile strengths of any material ever recorded [34].

However, the main features that make it a promising candidate for conventional electronic device construction are the predicted high carrier mobility, ballistic transport, ambipolar field effect and tuneable conductivity. As for non-traditional electronic devices, it has been suggested that carrier spin can be preserved on the micron scale [35], suggesting that graphene could play a major role in the advent of spintronic devices. Further, the pseudospin and valley degrees of freedom have been suggested as added dimensions for electronic signalling in so-called pseudospintronic [36] and valleytronic [37] devices.

Now that I have laid out just a few of the interesting and appealing properties of graphene and other 2D Dirac cone materials, I will describe the efforts that eventually led to the production of the first freestanding graphene sheet.

2.4 Synthesis and Characterization of Graphene Monolayers

There are two approaches to the fabrication of graphene, top-down methods in which graphene-like sheets are isolated from larger 3D structures, and bottom-up methods in which the graphene-like sheets are assembled from C atoms. Some of the earliest mesoscopic graphite samples were obtained from graphite oxide [38], a compound produced by exposing graphite powder to strong oxidizing agents. This inserts functional groups between the graphitic sheets, forcing them to separate significantly from each other while preserving their hexagonal ring structure (though not their planarity). Quickly heating graphite oxide results in the deflagration of extremely thin graphite oxide flakes, which were first observed through transmission electron microscopy (TEM) by Ruess and Vogt in 1948 [39]. Boehm and Hoffman would later improve slightly on their imaging techniques, but while both groups produced samples that most likely contained graphene-like monolayers, isolation and characterization of a particular flake from the dried reduction products was not feasible at the time. Further, TEM alone has been shown to be insufficient for distinguishing graphene monolayers from

few-layer graphene sheets [25].

A number of other lamellar intercalated graphite structures exist in which the planar structure of the graphite is conserved. In these graphene intercalation compounds, the only interaction between the graphene sheets and intercalants is charge transfer, as opposed to graphite oxide in which the functional groups are covalently bonded to the graphene sheets. Since graphene is amphoteric, the intercalant can be either a Lewis acid or base [40]. Typical intercalants have included donors such as alkali metal compounds, alkaline earth metals and lanthanides, while acceptors have included halogens, bromides, fluorides and oxyhalides [41, 42]. Though these structures also spatially separate the graphite layers and therefore reduce the van der Waals forces between them, the end product typically has a higher exfoliation energy than graphite due to the charge transfer between the graphene sheets and the intercalant [43].

Rather than the top-down approach of exfoliating graphene layers from modified graphite structures, many researchers have opted for the bottom-up approach of synthesizing graphene and thin graphite on the surfaces of crystals through epitaxial growth, deposition on amorphous surfaces or impurity segregation. In chemical vapour deposition (CVD), the carbon is sourced from a gaseous molecule (typically methane), which adsorbs to the substrate surface and is then decomposed to leave only C atoms behind. Depending on the process, this decomposition can occur as the gas adsorbs (i.e., the exposure to the carbon-containing gas is done with the substrate at temperature), or the decomposition can be initialized once the substrate surface is completely covered in the adsorbant. Segregation methods typically involve heating the substrate in a carbonic gas until it becomes soluble to carbon and the gas gets absorbed into the substrate bulk. Upon cooling, the substrate reverts to an insoluble state, and the carbon segregates to the surface to form graphene islands. A more recent technique for graphene production involves the high-temperature sublimation of Si from 4H- and 6H-SiC, which can result in the growth of large-area graphene monolayers and few-layer graphene on either a Si-terminated or C-terminated face [44]. These samples show some indication of 2D character including a non-trivial Berry phase [44], but have much lower mobilities than that expected of freestanding graphene.

However, it would be a relatively simple top-down method that led to the first confirmed

freestanding graphene monolayer. In 2004, Novoselov *et al.* mechanically exfoliated thin sections of highly oriented pyrolitic graphite (a graphite polycrystal with almost perfectly aligned crystallites, produced through the thermal stressing of natural graphite [45]) with adhesive tape. The flakes were then suspended in acetone and deposited onto the surface oxide of an n^+-doped Si wafer, followed by sonication in propanol to remove thicker flakes. Candidate monolayers were selected based on their simultaneous presence in scanning electron microscope (SEM) images and absence in optical microscopy, and their thicknesses were measured with non-contact atomic force microscopy (nc-AFM) to count the number of graphene layers present. This work was remarkable for a number of reasons, including the simple and inexpensive mechanical exfoliation process that they introduced, their method of differentiating graphene monolayers and thin multilayers from nm-thick graphite through optical contrast imaging and their production of large-area few-layer graphene (up to 10 μm in lateral size) that were stable on an amorphous surface and in liquid suspension.

While monolayer graphene samples were observed in their 2004 study, they were not isolated nor were they electronically characterized. Instead, only crystals of few-layer graphene were lithographically patterned so that their electronic properties could be quantified across a range of gating voltages and temperatures. Carrier mobilities of up to 1.5×10^4 cm^2 V^{-1} s^{-1} were observed at room temperature, an order of magnitude larger than those typically quoted for bulk Si. A significant ambipolar field effect was observed, with resistivity of the sheet changing by two orders of magnitude through the tuning of the gate voltage. Few-layer graphene is calculated to be a semi-metal with a significant overlap between the VB and CB, so it is not surprising that a high conductivity was measured even in the low-temperature, low-field experiments. Overall, it was found to possess characteristics that would make it an excellent transparent conductor, but as a semi-metal with a high zero-bias conductivity it would be a poor choice for transistors. In such devices, an on-off conductivity ratio of at least 10^4 (ideally 10^7) is necessary for the viable production of logic signals [46].

In another experiment a year later, Novoselov *et al.* would successfully isolate graphene monolayers and perform similar measurements of their electronic characteristics [16]. They found similar carrier mobilities to the few-layer graphene samples, but were able to demonstrate definitively that the carriers behaved like Dirac fermions by observing the square root

relationship between cyclotron mass and carrier concentration. From this relationship, Geim and Novoselov inferred a Fermi velocity that agreed with its predicted value of 1×10^6 m s^{-1}. Additionally, they extrapolated a phase shift in the Landau quantization that is consistent with a Berry phase of π.

Two years later, these graphene monolayers were shown to be stable when suspended in ambient conditions, demonstrating that the inherent instability predicted decades earlier was not as prohibitive as once thought. [47]. A low-energy electron diffraction (LEED) measurement of their structure found a long-range (about 10 nm) rippling within the sheet rather than a perfectly flat geometry like that of idealized graphene. It is this rippling that contributes to the stability of the material, allowing for the existence of large-scale graphene sheets that would otherwise be thermodynamically unstable [48]. However, it also introduces a chemical potential to the regions surrounding peaks and valleys in the sheet that is proportional to the local curvature [49]. As such, the Fermi level in graphene is not consistent throughout the sheet, resulting in regions of unavoidable n- and p-type doping. This produces a residual concentration of excess carriers even at low temperatures and zero gating voltage, which means that the conductivity of the graphene sheet can never be turned completely off. Monolayer graphene is therefore better described as a semi-metal than a zero-gap semiconductor, and as such is undesirable for transistor construction as it invariably results in poor switching ratios.

Since 2004, increasingly larger and higher quality graphene sheets have continued to be produced. The carrier mobility of 1.5×10^4 cm^2 V^{-1} s^{-1} reported by Geim and Novoselov was found to be limited by surface phonons in the SiO_2 substrate [50]; published reports of mobilities up to 2×10^5 cm^2 V^{-1} s^{-1} now regularly occur [51, 52], and one report of the mobility exceeding 10^6 cm^2 V^{-1} s^{-1} [53] has surfaced. CVD-derived graphene polycrystalline sheets have nearly reached the scale of metres [54], and recent advances in controlling CVD nucleation have resulted in single crystal domains on the order of a few hundred microns [55]. However, the incorporation of these sheets into electronic devices has been hindered by the uncontrollable high conductivity that results from the combination of a negligible spin-orbit coupling (SOC) induced bandgap and the unavoidable carrier concentration induced by its rippled surface.

A number of strategies for widening the bandgap in graphene monolayers have been proposed or experimentally explored. One avenue involves removing the inversion symmetry, which can be accomplished by adsorbing atoms or molecules to one face of the graphene crystal or placing the sheet on an interacting substrate. Some possible adsorbants include water [56, 57], Na [58] and Ni [59], with gaps up to 740 meV reported for Na-adsorbed graphene placed on an Ir superlattice [58]. Substrate-induced bandgaps have been observed on Ir(111) [60] and are predicted to occur in graphene on hexagonal BN [61] and graphene sandwiched between two layers of hexagonal BN [62], but any misalignment between the sheets is expected to result in semi-metallic graphene [63], which explains why experimentally no gap has yet been observed [64, 65].

While the Dirac cone is topologically protected against low concentrations of impurity sites, impurity concentrations of a few percent have been shown to produce bandgaps of up to 0.67 eV [66]. Defects in the graphene structure can also cause a global bandgap opening in the sheet at significant concentrations [67]. Reducing the dimensionality of graphene by cutting it into nanoribbons a few Å wide can open a bandgap, the size of which is dependent on the width of the nanoribbon and the type of edge termination [68].

Finally, it is worth mentioning bilayer graphene as a means of producing a gapped 2D material. Freestanding bilayer graphene is semi-metallic and possesses band extrema that are neither parabolic nor conical [69], though a Dirac cone may be induced by slightly rotating the sheets relative to each other [70]. Whether AA- or AB- stacked, bilayer graphene is inversion symmetric. This symmetry can be broken by any of the methods mentioned for monolayer graphene, like one-sided adsorption or an interacting substrate. Unlike in monolayer graphene, the inversion symmetry can also be broken through a gate voltage since it raises the potential of one sheet relative to the other. As a result, gated bilayer graphene has a bandgap that is tuneable from semi-metallic up to 250 meV [69, 71] while retaining very high carrier mobilities comparable to those of single-layer graphene. Without a Dirac cone, though, it is not anticipated to exhibit any of the other desirable characteristics associated with massless Dirac fermion-like carrier propagation. Despite this, its massive charge carriers still exhibit chirality and are therefore also capable of Klein tunnelling [30], though to a lesser extent than monolayer graphene.

There have been numerous attempts at producing graphene-based FETs that might one day outperform the Si-based CMOS, the current industry standard. In Geim and Novoselov's 2004 report on the ambipolar field effect in few-layer graphene [4], the flakes deposited on the native surface oxide of doped Si were essentially back-gated transistors. However, such devices have implicit issues with parasitic capacitance from the oxide layer which increases power consumption and dynamic response time, and would be nearly impossible to integrate into a compact device layout. The first top-gated graphene field-effect device based on exfoliated few-layer graphene flakes was produced in 2007 [72] and was found to have mobilities exceeding those of the best Si-based devices, but standard transistor metrics were not measured. Since then, true FETs have been produced with single-layer graphene grown via epitaxy [73] and CVD [74]. Devices with cut-off frequencies in the few hundreds of GHz range have been reported [75], in keeping with the expectation that graphene-based devices should excel in fast switching applications.

However, the persistent problems of poor switching ratios and a lack of saturation behaviour [46] have prevented graphene-based FETs from outperforming their 3D Si-based counterparts. Proposed redesigns of device layout that better accommodate graphene's unique electronic properties include TFETs [76] and graphene bilayer pseudospin FETs [77], but traditional transistor designs could be implemented if only a graphene-like 2D material with a gapped Dirac cone could be produced. In the next section, I will outline the currently known members of the 2D material family, focusing on the characteristics that make silicene one of the most intriguing alternatives to graphene.

2.5 Alternative 2D Materials

It has been estimated that there may be more than 500 possible 2D materials of varying composition [78]. Carbon itself is capable of forming a variety of 2D sheets that are structurally distinct from graphene, such as the various forms of graphyne and graphdiyne (Figure 2.6(a)), planar materials that contain both sp and sp^2 hybridized C [79]. A number of the graphyne structures are calculated to host gapless Dirac cones [80] with a Fermi velocity of about half that of graphene [81]. Some forms are even expected to have anisotropic gapless Dirac cones,

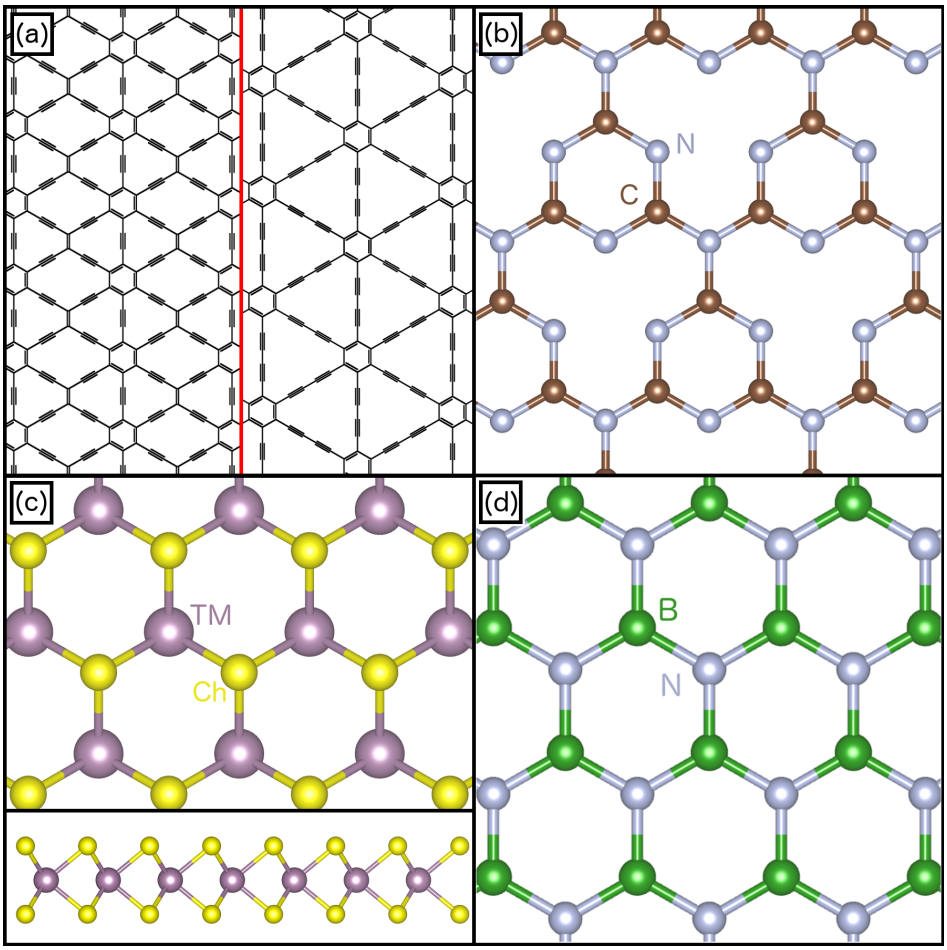

Figure 2.6: (a) Alternative C-based 2D materials 6,6,12-graphyne (left panel) and graphdiyne (right panel). (b) g-C_3N_4. (c) The general structure of monolayer TMDCs such as MoS_2. (d) Hexagonal boron nitride, an insulating, planar binary graphene analogue. Structural visualizations in (b), (c) and (d) created with VESTA software [8].

implying a directionally-dependent Fermi velocity [82]. In these materials, mechanical strain may be used to influence the absence or presence of Dirac cones [80,81]. Given that the C sites in graphyne are not equivalent and that the unit cells are much more complex than that of graphene (the first BZ of 6,6,12-graphyne is rectangular, for instance), the presence of Dirac cones in these materials indicates that the conditions required for their formation may be less strict than once thought. Graphdiyne, on the other hand, is expected to be a semiconductor with a direct bandgap of about 0.46 eV [83] in its α phase. However, this value is tuneable through the application of biaxial strain (which makes it more insulating) or unaxial strain (which can reduce the gap to zero and introduce a Dirac cone-like bandstructure) [84, 85]. These graphene alternatives certainly warrant continued investigation.

As mentioned previously, graphene's electronic structure can be modified significantly through the adsorption of atoms and molecules onto its surface. Of particular interest has been hydrogen adsorption, which if done in a periodic arrangement yields two new, chemically distinct compounds: graphane and graphone (or half-graphane). In graphane, the H atoms are located directly above the A sites and below the B sites, preserving inversion symmetry. However, because its C atoms are sp^3 hybridized, a Dirac cone is not present and a substantial direct bandgap (about 5 eV) opens. Graphone, in which H atoms are only patterned on one side of the sheet and attached to one particular sublattice of C sites, has a smaller, indirect bandgap (0.43 eV). Both materials have been suggested as candidate materials for FET applications [86], though their magnetic characteristics have been the primary focus of research.

Graphitic C_3N_4 is a material that is structurally similar to graphite – as its name suggests – but with N substituting in for one of the C sites and triangular vacancies permeating the sheet [87] (Figure 2.6(b)). It has a bandgap of 2.7 eV [88], and when used as a growth template for monolayer graphene, it is expected to open up a bandgap of 70 meV in the graphene sheet without significant changes to the linear bandstructure near the Dirac point [89].

Another class of materials relevant to the field of 2D electronics are the transition metal dichalcogenides (TMDCs, having the formula MX_2 where M = Nb, Mo, Ta, W and X = S, Se, Te). Similar to graphene, these materials consist of stacked layers with a weak inter-plane interaction, allowing for the mechanical exfoliation of monolayers. In bulk, the Nb and Ta dichalcogenides are metallic [90, 91], and are known to exhibit superconductivity, and the Mo and W dichalcogenides are semiconductors with bandgaps in the 1.0 eV – 1.4 eV range. When reduced to a single layer of thickness, bandgaps in the Mo and W dichalcogenides are expected to increase slightly and transition from indirect to direct, which has led to their candidacy for nanophotonic applications [92]. While the electronic states in transition metal dichalcogenides do not exhibit the Dirac cone dispersion characteristic to graphene, there is evidence to suggest that the excitonic states in these materials behave as massless Dirac fermion quasiparticles [93].

Hexagonal BN has attracted significant interest since it has the same basic structure as graphite and a similar lattice constant, but is a binary compound and a bulk insulator with a

direct gap of > 5 eV. While the electronic properties of hexagonal BN itself are not conducive to 2D electronic devices, monolayer structures consisting of extremely small, randomly scattered regions of sp^2-hybridized hexagonal BN and graphene have been synthesized [94], and show electronic properties that are distinct from pure graphene or hexagonal BN. By varying the ratio of C to BN, the authors were able to tune the bandgap to values intermediate between graphene's semi-metallic 0 eV and hexagonal BN's insulating > 5 eV.

2.6 Monoatomic Graphene Analogues

Silicon and the other Group 14 elements have valence electron structures similar to that of carbon, and as such the possibility of producing graphene analogues out of these materials (silicene, germanene, stanene and – plumbumene, I suppose – though a Pb-based graphene analogue has not yet been explored in the literature) has been considered for some time [95]. Of these, silicene is the most well-known and intensely researched. Si has a larger atomic radius and bond length than C, which results in much weaker π orbital overlap giving it a strong energetic preference for the purely σ-bonded sp^3 hybridization scheme. For this reason, there is no Si-based graphite analogue since it would be prone to clustering into the tetrahedral bulk silicon structure. Silicene therefore cannot be sourced from micromechanical cleavage, like the exfoliation of graphene from bulk graphite.

Interestingly, early *ab initio* structural investigations of the Si-based analogue to benzene, called hexasilabenzene, actually did suggest that the planar, sp^2-hybridized D_{6h} structure was the energetically favoured one [96,97]. However, this structure was soon calculated to have a vibrational frequency bordering on imaginary, leading to its dismissal as unstable. Instead, corrugated hexasiliabenzene in the form of the "chair-like" D_{3d} symmetry was found to be the optimal stable structure.

Hypothetically, if a single layer were to be removed from the Si(111) crystal shown in Figure 2.7(a), it would essentially result in a graphene-like monolayer with the hexasilabenzene-like chair buckling configuration. This monolayer, like graphene, would be inversion symmetric as the A sites all protrude the same distance above the central plane as the B sites protrude below it (Figure 2.7)(b)). When isolated, the buckling distance Δ for such a mono-

layer would be unlikely to have the same value that it did while it was embedded in the Si(111) crystal, and it is reasonable to assume that this value would decrease when the σ bonds with the Si sites above and below the monolayer are severed.

It could be expected, then, that if a stable inversion-symmetric form of silicene exists it would likely have a corrugation somewhere between that of graphene (0 Å) and Si(111) (0.78 Å [98]). Early DFT calculations found two stable buckling values for silicene, called the "low-buckling" (LB) and "high-buckling" (HB) structures [99]. LB silicene was found to have a buckling distance of $\Delta = 0.44$ Å and a Si–Si distance of $d_{Si} = 2.25$ Å, with $\Delta = 2.13$ Å and $d_{Si} = 2.62$ Å for the HB structure. The HB structure was found to have imaginary phonon frequencies and the tendency to cluster in DFT calculations, suggesting that it is inherently unstable. Henceforth, any mention of freestanding silicene will be referring to the much more likely LB structure.

Even though inversion symmetry is present in freestanding silicene, the TB derivation of its low-energy electronic bandstructure differs significantly from that of graphene, owing to the characteristics of the valence state (a superposition of sp^2 and sp^3 orbitals, as well as the presence of the unoccupied $3d$ orbitals) and the non-negligible SOC in Si. These effects combine to introduce a small energy $\Delta\epsilon$ into the diagonal of the Hamiltonian matrix [100] (shown here near the K point):

$$\hat{H}(\vec{q}) = \begin{pmatrix} \Delta\epsilon & v_F(q_x - iq_y) \\ v_F(q_x + iq_y) & \Delta\epsilon \end{pmatrix}. \tag{2.16}$$

such that the energy dispersion is given by

$$E(\vec{q}) = \pm\sqrt{\Delta\epsilon^2 + v_F^2 \left|\vec{q}\right|^2}. \tag{2.17}$$

At $\vec{q} = 0$ (i.e., $\vec{k} = \vec{K}$), this term opens up a gap of $E_g = 2\Delta\epsilon$, which is typically quoted at a few meV [100], but does not distort the Dirac cone to any significant degree. Therefore freestanding silicene, unlike graphene, has a small but non-negligible direct band gap at the K and K' points, though both materials are calculated to have charge-carrying quasiparticles that resemble massless Dirac fermions. As I will discuss in the next section, silicene's corrugation and the resulting bandgap allow it to avoid some of the pitfalls that

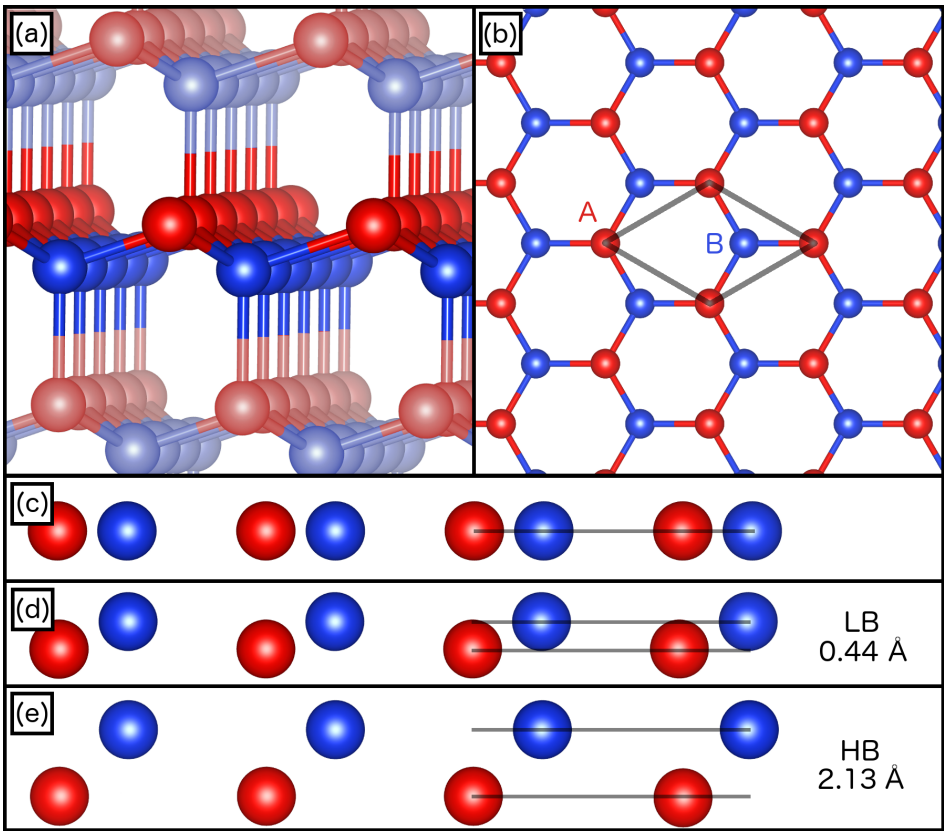

Figure 2.7: (a) The structure of bulk Si with a single (111) plane highlighted. (b) Top view of the potential silicene structures, showing the A and B sites and the unit cell. (c) Side view of the unstable planar silicene structure with no buckling. (d) Side view of LB silicene showing the corrugation in the sheet that separates the A and B sites in the vertical direction. (e) Side view of HB silicene with a larger vertical separation between A and B sites. Structural visualization created with VESTA software [8].

have hindered graphene's uptake into semiconductor device manufacturing. In addition, the industry is already well-equipped to handle Si-based devices, so incorporating silicene into modern electronics would require less retooling than it would for graphene.

With respect to producing silicene by top-down means, while the Si(111) crystal can be imagined as stacked sheets of buckled silicene-like planes, the inter-sheet bonding in this scenario is exactly as strong as the intra-sheet bonding, so cleavage along a single Si(111) face should not be expected. A corrugated, silicene-like sheet of Si atoms is one of the main components of the "3R" structure of $CaSi_2$, which structurally appears similar to the graphite intercalation compounds. The material as a whole is metallic, but DFT calculations and angle-resolved photoemission spectroscopy (ARPES) measurements indicate that a Dirac

cone-like dispersion may exist at the Si K and H corners of the 3D Brillouin zone. Considering the chemical exfoliation of graphene from graphite oxide or graphite intercalation compounds, it is reasonable to think that one could derive silicene-like Si nanosheets from $CaSi_2$. In the first reported attempt [101], in order to weaken the ionic bonding between layers the Si sheet was heavily and irreversibly doped with an appreciable concentration of Mg, drastically altering the electronic structure. Further, upon exfoliation the $Si_{1.85}Mg_{0.15}$ sheet became completely oxidized, which is to be expected for an uncapped, isolated silicene-like sheet exposed to ambient conditions. A subsequent study [102] diffused K into the lattice, which substituted into the Ca and Si sites and weakened the interaction between them enough for exfoliation, but could thereafter be retrieved with HCl. As a result, the authors observed the formation of nanosheets composed almost entirely of Si. LEED and TEM data of these sheets were interpreted as suggesting a structure that was not simply the Si(111) face of a bulk crystal, but atomic-resolution imaging techniques were not employed to further analyze the structure and it remains unclear whether or not it is truly silicene-like [103]. Bottom-up silicene growth methods will be discussed later in this Chapter, as well as in greater detail in Chapter 3.

Clearly, given the presence of a gapped Dirac cone in LB silicene's bandstructure, this material deserves a thorough examination to determine whether it would be more suitable for electronic applications than its C-based cousin. While silicene research is still in its relative infancy, already it appears to suggest that silicene will have many of the desirable characteristics of graphene, and the corrugated structure opens the possibility for many more. I will now review the salient theoretical literature on freestanding silicene, after which I will describe the efforts that have been made to grow physical silicene samples and the difficulties that lie therein.

2.7 Theoretical Properties of Freestanding Silicene

Takeda and Shiraishi [95] were the first to determine that silicene (and germanene) monolayers were more stable in a corrugated phase than a planar one, and published an *ab initio* DFT calculation of its electronic bandstructure. Since their calculation neglected spin-polarization

the SOC-induced meV bandgap did not appear and the silicene was instead determined to be a zero-gap semiconductor with a linear dispersion near the K and K'-points, much like graphene. However, the authors did not consider the implications of the Dirac cone in their study or quantify the Fermi velocity in silicene, perhaps because this study predated the first successful synthesis of graphene.

A later study by Cahangirov *et al.* more thoroughly examined the electronic structures of planar, LB and HB silicene and germanene [99]. While the HB silicene structure was determined to be metallic, both the planar and LB silicene structures were shown to host gapless Dirac cones (the calculations were not spin-polarized, so the SOC-induced gap did not appear) with Fermi velocities approximately equal to that of graphene, i.e. 10^6 m s^{-1}. In order to refine this Fermi velocity estimate, I have performed a similar DFT calculation and plotted the bandstructure alongside that of graphene, shown in Figure 2.8. As is apparent in the inset, which shows the bandstructures in the vicinity of the Dirac point, the slope of LB silicene's Dirac cone is significantly smaller than that of graphene's, so much so that the Fermi velocity in silicene should actually be closer to 0.5×10^6 m s^{-1}, or about half that of graphene. This value is still about an order of magnitude larger than the saturation velocity in most semiconductors, indicating that silicene would also be a good candidate for fast transistors, though it would be slightly slower than an equivalent device based on graphene.

As a Dirac cone host, silicene is also expected to exhibit a strong ambipolar field effect. As derived in Equation 2.15, the carrier concentration is inversely proportional to v_F^2, so the number of free carriers produced per unit of applied field will be about four times smaller in silicene than in graphene. However, in addition to shifting the Fermi level in the silicene, the application of a perpendicular electric field will also break the inversion symmetry of the sheet. Much like in bilayer graphene, where the external field puts one sheet at a higher potential than the other, the corrugation of silicene puts one sublattice at a higher potential than the other when a similar field is applied. It has been estimated that this will allow for a tuneable bandgap of up to 0.2 eV in single-layer silicene [104] and perhaps even more if the silicene is sandwiched between layers of hexagonal BN [105].

Tsai *et al.* realized shortly thereafter that the magnitude of the band opening under an external field will depend on the spin and valley of the carriers [106]. Suitably gated

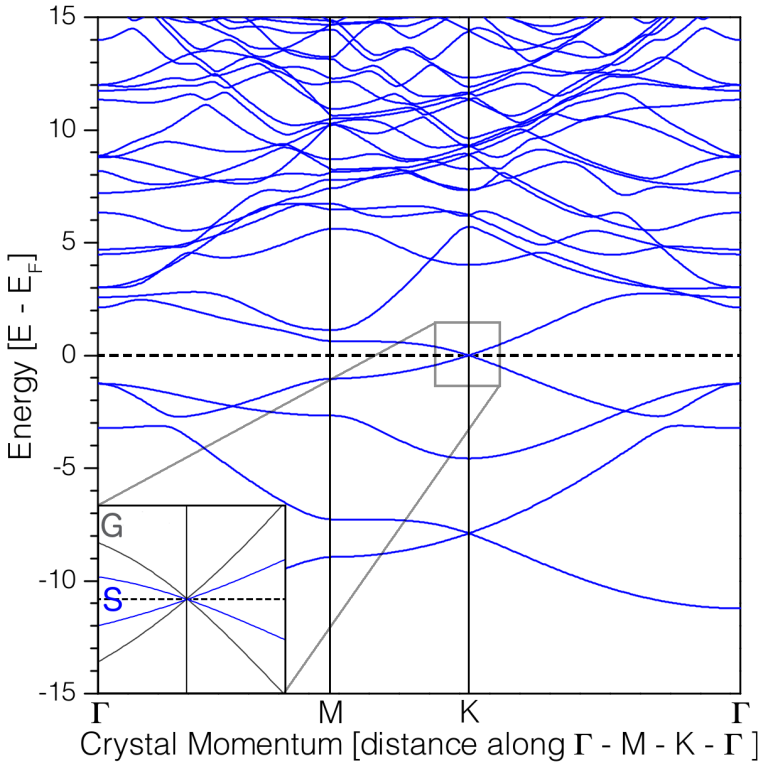

Figure 2.8: The DFT-calculated bandstructure of freestanding silicene, exhibiting a gapless linear band crossing at the K momentum and the Fermi level E_F. In the inset, the Dirac cone region is compared to a similar DFT calculation of the bandstructure of graphene, allowing for the comparison of their Fermi velocities.

monolayer silicene can be used to provide almost completely spin-polarized carriers, with Tsai *et al.* estimating up to 98% spin polarization possible depending on the shape of the filter. This has obvious implications toward spintronic devices, and the authors provide a blueprint for developing a spin injection system from a single sheet of gated silicene. Further, with its appreciable SOC, silicene has been suggested as a possible arena in which one can observe the quantum spin Hall effect [107] at experimentally attainable temperatures, though with even heavier Group 14 monolayers the SOC effect increases and the quantum spin Hall effect may even appear near room temperature [108].

Another consequence of silicene's corrugation and the preference for Si to participate in sp^3 hybridization is an increased chemical sensitivity compared to graphene. Graphene's π

network is complete, so that there are no dangling bonds for atoms or molecules to attach to. The same cannot be said for silicene, as the dissolution of the weak π network to form pure sp^3 bonds is a highly exothermic process, and is expected to happen with a variety of atoms or molecules. Silicene sheets are therefore expected to be much less stable than their carbon-based counterparts in ambient conditions, which limits their utility unless they can be passivated or stabilized in some other manner, but this also implies that a variety of materials with the potential that have the potential to alter silicene's electronic structure in beneficial ways [109].

For example, complete H saturation of a silicene sheet produces silicane, the Si-based analogue to graphane. Silicane has been calculated to have a bandgap of 2.9 eV that is tuneable with H concentration [110, 111], but it is indirect and therefore not ideal for many optical and electronic purposes. Perhaps the most interesting species for adsorption onto silicene are the halogens, particularly fluorosilicene. Halogenated silicene is expected to have a tuneable direct bandgap and to maintain high carrier mobility [112], though the Dirac cone would be lost and the carriers would inherit a small mass [113]. However, the major advantage to halogenation is that it shoud confer stability to the silicene sheets [112, 114] as well as passivate them from the influence of other gases. Lithiation of silicene is also expected to improve stability, but only introduces a small direct gap [115].

Freestanding mulitlayers of silicene have also been theoretically explored. Unlike few-layer graphene, the inter-layer interaction in multilayer silicene is expected to be just as strong as the intra-layer bonding, so multilayer silicene should not be expected to retain any sp^2-like electronic character. Bilayers have been reported with both AA- and AB-stacking, with their preferred stacking arrangement being somewhat controversial [116–118]. Further, they have been reported as metallic [116, 119] or semiconducting with an 0.22 eV [118] or 0.55 eV [114] gap. The semiconducting case would seem to be the more plausible one, as the bonds in bilayer silicene are more sp^3-like than in monolayer silicene. When a transverse electric field is applied to bilayer silicene, a widely-tuneable gap of up to 1.13 eV is predicted [117], which far surpasses the 250 meV gap that can be induced in bilayer graphene [69, 71] or hexagonal BN-sandwiched monolayer silicene [105]. Thicker multilayers have been calculated as preferring an ABC-stacking scheme and having a semi-metallic bandstructure [116], but this prediction

seems to contradict the notion that thick multilayers should slowly become more and more bulk-like as the sample leaves the mesoscopic regime.

In summary, in terms of the qualities most relevant to electronic devices, there are a number of ways in which graphene and silicene are similar, and a few key aspects in which they differ. At a glance, both are expected to have very high electron mobilities, ambipolar field effects and carriers that behave like massless Dirac fermions. Silicene, however, is expected to have a bandgap and spin-polarization that are tuneable through gating at monolayer thickness, and should therefore be easier to integrate into electronic and spintronic devices. Unfortunately, with no Si-based graphite analogue, producing silicene is not as simple as exfoliation from a bulk crystal with adhesive tape. Instead, silicene has to be grown on a supporting substrate in a bottom-up rather than a top-down process. The particular substrate should be chosen such that it will interact weakly with the silicon, otherwise it is likely to just form a bound adlayer on the top.

2.8 Epitaxial Silicene Monolayers on Ag(111)

The interaction between Ag and Si is typically quite weak [120], so Ag substrates have been of considerable interest since the first attempts at the epitaxial growth of silicene. Atomically thin structures of Si were imaged with scanning-tunnelling microscopy (STM) on the Ag(110) [121] and Ag(001) [122] faces in the form of long, aligned nanoribbons and more disordered arrays of nanowires, respectively. They showed a remarkable resistance to oxidation along their edges, which was observed to start at the ends and travel inward like a burning match. The nanoribbons on Ag(110) were thought to be composed of hexagonal rings with a zigzag termination, and were eventually observed to come in a range of widths.

ARPES measurements of the Si/Ag(110) system were interpreted as suggesting the presence of a gapped Dirac cone [123]. The gap was thought to originate from an arching of the silicene nanoribbons that resulted from being anchored to the Ag substrate along their edges, which was likely the reason for their resistance to oxidation along their edges. Due to transfer from the Ag substrate into the nanoribbons, their Fermi level was shifted from the centre of the gap into the CB portion of the cone. However, it is important to note that the linear

bandstructure was only displayed in the k_x plane and the dispersion on the k_y plane was not reported, so it could not be confirmed that the electronic structure actually corresponded to an isotropic Dirac cone. My own DFT analyses of epitaxial nanoribbons were not fruitful, as I was unable to find a stable hexagonal nanoribbon structure that would be consistent with the STM images of the surface. These structures would eventually be shown to be the result of an STM tip artefact [124].

Still, the growth of monolayer Si structures on the Ag(110) and Ag(001) faces led researchers to believe that a large-area 2D silicene sheet would be viable on the Ag(111) face [125]. Indeed, the first report of such a structure appeared within a year of this prediction, in the form of STM and LEED measurements of a $(\sqrt{7} \times \sqrt{7})$R19.1° silicene supercell on the $(2\sqrt{3} \times 2\sqrt{3})$R30° Ag(111) template by Lalmi *et al.* [122]. Their sample was produced through the resistive heating of a Si wafer with a direct current source near a single crystal of Ag(111) heated to 250 °C. They reported a rate of about 0.1 monolayer min^{-1}, and inferred a slight corrugation in the sheet. The Si–Si bond distance was found to be between 1.8 Å and 2 Å, which is appreciably shorter than the shortest Si–Si bond length ever observed (2.06 Å for the Si–Si triple bond in disilyne [126]). This unrealistically small value indicates that either the corrugation was actually much larger than the authors anticipated or their structural model of hexagonal Si was invalid.

Vogt *et al.* [127] argued that the hexagonal STM pattern observed by Lalmi *et al.* was actually the bare Ag(111) surface, but with a tip-induced contrast that flipped the dark and light regions. This hypothesis agrees well with the apparent spacing of about 3 Å between points, as the distance from surface Ag atom to surface Ag atom on the Ag(111) face is 2.88 Å. However, it does not account for the observed $(2\sqrt{3} \times 2\sqrt{3})$R30° LEED pattern, which was alluded to but not shown in Lalmi *et al.* [122].

In the same paper, Vogt *et al.* presented their own epitaxially-grown monolayer. Theirs was produced under similar conditions to the Lalmi sample, but their observed deposition rate was much slower at 1 ML h^{-1}. Vogt *et al.* inferred a $(3 \times 3)/(4 \times 4)$ Si/Ag(111) structure from LEED and STM analysis (see Figure 3.1 and the surrounding text for a description of Wood's notation), a model of which is shown in Figure 2.9. Using DFT calculations, this model was shown to be energetically stable. Corrugation in this model produces two

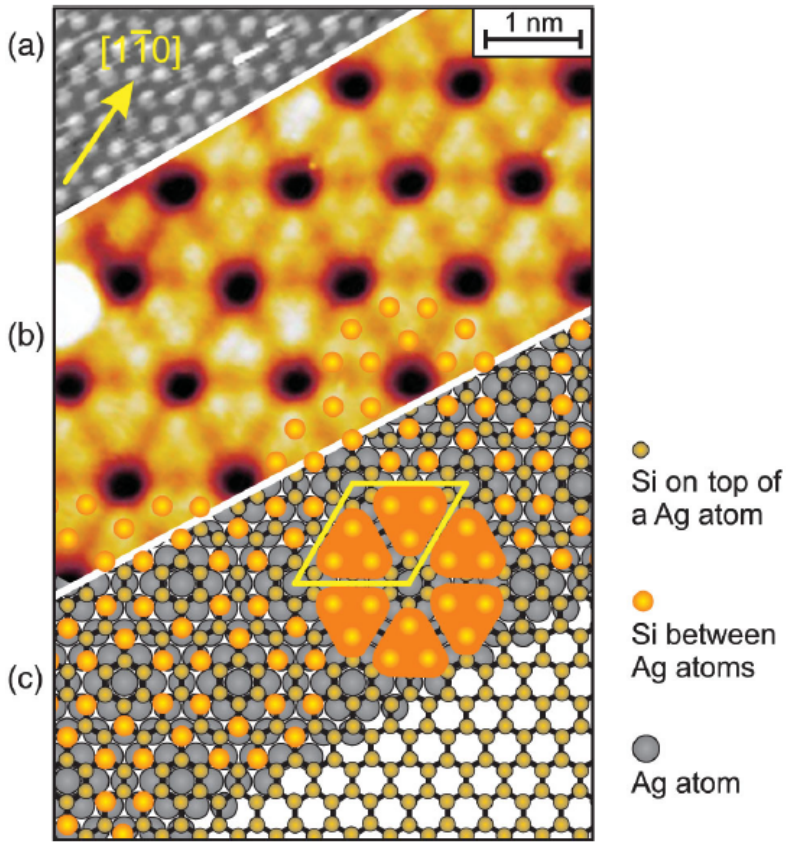

Figure 2.9: STM images of (a) the bare Ag surface and (b) the $(3 \times 3)/(4 \times 4)$ epitaxial silicene reconstruction, with (c) an atomic model that describes the measured STM image. Reprinted figure with permission from P. Vogt *et al.*, *Physical Review Letters* **108**, 155501 (2012) [127]. Copyright 2012 by the American Physical Society.

inequivalent rings, one with entirely lower-tier Si sites and the other with alternating upper- and lower-tier sites. Each unit cell contains 18 Si atoms, with 6 occupying the upper-tier and 12 in the lower-tier. Si–Si distances range from 2.28 Å in the flat lower-tier rings to 2.32 Å in the corrugated mixed-tier rings, with bond angles ranging from 110° in the corrugated rings to 120° in the flat rings. The optimal buckling distance was found to be 0.75 Å, which is only slightly smaller than the buckling of a single sheet of Si(111) and much larger than that of LB silicene. The authors interpret these structural parameters as indicating a mix of sp^2-like and sp^3-like sites, but that interpretation assumes that no bonding occurs between the lower-ring silicene and the substrate.

An ARPES measurement at the Si K point (similar to that shown in Figure 2.10 (b)) exhibited a single linear band terminating 0.3 eV below the Fermi level that was not present

on the bare Ag substrate. This feature was interpreted as being a single arm of a gapped Dirac cone, with the other arm hidden by photoemission interference effects like those often seen in graphite [128] and graphene [129] samples. Similar to the nanoribbons on Ag(110), the Dirac cone-like feature was only reported on a single plane in momentum space. The slope of this linear feature corresponds to a Fermi velocity of 1.3×10^6 m s^{-1}, slightly larger than that of graphene and in contrast to the calculated Fermi velocity for freestanding silicene of 0.5×10^6 m s^{-1}. The ARPES-derived bandgap agreed relatively well with the gap of about 0.3 eV predicted by DFT calculations of the electronic structure of the $(3\times3)/(4\times4)$ silicene monolayer that do not include a substrate [130]. That is, the gap appeared to be primarily due to broken inversion symmetry in the silicene monolayer, and interaction with the Ag substrate was therefore taken to be relatively minimal.

A more rigorous ARPES mapping [131] of the $(3 \times 3)/(4 \times 4)$ silicene/Ag(111) system called this interpretation into question. In this study, the authors also observed the same wedge profile as Vogt *et al.*, but in a perpendicular momentum plane they saw a more gradual, parabolic dispersion. Together, these observations indicate that the bandstructure is best described as two perpendicular parabolas, one upright and one inverted, forming a saddle point at the Si K point and -0.3 eV (Figure 2.10(e)). This metallic surface band, given its proximity to the metallic *sp* band in bulk Ag, likely represents a hybridization between the epitaxial silicene and the underlying surface Ag atoms. ARPES measurements therefore contradicted the notion of a Dirac cone in epitaxial silicene on Ag(111), not confirm it.

The conclusion of a hybrid metallic surface was further supported by a number of DFT calculations [130, 132, 133] and the absence of Landau levels observed in the scanning tunnelling spectroscopy (STS) spectrum [130]. However, counter-arguments had been made for the presence of a Dirac cone based on DFT calculations [134] and further ARPES measurements [135]. At the heart of this controversy was the identity of the linear bands near the Fermi level and whether they belonged solely to an isolated 2D silicene sheet, were indicative of Si–Ag hybridization or were induced in the surface Ag atoms. Clearly, an element-specific method for measuring only those states that belong to Si atoms was needed for resolution of this problem. My study of this system, which was published in *Advanced Functional Materials* in 2014 [136] and employs complementary DFT calculations and element-specific soft

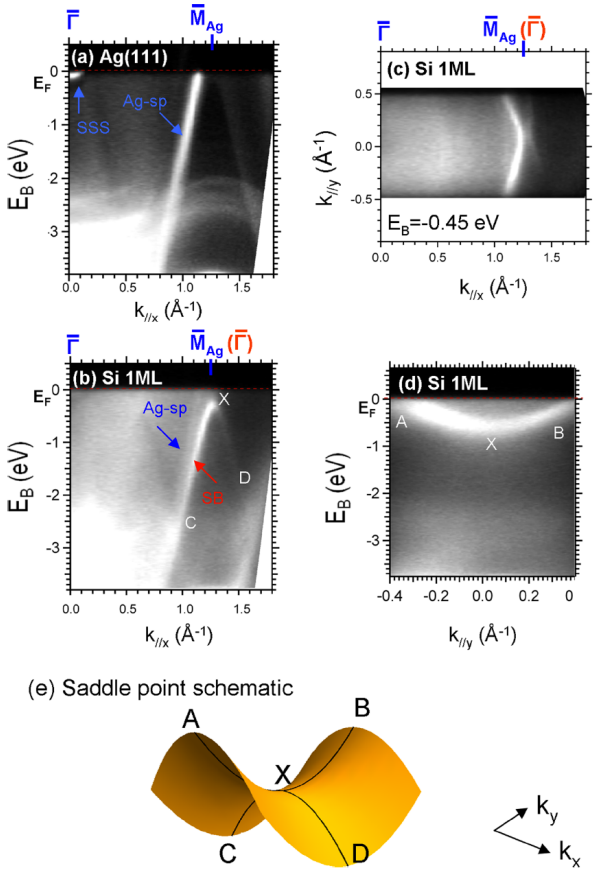

Figure 2.10: ARPES measurements of the bandstructure of (a) bare Ag(111) and (b)-(d) monolayer silicene deposited on Ag(111). In contrast to the gapped Dirac cone interpretation of an ARPES measurement similar to (b) in Reference 127, the authors model the bandstructure as a saddle point, as shown in (e). Reprinted with permission from D. Tsoutsou *et al.*, *Applied Physics Letters* **103**, 231604 (2012) [131]. Copyright 2012, AIP Publishing LLC.

X-ray spectroscopy measurements of the electronic structure of epitaxial silicene monolayers on Ag(111), is included in Chapter 6.

The $(3 \times 3)/(4 \times 4)$ silicene monolayer is not the only stable structure on the Ag(111) surface. There are also STM and LEED measurements and DFT calculations that suggest the existence of three types of $(\sqrt{7} \times \sqrt{7})$R19.1° [137,138] and one (3×3) [139] silicene sheet on the $(\sqrt{13} \times \sqrt{13})$R13.9° Ag(111) supercell and a $(\sqrt{7} \times \sqrt{7})$R19.1° silicene structure on the $(2\sqrt{3} \times 2\sqrt{3})$R30° Ag(111) template. Which silicene layer is produced in a particular deposition is heavily dependent on the substrate temperature and deposition rate [137]. Typically at 250 °C and deposition rates around 1 monolayer hr^{-1}, the $(3 \times 3)/(4 \times 4)$ and

$(\sqrt{7} \times \sqrt{7})$R19.1°/$(\sqrt{13} \times \sqrt{13})$R13.9° structures grow in concert, though fine-tuning the temperature and deposition rate can result in a sample that is mostly of the $(3 \times 3)/(4 \times 4)$ variety. Of all of these structures, perhaps the most intriguing is the $(3\times3)/(\sqrt{7}\times\sqrt{7})$R19.1° structure of Arafune and Lin [139], as it is the only one in which the epitaxial silicene monolayer is inversion symmetric, closely resembling the structure of freestanding silicene.

Regardless of whether epitaxial silicene on Ag(111) is metallic, semimetallic or semiconducting, it is desirable to be able to modulate its bandgap for both electronic and optical applications. One suggested method for bandgap modulation is intentional oxidation. Two DFT investigations of oxidized silicene monolayers explored different oxygen concentrations on the $(3 \times 3)/(4 \times 4)$ system; one having one O atom adsorbed per unit cell [140] and one having 9 O atoms per unit cell for 50% coverage [141]. Their DFT calculations indicated an average gap opening of about 0.1 eV with the adsorption of a single O atom, but the other study found no bandgap opening with 9 adsorbed O atoms. Both authors presented experimental STS data indicating a bandgap opening in the silicene after oxidation, and DFT and ARPES [141] results seemed to indicate a significant oxygen-induced decoupling of the silicene from its substrate. In Chapter 7, I perform a full-potential DFT calculation of the oxidized silicene/Ag(111) system and compare the calculated soft X-ray spectra to the experimental spectra of an epitaxial silicene monolayer slowly oxidizing during beam exposure. This study was recently published in *Scientific Reports* [142].

One controversial structure that deserves special mention is the proposed $(3\sqrt{3}\times3\sqrt{3})$R30° $/(7\times7)$ silicene/Ag(111) monolayer. This particular structure is typically invoked to explain the hexagonal honeycomb pattern observed on some silicene samples that are expected to be monolayers [143]. Low-temperature STS and the observation of quantum phase interference ripples in STM images both provided evidence for a Dirac cone electronic structure [144], which was even suggested to have hexagonal warping and observable chirality effects [145]. This claim was bolstered by DFT calculations of this particular structure [133, 134, 143]. However, the stability of such a monolayer has never been definitively shown, and there have been many claims that the $(\sqrt{3} \times \sqrt{3})$R30° silicene periodicity actually corresponds to multilayer growth [146].

2.9 Epitaxial Silicene Multilayers on Ag(111)

By extending deposition beyond the time needed to form a monolayer, one of two outcomes were thought possible: the formation of a stable multilayer system or the clustering of Si atoms into bulk-like crystals. Arched nanoribbon multilayers were shown to form on the Ag(110) surface, and ARPES measurements indicated a Dirac cone in their bandstructure [147]. Early evidence for the formation of multilayered sheets [148] also indicated the presence of a Dirac cone, albeit with the Dirac point buried 0.25 eV below the Fermi level due to interactions with the substrate. LEED patterns indicated a $(\sqrt{3} \times \sqrt{3})$R30° reconstruction relative to the (1×1) silicene unit cell, though points originating from the initial $(3 \times 3)/(4 \times 4)$ monolayer appeared to be unaffected by the addition of several extra layers. It was hypothesized that the bottom $(3 \times 3)/(4 \times 4)$ layer, in retaining its initial configuration, protected the multilayer from the influence of the substrate allowing for the formation of Dirac cones.

The $(\sqrt{3} \times \sqrt{3})$R30° surface reconstruction is found to persist at 250 °C even at tens of layers thick [149], which is unexpected given the energetic release that would be associated with reversion to bulk Si crystals. Further, these thick multilayers were also suggested to be Dirac cone hosts, and were shown to retain their electronic character even when exposed to ambient conditions for 24 h [149]. It was suggested that, in these thick samples, atmospheric oxygen was only able to interact with the topmost layers of the silicene multilayer sample, and the formation of an oxide layer on the surface passivated the layers underneath [149].

Resta *et al.* used nc-AFM and STM measurements of silicene samples near their edges to show that the sample steps up from bare Ag to $(3 \times 3)/(4 \times 4)$ silicene to $(\sqrt{3} \times \sqrt{3})$R30° with increasing sample thickness. This study also reconciled two distinct STM patterns (namely, hexagonal honeycombs and triangular lattices) associated with the $(\sqrt{3} \times \sqrt{3})$R30° surface as originating from the same structure [150].

Further evidence for the $(\sqrt{3} \times \sqrt{3})$R30° STM pattern corresponding to multilayer growth came from a DFT calculation of epitaxial silicene on the Ag(111) surface [151]. It was determined that A-B stacked bilayers on the Ag(111) (4×4) cell could take one of three energetically equivalent corrugation configurations, each with 3 raised Si sites per cell. These

cells all had the same basic structure, but with the 3 raised sites shifted by one silicene *nnn* vector between them. It was argued that, as the three configurations are energetically equivalent, the sheet would likely "flip-flop" between them over the scale of an STM measurement. Therefore, the observed STM pattern would be a superposition of the three of them, producing a triangular lattice similar to that seen in typical $(\sqrt{3} \times \sqrt{3})$R30° STM measurements.

However, a low-energy electron microscopy (LEEM) study of a large area of the silicene sample would show that, while the sample covered the Ag crystal as expected (nucleation out from initial seeding sites) up to a monolayer in thickness, the majority of the sample then clustered into bulk-like Si crystals upon the deposition of more silicon [152]. Further, some authors suggested that the $(\sqrt{3} \times \sqrt{3})$R30° pattern observed in STM was consistent with the honeycomb-chained triangle or inequivalent triangle models of Ag segregation on the Si(111) surface [153, 154], which would indicate that the samples did not represent a multilayered silicene, but instead a thin Si(111) crystal (or possibly Si(111) clusters).

While a number of small-area analyses indicated that controlled multilayer growth was occurring, though the precise structure of the multilayers were in question, large-area analyses of the depositions pointed toward the dewetting of the crystal and the formation of bulk-like Si clusters. My treatment of the thick silicene/Ag(111) system is provided in Chapter 8, and was also published in *Advanced Functional Materials* in 2015 [118].

Chapter 3

Silicene Growth and Structural Characterization

In Chapter 6, Chapter 7 and Chapter 8, I present three studies of the electronic structure of silicene monolayers and multilayers on Ag(111). Generally, each of these experiments can be broken down into similar steps: producing a silicene sample and characterizing its atomic structure, using the atomic structure as input for DFT electronic structure calculations, then measuring the electronic structure with soft X-ray spectroscopy to verify the predictions of DFT. The following three chapters will expound on these steps, starting with the production and structural determination of silicene on Ag(111).

Epitaxial growth refers to the formation of a crystalline film (the overlayer or epilayer) on a crystalline base (the substrate) in an ordered, periodic manner. The structure of epitaxial systems can be complicated, since it is rare for the (1×1) unit cell of the epilayer to be perfectly lattice-matched to the (1×1) unit cell of the substrate. More often, it is supercells of the epilayer and substrate that are commensurate, with the possibility of a relative rotation between the two. As I will discuss in the next chapter, before attempting to model any system with DFT it is beneficial to have the most complete and accurate description of its crystal structure possible. For epitaxial materials, the most important of the structural parameters are the substrate and epilayer supercells and their relative rotation and, if applicable, the corrugation pattern in the epilayer. Other details of the crystal like the substrate/epilayer distance and the substrate surface reconstruction will work themselves out during the DFT structural relaxation.

Throughout this manuscript, I will use Wood's notation for describing the epilayer/substrate supercell periodicity. In this notation, the supercell of the epilayer is described first, in the

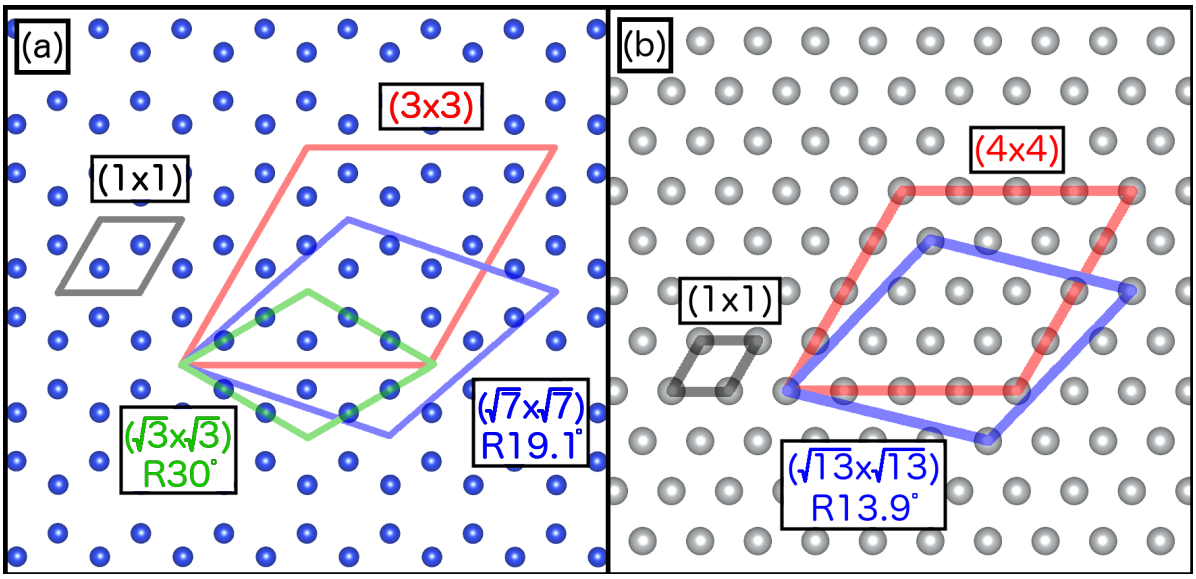

Figure 3.1: (a) A selection of the silicene supercells that are discussed in this thesis, along with the basic (1×1) silicene unit cell. (b) Selected supercells of the Ag(111) surface. Apart from the black (1×1) unit cells, colours that match between panels (a) and (b) indicate commensurate supercells.

form $(m \times n)\mathrm{R}\theta^{\circ}$, where m and n denote the size of the epilayer supercell in multiples of the (1×1) epilayer unit cell, and θ denotes the rotation of the supercell's basis translation vectors relative to those of the (1×1) epilayer unit cell. Figure 3.1(a) shows a number of the silicene supercells discussed within this manuscript. Following the epilayer description, Wood's notation ends with a description of the substrate supercell, which consists of an $(M \times N)$ array of substrate unit cells with translation vectors rotated by Θ° relative to the (1×1) substrate unit cell. Some of the Ag(111) supercells discussed in this manuscript are illustrated in Figure 3.1(b).

3.1 Physical Vapour Deposition of Silicene on Ag(111)

The CVD of Si using a gaseous precursor such as silane (SiH_4) or trichlorosilane ($HSiCl_3$) is common in the manufacturing process of photovoltaic cells [155]. However, it is yet to be explored for epitaxial silicene, possibly because the temperature range for efficient decomposition of silane [156] and trichlorosilane [157] borders on the melting point of many of silicene's suggested lattice-matched substrate materials. Instead, physical vapour deposition

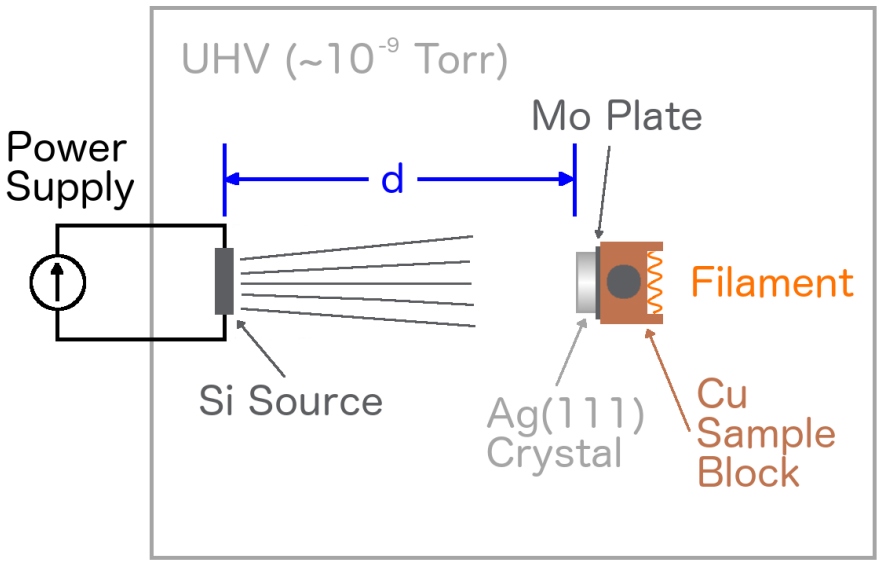

Figure 3.2: An illustration of the apparatus for the PVD of silicene on Ag(111) used to make the samples for the epitaxial silicene experiments in this manuscript. Current through the Si source increases its temperature until nanoparticles are able to sublimate off of the surface, depositing on the heated Ag(111) substrate held a distance d away. The Mo plate is compatible with both the deposition chamber and experimental chamber sample blocks, allowing for the *in vacuo* transfer of the substrate. The Ag(111) crystal is affixed to it with a spot-welded cage of tantalum wires, since the plate and fixture need to be able to withstand the annealing temperature of Ag.

(PVD) has thus far been its preferred growth method. In this process, a piece of elemental Si is heated to a high temperature in an ultra-high vacuum (UHV) chamber, either in a crucible or by running a large current through the Si itself. This results in the sublimation of small nanoparticles off of its surface which can then travel ballistically to the desired substrate provided that a direct line-of-sight exists between the two. The substrate is held at a high enough temperature that the nanoparticles are able to melt and then recrystallize into an atom-thick layer. A basic apparatus for the resistive-heating PVD of silicene on Ag(111) is illustrated in Figure 3.2.

In all of the epitaxial silicene experiments presented within this thesis, the substrate was a Czochralski-grown Ag(111) single-crystal disk of about 8 mm in diameter and 4 mm in thickness with a highly-polished surface. The Si source was a 1 cm $\times$ 1.5 cm fragment of

Si wafer, and it was mounted in a UHV chamber (base pressure 1×10^{-9} Torr) across two poles of a four-pole vacuum feedthrough connected to an external power supply capable of delivering up to 15 A of current. Prior to each experiment, if the Si wafer had been recently exposed to ambient conditions, the current through it was slowly increased until the power delivered to the wafer was about 40 W (10 A at 4 V), at which point it glowed a bright yellow colour. It was then held at this temperature for about 12 hours in order to sublimate the oxide layer that would have formed on its surface.

In order to ensure that the substrate surface was free of contaminants, it was sputtered for approximately 1 hour with 1 keV – 1.5 keV Ar^+ ions, depending on the expected level of contamination. As sputtering is likely to result in the pitting or fracturing of the otherwise atomically smooth Ag(111) surface, the substrate crystal was then held at an annealing temperature of 500 °C for 30 minutes in order to allow for recrystallization, after which it was allowed to radiatively cool to about 200 °C. This cycle of sputtering and annealing was repeated until the surface was judged to be sufficiently monocrystalline and free of contaminants through LEED. It was then brought up to deposition temperature and held there for 30 minutes, in order to ensure that the substrate had time to thermally equilibrate with the sample block so that its temperature would remain constant throughout the deposition.

The Si deposition rate depends on a number of parameters, including the Si source and Ag substrate temperatures, the source-to-substrate distance d and the UHV chamber pressure. Further, a variety of monolayer silicene reconstructions have been observed or predicted to exist on the Ag(111) surface, and more than one them may be present in any epitaxial silicene sample. Fortunately, LEED offers a way to measure the deposition rate of a monolayer as well as take inventory of the silicene reconstructions present on the surface and estimate their relative abundance.

3.2 Low-Energy Electron Diffraction

A LEED apparatus consists of four basic elements: an electron gun, a hemispherical phosphor screen to detect reflected electrons, a camera to record the pattern on the detector screen, and an array of hemispherical grids to reject any inelastically scattered electrons. The phys-

ical principle underlying LEED is backscattering-mode Laue diffraction, which describes the interference pattern produced when a plane wave reflects off of a periodic solid (rather than transmitting through it like in forward-scattering X-ray diffraction). In LEED, the incident plane wave consists of a collimated, monoenergetic beam of electrons that can be tuned between 20 eV and 200 eV, corresponding to a de Broglie wavenumber of about 2 Å^{-1} to 7 Å^{-1}. According to the Laue equation [158], constructive interference will occur whenever

$$\vec{k} - \vec{k}_0 = h\vec{b}_1 + k\vec{b}_2 + \ell\vec{b}_3, \tag{3.1}$$

where $\vec{k}$ is the wavevector of the reflected plane wave and $\vec{k}_0$ the wavevector of the incident plane wave, h, k and ℓ are all integers and $\vec{b}_i$ are the reciprocal lattice vectors of the crystal being measured. Since the hemispherical grids produce a potential that rejects any electrons that do not scatter elastically, the only electrons that are detected are subject to the constraint $|\vec{k}| = |\vec{k}_0|$. The shallow penetration depth of low-energy electrons in solids (typically less than 1 nm, so only a few interatomic distances) prevents a detectable diffraction pattern from forming in the $\vec{b}_3$ direction, so the Laue condition can be simplified to

$$\vec{k}_\parallel - \vec{k}_{0\parallel} = h\vec{b}_1 + k\vec{b}_2, \tag{3.2}$$

where $\vec{k}_\parallel$ and $\vec{k}_{0\parallel}$ are the wavevectors of the reflected and incident plane waves projected parallel to the sample surface. The electron gun is set to normal incidence by directing the $(h, k) = (0, 0)$ reflection back at the centre of the phosphorescent screen, meaning that $\vec{k}_{0\parallel} = 0$. Therefore, in a standard LEED experiment, the condition for constructive interference is finally given by

$$\vec{k}_\parallel = h\vec{b}_1 + k\vec{b}_2. \tag{3.3}$$

That is, the diffraction pattern is essentially an image of the in-plane reciprocal lattices of the first few layers of material being studied (though multiple-scattering effects can make the situation slightly more complicated [159]). The maximum (h, k) indices will be measured on the edges of the hemispherical detector screen, such that

$$|\vec{k}_{\parallel}| = |\vec{k}| = |\vec{k}_0|, \tag{3.4}$$

where the second equality comes from the rejection of inelastically scattered electrons by the hemispherical grids. A greater area of reciprocal lattice space can therefore be observed with a higher incident electron energy.

LEED is very useful for atomically thin epitaxial structures, as the epilayer's reciprocal lattice points can be observed simultaneously with those of the substrate, allowing for a comparison of the orientation and relative sizes of the two. As a demonstration of this concept, Figure 3.3(a) shows an illustration of a LEED pattern for the Ag(111) unit cell (see inset), which takes the form of a triangular lattice. One of the most commonly reported configurations of silicene on Ag(111) consists of a (3×3) silicene supercell commensurate with the (4×4) Ag(111) supercell, shown in the inset in Figure 3.3(b). In this structure, the length of the (1×1) silicene unit cell is 4/3 the length of the (1×1) Ag(111) unit cell in real space, so the Si reciprocal lattice vectors are 3/4 as long. When all Brillouin zones are considered, the net diffraction pattern of the (3×3) silicene looks like a triangular lattice with a lattice constant of (1/4), as shown in Figure 3.3(b). The unit cells of both the substrate and the epitaxial layer are aligned in this case, but if they were not it would manifest as a relative rotation of the reciprocal unit cells, a common example being the $(\sqrt{7} \times \sqrt{7})$R19.1°/$(\sqrt{13} \times \sqrt{13})$R13.9° silicene/Ag(111) system. Points resulting from this structure are visible in an experimental LEED pattern in Figure 8.1(a).

Typical LEED devices have a beam spot on the order of a few mm. LEEM studies of Ag(111) crystals similar to the one used for the depositions in this manuscript have revealed that they usually have a terraced surface, with atomically flat domains of about 10 nm in lateral size [152]. As such, LEED cannot resolve single-crystal domains of silicene in the sample, instead offering a superposition of all of the reciprocal lattices present on the surface. The relative abundance of these silicene species can be roughly estimated by the intensity of their LEED signal, but one must always be aware of the confounding effects of multiple-scattering.

LEED measurements on an epitaxial silicene sample provide two of the three parameters necessary to build an adequate structural model: the relative size and rotation of the substrate

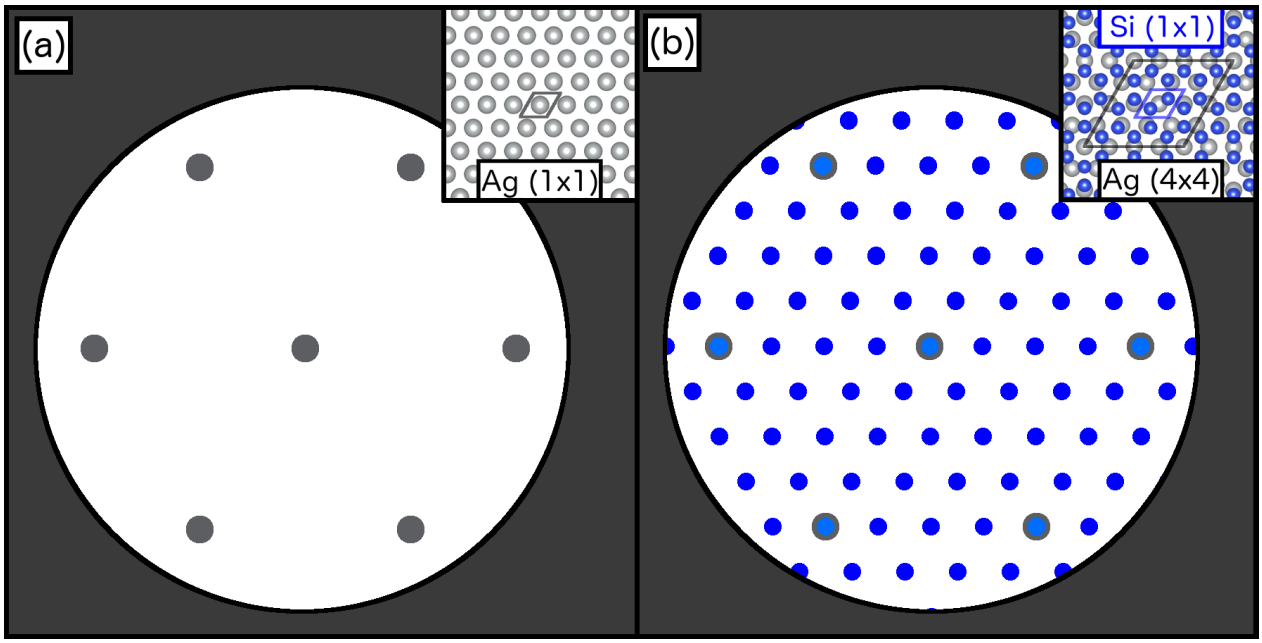

Figure 3.3: (a) A simulated LEED pattern of the bare Ag(111) crystal (inset), with the incident energy set so that the maximum observable (h, k) indices are (1,1). In a real measurement, the (0,0) point at the centre would be occulted from the phosphorescent screen by the electron gun. (b) A simulated LEED pattern of the $(3 \times 3)/(4 \times 4)$ silicene/Ag(111) system (inset), showing the triangular lattice of Si-derived points.

and epilayer supercells. However, it is not sensitive to the out-of-plane positions of the atoms, and therefore cannot elucidate the corrugation pattern in the silicene.

3.3 Scanning Probe Microscopy

Scanning Probe Microscopy (SPM) techniques are used to obtain a topographic map of a sample on the atomic scale, and include both STM and nc-AFM among others. These two techniques differ in the method used to produce an image of the surface but essentially produce the same results when applied to silicene on Ag(111).

The nc-AFM consists of a tip with a radius on the order of nanometers mounted to a micron-scale cantilever with a known resonant oscillation frequency. When the tip is drawn near a sample surface, interactions such as the van der Waals force, chemical bonding, electrostatic and magnetostatic forces may begin to occur. Their magnitude is a function of the distance between the tip and surface as well as the elemental makeup of the tip and the

identity of the surface atoms directly below it. As the tip is raster-scanned across a sample using piezoelectric crystals, its oscillation frequency is monitored by a monochromatic laser reflected off its back surface. When oscillation frequency of the tip is plotted as a function of lateral position, the resulting image reflects the atomic arrangement on the surface, modulated by a number of factors such as the chemical identity of the surface atoms, thermal noise, meniscus forces (if the measurement is not performed under UHV) and magnetostatic forces (if the tip is magnetic) [160].

STM is more sensitive to the electronic structure in the few eV around the Fermi level than it is to the atomic structure on the surface. In STM, a conducting tip with a bias on the order of a few eV is drawn near enough to the sample that tunnelling of surface electrons into the tip (or vice-versa) is possible. According to the Tersoff-Hamann approximation [161], which is applicable in the low-bias regime, the tip current is proportional to the spatial density of electronic states directly below it, integrated between the tip bias voltage and the Fermi level of the sample. There are two primary modes of STM operation, constant-current (sometimes called constant-interaction) and constant-height.

In constant-current STM, the tip height is adjusted with piezoelectric crystals as it is scanned across the sample such that the tunnelling current remains fixed. This results in a topographical map that essentially shows an isosurface of constant electron density integrated between the tip bias energy and the Fermi level. Because the tip is allowed to move in the vertical dimension, constant-current STM can measure the corrugation within a silicene sheet or the vertical distance between the sheet and substrate if performed near the sheet boundary.

Constant-height STM is a simpler technique in which the tip height is fixed and the tunnelling current is plotted as a function of lateral position on the sample. In this manner, a planar map of the electron density integrated between the tip bias voltage and Fermi level is obtained. This technique is much faster than constant-height STM as it does not require adjusting the height of the tip after each lateral move, but it does not produce quantitative values for vertical positions within the sample. Further, it can be problematic on terraced surfaces (such as the Ag(111) face) as there is a risk of collision between tip and sample. AFM is usually considered to be advantageous over STM because of its capacity to distinguish elements and its atomic resolution. However, given that the surface of epitaxial

silicene samples is expected to consist solely of Si atoms, the elemental specificity of AFM is not as important in these experiments.

The silicene/Ag(111) system has been explored thoroughly with AFM and STM, for both monolayer [127,137,139,145,150] and multilayer [149,150] depositions. The resulting sample topographies have led to adequate structural models of many of the silicene/Ag(111) monolayer reconstructions, which I use as the starting point for my DFT structural relaxations in Chapters 6 and 7. Some silicene structures, such as the $(\sqrt{3} \times \sqrt{3})$R30° reconstruction, still remain controversial [132,149,151,153,154,162]. In Chapter 8, I provide a plausible model of this structure as an AA-stacked epitaxial silicene bilayer. This model agrees with the observation that the $(\sqrt{3} \times \sqrt{3})$R30° LEED points do not appear if an incomplete monolayer has been deposited, as well as the observation of multilayers in SPM studies of samples exhibiting $(\sqrt{3} \times \sqrt{3})$R30° character [150].

In summary, a LEED measurement alone can often be adequate to structurally characterize an epitaxial silicene sample on Ag(111) such that it can be utilized as an input for DFT calculations. It directly provides the periodicities and orientation of the epilayer and substrate supercells, and the epilayer corrugation patterns corresponding to these supercells have for the most part been thoroughly catalogued with SPM. Finally, the monolayer deposition rate can be measured by monitoring for the emergence of the $(\sqrt{3} \times \sqrt{3})$R30° points, which allows for the estimation of the sample's thickness based on total deposition time.

Chapter 4

Density Functional Theory

DFT is a powerful theoretical tool that can be used to predict a number of material properties from first principles given only the material's atomic structure. In this chapter, I will first examine the theoretical underpinnings of the DFT formulation and then discuss its specific implementation in WIEN2k, the software suite that I use for the epitaxial silicene studies contained within this manuscript. I will then describe the special considerations that need to be made when dealing with 2D materials, both freestanding and epitaxial. Finally, I will close by explaining how DFT can be used to refine and verify an experimental structural model of silicene in order to ensure the accuracy of its predicted electronic characteristics.

4.1 The Many-Body Hamiltonian

A 3D crystalline solid is a system composed of a periodic unit cell containing N_n nuclei and N_e electrons. Each of the nuclei may be of a different element, with the j^{th} nucleus having charge $+eZ_j$, mass M_j, and position $\vec{R}_j$ relative to the origin. The electrons are indistinguishable except for their position; all of them have mass m_e and charge $-e$, with the i^{th} electron having position $\vec{r}_i$ relative to the origin. The Hamiltonian of such a system is given by:

$$\begin{aligned}\hat{H} = &-\frac{\hbar^2}{2}\left(\sum_i^{N_e}\frac{\nabla_i^2}{m_e}+\sum_j^{N_n}\frac{\nabla_j^2}{M_n}\right)+\\ &\frac{1}{4\pi\epsilon_0}\left(-\sum_{i,j}^{N_e,N_n}\frac{e^2Z_j}{\left|\vec{r}_i-\vec{R}_j\right|}+\frac{1}{2}\sum_{i\neq j}^{N_e}\frac{e^2}{|\vec{r}_i-\vec{r}_j|}+\frac{1}{2}\sum_{i\neq j}^{N_n}\frac{e^2Z_iZ_j}{\left|\vec{R}_i-\vec{R}_j\right|}\right).\end{aligned} \tag{4.1}$$

Here, the first two terms are the kinetic energy of the electrons and nuclei, respectively, while the final terms describe the Coulomb interaction between the electrons and nuclei, electrons and electrons and nuclei and nuclei, respectively. The factor of 1/2 leading the final two terms corrects for the double-counting of interactions within those sums. Simply inserting this Hamiltonian into the Schrödinger equation

$$\hat{H}\Psi = E\Psi \tag{4.2}$$

results in an intractable system of equations for all but the very simplest of systems, as the Hilbert space scales exponentially with the number of interacting bodies [163]. The first approximation that can be made in an effort to simplify the problem, the Born-Oppenheimer approximation, involves assuming that the nuclei are completely fixed in position. Therefore, the kinetic energies of the nuclei are zero and the nucleus-nucleus Coulomb interaction works out to a constant, which can safely be neglected (until geometric optimization is considered later in this chapter). With this simplification in place the many-body Hamiltonian for the electrons becomes

$$\hat{H}_e = -\frac{\hbar^2}{2}\sum_i^{N_e}\frac{\nabla_i^2}{m_e} + \frac{1}{4\pi\epsilon_0}\left(-\sum_{i,j}^{N_e,N_n}\frac{e^2 Z_j}{\left|\vec{r}_i - \vec{R}_j\right|} + \frac{1}{2}\sum_{i\neq j}^{N_e}\frac{e^2}{|\vec{r}_i - \vec{r}_j|}\right). \tag{4.3}$$

The first and last terms (the kinetic energy of the electrons $\hat{T}$ and the electron-electron interaction $\hat{V}_{ee}$) are independent of the particular system being studied. That is, they do not rely on the arrangement of nuclei and are only dependent in form on the number of electrons N_e. As such, these terms are often grouped together into a *universal operator* $\hat{F}$.

With the fixed atomic positions of the Born-Oppenheimer approximation, the nuclei produce a static scalar potential $v_{ext}(\vec{r})$ that is external to the electrons. The Hamiltonian of the system can now be abbreviated to

$$\hat{H}_e = \hat{T} + \hat{V}_{ext} + \hat{V}_{ee} = \hat{F} + \hat{V}_{ext} \tag{4.4}$$

with $\hat{V}_{ext}$ representing the electron-nucleus Coulomb attraction term in Equation 4.3. While not much has apparently been gained by rearranging terms in this manner, the problem is

now properly framed for the introduction of the two theorems of Hohenberg and Kohn, which lay the groundwork for DFT.

4.2 The Hohenberg-Kohn Theorems

The first theorem of Hohenberg and Kohn [164] outlines a one-to-one relationship between the external potential $v_{ext}(\vec{r})$ defined by the atomic arrangement and the ground-state electron density distribution $n_0(\vec{r})$, while the second theorem shows that all observables in the system are functionals of the ground-state electron density distribution $n_0(\vec{r})$.

In order to demonstrate the first theorem, it will be shown that a given external potential always elicits a unique ground-state total electron wavefunction $\Psi_0(\vec{r})$, and that this wavefunction uniquely corresponds to the ground-state electron density distribution $n_0(\vec{r})$. This is commonly written as the relationship

$$v_{ext}(\vec{r}) \longleftrightarrow \Psi_0(\vec{r}) \longleftrightarrow n_0(\vec{r}), \tag{4.5}$$

both legs of which will be proven by contradiction. In order to demonstrate the first leg, it is assumed that two given external potentials $v^a_{ext}(\vec{r})$ and $v^b_{ext}(\vec{r})$, which differ from each other by more than a constant term, are both capable of hosting N_e electrons with the same ground-state wavefunction $\Psi_0(\vec{r})$. Since the universal operator $\hat{F}$ will be the same in both systems, their electron Hamiltonians $\hat{H}^a_e$ and $\hat{H}^b_e$ will only differ in terms of $\hat{V}_{ext}$. The Schrödinger equations for both systems are as follows:

$$\hat{H}^a_e \Psi_0(\vec{r}) = E^a_0 \Psi_0(\vec{r}) \tag{4.6}$$

$$\hat{H}^b_e \Psi_0(\vec{r}) = E^b_0 \Psi_0(\vec{r}), \tag{4.7}$$

where E^a_0 and E^b_0 are the ground-state energies of system a and b, respectively. Subtraction of these two equations yields

$$(E^a_0 - E^b_0)\Psi_0(\vec{r}) = (\hat{H}^a_e - \hat{H}^b_e)\Psi_0(\vec{r}) = (\hat{V}^a_{ext} - \hat{V}^b_{ext})\Psi_0(\vec{r}), \tag{4.8}$$

For this relationship to hold true everywhere (for a non-vanishing ground-state wavefunction), the difference between the external potentials must be constant over the entirety of the unit cell. Since the definition of zero potential is arbitrary, the difference is trivial and the two potentials are therefore identical. This constitutes proof by contradiction that two external potentials cannot elicit the same ground-state wavefunction from the system of electrons or in other words

$$v_{ext}(\vec{r}) \longleftrightarrow \Psi_0(\vec{r}), \tag{4.9}$$

the first leg in Hohenberg and Kohn's first theorem. It is important to note here that this relationship only holds true for ground-state wavefunctions that are "*v-representable*". That is to say, for an arbitrary $\Psi_0(\vec{r})$ we have not shown that a corresponding $v_{ext}(\vec{r})$ will necessarily exist. However, for a valid $v_{ext}(\vec{r})$ there is a guaranteed one-to one, invertible relationship with the corresponding $\Psi_0(\vec{r})$.

It is convenient now to explicitly state the ground-state energy of the many-body system as follows:

$$E_0 = \langle\Psi_0|\hat{H}_e|\Psi_0\rangle = \langle\Psi_0|\hat{F}|\Psi_0\rangle + \int v_{ext}(\vec{r})n_0(\vec{r})d^3\vec{r}. \tag{4.10}$$

Here we have taken advantage of the fact that the energy associated with the electron-nucleus interaction is the same as if the electrons were subjected to an external potential $v_{ext}(\vec{r})$, and have accounted for the electrons being delocalized, having a density distribution rather than a single location. For a crystalline material the spatial integral is performed over the volume of the unit cell, while in an isolated atom or molecule it encompasses all of space.

For the next step in Hohenberg and Kohn's first theorem, it is assumed that there exist two systems (again called system a and system b) with different ground-state wavefunctions $\Psi_0^a(\vec{r})$ and $\Psi_0^b(\vec{r})$ that can both produce the same ground-state electron density distribution $n_0(\vec{r})$. That is,

$$|\Psi_0^a(\vec{r})|^2 = \left|\Psi_0^b(\vec{r})\right|^2 = n_0(\vec{r}). \tag{4.11}$$

From the previous proof, having different ground-state wavefunctions means that these

systems have non-trivially different external potentials $v^a_{ext}(\vec{r})$ and $v^b_{ext}(\vec{r})$ and therefore different Hamiltonians $\hat{H}^a_e$ and $\hat{H}^b_e$. Their ground-state energies E^a_0 and E^b_0 may or may not be the same value. From the variational principle, the definition of the ground-state energy in Equation 4.10 and the fact that the two Hamiltonians differ only in their external potential terms, we can write the following inequalities:

$$E^a_0 < \langle \Psi^b_0 | \hat{H}^a_e | \Psi^b_0 \rangle = \langle \Psi^b_0 | \hat{H}^b_e + \hat{V}^a_{ext} - \hat{V}^b_{ext} | \Psi^b_0 \rangle \tag{4.12}$$

$$E^b_0 < \langle \Psi^a_0 | \hat{H}^b_e | \Psi^a_0 \rangle = \langle \Psi^a_0 | \hat{H}^a_e + \hat{V}^b_{ext} - \hat{V}^a_{ext} | \Psi^a_0 \rangle. \tag{4.13}$$

Or,

$$E^a_0 < E^b_0 + \int \left[v^a_{ext}(\vec{r}) - v^b_{ext}(\vec{r}) \right] n_0(\vec{r}) d^3\vec{r} \tag{4.14}$$

$$E^b_0 < E^a_0 + \int \left[v^b_{ext}(\vec{r}) - v^a_{ext}(\vec{r}) \right] n_0(\vec{r}) d^3\vec{r}. \tag{4.15}$$

Simply adding Equations 4.14 and 4.15 results in the contradiction

$$E^a_0 + E^b_0 < E^a_0 + E^b_0, \tag{4.16}$$

which constitutes proof that two systems with different ground-state wavefunctions cannot produce the same density. This is the second leg of the first theorem of Hohenberg and Kohn,

$$\Psi_0(\vec{r}) \longleftrightarrow n_0(\vec{r}). \tag{4.17}$$

As a quick aside, the previous proofs have assumed that the ground-state is non-degenerate. That is, it has been assumed that there is only one net wavefunction that yields the ground-state eigenvalue in the Schrödinger equation. This is not necessarily the case, and a degenerate ground-state would cause the inequalities in Equations 4.12 and 4.13 to no longer be strict. As a result, the relationship in Equation 4.16 would not be contradictory. However, it has been demonstrated that even in this case the first Hohenberg-Kohn theorem can still be proven via the constrained search formalism [165].

It has now been shown that, given one of the *v-representable* ground-state density distribution, the ground-state wavefunction or the external potential, the others are automatically

determined. In a typical DFT calculation, the external potential (the crystal lattice) is the input, and the ground-state electronic structure and associated observables are the objectives. Since any observable X relies on the ground-state wavefunction as follows:

$$\langle X \rangle = \frac{\langle \Psi_0 | \hat{X} | \Psi_0 \rangle}{\langle \Psi_0 | \Psi_0 \rangle} = \frac{\langle \Psi_0 | \hat{X} | \Psi_0 \rangle}{N_e}, \tag{4.18}$$

and the ground-state wavefunction has a one-to-one relationship with the ground-state electron density, the observable can also be represented as a functional of the ground-state electron density. This includes the energy from the universal operator F and the external potential V_{ext}, so the ground-state energy of the system is also a functional of the ground-state density:

$$E_0[n_0(\vec{r})] = F[n_0(\vec{r})] + V_{ext}[n_0(\vec{r})]. \tag{4.19}$$

Together with the variational principle, this equation spells out the basic idea behind DFT: the energy of the system is minimized when the electron density is exactly its ground-state distribution. Any other test distribution entered into the right side of Equation 4.19 will invariably result in a higher energy than the ground-state. In this way, the true ground-state density can be found by iteratively improving on an initial test density, which will bring the calculated total energy to its minimum value. Once the ground-state density is known, all of the observables of the system will also be available.

Unfortunately, while the theorems of Hohenberg and Kohn guarantee that such a process exists, they do not explicitly spell out how to perform it. One major obstacle is finding the correct form for the universal function (now functional) $\hat{F}[n_0(\vec{r})]$. An early attempt to find a solution was the Thomas-Fermi model [166, 167], in which the kinetic energy was given the form

$$T_{TF}[n(\vec{r})] = \frac{3}{10}(3\pi^2)^{2/3} \int [n(\vec{r})]^{5/3} d^3\vec{r}, \tag{4.20}$$

and the electron-electron potential energy was constructed by considering each element of the total electron density as feeling the mean Coulomb field of the remainder of the density (called the Hartree potential):

$$V_H[n(\vec{r})] = \frac{1}{2}\int_{\vec{r}\neq\vec{r}'} \frac{[n(\vec{r})][n(\vec{r}')]}{|\vec{r}-\vec{r}'|} d^3\vec{r}\, d^3\vec{r}'. \tag{4.21}$$

While this model is acceptable for some isolated atoms, it fails in most cases that are currently of interest to condensed matter physicists. Further, the Hartree potential only considers the Coulomb interaction between electrons, while spin-spin interactions can also play a critical role in real samples. In fact, up until this point I have neglected to consider spin at all, nor has it been guaranteed that the total electron wavefunction satisfies the Pauli exclusion principle. I will briefly address this before moving on to the next step in the derivation of DFT, the equations of Kohn and Sham.

The spin $\sigma = (\uparrow, \downarrow)$ can be implicitly incorporated into the single-particle wavefunctions $\psi_i^\sigma(\vec{r}_i)$ and the electron-electron potential $\hat{V}_{ee}$, and the total electron density can be broken up into a sum of spin-up and spin-down densities without affecting the previous derivations. Further, the construction of the net wavefunction $\Psi(\vec{r})$ can be done in such a way that it is antisymmetric under the positional exchange of two electrons, a necessary condition for fermions to satisfy Pauli exclusion. This is accomplished by making the net electron wavefunction the Slater determinant of a matrix composed of the N_e individual electron wavefunctions, i.e.:

$$\Psi(\vec{r}) = \frac{1}{\sqrt{N_e}} \begin{vmatrix} \psi_1^\sigma(\vec{r}_1) & \psi_2^\sigma(\vec{r}_1) & \dots & \psi_{N_e}^\sigma(\vec{r}_1) \\ \psi_1^\sigma(\vec{r}_2) & \psi_2^\sigma(\vec{r}_2) & \dots & \psi_{N_e}^\sigma(\vec{r}_2) \\ \vdots & \vdots & \ddots & \vdots \\ \psi_1^\sigma(\vec{r}_{N_e}) & \psi_2^\sigma(\vec{r}_{N_e}) & \dots & \psi_{N_e}^\sigma(\vec{r}_{N_e}) \end{vmatrix}. \tag{4.22}$$

This way, for the net wavefunction to be non-zero, all of the single-particle wavefunctions must be unique.

4.3 The Kohn-Sham Equations

Kohn and Sham's approach to the difficulty of constructing the universal functional $\hat{F}[n_0(\vec{r})]$ begins by breaking the associated energy up into a number of specific terms:

$$\begin{aligned} F[n(\vec{r})] =& V_H[n(\vec{r})] + K_0[n(\vec{r})] + (V[n(\vec{r})] - V_H[n(\vec{r})]) \\ &+ (K[n(\vec{r})] - K_0[n(\vec{r})]) \end{aligned} \tag{4.23}$$

where $V_H[n(\vec{r})]$ the energy of the Hartree potential defined earlier, $K_0[n(\vec{r})]$ is the kinetic energy of N_e non-interacting electronic states $\phi_i(\vec{r})$, and $V[n(\vec{r})]$ and $K[n(\vec{r})]$ are the potential and kinetic energies of the many-electron system that is being considered, which are at this point unknown.

These non-interacting electronic states, called the Kohn-Sham orbitals, are defined such that they yield the same ground-state density as the ground-state electronic wavefunctions. That is,

$$\sum_i^{N_e} |\phi_i(\vec{r})|^2 = n(\vec{r}), \tag{4.24}$$

and their kinetic energy is given by

$$K_0[n(\vec{r})] = -\frac{\hbar^2}{2m_e} \sum_i^{N_e} \int \phi_i^*(\vec{r}) \nabla_{\vec{r}}^2 \phi_i(\vec{r}) d^3\vec{r}. \tag{4.25}$$

The final two terms in Equation 4.23, which contain the difference between the true electron-electron interaction energy and that of the Hartree potential, and the true interacting many-body kinetic energy and the non-interacting many-body kinetic energy, are called the *exchange energy* $E_x[n(\vec{r})]$ and the *correlation energy* $E_c[n(\vec{r})]$ respectively. These quantities are often combined into a single term, called the *exchange-correlation energy* $E_{xc}[n(\vec{r})] = E_x[n(\vec{r})] + E_c[n(\vec{r})]$. The associated operator is a potential, defined using a functional derivative:

$$\hat{V}_{xc}[n(\vec{r})] = \frac{\delta E_{xc}[n(\vec{r})]}{\delta n(\vec{r})}. \tag{4.26}$$

Therefore, one can simply add the external potential operator $\hat{V}_{ext}[n(\vec{r})]$, the Hartree potential operator $\hat{V}_H[n(\vec{r})]$ and the exchange-correlation operator $\hat{V}_{xc}[n(\vec{r})]$ into a single operator $\hat{V}_{KS}[n(\vec{r})]$, then write the Schrödinger equation for each non-interacting orbital in this system as

$$\hat{H}_{KS}\phi_i(\vec{r}) = \left[-\frac{\hbar^2}{2m_e}\nabla^2_{\vec{r}} + \hat{V}_{KS}[n(\vec{r})]\right]\phi_i(\vec{r}) = \epsilon_i\phi_i(\vec{r}), \tag{4.27}$$

which is just the equation for a single electron moving in a potential $\hat{V}_{KS}(n[\vec{r}])$. Kohn and Sham reduced the problem from one of N_e interacting particles to the much simpler case of N_e non-interacting particles. It is important to note that the energy eigenvalues ϵ_i are not the energies of the actual individual electronic states, but those of the non-physical, non-interacting Kohn-Sham orbitals. However, at least one of the eigenvalues does bear some physical significance, as it can be shown that the smallest energy eigenvalue is equal to the first ionization energy of the system [168]. Further, it should be noted here the total energy of the unit cell is not directly given by the sum of these energy eigenvalues, though the two are related.

The only unknown quantities in Equation 4.27 are the exchange-correlation functional $\hat{V}_{xc}[n(\vec{r})]$ and its associated energy $E_{xc}[n(\vec{r})]$, which are contained within $\hat{V}_{KS}[n(\vec{r})]$. If the precise form of the exchange-correlation potential was known the ground-state density (and therefore all the observables of the system by the second Hohenberg-Kohn theorem) could be exactly calculated. Unfortunately it is not known, but a variety of useful approximations exist for these expressions and can be chosen based on the material being considered, what one wishes to learn about the material and to what degree of accuracy, and the computational resources at hand.

The simplest of these is the local-density approximation (LDA), which incorporates the exchange-correlation energy per unit volume $\epsilon_{xc}(n)$ of a homogeneous electron gas with density n. The exchange energy of such a gas is known analytically [169] while the correlation energy has been solved numerically using Monte Carlo simulations [170]. The LDA exchange-correlation energy is therefore:

$$E^{LDA}_{xc} = \int \epsilon_{xc} n(\vec{r}) d^3\vec{r}. \tag{4.28}$$

There are some applications for which the LDA is adequate, but it can usually be significantly improved upon by incorporating not just the local electronic density but also the local electronic density gradient, $\vec{\nabla} n(\vec{r})$, into the exchange-correlation energy. This is especially helpful when the electron density has sharp spatial features, something that the LDA cannot

describe well. Functionals that incorporate the density gradient are broadly referred to as generalized gradient approximations (GGA), and since the incorporation can happen in a number of ways there are a variety of GGA exchange-correlation functionals available. The most popular of these is the GGA of Perdew, Burke and Ernzerhof (PBE-GGA) [171]. This is largely because the PBE-GGA is parameter-free, meaning it was completely formulated without input from experimental data and so it can be applied to a wide variety of materials.

Most of the calculations I present in later chapters use the PBE-GGA exchange-correlation functional for both the structural optimizations and the electronic structure calculations. However, it should be noted that both GGA and LDA techniques are known to underestimate the bandgap [172], which is one of the most important characteristics of a material. The modified Becke-Johnson (mBJ) functional [173, 174] was developed specifically to improve upon the bandgap estimations of GGA, so in most cases I will perform mBJ calculations in addition to PBE-GGA [175, 176].

4.4 Basis Sets and Calculation Economy

In all-electron, full-potential DFT programs such as WIEN2k [177], every electronic state from the most tightly-bound core-level up to those at a pre-defined cutoff energy (typically placed in the continuum states) are included in the density calculation. This range encompasses both highly localized core states and delocalized valence and conduction states. While the Kohn-Sham orbitals $\phi_i(\vec{r})$ can be expanded in any complete basis set, it is computationally efficient to try to represent them with the smallest number of basis functions possible.

Typically, a basis set that is good at describing the localized core electronic states is a poor approximation of the delocalized valence and conduction states, and *vice versa*. It is therefore economical to define two distinct spatial regions in the unit cell: ones that are expected to house localized, atomic-like orbitals and ones that are more likely to house delocalized, free particle-like orbitals. This is done by defining a set of non-overlapping "muffin-tin" radii, one for each individual atomic site α in the lattice. The size of the muffin-tin radius is dependent on the atomic species and is typically larger for heavier atoms. Within the muffin-tin, the basis functions $\chi_{\alpha,\vec{k}_n}$ have an atomic-like form consisting of a linear combination of the

solutions to the radial Schrödinger equation $u_l(r, E_l)$, multiplied by the spherical harmonics $Y_{lm}(\hat{r})$:

$$\chi_{\alpha,\vec{k}_n} = \sum_{lm} \left[A_{lm,\vec{k}_n} u_l(r_\alpha, E_l) + B_{lm,\vec{k}_n} \dot{u}_l(r_\alpha, E_l) \right] Y_{lm}(\hat{r}_\alpha). \tag{4.29}$$

Outside the muffin-tin, the preferred basis set consists of plane waves that satisfy Bloch's theorem:

$$\chi_{\vec{k}_n} = \Omega^{-1/2} e^{i\vec{k}_n \cdot \vec{r}} \tag{4.30}$$

Here, $\vec{k}_n = \vec{k} + \vec{G}_n$, with $\vec{G}_n$ being an integer multiple of a reciprocal lattice vector. The coefficients $A_{lm,\vec{k}_n}$ and $B_{lm,\vec{k}_n}$ are chosen such that the net wavefunction remains normalized as well as continuous and smooth at the muffin-tin boundary, where the transition between atomic-like and plane wave bases occurs. Finally, Ω is the unit cell volume, which normalizes the plane wave basis.

It is possible to further improve the computational economy by utilizing local orbitals, which are basis functions that are known to describe specific semi-core states of a particular atomic species well. These local orbitals are defined such that their magnitude and derivative are both zero at the muffin-tin radius so that they can be ignored when matching coefficients to smooth the net wavefunction at the muffin-tin boundary. The number of local orbitals and their particular form are chosen based on the specific elements that compose the unit cell.

Since the core and semi-core states generally take on a form quite close to their atomic-like or local orbital bases, the bulk of the computation time is spent on the plane waves in the interstitial region. How long it takes to solve the Kohn-Sham equations in this region is proportional to the number of plane waves N_{PW} in the basis set, which is related to the maximum magnitude of G_n used in the calculation and the unit cell volume Ω as follows:

$$N_{PW} = \frac{V_{FS}}{V_{BZ}} \propto \Omega G_{max}^3, \tag{4.31}$$

where V_{FS}, the volume of the Fermi sphere in momentum space is proportional to G_{max}^3 and V_{BZ}, the volume of the first Brillouin zone is proportional to Ω^{-1}. Therefore the computation

time can be reduced by either reducing the volume of the unit cell (typically out of one's control for 3D materials with a fixed structure) or reducing the value of G_{max}. However, a more restricted basis set implies that the representation of the Kohn-Sham orbitals will be poorer, so a balance must be struck between the desired accuracy of the ground-state density and the computational expenditure. In WIEN2k, G_{max} is determined by the parameter RK_{max}, the product of the smallest muffin-tin radius in the structure and G_{max}. For typical calculations this value is kept in the range $6 - 9$, and is more important when small atomic species like H are present in the unit cell [177].

Finally, a number of the terms in the Kohn-Sham equations contain integrals taken over the first Brillouin zone in k-space. To numerically evaluate these integrals, DFT programs discretize the first Brillouin zone into a mesh consisting of points evenly distributed along the reciprocal lattice vectors. Calculation time therefore scales linearly with the number of inequivalent k-points on this mesh, but a denser k-mesh also means that the computation of the integrals is more accurate. Given that these integrals occur in the expression of the total energy of the unit cell and that the convergence of this energy determines when the ground-state density has been reached, the importance of choosing an adequately dense k-mesh cannot be understated.

4.5 DFT for 2D Materials

The equations at the heart of DFT programs like WIEN2k assume that the input structure is 3D. Further, most exchange-correlation functionals are explicitly 3D, and in some cases diverge when applied to a strictly 2D system [178]. Therefore, care is required when attempting to model a freestanding monolayer with DFT. The typical approach to handling such structures is called the "slab method", which involves generating a 3D crystal that consists of a periodic array of isolated monolayers with thick slabs of vacuum inserted between them. I will use the example of graphene to illustrate some important aspects of slab calculations.

A typical slab representation of freestanding graphene is shown in Figure 4.1. The C–C distance is determined by the size of the unit cell in the $\vec{a}_1$ and $\vec{a}_2$ directions, while the inter-plane distance is controlled by its extent in $\vec{a}_3$. This inter-plane distance must be large

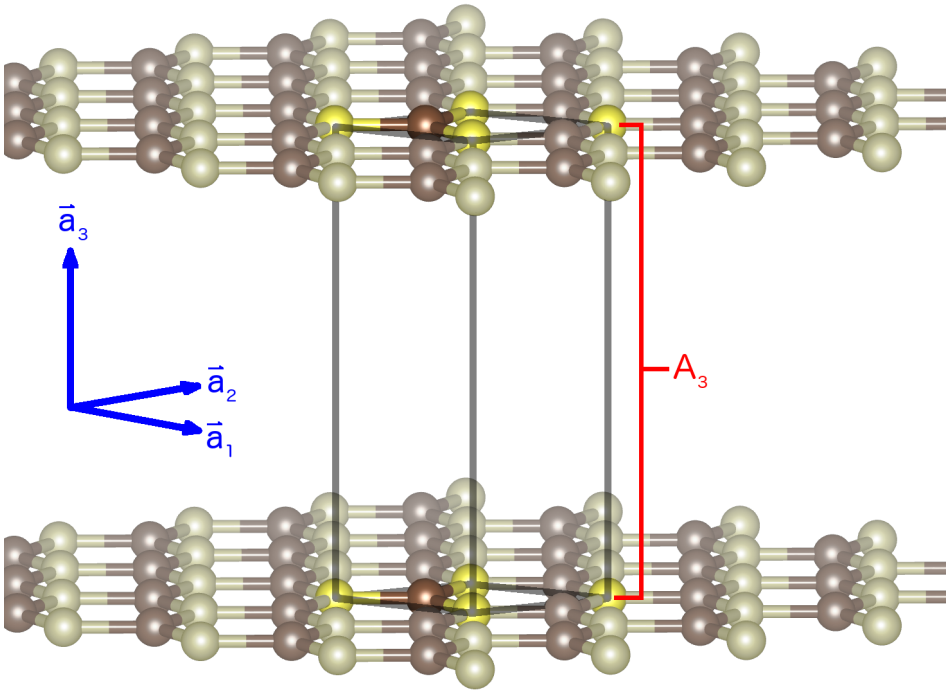

Figure 4.1: A 3D slab structure representation of 2D graphene. The inter-layer distance is controlled by the extent of the $\vec{a}_3$ axis of the unit cell, A_3. The unit cell is outlined, and atoms falling within it are highlighted.

enough to guarantee that there is no electronic interaction between adjacent graphene sheets, but with increasing vacuum thickness (and therefore unit cell volume) the calculations require more plane waves in the basis set and are therefore more resource-intensive, amounting to a practical limitation on the size of $\vec{a}_3$.

A good metric for measuring the interaction between graphene sheets is the total energy of the unit cell. As the vacuum slabs thicken and the planes drift apart, the energy of the system should tend toward a constant value as the interaction energy tends to zero. Figure 4.2 shows the unit cell energy for graphene with the vacuum between sheets ranging from 3.3 Å (the inter-sheet distance in graphite [98]) up to 15 Å. The convergence of the unit cell energy to a constant value is apparent, and seems to begin around 9 Å separation distance. Also plotted is the time per self-consistent field cycle in the WIEN2k DFT execution, which is a good measure of computational economy. The linear dependence on cycle time versus sheet separation reflects the linear dependence of N_{PW} on Ω. Common practice is that the

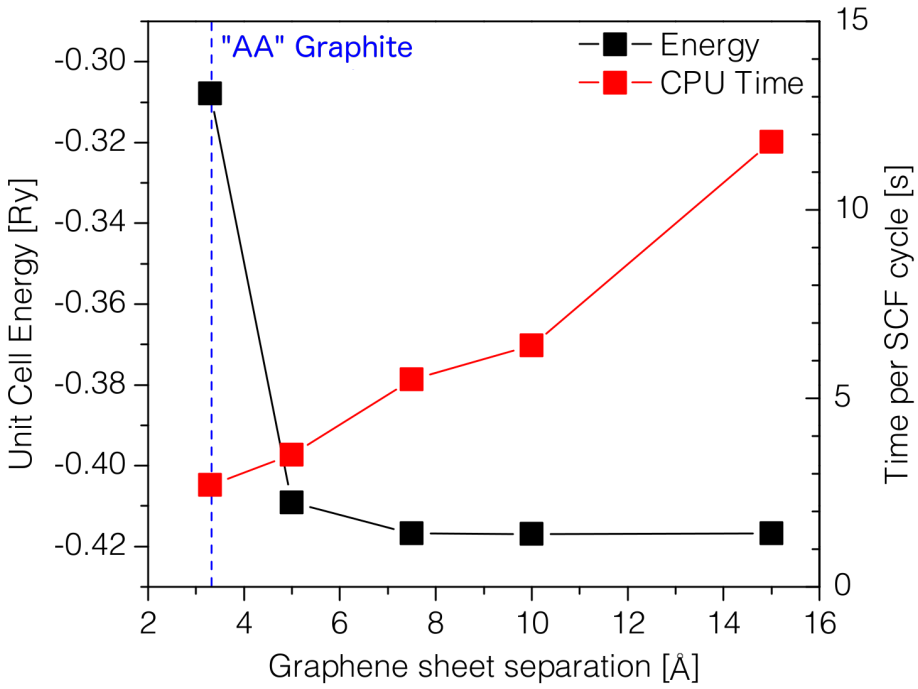

Figure 4.2: A plot of the unit cell energy (black) and cycle time (red) for slab graphene as a function of the vacuum thickness in the calculation. For clarity in the plot, the energy values are shifted by +152 Ry. Convergence in energy begins around 9 Å separation, and the computation time per cycle increases linearly with unit cell volume.

vacuum slab should be at least 10 Å, and ideally as close to 15 Å as one's computational resources will allow.

Selecting a k-mesh for 2D materials is significantly different from the 3D case. For a 3D crystal with unit cell dimensions $(A_1\hat{a}_1, A_2\hat{a}_2, A_3\hat{a}_3)$, one would typically select a k-mesh of the form $\mathrm{C}(A_1^{-1}\hat{b}_1, A_2^{-1}\hat{b}_2, A_3^{-1}\hat{b}_3)$, where C is larger for more dense meshes, $\hat{b}_n$ are the reciprocal lattice unit vectors, and the resulting values should be rounded to the nearest integer. This is known as the Monkhorst-Pack scheme [179]. However, in a 2D slab calculation with adjacent sheets separated by one unit cell length in the $\hat{a}_3$ direction, it is important to choose only one k-point in the $\vec{b}_3$ direction, since the adjacent sheets are supposed to be electronically isolated. Additional k-points in this direction would describe plane-waves that travel between sheets, forcing them to experience a spurious interaction.

For epitaxial 2D materials on macroscopically thick substrates, the best description of the material would be semi-infinite in the $\vec{a}_3$ dimension and periodic along $\vec{a}_1$ and $\vec{a}_2$. In order to

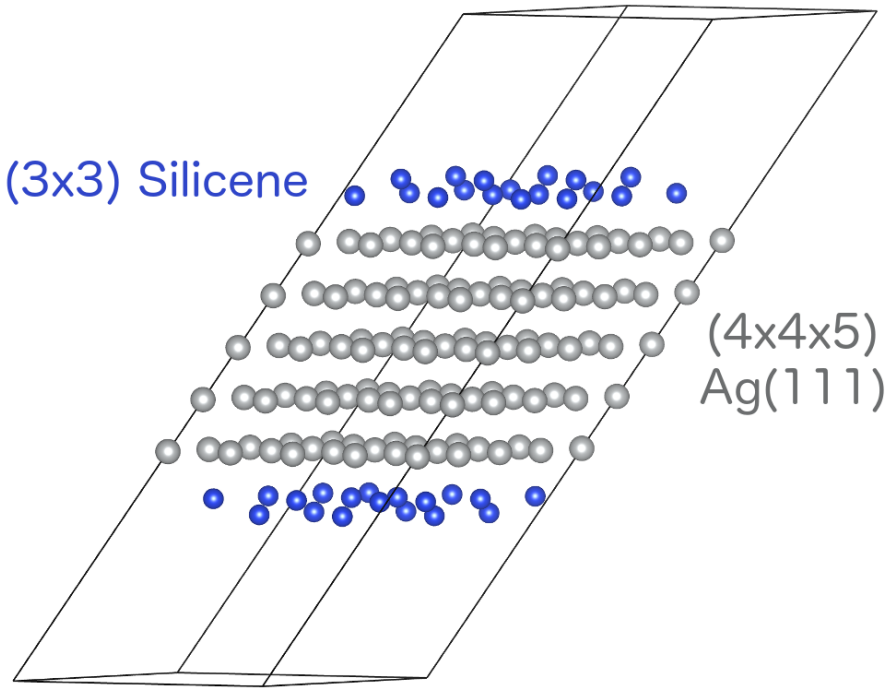

Figure 4.3: Two-sided (symmetrical) slab model of $(3 \times 3)/(4 \times 4)$ epitaxial silicene on a five layer thick Ag(111) supercell.

approximate such a structure with a finite 3D unit cell, one can stack layers of the substrate with the appropriate face termination, such as the $(4 \times 4 \times 5)$ Ag(111) slab shown in Figure 4.3, and then insert vacuum on either side of the resultant supercell to convert it into a slab. The epitaxial material can then be added to one side of the slab with vacuum maintained on the other side, or as I have shown in Figure 4.3, it can be added symmetrically to both sides to reduce the number of unique atomic positions in the calculation while maintaining a relatively thick substrate slab. Such models become more realistic with a thicker substrate slab, as they are more representative of the actual case of an essentially semi-infinite substrate. However, the resource demands of the calculation rapidly increase with added substrate layers, both because of the increased number of atoms and, to a lesser extent, the increased volume of the unit cell. Again, as with parameters like the vacuum slab thickness, k-mesh density and RK_{max}, it is good practice to select the number of substrate layers by iteratively increasing it until the calculated electronic structure stabilizes.

4.6 Atomic Forces and Structural Optimization

A DFT calculation is only as good as the structural model it is based on. That is, given an inaccurate set of atomic coordinates (and therefore $v_{ext}(\vec{r})$), it should be no surprise that the calculated $n_0(\vec{r})$ and the associated electronic observables should also be inaccurate. Fortunately, the WIEN2k suite includes efficient functions for improving the internal positions of atoms during the ground-state density calculation.

One very inefficient way to optimize a unit cell would be to simply calculate the ground-state energy with a number of different atomic positions and select the structure that returns the lowest value, keeping in mind that the nucleus-nucleus repulsion now has to be included in the total energy. This could be tenable for small unit cells in which there are few atoms, or a number of them reside on highly symmetric points and are therefore locked in place. For epitaxial silicene calculations, this is not the case.

A more reasonable approach would be to calculate the ground-state energy $E_0[n(\vec{r})]$ of the system with one set of atomic positions, slightly shift the ith atom by $\delta\vec{R}_i$ and then re-calculate the ground-state energy once more. The magnitude of the force F_i on that atom in the direction of $\delta\vec{R}_i$ would then be given by:

$$\vec{F}_i = \frac{\delta E_0}{\delta R_i}\delta\hat{R}_i. \tag{4.32}$$

Optimizing the structure could then be accomplished through the following algorithm:

- Calculate the ground-state energy for the initial configuration, which requires iteratively solving the Kohn-Sham equations once.
- Calculate the force in all three dimensions for every atom. This requires re-calculating the ground-state energy after shifting each atom by $\vec{R}_i$ three times, once for each spatial dimension. This amounts to an additional $3N_n$ iterative solutions of the Kohn-Sham equations. If all of the forces fall below an acceptable value (typically 1 mRy a.u.$^{-1}$), the optimization is finished. If not, continue the process.
- Shift all atoms according to their calculated net forces, and return to the first step with the updated structure.

Even this algorithm can be untenable, since a single calculation of the ground-state energy could take days or even weeks, and hundreds to thousands of cycles may be needed depending on the size of the system and how close the initial configuration is to being optimized. Fortunately, a better approach exists.

The Hellmann-Feynman theorem [180, 181] relates the change in calculated ground-state energy $E_0(\lambda)$ with any unit cell parameter λ to the change in the Hamiltonian $\hat{H}$ of the system with λ. Taking a derivative of the definition of the ground-state energy with respect to λ,

$$\frac{\delta E_0(\lambda)}{\delta \lambda} = \frac{\delta}{\delta \lambda} \langle \Psi_\lambda | \hat{H}(\lambda) | \Psi_\lambda \rangle \,, \tag{4.33}$$

where Ψ_λ is the net ground-state electronic wavefunction of the system given a specific value of λ. Carrying out the derivative on the right-hand side:

$$\frac{\delta E_0(\lambda)}{\delta \lambda} = \langle \frac{\delta \Psi_\lambda}{\delta \lambda} | \hat{H}(\lambda) | \Psi_\lambda \rangle + \langle \Psi_\lambda | \hat{H}(\lambda) | \frac{\delta \Psi_\lambda}{\delta \lambda} \rangle + \langle \Psi_\lambda | \frac{\delta \hat{H}(\lambda)}{\delta \lambda} | \Psi_\lambda \rangle \,. \tag{4.34}$$

Since $|\hat{H}(\lambda)\,|\Psi_\lambda\rangle = E_0(\lambda)\,|\Psi_\lambda\rangle$ and $\langle\Psi_\lambda|\,\hat{H}(\lambda)| = E_0(\lambda)\,\langle\Psi_\lambda|$,

$$\frac{\delta E_0(\lambda)}{\delta \lambda} = E_0(\lambda) \left(\langle \frac{\delta \Psi_\lambda}{\delta \lambda} | \Psi_\lambda \rangle + \langle \Psi_\lambda | \frac{\delta \Psi_\lambda}{\delta \lambda} \rangle \right) + \langle \Psi_\lambda | \frac{\delta \hat{H}(\lambda)}{\delta \lambda} | \Psi_\lambda \rangle \,. \tag{4.35}$$

But since the first term is just $E_0(\lambda) \frac{\delta}{\delta \lambda} \langle \Psi_\lambda | \Psi_\lambda \rangle = 0$, then

$$\frac{\delta E_0(\lambda)}{\delta \lambda} = \langle \Psi_\lambda | \frac{\delta \hat{H}(\lambda)}{\delta \lambda} | \Psi_\lambda \rangle \,. \tag{4.36}$$

If the parameter λ is chosen to be the position of the i^{th} atom $\vec{R}_i$, then the quantity on the left-hand side is an energy gradient and therefore represents a force on that atom. It is possible, then, to calculate the force on every atom in the cell by evaluating the how the Hamiltonian and the ground-state wavefunctions vary with a small shift in each atom's position.

It may seem unclear what has been gained by rewriting the force in this manner, as calculating the ground-state wavefunction takes just as much computing power as calculating the ground-state energy in the previous approach. However, it can be shown [182] that the dominant contribution to the change in ground-state energy with changing atomic positions

comes from the new definition of the Hamiltonian, not the evolution of the ground-state wavefunction. That is, the ground-state electronic density can be assumed to be "rigidly dragged" along with the atom as it is shifted by $\delta\vec{R}_i$ and the resulting force will still be of acceptable accuracy.

Using this method, the net force on every atom can be found after solving the Kohn-Sham equations only once. The optimization process is then:

- Calculate the ground-state wavefunctions for an initial configuration, which requires iteratively solving the Kohn-Sham equations once.
- Calculate the force in all three dimensions for every atom. This only requires varying the atomic positions within the Hamiltonian, as the ground-state wavefunctions can be assumed to be negligibly affected. Check to see if the forces fall below an acceptable level.
- Shift all atoms according to the calculated force, and return to the first step with the updated structure.

Obviously, this is much more efficient than the previous algorithm. It is important to note that some spurious forces may appear due to the incompleteness of the basis set and the transition between bases at the muffin-tin boundary, but these have been corrected for in the WIEN2k code [182–184].

4.7 Verifying DFT-Derived Structures

The better the initial structural model, the fewer the number of optimization cycles needed to reach force convergence. However, computational efficiency is not the only benefit of a good initial guess at the material's structure. Another is the potential to avoid false convergence at metastable solutions, wherein the forces on the atoms have been minimized but the energy of the cell is only a local minimum instead of the global one. Even shallow local energy minima can be inescapable within the rules of the force minimization algorithm (atoms always move in a direction that lowers the net force they feel). It is therefore important to

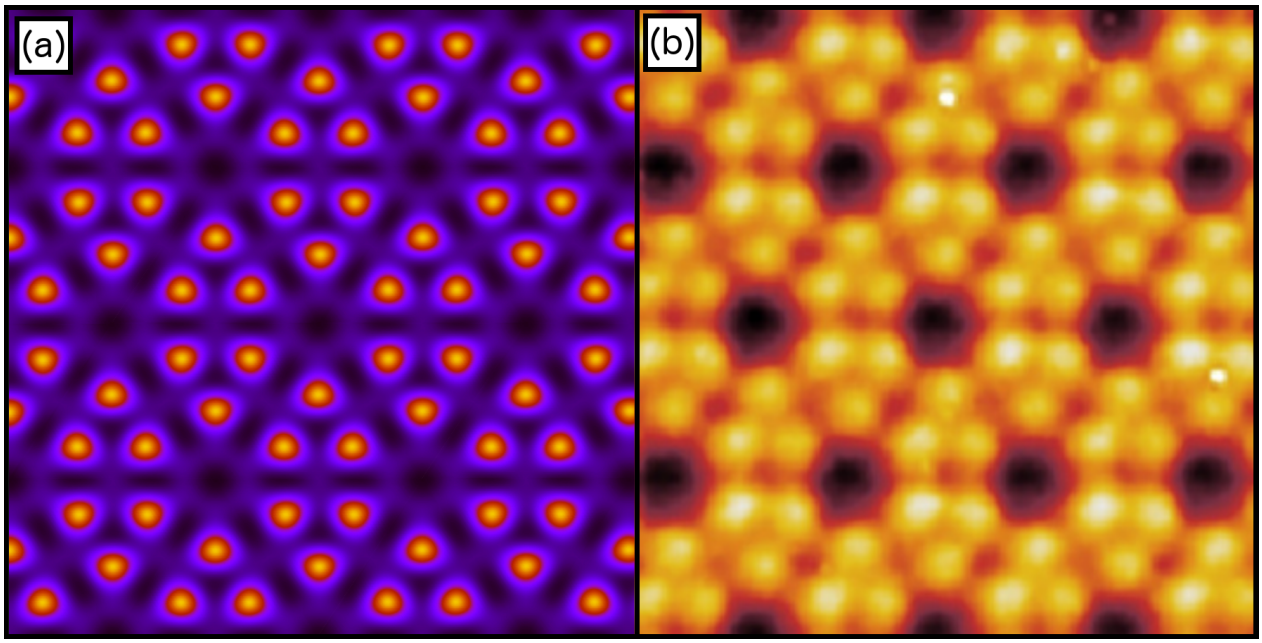

Figure 4.4: (a) A simulated constant-height STM measurement of the $(3 \times 3)/(4 \times 4)$ silicene/Ag(111) surface (after structural relaxation), with a -1 V tip bias and 1 Å tip-to-surface separation. (b) 0.65 nA constant-current STM image of the $(3 \times 3)/(4 \times 4)$ silicene/Ag(111) system, with a -1.12 V tip bias, adapted with permission from Reference [136].

verify that the results of a DFT structural optimization are in accordance with the structural characterization of the physical samples.

For epitaxial silicene, checking the optimized structure against LEED data is trivial since LEED only describes the characteristics of the unit cell, which are not altered by the structural optimization. SPM measurements, on the other hand, are sensitive to the atomic positions within the unit cell, which can change during relaxation. Of all of the SPM techniques, constant-height STM is simplest to simulate in the WIEN2k implementation of DFT.

When a WIEN2k calculation converges (i.e., the ground-state energy has been achieved), the spatial density of electronic states is immediately retrievable. However, it encompasses electrons of all energies, including those that would not be able to tunnel into a low-bias STM tip. The built-in WIEN2k routine "lapw2" is responsible for determining the value of the Fermi energy and "filling" the electronic states up to that level [177]. If this routine is re-run on a converged calculation with explicit instructions to only fill states above, for example, 1 eV below the Fermi energy, one can effectively remove every electron in the system except

for those that would be detectable with a -1 V STM tip. The WIEN2k subroutine "lapw5" plots the spatial density of electrons along a specified plane in the crystal [177]. If this plane is placed parallel to and slightly above the surface of the silicene, the resulting density plot will be a good representation of a constant-height STM image of that particular silicene structure, at least within the Tersoff-Hamann approximation. As an example, Figure 4.4(a) shows a constant-height STM simulation of the $(3 \times 3)/(4 \times 4)$ silicene/Ag(111) structure, while Figure 4.4(b) shows a corresponding STM image adapted from Reference [136]. In addition, I use the same method to bolster my conclusion that the $(\sqrt{3} \times \sqrt{3})$R30° epitaxial silicene structure is best described by an AA-stacked bilayer model in the study contained in Chapter 8.

Chapter 5

Soft X-Ray Spectroscopy

Most of a material's properties of interest, including its conductivity, optical absorption and magnetism, are entirely dependent on the characteristics of the electronic states within a few eV of the Fermi level. Therefore, mapping out these states can directly yield a wealth of information about the material, especially when combined with the predictions of DFT calculations. On the other hand, the structure of the deep core-level electronic states is almost entirely determined by the elemental identity of their parent atom, regardless of that atom's chemical environment. While this consistency implies that core-level states contain very little information about the material, they do offer a nearly fixed platform from which the more illuminating VB and CB states can be probed.

Core-level spectroscopic techniques involve provoking and monitoring electronic transitions between the core-level states of an atom and its states of interest in the VB and CB. Generating core-level vacancies in adequate numbers and being able to handle a variety of atomic species requires access to a high-flux widely-tuneable energy source, of which the modern synchrotron light source is a shining example. I will now briefly discuss the manner in which synchrotron radiation is generated and tuned for core-level spectroscopy experiments. I will then describe XES and XAS, two specific techniques that I have used to study the electronic structure of epitaxial silicene on Ag(111). Finally, I will close with a discussion of the practical aspects of carrying out soft X-ray spectroscopy on 2D materials, with a specific focus on the epitaxial silicene/Ag(111) system.

5.1 Synchrotron Radiation and Insertion Devices

Synchrotron radiation and cyclotron radiation are generated in much the same manner, namely when a moving charged particle is accelerated in a direction perpendicular to its trajectory, usually by a magnetic field. The distinction between the two is that cyclotron radiation is emitted by particles moving at non-relativistic speeds, while synchrotron radiation is emitted from highly relativistic particles. Both have the same toroidal angular distribution in a rest frame that is co-moving with the charged particle, and since the particles that emit cyclotron radiation are non-relativistic a toroidal distribution will also be observed in the laboratory frame. For synchrotron radiation, the relativistic particle's frame is spatially compressed relative to the laboratory frame. This results in the "beaming" of most of the radiated power into a narrow lobe in the direction of the particle's travel, with a small fraction of the radiation emitted into a wider trailing lobe (when viewed in the lab frame). The opening angle of the forward radiation cone is approximately $2\gamma^{-1}$ radians [185], and the average power radiated by a relativistic charged particle varies with γ^2 [186], where γ is the particle's Lorentz factor. The resulting radiation is therefore highly collimated and brilliant, especially from highly relativistic sources. Synchrotron radiation can be generated anywhere that relativistic charged particles exist, including natural sources like the jets of active galactic nuclei. However, the relevant form for condensed matter physics is the high-intensity light emitted from bending magnets and insertion devices in an electron storage ring or, more recently, at the end of a free electron laser.

First-generation synchrotron radiation experiments operated parasitically, siphoning off the waste radiation from the storage rings of particle collision experiments. Because the primary focus of these facilities were the collisions, the storage ring parameters were far from optimal for yielding the best beam characteristics. As researchers began to realize the potential of synchrotron radiation for the study of condensed matter, second-generation facilities consisting of storage rings dedicated to the production of synchrotron radiation began to appear. The workhorse of such facilities was the bend magnet, a region of strong, uniform magnetic field normal to the plane of the ring. The spectrum of synchrotron radiation produced by this uniform magnetic field is broad, peaking around a critical energy given by

the equation

$$E_c = \frac{3\hbar c\gamma^3}{2\rho} = \frac{3\hbar eB\gamma^2}{2m_0}, \tag{5.1}$$

Here, ρ is the radius of curvature of the particle as it travels through the region of uniform magnetic field, B is the magnetic field strength and m_0 is the rest mass of the charged particle, which is typically an electron. Since the particle energy (and therefore γ) is a fixed parameter of the storage ring, the critical energy is tuned by varying B in an attempt to maximize flux in the desired energy range. In most core-level X-ray spectroscopy experiments, only a small portion of the bandwidth corresponding to a particular core-level transition is desired. As a result, the majority of the bend magnet's emission profile would be discarded, which is both wasteful and can cause issues with thermal loading.

Insertion devices such as the wiggler and the undulator – the hallmarks of third-generation synchrotron facilities – were an important development toward increasing the usable flux of the beam. They consist of a periodic arrangement of magnets configured to produce a sinusoidal magnetic field with N spatial periods, each λ_{ID} in length. The average magnetic field experienced by the particle is therefore $B_0 = B/\sqrt{2}$, but the field strengths achievable in wigglers and undulators are typically higher than those of standard bend magnets due to the use of powerful permanent magnets [187]. An illustration of a simplified insertion device layout is shown in Figure 5.1.

The distinction between wigglers and undulators lies in their unitless deflection parameter K, defined as

$$K = \frac{eB_0}{2\pi m_0 c}\lambda_{ID}. \tag{5.2}$$

This value acts as a ratio of the maximum angular deflection δ of the electrons to the opening half-angle of the synchrotron radiation, γ^{-1}:

$$\delta = K\gamma^{-1} \tag{5.3}$$

For a wiggler, the period of the magnetic array is large enough that $K >> 1$. As shown in Figure 5.1, the electrons only emit radiation in the forward direction during a small portion of

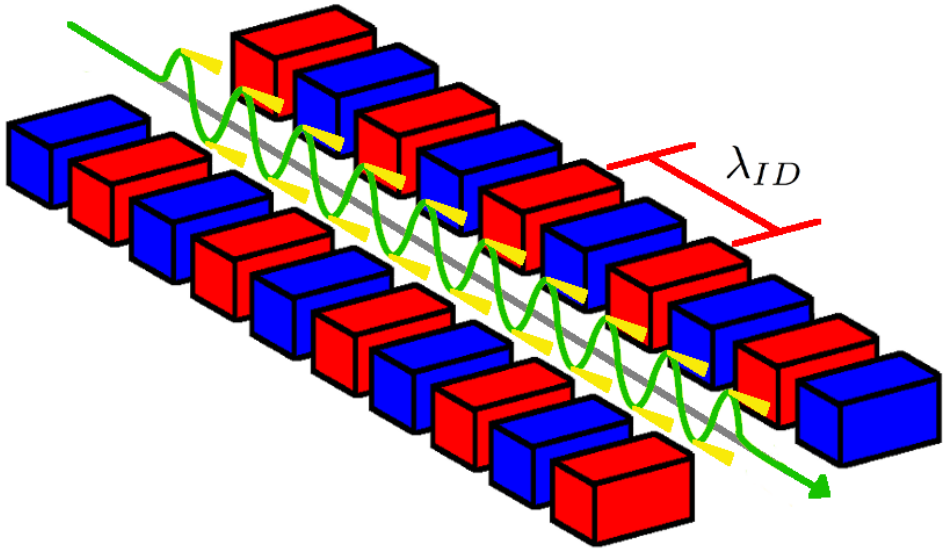

Figure 5.1: An illustration of the general layout of an insertion device. This device would be classified as a wiggler, since the maximum deflection angle of the electrons (green) is larger than the opening angle of the emitted light (yellow). The colour of the magnets (red and blue) indicate their polarity.

their sinusoidal trajectory, twice per insertion device period (see Figure 5.1). They therefore behave much like $2N$ bend magnets lined up end-to-end, with a similar emission profile and critical energy [188].

In undulators the period of the magnets is much shorter (such that $K \leq 1$), meaning the maximum angular deflection of the insertion device is less than the opening angle of the synchrotron radiation. This allows for coherent interference between the electrons and radiation field, which has a number of effects on beam characteristics. First, the angular spread of an undulator beam is reduced by a factor of $\sqrt{N}$ [185], which when combined with the enhancement factor of N from having multiple bend sections means that the undulator will have a factor of about N^2 the emitted power of a single bend magnet [185]. The coherent interference also narrows the (in-plane) spectrum into sharp peaks located at the odd harmonics of a single wavelength, as the even harmonics are subject to destructive interference [189].

Since K is proportional to B, stronger magnetic fields in undulators must be tempered by smaller magnet periods, typically limiting their range to below 10 keV even in their higher harmonics. Wigglers and superconducting superbend magnets on the other hand are able to produce photons exceeding 100 keV. Since the core levels of Si all reside below 2 keV binding

energy, an undulator-based soft X-ray beamline is ideal for silicene experiments, especially considering their characteristic high flux and the atomically thin nature of the samples. I will now describe the general layout of a soft X-ray endstation, as well as the particular details of the XES endstation of the Resonant Elastic and Inelastic X-ray Scattering (REIXS) beamline at the 2.9 GeV Canadian Light Source (CLS) in Saskatoon, Saskatchewan and the Soft X-ray Fluorescence (SXF) endstation of beamline 8.0 (BL8) at the 1.9 GeV Advanced Light Source (ALS) in Berkeley, California, two soft X-ray spectroscopy beamlines that I have used in my research into the silicene/Ag(111) system.

5.2 Soft X-Ray Endstations

Definitions vary, but the soft X-ray regime is typically considered as being between 50 eV and 2 keV, or about 0.5 nm to 25 nm in photon wavelength. On the low-energy side, the soft X-rays are bordered by vacuum ultraviolet (VUV) radiation, and the two are differentiated based on whether they typically excite valence (VUV) or core (soft X-ray) states. On the high-energy side, the soft X-rays blend into the hard X-rays, and the demarcation between the two is usually considered to be whether the photon wavelength lends itself to monochromatization by a diffraction grating (soft X-ray) or Bragg diffraction in a crystal (hard X-ray).

In general, a soft X-ray endstation will contain the following elements: a diffraction grating to disperse the radiation from the insertion device or bend magnet by energy, a moveable aperture to select a small energy range from the grating's output and highly-reflective mirrors to focus the beam and direct it to the target, all working within a UHV environment so that the soft X-ray beam is not attenuated by air. At the end of the beamline is the experimental endstation, a chamber that contains a number of instruments to monitor the sample's electronic, optical, and X-ray output as it is exposed to the soft X-ray beam. These chambers also commonly contain equipment for controlling the orientation and temperature of the sample.

The REIXS beamline uses an elliptically polarizing undulator (EPU, insertion device 10ID-2 of the CLS) to produce soft X-rays ranging from 80 eV – 2000 eV. The monochromator's energy resolving power ($E/\Delta E$) varies across this range, from about 10^5 near 100 eV to

10^4 near 1000 eV, and similarly the beam flux ranges from 10^{12} photons per second per 0.1% bandwidth at 100 eV to 10^{11} photons per second per 0.1% bandwidth at 1000 eV [190]. The REIXS XES endstation is outfitted with a channel electron multiplier for measuring the total fluorescence yield (TFY) XAS, a fluorescence spectrometer for performing XES and partial fluorescence yield (PFY) XAS, and the sample arm is grounded through a picoammeter for measuring the renormalization current in total electron yield (TEY) mode XAS. The specifics of these techniques will be discussed in the next section.

BL8 at the ALS is another undulator-based beamline with an energy range of 80 – 1250 eV. It has a slightly lower energy resolving power than REIXS at 7×10^3 [191] but offers a higher flux by about an order of magnitude [191,192], partly due to the typical flux/resolution trade-off and in partly due to the fact that the ALS runs at 500 mA ring current, while the CLS runs at 250 mA. The BL8 soft X-ray fluorescence endstation (recently upgraded to the iRIXS endstation) was outfitted similarly to the REIXS endstation, albeit with a lower-resolution XES spectrometer.

While silicene depositions and measurements have been performed at both REIXS and BL8, the data used in Chapters 6–8 are exclusively from the REIXS experiments. This is because in the early BL8 experiments, the silicene samples had to be deposited in one UHV chamber and measured in another with no possibility of *in vacuo* transfer between the two. Instead, the samples were transferred in a glove bag purged with dry N_2 gas, which was found to be insufficient for preventing oxidation. REIXS, on the other hand, has a vacuum transfer cart that is compatible with both the deposition chamber and the XES sample garage, allowing for the samples to be produced and measured without leaving UHV conditions.

5.3 X-ray Absorption Spectroscopy

An XAS measurement involves scanning the soft X-ray beam energy over a range that encompasses the binding energy of the target core-level electron, typically a few tens of eV in width. When the beam energy is below the binding energy, there are no unoccupied states available for the core-level electron to be excited into, so no transitions will occur. When

the beam energy exceeds the electron's binding energy, the electron can be excited into unoccupied states in the CB. The rate of these transitions is related to the number of states available in the CB with the appropriate angular momentum quantum number (see Appendix B for a more detailed discussion of core-level transition probabilities and the definition of the transition-weighted partial density of states (tw-pDOS)).

Therefore if the transition rate is plotted as a function of incident beam energy it should map out the tw-pDOS in the conduction band. The transition rate can be inferred in a number of ways. The first, which is more common in experiments using hard X-rays because of their increased penetration depth, involves measuring the attenuation of the incident beam through a thin foil of the material of interest. A greater attenuation corresponds to more frequent excitations, which means that the tw-pDOS is greater at the energy the core-level electrons are being excited in to. However, soft X-rays typically have a maximum penetration depth of a few hundred nm, which is far too thin to be practical for films of most bulk materials. 2D materials are by definition thinner than this, so in principle transmission-mode soft X-ray absorption measurements should be feasible. However, this would only be true for freestanding sheets, a form in which silicene does not yet exist.

The final state of the X-ray absorption process includes an electron in the CB and a hole in a core state. This configuration rapidly relaxes when the core hole is refilled by any higher-lying electron, including less tightly-bound core states or VB states. The rate of core-hole refilling is related to the rate of core-hole creation, and can therefore be used as a proxy for the transition rate. There are two processes by which the core-hole refilling can take place. The first, which is the most common for low Z materials like Si, is non-radiative Auger emission. This process is illustrated in Figure 5.2(c).

In Auger emission, the energy released when an electron fills core hole is absorbed by a second electron in a higher orbital, known as the Auger electron. It is ejected from the atom into the bulk of the material and carries with it a kinetic energy equal to the difference between its binding energy and the energy of the de-excitation. If the absorption event happened within a few nm of the sample surface, the Auger electron may escape the sample completely, leaving it with a net positive charge. With enough kinetic energy, it may also ionize a number of other atoms along the way, resulting in a cascade of secondary electrons

escaping from the surface.

In XAS experiments, the Auger and secondary electrons are intentionally drawn from the surface with an electric field, and the sample is electrically grounded. In this way, the rate of electrons ejected via Auger emission can be measured through the sample's renormalization current. Since this current is equal to the number of electrons leaving the surface, it is proportional to the core hole refilling rate, which is once again a proxy for the transition rate and therefore the tw-pDOS. Such XAS measurements called TEY-mode, and are typically considered to be surface-sensitive due to the limited escape depth of Auger electrons. However, since 2D monolayer and multilayer silicene samples are typically less than 1 nm in thickness, TEY actually represents a bulk-sensitive technique for these materials.

Another de-excitation mode is radiative X-ray fluorescence, shown in the Figure 5.2(d). In this process, rather than the energy of the de-excitation going to a higher-lying electron, it escapes the atom as an X-ray photon. A nearby detector counts these photons, and the count rate can be used as a proxy for the tw-pDOS. However, it is important to note that the X-ray photons resulting from the de-excitation may not be the only photons picked up by the detector. X-ray photons may also be produced when the vacancy left by an Auger electron is refilled, and optical fluorescence from secondary processes in the CB and VB. In X-ray excited optical luminescence (XEOL), the rate of optical photon production is monitored as a proxy for absorption, while in TFY measurements, the optical photons are rejected and only X-ray fluorescence (> 13 eV for the detector at REIXS) from filling core holes and holes left by deep Auger electrons are counted. In PFY XAS measurements, a spectrometer is utilized to select only those X-ray photons that result from direct VB to core hole transitions.

For Si $2p$ core-level spectroscopy, which is the basis for the transition diagrams illustrated in Figure 5.2, the only filled states that are less bound than the core-level are the Si $3s$ and $3p$ states in the VB. Auger emission will therefore always result in a hole in the VB, which will then recombine with an electron higher in the VB. The maximum energy of such a recombination is equal to the energy difference between the VB maximum and minimum, about 10 eV. Thus, Auger emission cannot produce any photons that are measurable with the TFY detector at REIXS. Therefore, both TFY and PFY measurements should only be sensitive to the VB $\rightarrow 2p$ transition, which is why they can be plotted together in Figure 5.2.

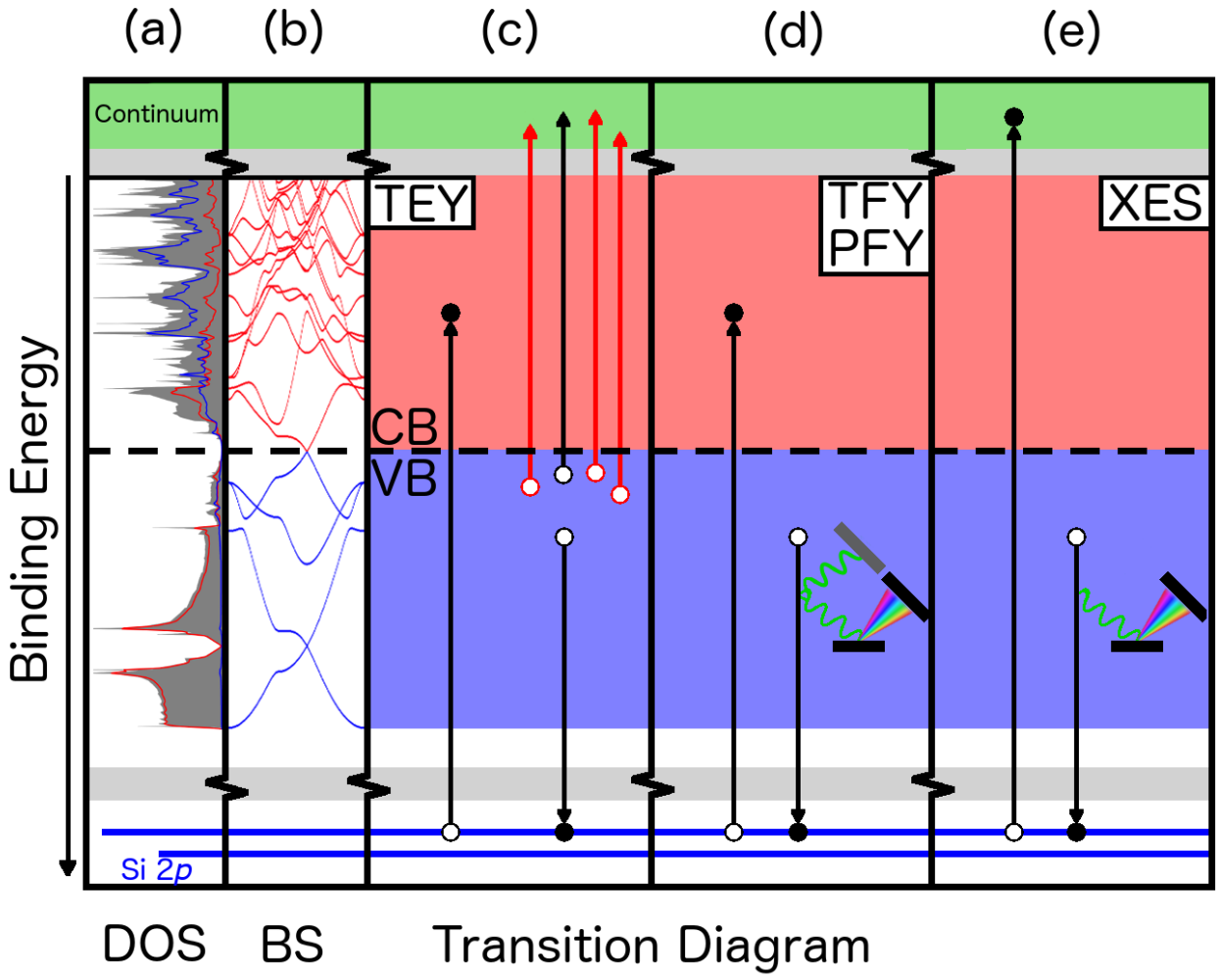

Figure 5.2: (a) s and d pDOS for a freestanding silicene sheet (red and blue, respectively), plotted with their tw-DOS (grey) for a transition from the Si $2p$ core-level (blue lines at the bottom). (b) VB (blue) and CB (red) bandstructure for freestanding silicene, with the Dirac cone visible at the Fermi level. (c) A schematic of the transition involved in TEY-mode XAS. The core-level electron is excited into the CB, and the core hole is filled with an Auger decay. The Auger electron (black, a VB electron in Si $2p$ spectroscopy) is ejected from the atom, and can ionize other atoms as it escapes the sample, bringing secondary electrons (red) with it. (d) A schematic of the transition involved in TFY- and PFY-mode XAS (the same only because it is Si $2p$ spectroscopy, see text). In this mode, the core hole refilling results in an X-ray photon, which is counted by a fluorescence detector. (e) A schematic of the transition involved in TEY-mode XES, similar to (d) except the excitation puts the core-level electron into the continuum states, and the fluorescent decay is always measured with a spectrometer.

XEOL measurements are only feasible on samples that exhibit strong luminescence, and are better suited for bulk samples ($>$ 100 nm thick) such that optical luminescence can occur all throughout the escape depth of the optical photons. Both TFY and PFY can suffer from saturation effects, which are the most pronounced when the absorption only takes place on the surface of the material, and secondary self-absorption is not present [193]. This effect can be mitigated by monitoring a lower-energy transition in the material, usually in a lighter atomic species like O or N [194], in a technique known as inverse PFY (IPFY). Since silicene is entirely composed of surface atoms and no higher-lying emission lines are available to monitor for IPFY, fluorescence-dependent XAS can be safely ruled out. Further, both of these techniques rely on the fluorescence decay path which is less likely for a low-Z atom like Si. Instead, because it is surface-sensitive and given the excellent conduction characteristics of the Ag(111) substrate, TEY-mode XAS is by far the best method for epitaxial silicene samples.

5.4 X-ray Emission Spectroscopy

The direct de-excitation of VB electrons into core-level vacancies also allows for the mapping of the tw-pDOS in the VB. This process is similar to PFY, in which a spectrometer is utilized to select only those X-ray photons that correspond to de-excitations from the VB into the primary core hole, but instead of simply summing the number of counts across the detector, the energy spectrum of the photons is preserved.

Emission measurements can be classified as non-resonant XES (NXES, sometimes also called normal XES), or resonant XES (RXES) depending on the excitation energy of the incident beam. In NXES (shown in Figure 5.2), the core-level electron is excited high into the continuum states, while in RXES the incident energy is tuned to match a feature in the XAS spectrum. If this CB feature primarily consists of states from a single inequivalent atomic site, more de-excitations will originate from that site and the resulting emission profile will primarily represent its VB tw-pDOS. The NXES spectrum, on the other hand, will be an average of all of the VB tw-pDOS for every atom of the target element in the sample, since all of them will have the same transition probability into the continuum states.

RXES requires that excitations take place relatively low into the CB, and the boundaries of the emission spectrometer are set to encompass the whole VB. This means that one will often detect a reflection of the incident beam in the XES spectrum, which will appear as a sharp monochromatic peak. This can be useful for calibrating the monochromator to the XES spectrometer, as I mention in the publications in later chapters. However, it also makes RXES measurements of epitaxial silicene on Ag(111) virtually impossible. The highly-polished Ag surface strongly reflects any photons not absorbed by the atom-thick layer of Si. Even with the exit slit set as thin as feasible, so that the beam is highly monochromatic and greatly reduced in flux, the tail of the elastic scattering peak still dominates the XES spectrum. At the SXF beamline at the ALS, the elastic feature was even bright enough to saturate the fluorescence detector and cause a number of spurious features to appear in the spectrum. Because of this reflectivity problem, only NXES measurements are performed.

5.5 Considerations for 2D Epitaxial Silicene

The Si $1s$, $2s$ and $2p$ core levels are all within the soft X-ray regime (binding energies of 1839 eV, 149.7 eV and 99.6 eV, respectively [195]). Two major considerations one has to make when selecting an appropriate core-level are the natural linewidth of the core hole and the angular momentum of the states of interest. Immediately, one can rule out the Si $2s$ core-level as a candidate, because its natural linewidth is around 1 eV [196], which would lead to unacceptably poor energy resolution in the resulting spectra. The most interesting states in silicene are probably the $3p$ states, given that they would be responsible for the Dirac cone (should one exist). However, the $3s$ states would also be a good metric for observing σ-like bonding with the other Si atoms or the substrate.

Unfortunately, $1s$ core-level spectroscopy is not feasible for a number of reasons. First, the penetration depth of the incident beam increases with beam energy. Obviously, this is undesirable when measuring a sample that is only about 3 Å thick. It is possible to somewhat mitigate this effect by utilizing a grazing incidence geometry, where the normal of the substrate surface is around $80° - 85°$ away from the incident beam direction. This causes the path length through the sample, and therefore its effective thickness, to be greater.

However, the attenuation length of $\sim$ 1.8 keV photons in Si is about 10 μm [197], which corresponds to an unfeasibly extreme grazing incidence to reach a similar level of effective sample thickness. Further, the XES spectrometer is equipped with a slit so that the beam spot on the sample is clipped down to approximate a point source, as a spatially extended source would result in poor energy resolution. Highly grazing incidence spreads the footprint of the beam across the sample, and therefore lowers the beam flux that is in view of the spectrometer slit.

The attenuation length for $\sim$ 100 eV photons, which are capable of exciting the Si $2p$ core-level electrons, is about 0.5 μm [197], so the number of photons interacting with the atom-thick Si layer should be more than an order of magnitude larger. Furthermore, there are six core-level electrons available for excitation (two $2p_{1/2}$ and four $2p_{3/2}$), which increases the probability of an absorption event occurring over the two $1s$ or $2s$ core levels. Finally, the two undulator-based beamlines that we use in our experiments, selected in part because of their having appropriate deposition chambers, are able to produce much more flux around 100 eV than 1800 eV. For these reasons, X-ray spectroscopy experiments are performed at the Si $2p$ core-level. While such experiments cannot directly yield information about the important Si $3p$ states, comparison of the XES and XAS spectra to the $3s$ and $3d$ states from DFT calculations can be used to verify the theoretical models. In turn, these models contain predictions about the structure of the $3p$ states.

5.6 Spectral Broadening and Simulating Soft X-ray Spectra in WIEN2k

Several factors contribute to the broadening of the tw-pDOS features in a soft X-ray spectroscopy measurement. Already mentioned was the natural linewidth of the transition, which is a result of the femtosecond-scale lifetime of core holes and the uncertainty principle of Heisenberg. The lifetime of a particular core hole depends on the number of states that are able to decay into it as well as the energetics of those decays. Natural linewidths for most core holes in materials have been tabulated [198], and the effect can be modelled as a Lorentzian broadening of the tw-pDOS when simulating soft X-ray spectra. Next, the instrumental res-

olution of the monochromator should be considered when modelling XAS spectra (or RXES spectra). There should be a spread in the energy produced by the monochromator because of the finite size of the exit slit as well as any imperfections in the monochromator grating. For NXES spectra, the same is true of the emission spectrometer, and the resolution of the detector also has to be considered. A convolution of these two instrumental broadening profiles can be observed directly by reflecting the incident beam into the emission spectrometer slit, which also allows for the two devices to be calibrated to each other in energy space. Finally, there are broadening effects associated with the lifetimes of the electron in the CB in the final state of an absorption event and the hole in the VB in the final state of an emission event. These lifetimes will be smaller (and therefore the associated broadening larger) for a hole in the bottom of the VB or an electron high in the CB [199].

Another consideration that must be made in modelling XES and XAS measurements is core-level splitting. As mentioned previously, the Si $2p$ level contains six electrons, two in the $2p_{1/2}$ orbitals and four in the $2p_{3/2}$ orbitals, typically separated by 0.4 eV. Each core-level will produce its own map of the tw-pDOS in an XES or XAS measurement, shifted from each other by the core-level separation energy and scaled by the number of core-level orbitals available. In all four publications presented in this manuscript, broadening and core-level splitting effects are modelled using Broadsword, custom software written by Dr. Teak Boyko specifically designed to accept the output of WIEN2k calculations.

Finally, the core hole present in the final state of an XAS measurement can significantly alter the structure of the CB states that the measurement meant to probe, as it reduces the screening of the nuclear charge. Typically, the effect of the core hole is to add spectral weight to the states near the bottom of the CB, but it can also shift the CB minimum downward in energy. Since an XES measurement does not contain a core hole in the final state, this shift will only occur in the absorption spectrum and thus the apparent experimental bandgap can be reduced. In an all-electron, full potential implementation of DFT like WIEN2k, this effect can be modelled by removing a core electron from one atom and placing it as a background charge to keep the structure neutral. However, at one core hole per unit cell, this will likely overestimate the core hole effect and introduce spurious core hole – core hole interactions that would not be present in an actual XAS measurement. In order to remedy this overestimation,

core hole calculations are typically performed on a large supercell of the original structure, but are therefore computationally expensive. In Chapter 6 I determine that core hole effects are not significant in DFT calculations of epitaxial silicene on Ag(111), but the calculations of $LiGaO_2$ in Chapter 9 demonstrate both the weighting and shifting effects that the core hole can have on the CB minimum.

Chapter 6

The Metallic Nature of Epitaxial Silicene Monolayers on Ag(111)

Authors: *Neil W. Johnson, Patrick Vogt , Andrea Resta , Paola De Padova , Israel Perez , David Muir , Ernst Z. Kurmaev , Guy Le Lay , and Alexander Moewes*

Reference: N.W. Johnson *et. al*, *Advanced Functional Materials* **24**, 5253 (2014). [136]

This manuscript contains my first published work on silicene, an exploration of the electronic structure of epitaxial silicene monolayers deposited on Ag(111). The initial experiments leading to this publication were performed at BL8 at the ALS in May of 2012. Prof. Guy Le Lay, Dr. Patrick Vogt and Dr. Paola De Padova, three members of the research group that had given the first report of the $(3 \times 3)/(4 \times 4)$ silicene reconstruction on Ag(111) one month earlier [127], produced the sample for the experiment using the nanoNEXAFS endstation's deposition equipment. The best available method for transferring the silicene between nanoNEXAFS and SXF, where the XAS and XES measurements were to be performed, involved purging both loading chambers and a glove bag with dry N_2 gas, using the glove bag as a transport container. This was found to be inadequate because even the trace residual gases in the bag and chambers was enough to completely oxidize the samples, evident by the SiO_2-like features in the XAS and XES after transfer. These initial results were therefore not published.

In a later experiment performed at the CLS in June of 2013, Prof. Guy Le Lay, Dr. Patrick Vogt, Dr. Andrea Resta, Dr. Israel Perez, Dr. David Muir and I worked on narrowing down the optimal parameters for the growth of a monolayer using the deposition chamber located

at our group's own REIXS beamline. During this time, we produced and performed the first XAS and XES measurements of unoxidized silicene, though the beam time available was not sufficient enough to result in publishable spectra. Over the coming months I worked to refine the deposition parameters, and in December of 2013 I performed the deposition, LEED characterization and soft X-ray experiments that appear in Figure 6.3. Dr. Patrick Vogt provided the STM images that appear in Figure 6.5.

Beginning in May of 2012, I also began performing DFT calculations on the $(3 \times 3)/(4 \times 4)$ and $(\sqrt{7} \times \sqrt{7})$R19.1°/$(\sqrt{13} \times \sqrt{13})$R13.9° silicene/Ag(111) systems, as these were the structures we expected to grow in our experiments. The results of the DFT structural relaxations are presented in Figure 6.1, the calculated DOS in Figure 6.2 and the simulated XES and XAS spectra in Figure 6.3. I was the sole author of this manuscript aside from the caption of Figure 6.5 which was written by Dr. Patrick Vogt.

I am licensed to reproduce this manuscript within the pages of this thesis. See Appendix C for more information. The figure numbers, section headings and general formatting have been altered to ensure the consistency of this thesis. No other substantial alterations have been made to the manuscript.

6.1 Abstract

Silicene is a two-dimensional structure composed of a buckled hexagonal honeycomb lattice of silicon atoms. Freestanding silicene is yet to be synthesized, but epitaxial silicene monolayers have been directly observed or predicted to exist on a number of supporting substrates. Herein the atomic and electronic structures of five distinct epitaxial silicene morphologies on Ag(111) are examined through the complementary techniques of density functional theory and soft X-ray spectroscopy at the Si $L_{2,3}$ edge. Hybridization with the Ag(111) substrate is shown to cause these silicene monolayers to become strongly metallic, and the specific electronic interactions that are responsible for this metallic nature are determined. The results imply that epitaxial silicene on Ag(111) does not possess the Dirac cone electronic structure that is characteristic of freestanding silicene and graphene sheets.

6.2 Introduction

Early theoretical investigations into a silicon-based analogue to graphene, including tight-binding models [200] and density functional theory (DFT) calculations [99], supported the idea that freestanding silicene monolayers possess the same zero-bandgap Dirac cone electronic structure that is responsible for graphene's intriguing electronic and magnetic characteristics [5]. However, freestanding silicene has not yet been isolated in the laboratory largely due to the lack of a naturally occurring silicon-based analogue to graphite. Silicene is an attractive alternative to graphene as semiconductor device manufacturers are already well-equipped to deal with silicon-based components, whereas the transition to carbon-based electronics could present significant challenges in device manufacturing and design. Further, the buckling inherent in silicene could allow for the tuning of its bandgap and polarized spin-states in the presence of an external electric field [104, 106], making it a good candidate material for spintronic applications. Freestanding silicene is also predicted to be a two-dimensional topological insulator due to quantum spin Hall effects. [108] An excellent review of this novel material has recently been published [201].

While it is possible to chemically exfoliate thin sheets of Si, and possibly even Si monolay-

ers, from $CaSi_2$ [101], most reports of silicene monolayers have involved physical deposition of Si on a supporting substrate. Typically the substrate used is Ag(111) [109, 127, 202] (the focus of this investigation), but stable monolayers have also been reported on Ir(111) [203] and ZrB2(0001) [204], and simulations have suggested it may also be possible to deposit a silicene monolayer on h-BN [205,206]. However, the atomic and electronic structures of these epitaxial silicene sheets can deviate significantly from those of freestanding silicene due to electronic interaction with the substrate, in contrast to graphene which has been shown to be minimally perturbed by an underlying Ag(111) substrate [207]. Understanding the nature of this interaction and knowing its effects on the electronic properties of the epitaxial silicene monolayer will be an important step toward the realization of the potential applications for this novel material.

Scanning tunneling microscopy (STM) and DFT investigations of epitaxial silicene on Ag(111) suggest that it is capable of taking on a number of stable forms, depending on the deposition rate and substrate temperature during growth [109,137,138,208]. The first report of epitaxial silicene depicted a monolayer (3×3) Si reconstruction on a (4×4) Ag(111) supercell [127]. Angle-resolved photoemission spectroscopy (ARPES) measurements were initially thought to indicate the presence of a Dirac cone with a bandgap opening [127], but a subsequent DFT bandstructure calculation suggested that the observed linear band was the product of Si hybridization with Ag states [132], not an arm of silicene's Dirac cone. Presently, it remains controversial whether silicene on Ag(111) is inherently metallic [131–133] or a semiconductor with a small gap [134, 135], though the majority of publications seem to support the former conclusion.

A number of other stable silicene morphologies on Ag(111) have since been observed or predicted, including silicene reconstructions on $(2\sqrt{3} \times 2\sqrt{3})$R30° [137], $(\sqrt{7} \times \sqrt{7})$R19.1° [137], and $(\sqrt{13} \times \sqrt{13})$R13.9° [109, 137, 139, 150, 209, 210] Ag(111). In this study, we use the complementary techniques of DFT calculations and synchrotron-based soft X-ray spectroscopy to explore the electronic structures of monolayer silicene reconstructions on (4×4) and $(\sqrt{13} \times \sqrt{13})$R13.9° Ag(111), the two most commonly observed reconstructions in the literature. We report that *ab initio* DFT calculations predict a metallic electronic structure for both of these epitaxial monolayers; a prediction which we support by experimentally prob-

ing the valence and conduction bands with soft X-ray absorption and non-resonant emission spectroscopy (XAS and XES).

6.3 Density Functional Theory Calculations

DFT refinements of the atomic structures and calculation of the electronic structures of epitaxial silicene sheets were performed with the WIEN2k software package, [177] which is based on the full-potential linearized augmented plane wave + local orbitals method. The epitaxial silicene was modelled as sheets of Si covering both faces of a five unit cell thick slab of Ag(111) in the Pm (No. 6) space group. This space group is symmetric about the plane z = 0.5 where **z** is in the direction perpendicular to the Ag(111) surface. 15 Å of vacuum in the **z** direction separated each silicene sheet in order to isolate adjacent slabs from each other. All calculations were performed on a (10×10×1) k-point mesh with a -6.0 Ry plane-wave cutoff energy and an RK_{MAX} of 5.0. Calculations were considered to have converged when energy and charge steps in self-consistent field iterations dropped below 10^{-4} Ry and 10^{-3} e, respectively. The internal positions of atoms were optimized such that the net force on each atom fell below 1 mRy/a.u. Both structural relaxations and electronic structure calculations used the generalized gradient approximation of Perdew, Burke and Ernzerhof [171] (PBE-GGA). Calculations using the modified Becke-Johnson exchange-correlation functional were also performed, as these usually provide better estimates of the bandgap, [173] but the results were found to be virtually identical to the PBE-GGA calculations in terms of the DOS in the vicinity of the Fermi level.

We first perform DFT optimizations and electronic structure calculations on freestanding silicene as a test of the validity of our theoretical approach. An optimization of the buckling distance and SiSi bond length is found to reproduce the structural parameters of low-buckled (LB) silicene reported in Reference [99]. This relaxed structure is shown in Figure 6.1(a).

Our internal force minimization of the epitaxial silicene sheets uses the published structures of (3 × 3) silicene on a coincident (4 × 4) Ag(111) supercell [109], three unique configurations of $(\sqrt{7} \times \sqrt{7})$R19.1° silicene on a coincident $(\sqrt{13} \times \sqrt{13})$R13.9° Ag(111) supercell [137,138,209,211] (hereafter $(\sqrt{7}\times\sqrt{7})/(\sqrt{13}\times\sqrt{13})$), and (3×3) silicene on a coincident

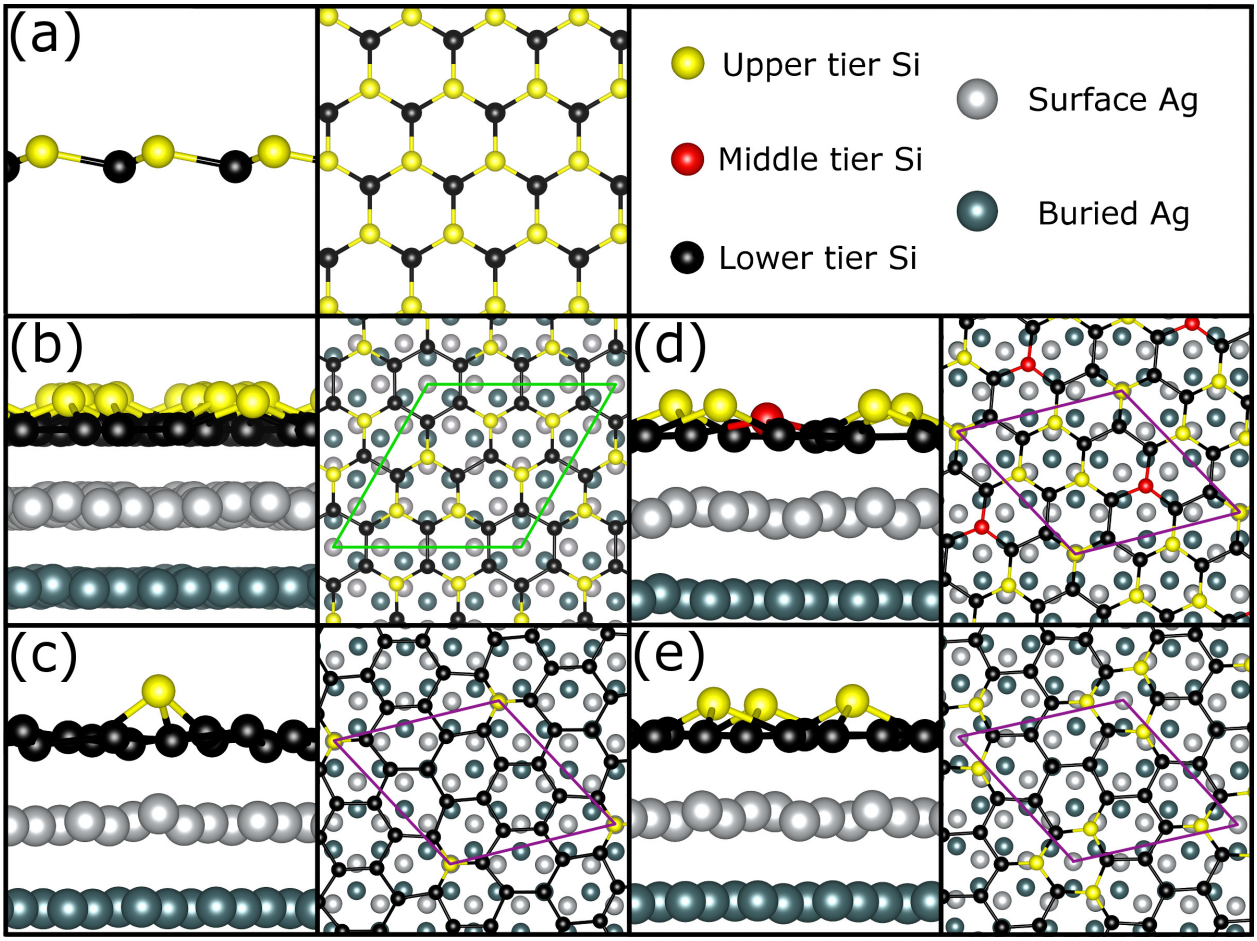

Figure 6.1: (a) The structure of low-buckled freestanding silicene. Note the sublattice inversion symmetry of the upper and lower layers. The relaxed structures of (b) $(3 \times 3)/(4 \times 4)$ and (c)-(e) $(\sqrt{7} \times \sqrt{7})/(\sqrt{13} \times \sqrt{13})$ epitaxial silicene. $(3 \times 3)/(4 \times 4)$ silicene has 18 Si atoms per nit cell for a coverage ratio of 1.125 Si:Ag, while the $(\sqrt{7}\times\sqrt{7})/(\sqrt{13}\times\sqrt{13})$ silicene structures contain 14 Si sites per unit cell for a coverage ratio of 1.077 Si:Ag. Visualization provided by the VESTA software package [8].

$(\sqrt{13}\times\sqrt{13})$R13.9° Ag(111) supercell [130] (hereafter $(3\times3)/(\sqrt{13}\times\sqrt{13})$) as initial configurations. We find most of these structures to be nearly optimal already, with the exception of $(3 \times 3)/(\sqrt{13} \times \sqrt{13})$ which we observe to deviate significantly from the simple buckled structure reported in Reference [130], resulting in a relaxed structure that can no longer be said to contain a hexagonal honeycomb of Si atoms on the surface. By explicitly imposing hexagonal symmetry, the Si surface structure is found to relax to a distorted, highly buckled honeycomb closely resembling the simulated STM image in Reference [130], but this configuration is unstable when the symmetry constraints are subsequently removed. As such, we

do not consider this particular configuration any further in this study, and suggest that it is not likely to be physically realized. The optimized structures of $(3 \times 3)/(4 \times 4)$ and the three forms of $(\sqrt{7} \times \sqrt{7})/(\sqrt{13} \times \sqrt{13})$ silicene are described in Figure 6.1(b)-(e).

With the freestanding and epitaxial silicene structures optimized, the ground-state density of states (DOS) for each can be explored in detail. Figure 6.2 shows the calculated partial and total Si DOS for freestanding silicene, which are in good agreement with previous DFT and tight-binding model calculations. [99] The lowest-lying states in the valence band are predominantly Si s states, which give way to Si sp hybrid states in the range of -8 eV to -3 eV (Si–Si σ bonding). The top of the valence band and bottom of the conduction band are composed primarily of p_z states, akin to the π bonding states observed in graphene. The DOS exhibits a similar zero-bandgap electronic structure, the result of occupied and unoccupied Si p_z bands that have a linear dispersion relation in the vicinity of the Fermi energy. It is worth mentioning that this is only true for calculations that use a single k-point in the direction perpendicular to the silicene plane, as including more k-points in this direction forces interaction between adjacent sheets and moves the band crossing away from the Fermi level.

We perform similar electronic structure calculations on the epitaxial silicene sheets, both with and without the underlying Ag(111) slab (Figure 6.1(b)-(e)). As the electronic structures of the three types of $(\sqrt{7} \times \sqrt{7})/(\sqrt{13} \times \sqrt{13})$ silicene are found to be virtually indistinguishable, only the results of calculations derived from the silicene structure in Figure 6.1(c) will be displayed and discussed.

The bandstructure of silicene in the $(3 \times 3)/(4 \times 4)$ configuration in the absence of a supporting Ag(111) slab has already been reported in the literature. [130] We confirm these theoretical results, observing that the DOS is largely unchanged from that of LB silicene, save for the opening of a 0.3 eV bandgap owing to the sublattice symmetry-breaking causing the degeneration of the Dirac cone (Figure 6.2(b)). When extending the same treatment to $(\sqrt{7} \times \sqrt{7})/(\sqrt{13} \times \sqrt{13})$-type silicene structures, we also report the opening of a 0.2 eV bandgap in these materials in the absence of a supporting substrate (Figure 6.2(d)). In the $(3 \times 3)/(4 \times 4)$ case, we see the Si p_z states leaking further down into the valence band, suggesting a more sp^3-like hybridization scheme than in the freestanding silicene. This is not

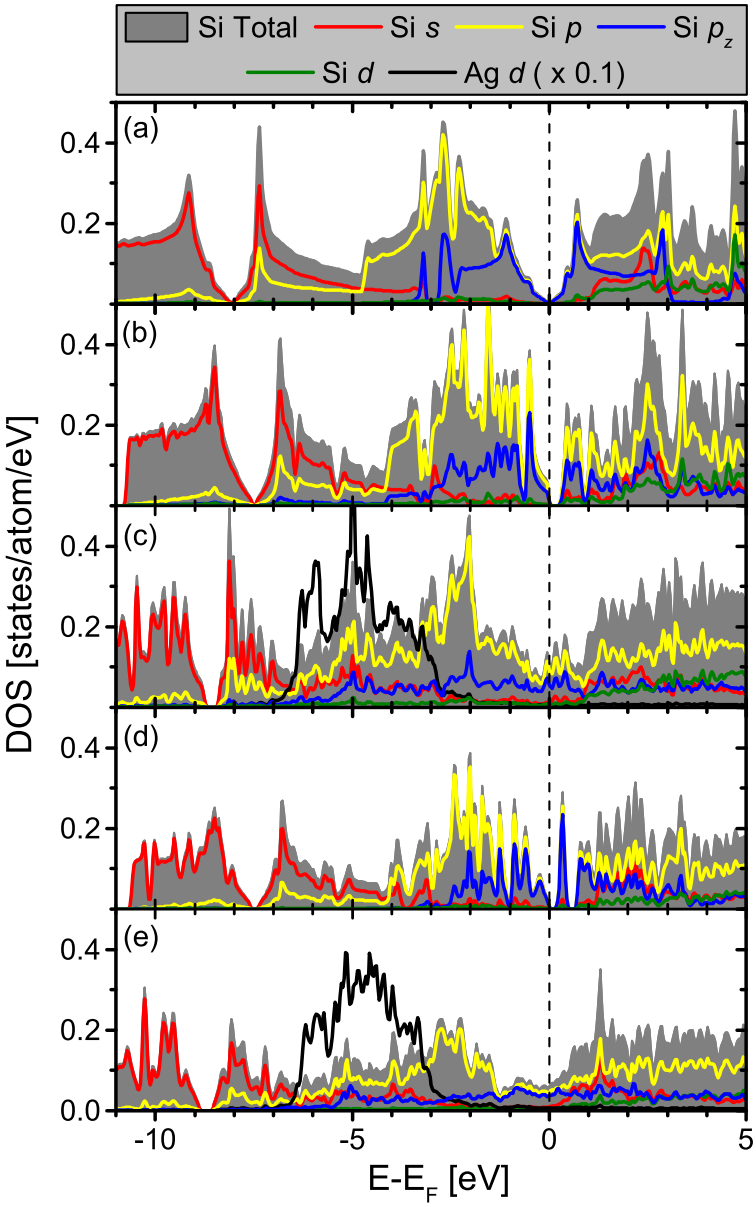

Figure 6.2: a) The calculated DOS of freestanding silicene, exhibiting a zero-bandgap electronic structure. b,d) The calculated DOS of $(3\times3)/(4\times4)$ and $(\sqrt{7}\times\sqrt{7})/(\sqrt{13}\times\sqrt{13})$ silicene (respectively) in the absence of a supporting Ag(111) substrate. In this case, symmetry-breaking causes the degeneration of the Dirac cone, opening up a small band gap. c,e) The calculated DOS of $(3\times3)/(4\times4)$ and $(\sqrt{7}\times\sqrt{7})/(\sqrt{13}\times\sqrt{13})$ silicene (respectively) including the Ag(111) substrate. In these structures, hybridization with the Ag d states and the presence of the Ag sp band cause the Si p_z states to span the Fermi level, resulting in metallic silicene.

apparent in the $(\sqrt{7} \times \sqrt{7})/(\sqrt{13} \times \sqrt{13})$ case, which is expected as the coverage factor is lower for these sheets, resulting in a more planar configuration.

However, when the Ag slab is included in the DFT calculations, the results are markedly different. For $(3 \times 3)/(4 \times 4)$ silicene (Figure 6.2(c)) as well as each of the $(\sqrt{7} \times \sqrt{7})/(\sqrt{13} \times \sqrt{13})$ silicene structures (Figure 6.2(e)), the resulting DOS is strongly metallic, with a continuation of Si p_z states across the Fermi level. These p_z states are almost uniformly spread across the DOS from the bottom of the Ag d states upwards, exhibiting strong hybridization with the Si s and Ag d states at about 5 eV below the Fermi level. This indicates that the p_z states are playing a large role in σ bonding, which is indicative of the sp^3 hybridization scheme. As a result, the π-like bonds in these epitaxial silicene monolayers deteriorate and their constituent p_z states bend downward across the Fermi level. Our interpretation is that the strong hybridization between Si p and Ag d states significantly perturbs the electronic structure of the silicene sheet, and the availability of the Ag sp states for hybridization allows for the Si p states to populate what would normally be the gap region of the isolated silicene sheet. This rehybridization scenario can be contrasted against the rigid band model that describes alkali-metal-doped Si clathrates [212], in which the introduction of a metallic donor species simply shifts the Fermi energy without significantly affecting the bandstructure of the material.

The WIEN2k utility XSPEC is used to estimate ground-state Si $L_{2,3}$ emission spectra from the occupied DOS and absorption spectra from the unoccupied DOS (Figure 6.3(a)), for comparison to their corresponding soft X-ray measurements. Because the final state of an X-ray absorption process contains a core-hole (a Si $2p$ core-hole in our case), we do not expect the ground state absorption spectra to agree completely with our XAS measurements as the core-hole tends to enhance features at the bottom of the conduction band and occasionally shifts the bottom of the conduction band downward in energy, reducing the apparent band gap of the material. To account for this effect we also perform DFT calculations with a Si $2p$ core-hole present in each of the unique Si sites within each of the epitaxial silicene structures, which are averaged together for each material to produce the core-hole absorption spectra represented by dashed lines in Figure 6.3.

As Si $L_{2,3}$ absorption and emission spectra are related to transitions to and from the Si $2p$

core level, we expect them to predominantly resemble the s and d character in the conduction and valence bands due to the dipole selection rule for electronic transitions. Indeed, the two most prominent features in the calculated emission spectrum of freestanding silicene are due to the low-lying s states at 7 eV and 10 eV below the Fermi energy, including the ones in the σ bonding region near the middle of the valence band (Figure 6.3(a)). The intensity drops off near the high end of the valence band, as this energy region is dominated by Si p states. The calculated ground-state Si $2p$ XAS spectrum has a gradual onset, with the lowest energy peak a couple of eV above the Fermi level owing to the Si s and d states concentrated near the bottom of the conduction band. Features further up the absorption spectrum are the result of the sharp peaks in the conduction band DOS, largely composed of Si d character. When one full Si $2p$ core-hole is included in a $(5 \times 5 \times 1)$ supercell (to prevent the overestimation of core-hole effects due to core-hole/core-hole interaction), the onset becomes sharper due to the enhancement of states at the bottom of the conduction band, but does not seem to shift downward in energy appreciably. The small overlap of the calculated XAS and XES in the vicinity of the Fermi level is due to the 0.6 eV spin-orbit splitting of the $L_{2,3}$ core levels and the intentional broadening applied to the transition-weighted partial density of states (pDOS) to simulate the instrumental broadening that occurs in the actual measurements.

Similar calculations of the Si $L_{2,3}$ XES and Si $2p$ XAS spectra for epitaxial silicene are also shown in Figure 6.3(a). In these spectra, the two major features in the freestanding silicene XES are shifted down in energy in the spectra of the epitaxial sheets, and the valence band width appears to be somewhat larger. The shoulder at the top of the valence band is less pronounced, owing to the broadening of the Si s states in this region. The calculated XAS spectra contain far fewer features, as the Si d states are relatively smooth in the conduction band, in contrast to those of freestanding silicene. The absorption edge onset also appears to occur at a lower energy, owing to the increased intensity of Si s states at the bottom of the conduction band, as well as the weak continuation of s and d states across the Fermi level. Again, including a core-hole has the effect of enhancing low-lying conduction states without appreciably shifting the nominal absorption onset. Unlike with freestanding silicene, the epitaxial silicene core-hole calculations were not performed on a supercell, as we consider the size of the epitaxial unit cell to be large enough to ensure adequate core-hole separation.

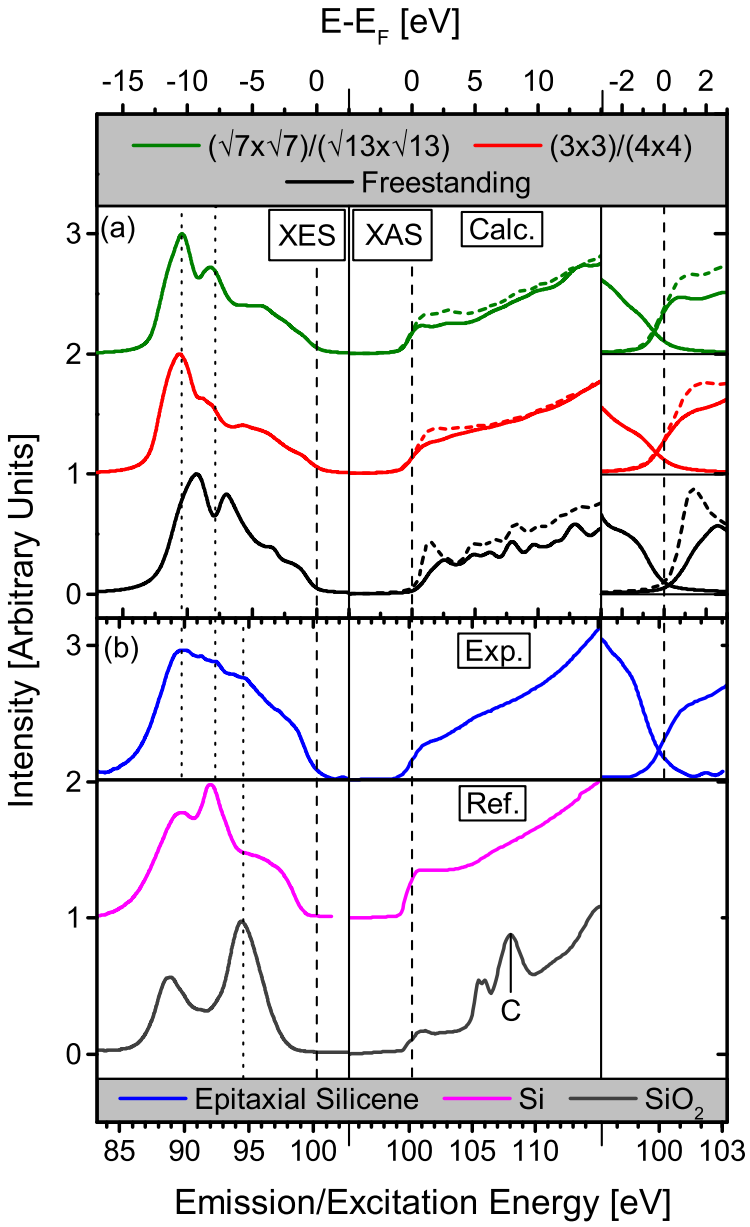

Figure 6.3: a) Theoretical XES and XAS spectra obtained from the calculated Si pDOS for epitaxial and freestanding silicene. The Fermi energy is marked by a dashed vertical line. Calculated XAS spectra including a Si $2p$ core-hole are indicated by a dashed line. b) XES and XAS measurements of epitaxial silicene and Si references (a sputtered crystalline Si wafer in fuchsia and an amorphous SiO_2 crystal (XES) and native SiO_2 oxide on a Si wafer (XAS) in black. Dotted lines indicate peaks in the XES spectrum and the calculated or measured features they are attributed to. The overlaps of the measured and calculated XES and XAS spectra, which are used as a metric for the degree to which the substances are metallic, are shown in the rightmost panels, magnified 2× vertically and on an enlarged horizontal range.

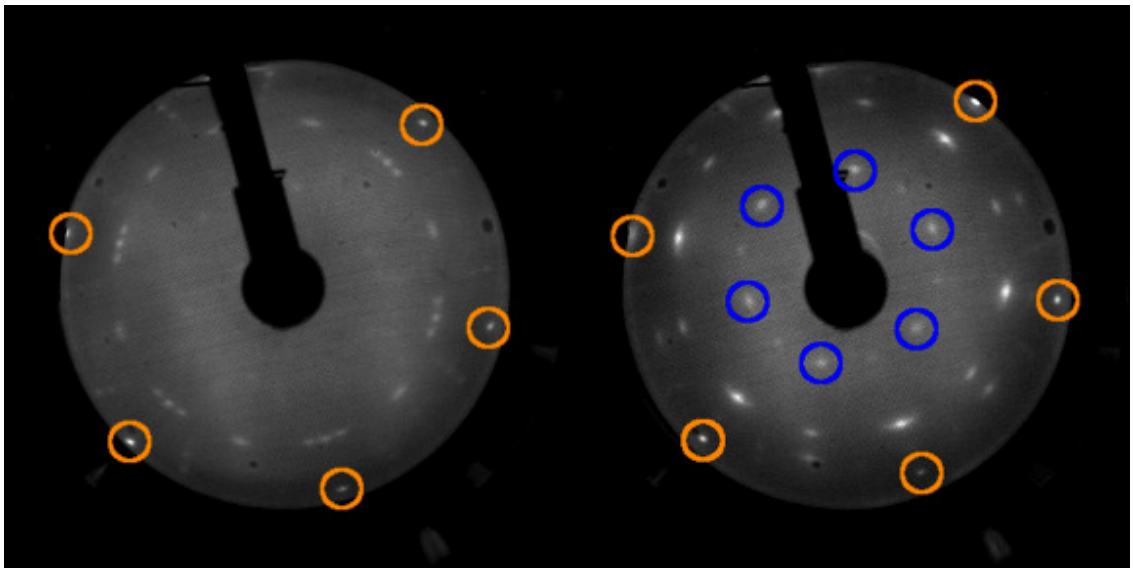

Figure 6.4: 59 eV LEED patterns for our epitaxial silicene monolayer (left, 1 h deposition) and a thin multilayer (right, 2 h deposition) grown on Ag(111). Orange circles indicate the underlying Ag(111) points, and blue circles indicate points resulting from the reconstruction on the first layer that is typically attributed to the growth of a second layer. The faintness of these points in the LEED pattern of our sample indicates that we deposited very close to a single monolayer. Points originating from (4×4) and $(\sqrt{13} \times \sqrt{13})$R13.9° reconstructions dominate the silicene LEED pattern.

Owing to the encroachment of s and d states toward the Fermi level, the band overlaps observed in the calculated epitaxial silicene spectra are visibly larger than that of freestanding silicene. Observing a similar degree of band overlap in soft X-ray spectroscopy measurements of epitaxial silicene would then suggest an experimental confirmation of its predicted metallic nature.

6.4 Sample Synthesis

Our experiments use a single crystal Ag(111) disk, 8 mm in diameter, as a substrate for silicene growth. The disk is treated with two consecutive cleaning cycles, each consisting of sputtering with 1 kV Ar^+ ions at 10^{-6} Torr for 1 hour and annealing at 500 °C for 20 minutes, in order to remove surface contaminants and ensure a uniform substrate. Si atoms are deposited onto the Ag(111) surface through the resistive heating evaporation of a Si wafer under ultra-high vacuum ($< 5 \times 10^{-9}$ Torr) at a distance of 15 cm from the Ag disk. With

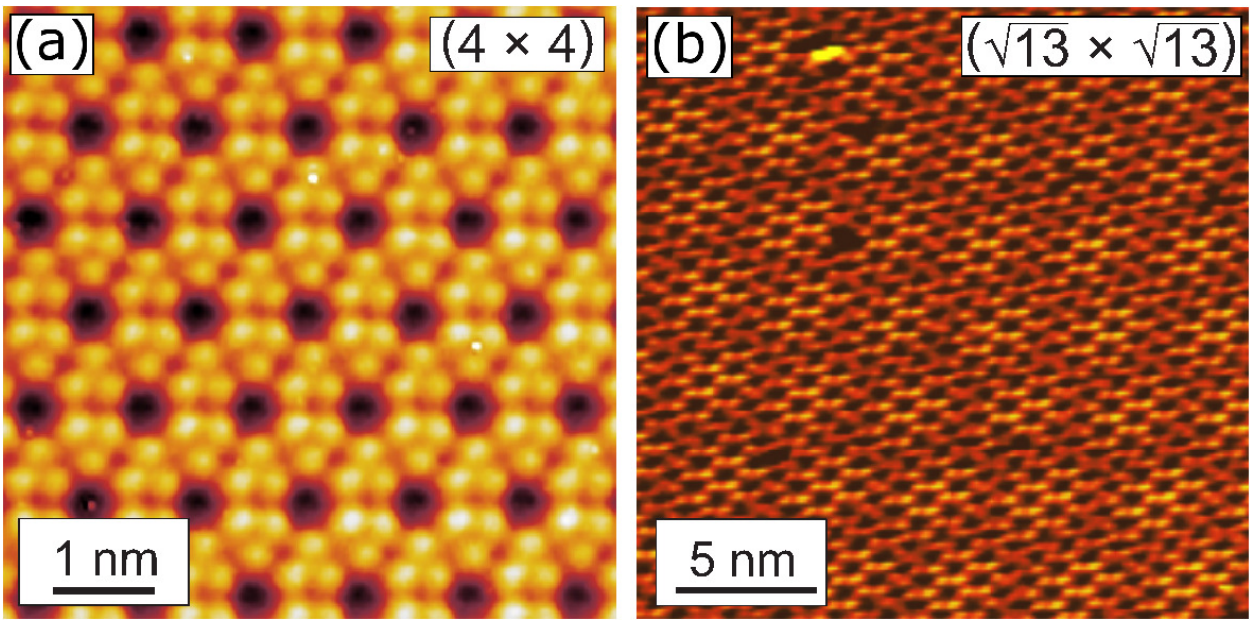

Figure 6.5: a) High-resolution STM topograph (6×6 nm, $U_{bias} = -1.12$ V, I = 0.65 nA) of the (4×4) silicene monolayer. Clearly visible is the "flower-like" pattern that results from the upward displacement of 6 of the 18 Si atoms in the honeycomb structure. b) STM topograph (21.6×21.6 nm, $U_{bias} = -1.20$ V, I = 1.08 nA) of "$(\sqrt{13} \times \sqrt{13})$" silicene. This "$(\sqrt{13} \times \sqrt{13})$" structure has a clear Moiré-like surface pattern, related to locally well-ordered areas that appear bright in the filled-states STM image which are surrounded by less-ordered (dark) areas. This means that the long-range order and thus the translational symmetry are disturbed. However, since this structure has a $(\sqrt{13} \times \sqrt{13})$-like LEED pattern, it is referred to as "(R13×R13)". STM topographs were obtained under UHV conditions ($< 2 \times 10^{-10}$ Torr).

our source and sample geometry, a deposition time of 1 hour is determined to be sufficient for producing a silicene monolayer, supported by the absence of strong $(\sqrt{3} \times \sqrt{3})$ points with reference to the underlying silicene monolayer on the low energy electron diffraction (LEED) pattern (Figure 6.4) that indicate the presence of a second layer, and remain through the deposition of a multilayer. [139, 148, 214, 215] A constant substrate temperature of about 270 °C is found to produce a monolayer containing silicene reconstructions on both (4×4) and $(\sqrt{13} \times \sqrt{13})$R13.9° Ag(111). STM topographs of a sample grown under similar conditions show the large domains composed of these distinct morphologies (Figure 6.5). After synthesis, the sample is exposed to a high-vacuum environment ($< 2 \times 10^{-7}$ Torr) for approximately 15 minutes during transport to the soft X-ray spectroscopy chamber, resulting in a net exposure of about 90 langmuir prior to measurement.

6.5 Soft X-Ray Spectroscopy

We report non-resonant soft X-ray emission spectroscopy (XES) and soft X-ray absorption spectroscopy (XAS) measurements performed on epitaxial silicene monolayers on Ag(111). XES at the Si $L_{2,3}$-edge is used to map the occupied Si s and d pDOS in the valence band, while Si $2p$ XAS in the surface-sensitive total electron yield (TEY) mode is used to probe the unoccupied Si s and d pDOS in the conduction band. Si K-edge XES and XAS measurements were attempted in order to probe the occupied and unoccupied Si p states in the valence and conduction bands, but the resolution and statistical power of these measurements were found to be inadequate for bandgap determination. In order to obtain an adequate energy resolution at the Si K-edge, the resolving power of the beamline must be $18\times$ higher than it would be for the same resolution at the $L_{2,3}$-edge. While this is achievable, it inevitably reduces the statistical power of the measurements. Another issue arises from the increased penetration depth of the Si K-edge photons, which results in a greater contribution from the bulk of the Ag substrate that drowns out the signal from the epitaxial Si monolayer.

The Si $L_{2,3}$-edge soft X-ray spectroscopy measurements were performed at the XES endstation of the REIXS beamline (10-ID2) at the Canadian Light Source at the University of Saskatchewan. The monochromator resolving power ($E/\Delta E$) was 1×10^4 at the Si $L_{2,3}$-edge energy. The emission spectrometer, which uses diffraction gratings in a Rowland circle geometry as dispersive elements and is fitted with a microchannel plate detector, had a resolving power of $(E/\Delta E) = 10^3$ in the same energy region. Oxygen K-edge X-ray absorption spectra were obtained prior to Si $L_{2,3}$-edge measurements to ensure that the sample had not oxidized significantly during the *in vacuo* transfer from the preparation chamber to the measurement chamber. The elliptically polarizing undulator was tuned to produce horizontally polarized photons. All reported measurements were performed with an incidence angle of 70° from the normal, and the XES spectrometer collected photons at 90° from the incident beam.

XAS data were calibrated such that the SiO hybridization feature labelled C in Figure 6.3 in the TEY absorption spectrum of the native surface oxide on a Si wafer occurred at 108.1 eV. A series of elastic scattering measurements was used to scale and shift the energy axis of the spectrometer to agree with that of the monochromator, guaranteeing a consistent

energy calibration between the XES and XAS.

The measured XES and XAS spectra of our epitaxial sample (composed of $(3\times3)/(4\times4)$ and $(\sqrt{7}\times\sqrt{7})/(\sqrt{13}\times\sqrt{13})$ silicene) are shown in Figure 6.3(b), alongside those of Si reference materials. As predicted by our DFT calculations, the valence band width is found to be roughly 10 eV in the XES spectrum, and the most prominent feature occurs at the bottom of the valence band, at around 90 eV. There also appears to be a faint feature around 92.5 eV which occurs at the right energy to be a result of the Si σ bonding states. In general, though, the XES spectrum is fairly featureless, which is not unexpected as it is likely the summation of the contributions of two (or more) species of epitaxial silicene.

The weak feature at 95 eV was observed to fluctuate in intensity across the substrate, and slowly increase in intensity with exposure to the incident beam. While it is at approximately the right energy to correspond to SiAg d hybridization, it also coincides with the main emission feature in the spectrum of SiO_2, which leads us to attribute it to a very mild localized oxidization of the silicene sheet that is exacerbated by beam exposure. The high-energy shoulder near the Fermi level appears to be more pronounced in this measurement than it is predicted to be in any of the epitaxial silicene calculations, suggesting a higher concentration of Si s and d states at the top of the valence band. This could indicate a stronger hybridization between Si s and p states (i.e. more sp^3-like) than is predicted in the calculation.

As expected, the XAS is largely featureless and has a smooth onset. We find that it overlaps significantly with the high-energy side of the XES spectrum (shown in the right inset of Figure 6.3), much more so than what would be expected in a zero-bandgap material like freestanding silicene. It is for this reason, as well as the good general agreement between our calculated and measured soft X-ray spectra, that we suggest that our XES and XAS measurements confirm the DFT-predicted metallic nature of epitaxial silicene on Ag(111).

6.6 Conclusion

In this manuscript, we use full-potential DFT calculations to relax the predicted atomic structures of silicene reconstructions on (4×4) and $(\sqrt{13}\times\sqrt{13})$R13.9° Ag(111). We find

that one of the predicted silicene structures, $(3 \times 3)/(\sqrt{13} \times \sqrt{13})$, is unstable when no symmetry restrictions on the structure are imposed. We therefore rule out the only proposed silicene superstructure on $(\sqrt{13} \times \sqrt{13})$R13.9° Ag(111) that was not of the $(\sqrt{7} \times \sqrt{7})$R19.1° variety.

We show that full-potential DFT calculations predict that all of the epitaxial silicene monolayers we consider to be metallic in nature. While the substrate-induced sublattice symmetry breaking would normally open up a small bandgap in these structures, strong sp^3-like hybridization between Si atoms saw the Ag substrate's d states as well as the presence of the Ag sp band cause the Si p_z states to span the Fermi level, resulting in metallic epitaxial silicene. The results of these DOS calculations are verified by the excellent agreement between predicted and measured XES and XAS spectra, especially in the overlap region composed of the valence band maximum and conduction band minimum.

Recently, the validity of using LDA and GGA-based calculations for the electronic structures of epitaxial silicene on Ag(111) has been called into question as these techniques ignore the van der Waals (vdW) interaction, which may be quite significant in monolayers supported by metallic substrates. Some authors suggest that the inclusion of vdW forces will have little or no effect on the outcome of electronic structure calculations [130], while others think it may mean the difference between observing semiconducting and metallic silicene. [134] The excellent correspondence between our calculations and measurements imply that the effect of the vdW interaction is negligible, or at least is not enough to alter the metallic nature of the epitaxial silicene.

This study adds to the growing evidence supporting the conclusion that silicene on Ag(111) is unavoidably metallic due to the strong interaction between Si and Ag, and is therefore not a suitable candidate for exploiting the properties of a 2D material. We suggest that future investigations of monolayer silicene focus on the search for non-metallic substrates which interact more weakly with the epitaxial sheet and allow it to preserve its ideal LB structure. Recent evidence also suggests that silicene multilayers grown on Ag(111) may be a fruitful avenue in the pursuit of two-dimensional silicene. [148, 214, 215]

6.7 Acknowledgements

The authors gratefully acknowledge financial support from the Natural Sciences and Engineering Research Council of Canada (NSERC) and the Canada Research Chair Program, the 2D-NANOLATTICES" project of the Future and Emerging Technologies (FET) program within the 7th framework program for research of the European Commission under FET Grant No. 270749, the Deutsche Forschungsgemeinschaft (DFG) under Grant No. VO1261/3-1, support from CONACYT Mexico under grant 186142 and the Russian Foundation for Basic Research (Projects 14-02-00006). Calculations utilized Compute Canada's WestGrid HPC consortium. Research was performed at the REIXS beamline of the Canadian Light Source, which is supported by NSERC, the National Research Council (Canada), the Canadian Institutes of Health Research, the Province of Saskatchewan, Western Economic Diversification Canada, and the University of Saskatchewan.

Chapter 7

Oxidized Monolayers of Epitaxial Silicene on Ag(111)

Authors: *Neil W. Johnson, David Muir and Alexander Moewes*

Reference: N.W. Johnson, D.I. Muir and A. Moewes, *Scientific Reports* **6**, 22510 (2016). [142]

This manuscript extends my work on the monolayer silicene/Ag(111) system, focusing on the oxidation of epitaxial silicene as a means of bandgap-tuning. It was motivated in part by the observation of SiO_2-like XES features forming during the measurement of unoxidized monolayers [136], which seemed to suggest that synchrotron beam exposure under UHV conditions could be employed to measure the changes in the silicene's electronic structure during the process of controlled oxidation. It was also meant to address the claims of Du *et al.* [140] and Xu *et al.* [141], who had suggested that an oxidized 2D silicene sheet with a local bandgap opening was suggested by both DFT calculations and SXS measurements.

The experimental aspects of this study took place at the XES endstation of REIXS at the CLS in September 2014 through to August 2015. With the assistance of Dr. David Muir, I performed the depositions, structural characterizations and soft X-ray spectroscopy experiments reported. I alone performed the DFT calculations, analyzed and interpreted the results, and authored the manuscript.

I am licensed to reproduce this manuscript within the pages of this thesis. See Appendix C for more information. The figure numbers, section headings and general formatting have been altered to ensure the consistency of this thesis. No other substantial alterations have

been made to the manuscript.

7.1 Abstract

The properties of epitaxial silicene monolayers on Ag(111) at various levels of oxidation are determined through complementary density functional theory calculations and soft X-ray spectroscopy experiments. Our calculations indicate that moderate levels of oxidation do not cause a significant bandgap opening in the ESML, suggesting that oxygen functionalization is not a viable mechanism for bandgap tuning while the silicene monolayer remains on its metallic substrate. In addition, moderate oxidation is calculated to strongly distort the hexagonal Si lattice, causing it to cluster in regions of highest oxygen adatom concentration but retain its 2D sheet structure. However, our experiments reveal that beam-induced oxidation is consistent with the formation of islands of bulk-like SiO_2. Complete exposure of the monolayer to ambient conditions results in a fully oxidized sample that closely resembles bulk SiO_2, of which a significant portion is completely detached from the substrate.

7.2 Introduction

Freestanding silicene monolayers (FSMLs) are expected to exhibit many of the same electronic characteristics of their carbon-based counterpart, graphene [99,201,216]. This includes hosting charge-carrying quasiparticles that behave as massless Dirac fermions, with the Fermi velocity in FSMLs calculated to be approximately half that of graphene [108]. The buckled structure of FSMLs combined with the large spin-orbit coupling in Si may lead to properties that currently cannot be achieved by single-layer graphene, such as bandgap [104, 106] and spin-polarization [106] control through the application of a gating voltage. These characteristics have led to considerable interest in silicene-based electronic and spintronic devices. However, truly freestanding silicene is yet to be observed. The propensity for Si to assume the sp^3 hybridization scheme prevents it from forming a stable graphite-like layered structure, so silicene cannot be derived directly by exfoliation and must instead be constructed in a bottom-up manner via deposition on a supporting substrate. These epitaxial silicene monolayers (ESMLs) were initially observed on the Ag(111) face [127], and have since been reported on Ir(111) [203] and ZrB_2(0001) [204]. Further, it has been predicted that stable

ESMLs could exist on SiC(0001) [117], h-BN [117, 205] and Pb(111) [217]. In the case of ESMLs on Ag(111), the most thoroughly studied of the ESML systems, an unexpectedly strong interaction with the underlying substrate has been shown to induce semi-metallic character in the silicene [132, 133, 136, 218]. In the absence of a substrate, these ESMLs are expected to once again become semiconducting [130, 136], but the Ag(111) crystals that play host to the silicene are often too large and expensive to make substrate etching a technically feasible or economical option.

Recently, the first functioning transistor based on an ESML was reported [219]. An ultra-thin Ag(111) film deposited on a mica substrate acted as a growth template for the silicene. The ESML was then capped with Al_2O_3 and transferred to a silicon wafer along with the Ag(111), which had been mechanically separated from the mica. Due to the thinness of the Ag(111) film, etching it away was a viable method for exposing the bare ESML. It exhibited a brief period of transistor behaviour before becoming completely oxidized and losing functionality. The creation of such a device marks a significant step forward in silicene-based technology, but its short lifetime (on the order of a few minutes) in ambient conditions indicates that understanding and preventing the oxidation of ESMLs will be of great importance to further advances in this field. Controlled oxidation has been suggested as a possible manner in which a the bandgap of FSMLs could be modulated [220], but it is currently not clear how this affects the properties of ESMLs [140, 141].

In this study, we consider the effect of oxidation on the prototypical $(3 \times 3)/(4 \times 4)$ ESML on Ag(111). Using all-electron, full-potential density functional theory (DFT) refinements of the atomic structure, we show that these ESMLs are capable of dissociating O_2 molecules and that the O atoms prefer Si–Si bridging sites. Our calculations predict that the hexagonal structure of the ESML becomes highly distorted in the process of oxidation, but also indicate that the sheet will maintain a significant interaction with the underlying substrate and retain its semi-metallic nature. Through soft X-ray emission and absorption spectroscopy (XES and XAS, respectively) at the Si $L_{2,3}$ edge, we show that controlled, beam-facilitated oxidation is achievable. However, this does not result in a homogeneously oxidized ESML like that predicted by DFT, instead resembling islands of bulk-like SiO_2 within an otherwise unaffected ESML.

7.3 DFT Structural Relaxations and Electronic Structure Calculations

Specific details regarding the DFT calculation parameters are mentioned in the Methods section below. Previously [136], we noted a strong similarity between the electronic structures of the prototypical $(3 \times 3)/(4 \times 4)$ silicene/Ag(111) configuration and the $(\sqrt{7} \times \sqrt{7})$R19.1°/$(\sqrt{13} \times \sqrt{13})$R13.9° silicene/Ag(111) configurations that are usually observed simultaneously in ESML samples. For this reason, we only consider the $(3\times3)/(4\times4)$ superstructure in this oxidation study, since the results can likely be generalized to the other stable ESML structures. This structure is composed of 18 Si atoms per (4×4) Ag(111) supercell, with 12 of the Si sites located on the base layer and 6 Si sites protruding from it, as shown in Figure 7.4 (a) and (b). Each of the three structures considered in this study are initialized with nine O sites randomly scattered in a plane 1.5 Å above the topmost sheet of Si atoms, representing a coverage of 0.5 monolayers. Where the randomly generated O coordinates overlap, the first set of overlapping O atoms are separated to the O_2 bond distance (1.21 Å) and subsequent overlaps are resolved by selecting new random coordinates for one of the atoms. Two of the three structures generated in this manner contain one O_2 molecule, while one contains only atomic O sites. The initial configurations of an O_2 molecule-containing structure and the purely atomic O structure are shown in Figure 7.4 (a) and (b), respectively.

Through force relaxation, the O_2 molecule-containing ESML eventually evolves to the structure shown in Figure 7.4 (c). It is not found to become fully relaxed after a few hundred iterations, as two of the O atoms (highlighted with black circles in Figure 7.4 (c)) still experience forces larger than the convergence criterion. These atoms appear to have found a metastable force minimum directly above a protruding Si site, which they oscillate in as the surrounding lattice continues to readjust. We do not expect such O configurations to be physical as these calculated structural relaxations neglect the effects of thermal energy, which would likely allow the O atoms greater mobility over the Si lattice. However, as the molecular O_2 (light red in Figure 7.4 (a) and (c)) is observed to fully dissociate and settle into the silicene lattice, we can conclude that ESMLs are capable of dissociating atmospheric

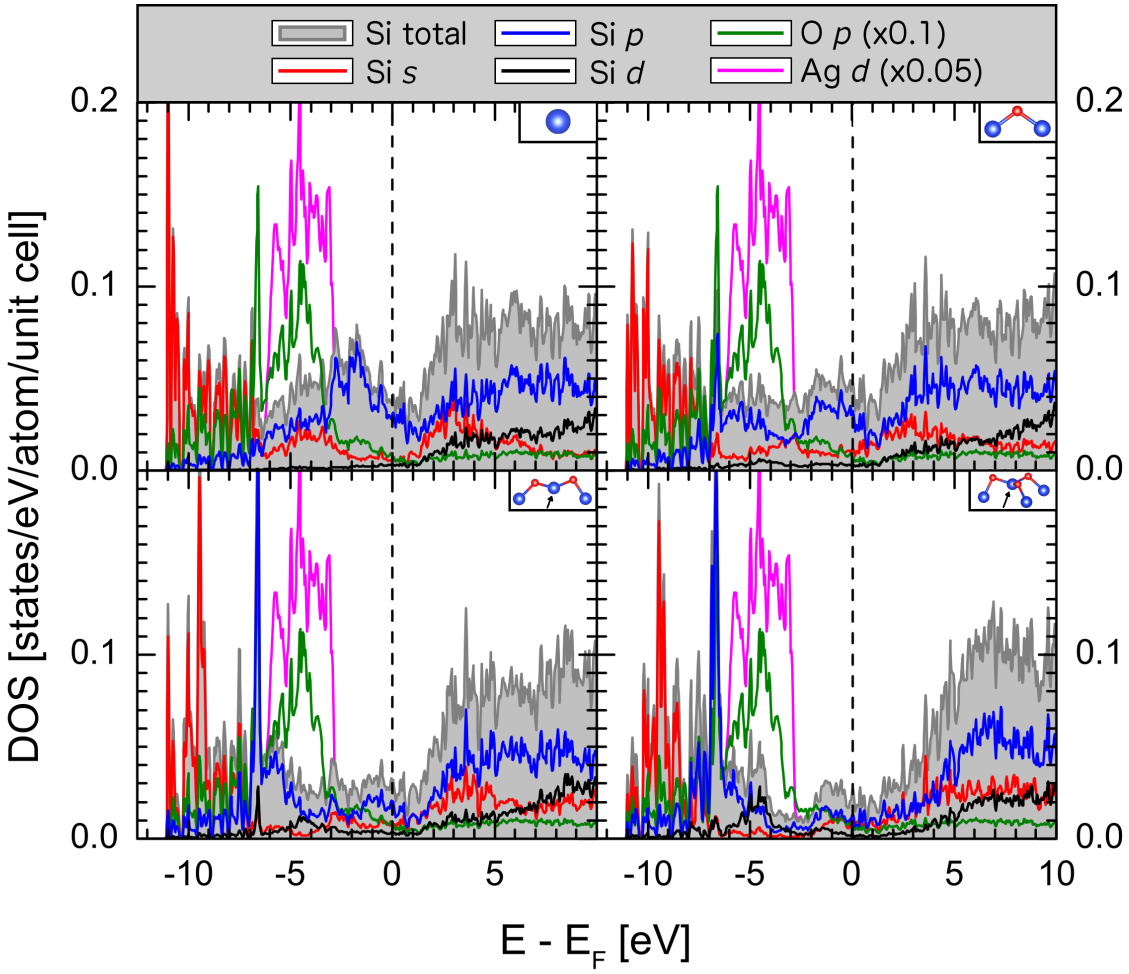

Figure 7.1: Partial and total Si DOS of the fully relaxed ESML initialized with atomic O are shown in solid lines, separated by the number of O bridge sites attached to the Si atom (see inset model). The p character of the O atoms in this model is shown in dotted lines in order to illustrate the Si p – O p hybridization peak that occurs at -6.7 eV.

O_2, even at zero temperature. This has previously been shown for FSMLs [221], but to our knowledge this is the first theoretical observation of O_2 dissociation on ESMLs in the literature. Going forward, we will not consider the electronic structure of this particular oxidized ESML as it is not fully relaxed.

The ESML initiated with a plane of atomic O is found to completely relax below the convergence criterion, resulting in the structure shown in Figure 7.4 (d). Each of the O atoms penetrates the silicene lattice and forms a bridge between adjacent Si atoms, in a Si–O–Si bond somewhat like those found in silica. However, the Si–O bond lengths (ranging

from 1.65 Å to 1.74 Å) are slightly longer and the Si–O–Si bond angles (ranging from 97.0° to 122.5°) are much sharper than the distribution of values typically found in silica [222]. Si atoms are observed to bond with anywhere from zero to three O atoms, forming sites that will henceforth be referred to as unoxidized, single-bridge, double-bridge and triple-bridge sites. Unoxidized and single-bridge Si atoms typically lie closer to the Ag substrate than the double-bridge and triple-bridge sites.

We find that the presence of 9 O atoms per unit cell strongly distorts the hexagonal silicene lattice, with Si–Si bond lengths ranging from 2.30 Å to 2.98 Å compared to the bond lengths of 2.28 Å to 2.31 Å in unoxidized $(3 \times 3)/(4 \times 4)$ ESMLs. The distortion manifests as a bunching of the Si atoms in the regions of highest O atom concentration and a corresponding stretching of the lattice in regions with fewer O atoms. In our simulations, oxidation does not promote any of the initially base layer silicene atoms to protruding silicene atoms, but some of the initially protruding atoms are pulled down to the base layer through local stretching. Further, the overall thickness of the ESML (calculated as the vertical distance between the lowest and highest Si atoms) increases from 0.75 Å for the unoxidized ESML to 2.20 Å for the oxidized ESML, in which the triple-bridge site has the highest vertical position.

A previous study performed by Du *et al.* [140] examined epitaxial silicene through DFT and scanning tunnelling microscopy (STM) in the weakly oxidized regime, at O concentrations of one or fewer atoms per unit cell. The authors found through DFT calculations that single O atoms tend to bridge protruding and base layer Si sites, pulling the protruding atom down to the base layer. In contrast, we find that oxidation of the protruding sites tends to increase their height above the Ag substrate, while the unoxidized protruding sites migrate into the base layer. We see instances of O atoms residing in protruding–protruding, protruding–base and base–base bridge sites at this level of oxidation.

Our calculations closely resemble the pseudopotential calculations of Xu *et al.* [141], who performed a similar structural optimization except that their initial O configuration appears not to have been randomized, instead being deliberately initialized either directly over Si sites or in Si-Si bridging positions. The authors suggest that the distortion observed in the ESML lattice is evidence for decoupling from the underlying Ag(111) substrate. However, their calculations as well as ours show that the structure of the underlying Ag(111) substrate

is strongly perturbed by the reorganization of the ESML resulting from oxidation, suggesting that ESML/substrate interactions are still significant even in the presence of 9 O atoms per unit cell.

The partial Si densities of states (pDOS) for the converged calculation are shown in Figure 7.1 (a)-(d), separated by the number of O atoms bonded to each Si site. Unoxidized Si atoms bear a strong electronic similarity to the net pDOS of unoxidized ESMLs that we presented in a previous publication [136], especially in terms of the Si p states. For example, there is a strong presence of Si s and p states spanning the Fermi level, indicative of hybridization with the Ag sp band in that region. In addition, there appears to be significant hybridization between the unoxidized Si s and p valence states and the Ag d states in the energy range of -7 eV to -3 eV. A number of trends emerge with the addition of more O bridging bonds. Among them, a noticeable weakening of the number of Si p states at the Fermi level, while the contribution from Si s and d states stay approximately constant. The majority of these p electrons move to the range of -8 eV to -5 eV relative to the Fermi level, which corresponds to Si p – O p hybridization, evident from the strong O p peak also located at that energy. Oxidation compresses most of the Si s states into a sharp feature ranging from the bottom of the valence band (VB) to -8 eV while the contributions elsewhere in the VB are weakened and moved toward the VB maximum. Notably, oxidation also is observed to push states away from the Ag d-dominated region, implying a significant weakening of direct hybridization with the substrate. This is to be expected, as oxidation introduces a large spatial separation between the Si atoms from the Ag substrate. In the case of double- and triple-bridged Si sites, there is a significant density of Si d states introduced into the valence band, mostly between -8 eV and -3.5 eV relative to the Fermi energy. These states also show signs of O p hybridization, much like the Si d – O p hybridization observed in alpha quartz [223]. In the conduction band (CB), the primary effect of oxidation seems to be an energetic shift upwards of features in the s, p and d pDOS, as well as an overall softening of their onset. In general, changes to the VB are much more pronounced than those of the CB under the addition of oxygen.

Finally, the calculations indicate that even the triple-bridge Si sites do not possess a bandgap, though the DOS in the vicinity of the Fermi level is significantly reduced. This

finding contradicts the scanning tunnelling spectroscopy (STS) observation of a local bandgap of 0.1 eV to 0.3 eV with an oxygen exposure of 20 L (approximately 3 nm between adjacent O adatoms) [140], and indicates that the oxidized ESML remains semi-metallic even at this heavier level of oxidation. This prediction verifies the DFT calculations performed by Xu *et al.* [141], in which the lack of a bandgap was also observed in the DOS.

Soft X-ray spectroscopy at the Si $L_{2,3}$ edge is sensitive to the Si s and d pDOS in the VB and CB, as it relies on monitoring radiative ($\Delta\ell = \pm 1$) transitions to and from the Si $2p$ core level. While it might be preferable to probe the Si p states directly by conducting Si K-edge soft X-ray spectroscopy, as the p states are responsible for the unique electronic characteristics of silicene, the penetration depth of the X-rays required to create a Si $1s$ core hole is too large to achieve a useable level of signal from a monolayer Si sample. In the following sections, we discuss the growth and oxidation of an ESML sample on Ag(111) and characterize the electronic changes induced by oxidation using soft X-ray emission and absorption spectroscopy (XES and XAS, respectively) at the Si $L_{2,3}$ edge.

7.4 Silicene Deposition and Soft X-ray Spectroscopy

Details regarding sample synthesis and obtaining soft X-ray spectra are provided in the Methods section. We begin by examining the XES spectra of the ESML, presented in the left panel of Figure 7.2 along with their smoothed profiles for clarity. The first emission spectrum, taken directly after transfer and the first XAS scan, has the somewhat featureless, wedge-shaped profile associated with ESMLs [136]. It consists of a broad emission peak around 90 eV, a very weak shoulder around 94.9 eV and the high-energy shoulder at around 98.5 eV that represents the Si s and d states near the VB maximum. Subsequent emission measurements show a separation of the main emission feature into two components – one fixed at around 91.7 eV and one that migrates downward with beam exposure ("A"). The very weak feature at 94.9 eV ("B") grows in strength with each consecutive scan, while the VB maximum ("C") decreases in spectral weight but does not appear to shift appreciably in energy. In a previous study of ESMLs, we hypothesized that this was a result of beam-induced oxidation as the peak at 94.9 eV agrees well with the main emission feature of SiO_2,

also shown in the left panel of Figure 7.2. Indeed, when the ESML has been fully exposed to ambient conditions, the resulting XES spectrum strongly resembles that of SiO_2, aside from a slight energetic shift of the lower peak, a difference in A:B peak ratios and a higher VB maximum with a broader tail.

The XAS is initially fairly featureless, only possessing a strong edge jump ("D") similar to that of the absorption spectrum of bulk Si, attributed to the CB onset [136]. Some very weak peaks are apparent at 105.8 eV and 108.1 eV ("E" and "F"), which are found to grow in intensity with continued beam exposure. With 1 hr of accumulated XES exposure, another feature is observed to emerge around 115.3 eV ("G"). Again, each of these features correspond well to those observed in the native surface oxide on a Si wafer, also shown in the right panel of Figure 7.2. In fact, when the sample is fully exposed to air, the resulting XAS spectrum is virtually identical to that of the native surface oxide on a Si wafer in terms of peak energies and ratios.

The WIEN2k utility XSPEC, which is based on the formalism described in Reference 213, is used to generate calculated Si $L_{2,3}$ XES and Si $2p$ XAS spectra from the Si pDOS, which are shown in the left and right panels of Figure 7.3 respectively. Spectra corresponding to unoxidized, single-bridge, double-bridge and triple-bridge sites are displayed individually, along with the weighted sum of these spectra representing the total XES and XAS spectra resulting from the whole sample and the fully oxidized measurements for comparison. Generally, the XES spectra show only minor changes from zero to two bonded O atoms, including a slight shift of the lowest energy feature from 88.7 eV to 90.0 eV as well as a narrowing of that same feature. However, with the third O bridge in place, the spectrum changes considerably, having three distinct peaks at 90.0 eV, 94.7 eV and 98.2 eV. The second peak corresponds closely to the feature in the XES spectra of the oxidized ESML that increases with beam exposure. However, were this the dominant mechanism for beam-induced oxidation in the ESML, the observed downward tracking of feature A would not be expected to occur and the weakening of the VB maximum region should not be as evident. The XES data are better explained as the direct sum of unoxidized silicene and bulk-like SiO_2 spectra than as the oxidized ESML derived through DFT structural optimization.

The calculated XAS spectra differ significantly from the measured spectra in that the

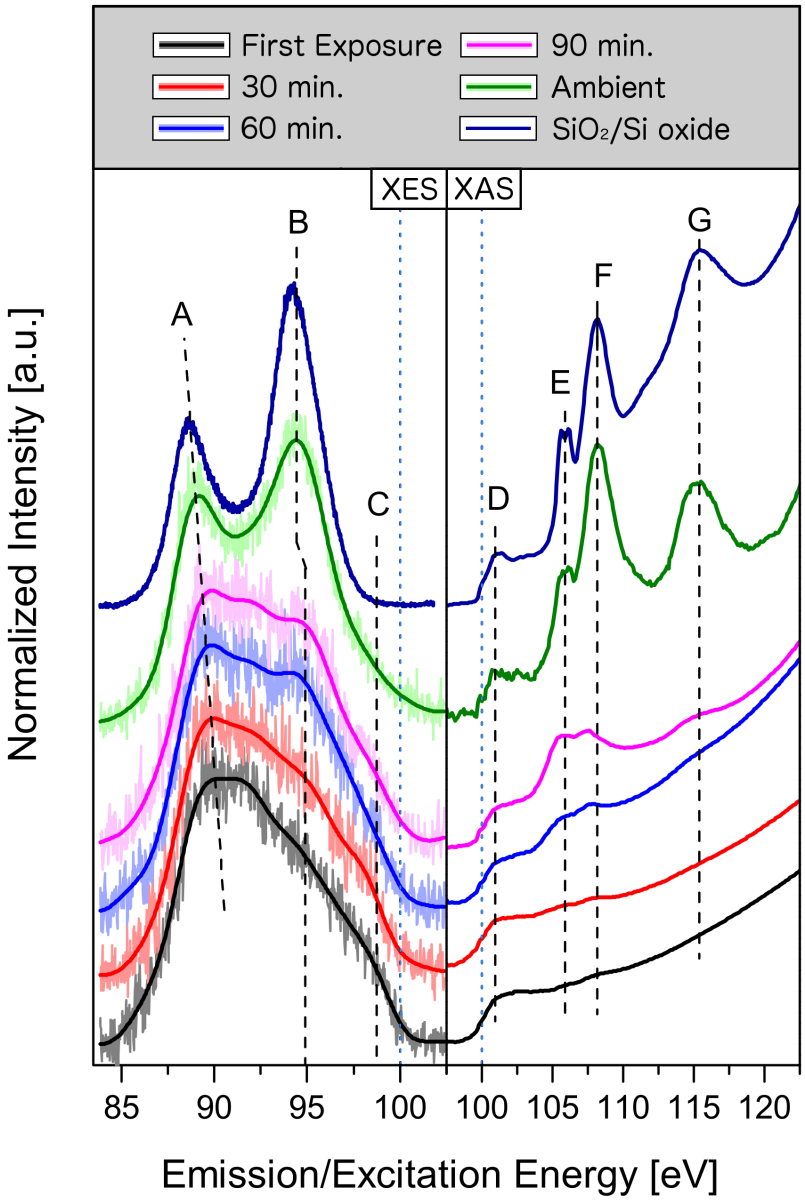

Figure 7.2: Si $L_{2,3}$ XES (left pane) and TEY-mode Si $2p$ XAS (right pane) measurements of ESMLs at various levels of oxidation, with a 15-point FFT smoothing overlaid on the monolayer XES data for clarity. Spectra obtained after the *in vacuo* transfer are labelled by the total amount of XES beam exposure prior to the measurement, while the fully oxidized ESML is labelled "Ambient". Also included is the emission spectrum of bulk SiO_2 and the absorption spectrum of a native surface oxide on a Si wafer for reference. Vertical blue dotted lines indicate 100 eV on both panes to show approximately where the XES/XAS overlap occurs.

absorption onset is much smoother in the calculations. This implies that the concentration of Si s and d states in the lower CB is larger in the experimental samples than the model predicts. Weak features are found at 105.6 eV in the single-bridged Si site, 109.5 eV and 112 eV in the double-bridged site, and 108.2 eV in the triple-bridged site. Only the single-bridged site feature corresponds well to a peak in the experimental oxidized ESML spectrum, but fails to adequately describe the entire absorption profile. Again, we draw the conclusion that the XAS indicates regions of bulk-like SiO_2 formation instead of an oxidized sheet of silicene.

Together, these spectral changes with beam-induced oxidation followed by complete ambient exposure indicate that the dominant mechanism by which ESMLs oxidize is the growth of bulk-like SiO_2 islands in an otherwise unoxidized monolayer. This mechanism explains the observation that the XES spectra appear to be the direct summation of an ESML spectrum and the SiO_2 spectrum, weighted by beam and oxygen exposure. It also explains the evolution of the XAS spectra with increasing oxidation. One thing that becomes apparent under this interpretation is that, even after 10 minutes of ambient exposure, there is still a detectable trace of ESML-like features in both the XES and XAS spectra. This includes the slightly higher energy of feature A, the A:B peak ratio that does not agree with bulk SiO_2, the presence of states around the ESML VB maximum at C, and the bulk Si-like absorption onset D, which is absent in the XAS spectrum of pure SiO_2 [224] but present in that of the native oxide on a Si wafer.

Another observation worth noting is the decreased signal strength observed in both the XES and XAS measurements after complete ambient exposure of the ESML. The count rate for the XES was approximately halved, and the noise level in the XAS spectrum increased appreciably. This occurred uniformly across the sample surface. That is, there were no spatial regions of increased count rate to balance the loss of counts elsewhere. A likely interpretation of this observation is that the complete oxidation of the ESML causes regions of the sample to flake off of the substrate, resulting in less overall Si on the surface.

Were oxidation to open a bandgap in the experimental samples, it would manifest as a reduction in overlap of the XES and XAS, or even a visible break between the two spectra if the gap exceeds the broadening introduced by instrumentation, core hole lifetime and Si $2p_{1/2}$–$2p_{3/2}$ core-level splitting. While it is difficult to pinpoint the exact energy of the VB

maximum owing to the weakness of Si s and d states in the upper VB, we see no convincing evidence of a bandgap opening in our measured spectra, indicating the continued existence of a semi-metallic or metallic Si species on the surface even after complete oxidation.

It could be argued that beam-induced oxidation is not a good analogue for controlled oxidation through low-level O_2 gas exposure, as soft X-ray beams can deposit a significant amount of energy into a material, breaking bonds in the sample and increasing its temperature. However, in the multiple oxidation experiments that we carried out (see Supplemental Information), samples that were transferred under higher pressure conditions had initial XES and XAS spectra that looked virtually identical to the reported sample's spectra after one or two cycles of XES and XAS measurements. That is, the spectra looked the same regardless of whether the sample had been oxidized by beam exposure or by exposure to higher pressures (and therefore more O_2 content) during the transfer process. This allows us to conclude that the soft X-ray beam simply accelerates the oxidation process and does not represent an entirely different oxidation mechanism from atmospheric exposure to O_2.

7.5 Discussion

DFT calculations indicate that ESMLs are capable of dissociating atmospheric O_2, with O atoms tending toward Si–O–Si bridge sites during oxidation. At a concentration of 9 O atoms per unit cell, the oxidized ESMLs are predicted to remain locally semi-metallic even at Si sites that possess three Si–O–Si bridge bonds. Oxidation causes the degradation of the hexagonal Si lattice, with Si sites clustering to the regions of highest O concentration and retracting elsewhere, and bonding with O atoms is found to draw Si sites upward out of the initial monolayer. This prediction is in contrast to the STS data that suggest a bandgap opening of 0.1 eV globally and 0.3 eV locally in weakly oxidized silicene sheets [140]. Structural relaxations also indicate that the substrate is significantly distorted by the oxidation of the ESML, suggesting that the substrate/ESML interaction is still significant even at a 2:1 Si:O ratio.

Experimentally, moderately oxidized ESMLs on Ag(111) are confirmed as retaining the semi-metallic nature of pristine ESMLs, suggesting that oxidation is not a suitable technique

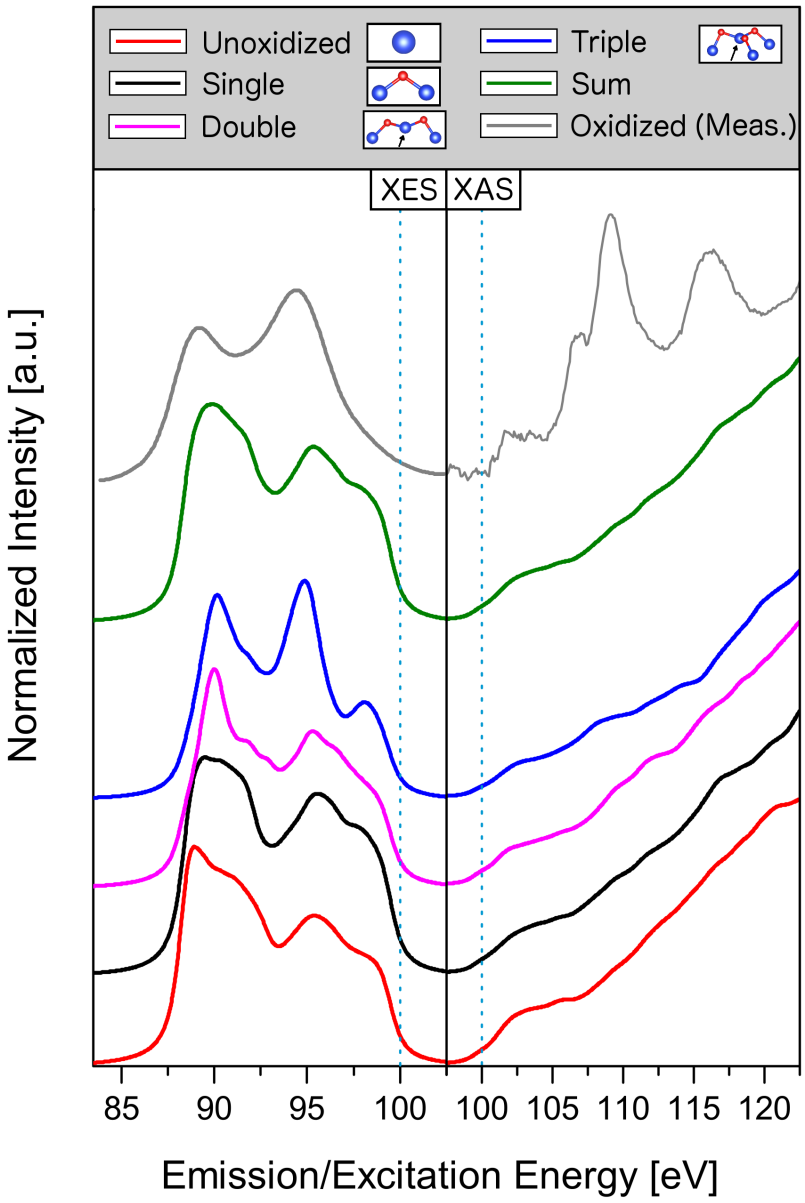

Figure 7.3: Calculated Si $L_{2,3}$ XES and Si $2p$ XAS spectra for the oxidized ESML model, separated by number of O bridging sites. Vertical blue dotted lines again indicate 100 eV to facilitate comparison with the measured spectra, of which the fully oxidized spectra are also shown here (grey, XES smoothed).

for bandgap modulation while the ESMLs remain on their substrate. Further, soft X-ray beam-induced oxidation and exposure to ambient conditions are both found to generate regions of bulk-like SiO_2 rather than evenly coating the ESML with adsorbed O. Ambient exposure is also found to cause some of the ESML to slough off of the substrate, likely in the form of very small, condensed SiO_2 crystals.

The disagreement between the theoretical and experimental oxidized structures is a result of the inability of DFT to properly model the dewetting of the Si sheet into SiO_2-like bulk crystals. DFT is constrained to produce a relaxed structure that conforms to the periodicity requirements of the unit cell, which prevents it from predicting the formation of bulk clusters that are much larger than a single cell. Further, DFT calculations occur at zero temperature and are therefore prone to converge at local energy minima and not the global energy minimum. It is therefore a distinct possibility that the DFT-predicted structure could be stable at low temperatures, but not at room temperature. However, our theoretical results are still valuable in that they demonstrate that a 2D oxidized structure cannot reproduce our XES and XAS spectra to the same degree as a model consisting of bulk-like SiO_2 and unoxidized silicene, and they allow us to characterize a 2D oxidized structure that may yet be produced, even if it is only stable at low temperatures.

While oxidation of FSMLs and ESMLs that have been etched from their Ag(111) substrates may result in silicene with tuneable electronic characteristics, complementary DFT calculations and soft X-ray spectroscopy measurements indicate that moderately oxidized ESMLs on Ag(111) retain the semi-metallic nature of their unoxidized counterparts, and fully oxidized ESMLs on the same substrate tend to crystallize into regions of bulk-like SiO_2. This result has significant implications toward the production of silicene-based electronics, which in the absence of a passivating substance are likely to experience atmospheric O_2.

7.6 Methods

DFT Calculations. As in previous studies [118, 136], we use the "slab method" to approximate the two-dimensional ESMLs in a way that satisfies DFT's requirement for a periodic three-dimensional structural input. The ESMLs are modelled as Si sheets on both faces of

a five unit cell thick slab of Ag(111) with 15 Å of vacuum inserted between adjacent unit cells in the direction normal to the ESMLs. This results in a layered structure consisting of slabs of Si-coated Ag extending infinitely in the **a** and **b** crystallographic directions separated from neighbouring slabs by a large vacuum gap. Along with the choice of a single k-point in the **c** direction, this gap prevents a spurious electronic interaction between adjacent silicene sheets.

All DFT calculations are performed using the *ab initio* all-electron LAPW+lo WIEN2k software suite [177], using the generalized gradient approximation of Perdew, Burke and Ernzerhof (PBE-GGA) [171]. The plane-wave cutoff energy is -6 Ry, and the k-point mesh and RK_{max} are set to $(3 \times 3 \times 1)$ and 5 respectively for the structural relaxation and $(5 \times 5 \times 1)$ and 6 respectively for the electronic structure calculations. Structural relaxations are considered converged when the net force calculated for each mobile atom (the middle plane of Ag atoms are fixed at their bulk Ag positions) falls below 1 mRy/au, and all calculations are considered converged when charge and energy steps fall below 10^{-3} e and 10^{-4} Ry, respectively.

Sample Preparation and Soft X-ray Spectrsocopy. ESMLs were synthesized through the physical vapour deposition of a Si wafer onto a single-crystal Ag(111) disk held at 250°C in an ultra-high vacuum (UHV) preparation chamber (base pressure 10^{-9} Torr). Prior to deposition, the disk surface was prepared with two cycles of annealing at 500°C and sputtering for 1 hr with 1 keV Ar^+ ions at an Ar pressure of 10^{-6} Torr. Deposition of a monolayer was found to take 35 minutes with a Si current of 12 A and a source-to-substrate distance of about 15 cm. The deposition was performed at the Resonant Elastic and Inelastic X-ray Scattering (REIXS) beamline of the Canadian Light Source (CLS).

The monolayer nature of the sample was confirmed with low-energy electron diffraction (LEED), as in our previous studies [118, 136]. As expected under these growth conditions, the sample was observed to contain a mixture of $(3\times3)/(4\times4)$ and $(\sqrt{7}\times\sqrt{7})$R19.1°/$(\sqrt{13}\times\sqrt{13})$R13.9° character. The ESML was then transferred to the soft X-ray spectroscopy measurement chamber via a high-vacuum (HV) transfer chamber with a base pressure of 5×10^{-8} Torr. Prior to measurement the total exposure of the sample was approximately 90 L. After all measurements on the fresh ESML were performed, the sample was then removed from the

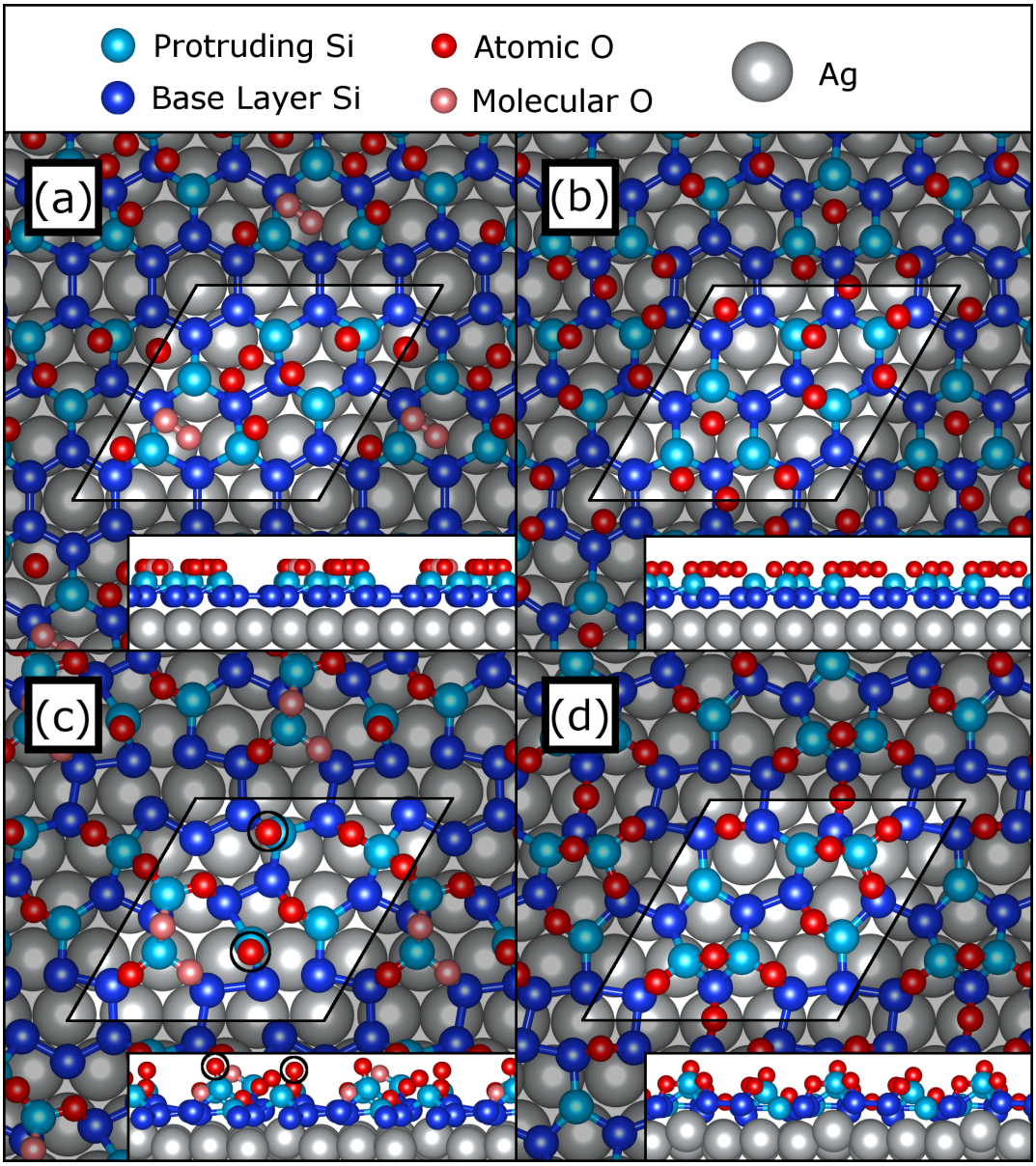

Figure 7.4: (a) and (b): Initial configurations of the oxidized $(3 \times 3)/(4 \times 4)$ silicene/Ag(111) system prior to structural relaxation, with (a) a mix of O atoms shown in dark red and an O_2 molecule shown in light red, and (b) 9 O atoms. Initially protruding Si sites are shown in light blue and initially base-layer sites are shown in dark blue, while the Ag(111) substrate is depicted as silver spheres. The highlighted window shows the unit cell of the calculation, which contains a (3×3) silicene cell commensurate with a (4×4) Ag(111) template. (c) and (d): Final configurations of (a) and (b), respectively. The dissociation of the O_2 molecule is visible in (c), despite the calculation not reaching force convergence due to the atoms circled in black. In (d), the entire structure has reached force convergence. Visualization provided by the VESTA software package [8].

measurement chamber and exposed to ambient conditions for 10 minutes in order to create a fully oxidized ESML, which was then reinserted into the UHV chamber for additional soft X-ray spectroscopy measurements.

All XAS spectra are calibrated such that the main absorption feature of the native oxide on a Si wafer (labelled "F" in Figure 7.2) occurs at 108.1 eV, while the emission spectra were calibrated using elastic scattering peaks so that they are consistent in scale with the monochromator and therefore the XAS measurements. The monochromator resolving power was 1×10^4 at the Si $2p$ absorption edge, while the emission spectrometer, which uses diffraction gratings in a Rowland circle geometry as dispersive elements and is fitted with a microchannel plate detector, had a resolving power of 1×10^3 at the Si $L_{2,3}$-edge. For each spot on the sample surface, a 20 minute XAS scan was performed in surface-sensitive total electron yield (TEY) mode with the exit slits at 25 μm, followed by a 30 minute XES exposure with a 200 μm exit slit. This XAS/XES cycle was then repeated three times per sample spot, in order to monitor for any changes to the electronic structure that may arise as a result of beam exposure. As the slit size and subsequent dose is much larger for XES measurements than XAS, any beam-induced changes to the sample should happen primarily during the XES measurements. Measurements are therefore grouped by the cumulative XES exposure prior to the spectrum being obtained.

7.7 Acknowledgements

The authors gratefully acknowledge financial support from the Natural Sciences and Engineering Research Council of Canada (NSERC) and the Canada Research Chair Program. Calculations utilized Compute Canada's WestGrid HPC consortium, which is a regional partner of the Compute Canada program, funded through the Canada Foundation for Innovation. Research was performed both at the REIXS beamline of the Canadian Light Source, which is supported by NSERC, the National Research Council (Canada), the Canadian Institutes of Health Research, the Province of Saskatchewan, Western Economic Diversification Canada, and the University of Saskatchewan.

Author Contributions

N.J. and A.M. conceived and designed the soft X-ray spectroscopy experiments which were performed by N.J. and D.M. N.J. and D.M. also synthsized the silicene samples, and N.J. performed and analyzed the DFT calculations. All authors reviewed the manuscript.

Additional Information

Supplementary information accompanies this paper at http://www.nature.com/srep

Competing financial interests: The authors declare no competing financial interests.

How to cite this article: Johnson, N. W. et al. Oxidized Monolayers of Epitaxial Silicene on Ag(111). Sci. Rep. 6, 22510; doi: 10.1038/srep22510 (2016).

Chapter 8

Stability and Electronic Characteristics of Epitaxial Silicene Multilayers on Ag(111)

Authors: *Neil W. Johnson, David Muir, Ernst. Z. Kurmaev and Alexander Moewes*

Reference: N.W. Johnson *et al.*, *Advanced Functional Materials* **25**, 4083 (2015). [118]

One of the more controversial epitaxial silicene structures was the so-called $(\sqrt{3}\times\sqrt{3})$R30° structure (measured with respect to the (1×1) silicene cell). While some suggested that it indicated silicene multilayer stacking [149, 150], others suggested it was due to Ag segregation [153, 154] and others yet suggested it could be a manifestation of "dumbbell" stacking in monolayers [132, 210]. The multilayer interpretation was perhaps the most interesting, as these multilayer silicene structures were reportedly stable even after hours of exposure to ambient conditions [148] and possessed a Dirac cone [214]. Since the notion of quasi-freestanding and passivated silicene was extremely attractive, I was motivated to test this model with with the complementary techniques of soft X-ray spectroscopy and DFT.

The experimental aspects of this study, including sample preparation and characterization and soft X-ray spectroscopy measurements, took place at the XES endstation of REIXS at the CLS in December 2013 and June 2014. I was assisted in performing them by Dr. David Muir. Once again, I was responsible for carrying out the DFT calculations and analyzing their results, and I authored the entire manuscript.

I am licensed to reproduce this manuscript within the pages of this thesis. See Appendix C for more information. The figure numbers, section headings and general formatting have been altered to ensure the consistency of this thesis. No other substantial alterations have

been made to the manuscript.

8.1 Abstract

In this study, the stability and electronic characteristics of epitaxial silicene bilayers and multilayers on the Ag(111) surface are investigated through synchrotron-based soft X-ray emission and absorption spectroscopy and first-principles, full-potential density functional theory simulations. Our calculations predict a novel tristable AA-stacked bilayer structure that can explain the $(\sqrt{3} \times \sqrt{3})$R30° honeycomb topography commonly observed through scanning tunnelling microscopy and non-contact atomic force microscopy. We report that the electronic structure of this epitaxial bilayer is similar to those of epitaxial monolayers on Ag(111), namely metallic and showing significant interaction with the underlying substrate. However, our soft X-ray spectroscopy experiments suggest that during multilayer growth a majority of the epitaxial silicon reverts to a bulk-like state, a result that has significant implications toward the existence of large-area epitaxial silicene multilayers.

8.2 Introduction

Two-dimensional (2D) electronic materials such as graphene and its silicon-based analogue silicene have been the focus of intense research of late due to their unique set of electronic, magnetic, thermal and mechanical properties. [5,201] As freestanding sheets of silicene are yet to be observed, research into this promising new material has generally fallen into one of two camps: theoretical simulations of freestanding silicene with a variety of external conditions and chemical modifications, and the experimental characterization of epitaxial 2D silicon sheets deposited on various substrates.

Theoretically, freestanding silicene is expected to possess a Dirac cone electronic structure similar to that of graphene, [99, 216] albeit with a small but finite bandgap opening due to the effects of spin-orbit coupling. [108] This suggests that if stable freestanding silicene were to be realized, it should be a candidate for many of the same applications for which graphene is currently being considered. In fact, silicene may even have some advantages over its carbon-based counterpart. Its inherent buckling could allow for bandgap control, [105] spin polarization control [106] and an ambipolar field effect [99] all through the application of a

gating voltage on an undoped freestanding silicene sheet. In addition, the transition to 2D electronics design and manufacturing should be much smoother if it remains based around the same element (silicon) as current 3D processes.

On the experimental side, honeycomb monolayer (ML) lattices of Si atoms have been observed on the Ag(111) face [127, 136–138, 209, 211], the Ir(111) face [203], MoS_2 [225] and the ZrB_2 (0001) face. [204] Further, stable MLs have been theoretically predicted on SiC(0001) [226] and h-BN. [205, 226] However, the degree to which these epitaxial MLs actually represent freestanding silicene has been called into question. The most thoroughly studied epitaxial silicene samples are those deposited on Ag(111), which were first observed in 2012 when Vogt *et al.* [127] reported a (3×3) silicene supercell commensurate with the (4×4) Ag(111) supercell (hereafter referred to as the $(3 \times 3)/(4 \times 4)$ ML). Since then, a number of rotated $(\sqrt{7} \times \sqrt{7})$R19.1° silicene MLs have been identified on the $(\sqrt{13} \times \sqrt{13})$R13.9° Ag(111) supercell [137, 138, 150, 209, 211] (hereafter the $(\sqrt{7} \times \sqrt{7})/(\sqrt{13} \times \sqrt{13})$ ML), and an unstable and highly defective $(\sqrt{7} \times \sqrt{7})$ silicene reconstruction on the $(2\sqrt{3} \times 2\sqrt{3})$R30° Ag(111) cell. [221] Initially, it was thought that the prototypical $(3 \times 3)/(4 \times 4)$ ML bore the hallmarks of a Dirac cone in its electronic structure. [127] However, it has now been shown that these ML configurations result in a metallic Si sheet interacting significantly with the underlying Ag substrate. As such, the resulting electronic structure is not desirable for 2D electronic applications. This result has now been reproduced through a number of theoretical and experimental techniques, including density functional theory (DFT) calculations, [131, 136, 220, 227] angle-resolved photoemission spectroscopy (ARPES), [131] scanning tunnelling spectroscopy [130] (STS) and soft X-ray emission and absorption spectroscopy [136] (XES and XAS, respectively). Epitaxial silicene ML research now primarily focuses on functionalization of the ML in order to weaken its interaction with the Ag(111), or ML silicene deposition on alternative, typically non-metallic substrates.

Recently, a major development in silicene research occurred when the first silicene-based transistor was manufactured and characterized, representing the first time epitaxial silicene has been observed away from its growth substrate. [219] Though the charge carrier mobility in the device was much lower than the theoretically predicted values for freestanding silicene and the monolayer rapidly oxidized after exposure, this achievement serves as an important

step toward realizing silicene-based technology. Passivation from atmospheric oxygen and the influence of the growth and transistor substrates will be essential to improving the performance and stability of silicene-based devices. Production of a silicene multilayer could serve both of these purposes simultaneously, and it has even been suggested that a multilayer of silicene grown on the Ag(111) surface might be host to a Dirac cone electronic structure. [148, 214]

Scanning tunnelling microscopy [150, 154, 215] (STM) and low-energy electron diffraction [148, 153] (LEED) patterns from depositions several times longer than what is required to create a ML indicate the formation of a structure with a $(\sqrt{3}\times\sqrt{3})$R30° periodicity relative to the (1×1) silicene ML unit cell, reportedly reconstructing through the deposition of enough Si to form tens of additional layers [149]. These structures are most often reported as having a hexagonal honeycomb appearance in STM, though the chemical nature of the tip apex can cause them to appear inverted in contrast, instead resembling a triangular lattice of large, bright points [150]. It has been suggested that the observed $(\sqrt{3} \times \sqrt{3})$R30° pattern could be a result of so-called "dumbbell" Si sites in an otherwise flat Si sheet, which is a highly stable configuration for isolated monolayers [132, 210]. However, it is uncertain whether such a structure will exist on the Ag(111) substrate or can stack to form a multilayer.

Presently, there are two favoured interpretations of the observed $(\sqrt{3} \times \sqrt{3})$R30° periodic structure: multilayer epitaxial silicene, and bulk-like layers of Si(111) with an Ag-terminated surface. Bilayer (BL) silicene has been previously predicted to assume an AB-stacked configuration with a triangular lattice of protruding Si atoms in the upper layer [151]. This structure is tristable with a small energy barrier between each of the three inequivalent structures, and the superposition of the three will result in the appearance of a honeycomb lattice when viewed through STM. X-ray diffraction (XRD), Raman spectroscopy and energy-dispersive X-ray reflectivity (EDXR) have all supported the conclusion that multilayer silicene is a distinct entity from Si(111) [148]. In addition, the ARPES-derived band dispersion is not consistent with Ag-terminated Si(111). [153]

However, the epitaxial silicene model fails to adequately explain the LEED intensity-voltage (I/V) curves for samples with greater than 1 ML of Si deposition. [153] Instead, it has been suggested that both the LEED I/V curves and the honeycomb topography [154]

correspond to the honeycomb-chained-triangle (HCT) or inequivalent triangle (IET) configurations of $(\sqrt{3}\times\sqrt{3})$R30° Ag on the Si(111) face. It is possible that both growth mechanisms can occur simultaneously, and that the presence or lack of Ag-segregation is highly sensitive to growth parameters such as substrate temperature or Si flux. Recent low-energy electron microscopy (LEEM) studies [152,228] determined that, shortly after the completion of a ML, additional deposition results in the dewetting of the Si and the formation of bulk Si crystals. At present, it is not fully understood how the deposition of additional Si onto an epitaxial silicene ML will affect the electronic or atomic structure of the material.

In this study, we use full-potential all-electron DFT calculations to explore the atomic structures of silicene BLs on the Ag(111) face and compare them to experimental STM results. We identify a novel, tristable AA-stacked BL structure on the (4×4) Ag(111) unit cell that is more energetically favourable than the current AB-stacked model [151], though the two look nearly identical in terms of topography. We also calculate their theoretical electronic structures to compare to the results of synchrotron-based XES and XAS performed on multilayer silicene samples at the Si $L_{2,3}$-edge. However, these measurements indicate that large-area multilayers do not form, as a significant proportion of the Si dewets into bulk-like Si crystals on the surface.

8.3 DFT Structural Relaxations of Epitaxial Bilayers

In order to calculate the electronic structure of BL epitaxial silicene, we must first determine a proper atomic structural model. In a typical silicene ML preparation the sample will consist of a mixture of $(3\times3)/(4\times4)$ and $(\sqrt{7}\times\sqrt{7})/(\sqrt{13}\times\sqrt{13})$ domains. [150] With a specific substrate temperature and deposition rate a nearly pure phase $(3\times3)/(4\times4)$ deposition can be achieved, [137] but the electronic characteristics of such a ML should be largely identical to the mixed-component ML. [136] The composition of any particular ML sample can be verified with LEED using an incident electron energy around 50 eV. With the deposition parameters used in our experiment, the LEED patterns show clearly that both types of silicene domain are present when a complete ML is formed (Figure 8.1(a)). Any BL that we are likely to achieve, then, could be commensurate with either the (4×4) or $(\sqrt{13}\times\sqrt{13})$

Ag(111) supercell and would initially have the (3×3) or one of the stable $(\sqrt{7} \times \sqrt{7})$ ML structures at its base. However, the addition of a second layer of Si atoms and the thermal energy available from the substrate (typically held at about 500 K during deposition) might cause a significant rearrangement of the initial ML, so it cannot be taken for granted that the underlying ML structures persist through the deposition of the BL.

In a previous study, [136] we evaluated several structural models of epitaxial MLs by simulating them as sheets of Si on either (111) face of a layer thick slab of Ag atoms. We based our initial Si atomic positions on existing STM data. STM topographies of epitaxial BLs do not provide us with a full picture of the BL structure, only a rough idea of the upper layer configuration. Therefore we must consider a larger number of initial configurations to obtain solutions that not only minimize internal forces on the atoms but also minimize the total energy of the unit cell in order to determine which solution is the most energetically likely to form. While we always initialize the topmost layer of Si atoms as a flat sheet in order to not force our final result to conform to the STM data, we consider cases in which the bottom layer of Si is initialized as a flat sheet, with simple buckling or with the lowest-energy ML silicene configuration belonging to each substrate supercell. We also consider both AA- and AB-stacked BLs, resulting in twelve total initial structures, six belonging to each of the (4×4) and $(\sqrt{13} \times \sqrt{13})$ Ag(111) substrate supercells. Structural relaxations are performed with the *ab initio*, full-potential LAPW+lo WIEN2k code. [177] The exchange-correlation energy is given by the generalized gradient approximation of Perdew, Burke and Ernzerhof [171] (PBE-GGA) with a plane-wave cutoff of -6.0 Ry. After each iterative calculation cycle, the charge density in the system is updated and the resulting force on each atom is calculated. The internal atomic positions are then changed to reduce this force and the calculation cycle begins again. Convergence is reached when the forces in the system fall below 1 mRy/au on each mobile atom (the Ag atoms in the middle layer are fixed in position) and the total energy and charge steps in the self-consistent field cycle fall below 10^{-4} Ry and 10^{-3} e, respectively. To improve calculation efficiency the structural relaxations are performed on a $(3 \times 3 \times 1)$ k-point mesh with an RK_{max} of 5. When these parameters are later increased for the higher-accuracy electronic structure calculations, it is ensured that the forces on each atom still fall within acceptable levels.

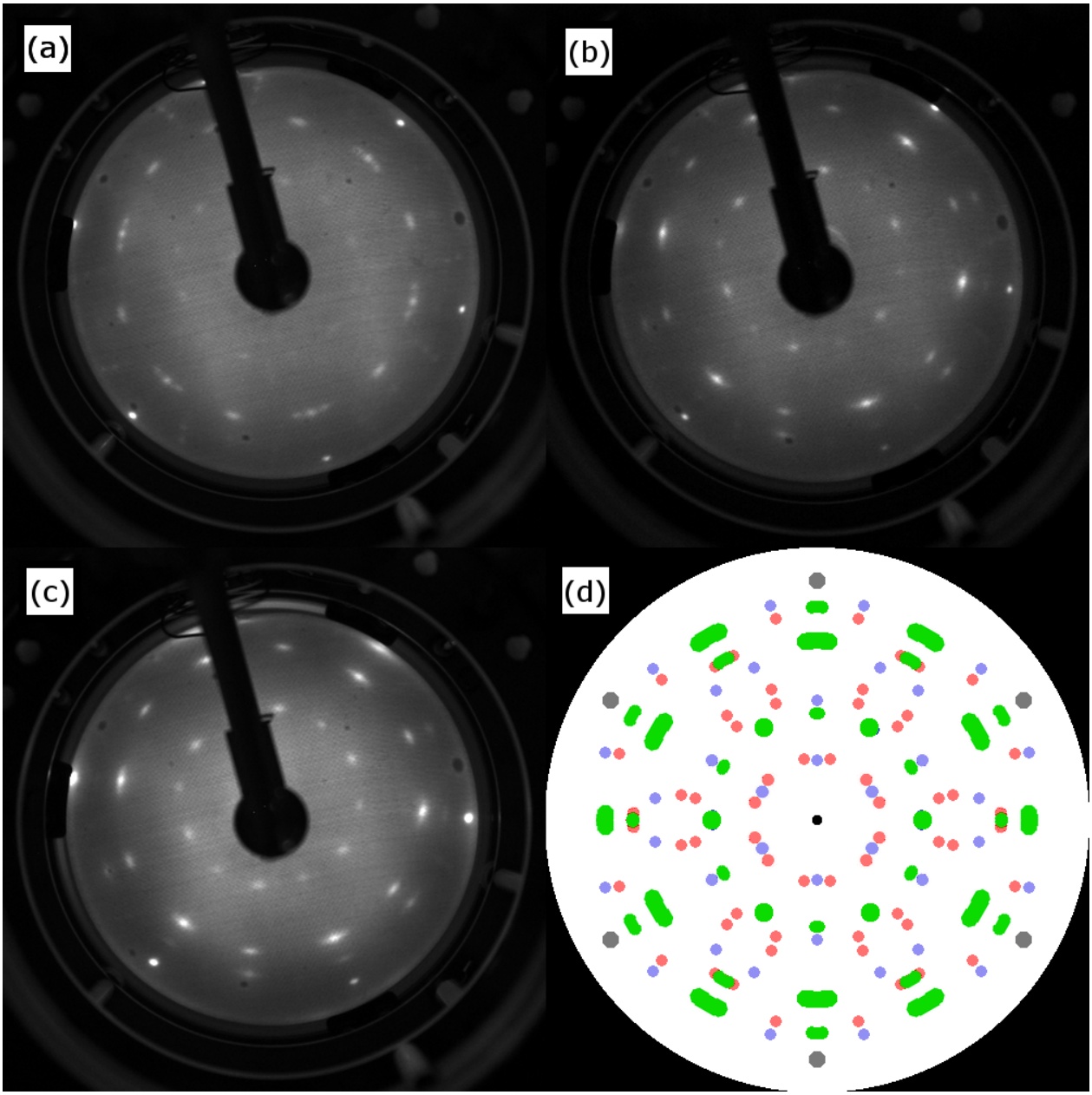

Figure 8.1: The LEED patterns after 1 hr of Si deposition (a), 2 hrs (b) and 3 hrs (c). A mixed $(3 \times 3)/(4 \times 4)$ and $(\sqrt{7} \times \sqrt{7})/(\sqrt{13} \times \sqrt{13})$ ML will exhibit the LEED components shown in red and blue in (d), respectively, while a multilayer will increasingly show the features labelled with green in (d).

We will begin our discussion with the structural optimization of AA- and AB-stacked freestanding silicene BLs in the absence of a supporting Ag(111) substrate. A previous calculation of the structural characteristics of freestanding silicene BLs [119] reported stability in the AA-stacked BL, but our full-potential calculations show that the AA-stacked system is unstable with a strong translational force between sheets that eventually settles it into an AB-stacking scheme. As a result, both the AA- and AB-stacked initial configurations converge to the same final freestanding structure, shown in Figure 8.2(a) and (d). As would be expected of an sp^2/sp^3-hybridized system like silicene, the initially flat BLs become corrugated with a buckling of 0.68 Å, which is larger than the 0.44 Å buckling expected of freestanding, low-buckled ML silicene [99] and in agreement with the BL structure reported by Mohan et al. [119] Within each sheet, the average Si–Si distance is found to be 2.32 Å and the gap between the sheets is 2.53 Å, in good agreement with previously reported values. The vertically overlapping Si positions are shifted toward the centre of the BL, resulting in a bonding environment for these atoms that closely resembles that of a tetrahedral sp^3 network, aside from an elongated bond extending into the adjacent sheet.

Of the six epitaxial BL structures tested on the (4×4) Ag(111) supercell, all were found to eventually converge with a simple buckling scheme in their bottom layer. The lowest energy configuration, the AA-buckled structure shown in Figure 8.2(b) and (e), was found to be about 0.15 eV per Si atom more stable than the next lowest energy structure, an AB-stacked structure that bears a striking resemblance to it apart from the stacking scheme. This slightly less energetically favourable structure was the subject of a previous DFT study [151] and will be discussed later. In our AA-stacked structures bottom layer, the Si atoms are arranged in a simply buckled sheet with a 0.75 Å buckling height. The Si-Si distances range from 2.35 Å to 2.39 Å , and the bond angles within the hexagonal rings comprising the bottom layer are found to vary between 104.7° and 112.4°. All of the raised sites within the bottom layer have a lowered counterpart in the upper layer, with distances ranging from 2.45 Å to 2.48 Å between them. Notably, only 3 of the Si atoms residing above lowered sites in the bottom layer have emerged significantly from the upper layers plane (about 1.2 Å above the lowest upper layer Si atom), with the rest only slightly buckled upward. As for the $(\sqrt{7}\times\sqrt{7})/(\sqrt{1}3\times\sqrt{1}3)$ epitaxial BLs, four of the six structures were found to converge with

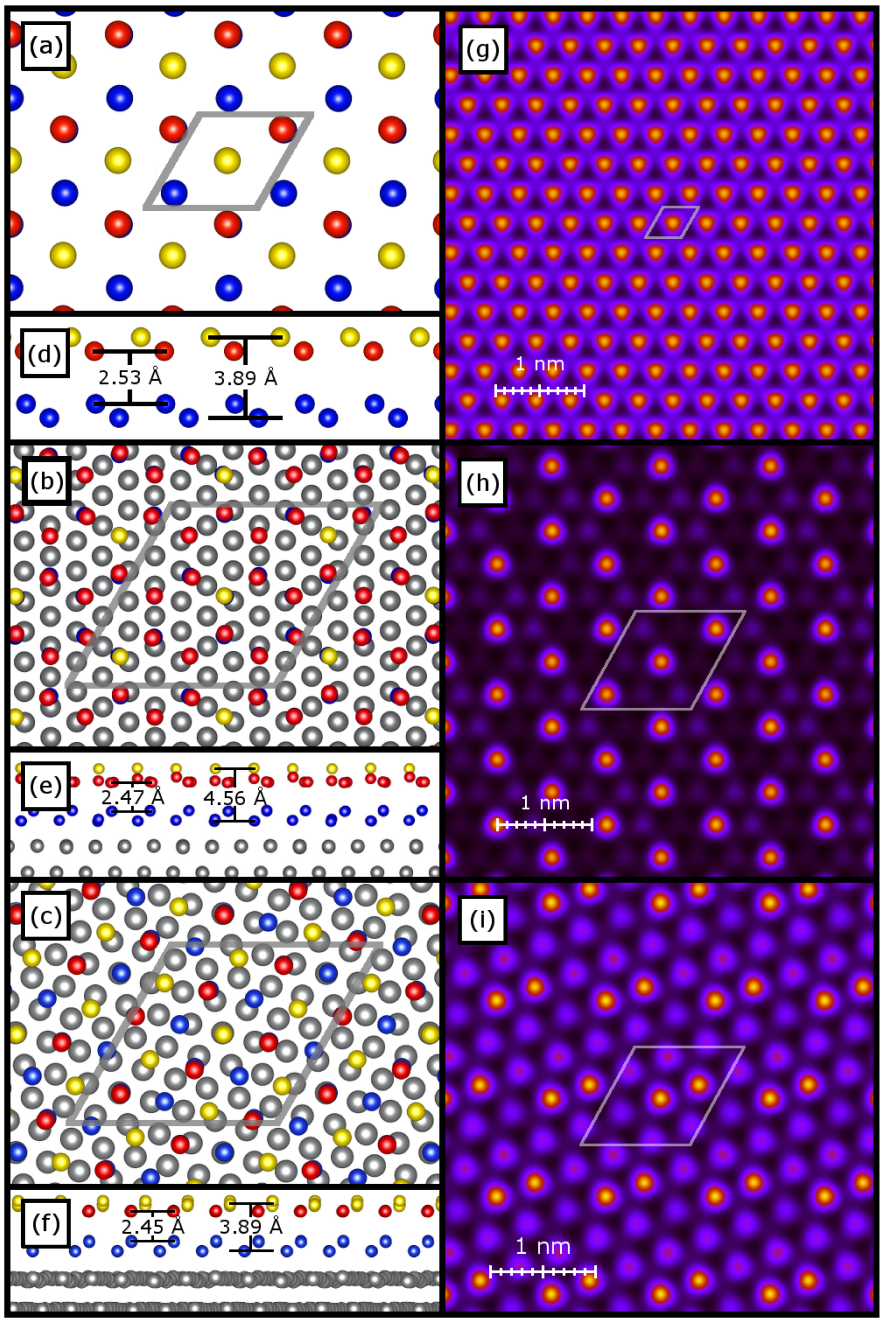

Figure 8.2: Top-down views of the freestanding, $(3\times3)/(4\times4)$ and $(\sqrt{7}\times\sqrt{7})/(\sqrt{13}\times\sqrt{13})$ BLs are shown in (a)-(c), respectively. The unit cell boundaries of each are labelled with gray lines, centred on the most vertically prominent Si atom. Side views of the BLs are shown in (d)-(f), with distances between the various levels of the BL labelled. Charge density plots, which should resemble constant-height, filled-states, low bias STM images of the surfaces are shown in (g)-(i) on an arbitrary scale. Structural visualizations are provided by the VESTA software. [8]

a simple buckling scheme in the lower layer. The two that did not had about 0.5 eV per Si atom more total energy in the unit cell than the lowest energy configuration shown in Figure 8.2(c) and (f), an AB-stacked BL. The simply buckled bottom layer has a buckling distance of about 0.81 Å with a Si-Si distance ranging between 2.38 Å and 2.42 Å and bond angles ranging from 108.3° to 111.9°. In this BL the upper layer is also essentially simply buckled with a structure that closely resembles a freestanding AB-stacked BL or a single plane of Si(111).

Once these atomic structures have been finalized, their electronic structures can be calculated. As mentioned earlier, these calculations take place on a denser k-point mesh of $(7 \times 7 \times 1)$ with an increased RK_{max} (5.5). We find that the calculated electronic structures are stable under further increasing these values to $(10 \times 10 \times 1)$ and 6.0, implying that our calculations are fully converged. However, before we delve into the electronic structure of these materials we will first complete the structural picture with a discussion of the spatial electron densities calculated on this denser mesh.

For an STM operating on a metallic surface in filled-states constant-height mode and with a small tip bias, the resulting STM signal will be approximately proportional to the total electron density between the tip bias energy and the Fermi level (E_F) at a certain point in space. [161] From our WIEN2k calculations, we are able to extract the total electron density between E_F – 2 eV and E_F in a plane 1.5 Å above the topmost Si atom for each of the bilayers shown in Figure 8.2. This results in the electron density plots shown in 8.2(g)-(i), which should bear resemblance to STM images of these freestanding and epitaxial BLs.

The simple buckling of the AB-stacked freestanding silicene BL produces a triangular lattice of points in the simulated STM with 3.85 Å between adjacent maxima. This topography does not conform to any known observation of the Si/Ag(111) surface, implying that BL silicene on Ag(111) cannot be considered to be freestanding. In the epitaxial BL commensurate with the (4×4) Ag(111) substrate, the three vertically displaced Si atoms in the upper layer dominate the simulated STM pattern. This also results in a triangular lattice pattern, this time with a spacing of 6.65 Å. Finally, on the $(\sqrt{13} \times \sqrt{13})$ Ag(111) template, the simulated STM image consists of two triangular lattices: one is a result of the simple buckling and has a spacing of 3.95 Å and the other is the result of two top-layer Si sites that are raised slightly

more than the others and has a periodicity equal to the unit cell dimension of 10.4 Å. As is the case with the freestanding BL, this topography does not conform to any known STM observations.

The novel AA-stacked BL on (4×4) Ag(111) is found to two have stable, energetically similar counterparts wherein the raised Si atoms are shifted by one honeycomb lattice position. This tristability, like that observed previously for the AB-stacked BL on (4×4) Ag(111) [151], allows for the reconciliation of the triangular lattice pattern shown in Figure 8.2(h) and the honeycomb pattern typically observed in STM measurements [150, 154, 215]. As we find that the AA-stacked BL configuration is energetically favoured over the AB-stacked structure and that it is equally capable of explaining the existing STM data, we suggest that this novel structure is the most likely description of epitaxial BL silicene.

The lack of an observed STM topography that agrees with that predicted for the ($\sqrt{13} \times \sqrt{13}$) BL suggests that such a structure does not exist in multilayer silicene samples. It is feasible that, due to this reduced substrate interaction, ($\sqrt{7} \times \sqrt{7}$)/($\sqrt{13} \times \sqrt{13}$) ML domains do not promote multilayer growth but instead "seed" the dewetting process observed directly through LEEM. [152,228] Given their strong resemblance to layers of Si(111), it is also feasible that these domains are responsible for observations of HCT- or IET-like Ag segregation, which occurs on the Si(111) face.

8.4 Electronic Structures of Bilayers

Having explored their atomic structures, the discussion can now move on to the electronic characteristics of the freestanding and epitaxial BLs. The total and partial densities of states (DOS and pDOS, respectively) of these BLs in the vicinity of the Fermi energy are shown in Figure 8.3.

We will begin by discussing the Si pDOS of freestanding BL silicene, comparing it to that of freestanding ML silicene which we have previously reported. [136] We note a significant Si s and d contribution to the states bordering the bandgap, which suggests the lack of a p-dominated Dirac cone-like structure. We also report a bandgap opening of 0.22 eV. This is at odds with previous DFT treatments of freestanding BL silicene [116, 119] which predicted

a metallic electronic structure. We would argue that the insulating case is more likely, as the BL formation breaks the inversion symmetry of the ML (which is known to introduce a bandgap into silicene), and the BL represents an intermediate step between the small-gap ML case and the large-gap bulk Si(111) case.

As for the $(3 \times 3)/(4 \times 4)$ epitaxial BL, the pDOS shows a metallic electronic structure with significant hybridization between the Ag d states and the Si s and d states in the region ranging from –6.5 eV to –3 eV, as indicated by the coincident peaks in the respective pDOS. This hybridization is less apparent than in the epitaxial $(3 \times 3)/(4 \times 4)$ ML, [136] perhaps an indication of a weakened interaction between the underlayer and substrate introduced by the presence of the overlayer. However, qualitatively the Si s and d pDOS are similar to that of the epitaxial ML, suggesting that a soft X-ray spectroscopy study of the BL should result in similar spectra.

The $(\sqrt{7} \times \sqrt{7})/(\sqrt{13} \times \sqrt{13})$ epitaxial BL also possesses a metallic electronic structure, this time with a modest peak of Si s and p states centred at EF . Here Si sp – Ag d hybridization is far less apparent, again indicating a weakened interaction between the BL and the substrate. However, for a completely non-interacting BL on $(\sqrt{13} \times \sqrt{13})$ Ag(111) we would expect to see a pDOS similar to that of the freestanding BL given their structural similarities. We do not, which leads us to assume that hybridization with the Ag sp band, located within a few eV of the Fermi level, is still significant. We conclude that both epitaxial BLs possess similar electronic properties to their epitaxial ML counterparts. Namely, they are metallic in nature and have fairly strong hybridization with the underlying substrate. However, at least for the BL on $(\sqrt{13} \times \sqrt{13})$ Ag(111), there are some signs of weakened coupling with the substrate, which could be taken as further evidence for these structures acting as "seeds" for bulk-like crystallization.

The WIEN2k utility XSPEC, which is based on the formalism presented in Reference [213], can be used to simulate the results of XES and XAS measurements of the valence and conduction states using the calculated pDOS and experimental spectral broadening parameters. The calculated Si $L_{2,3}$ XES and $2p$ XAS for the freestanding and epitaxial BLs are presented in Figure 8.4(a). The XES show the same wedge-like profile that we have previously reported for epitaxial MLs on Ag(111), which is to be expected based on their similar

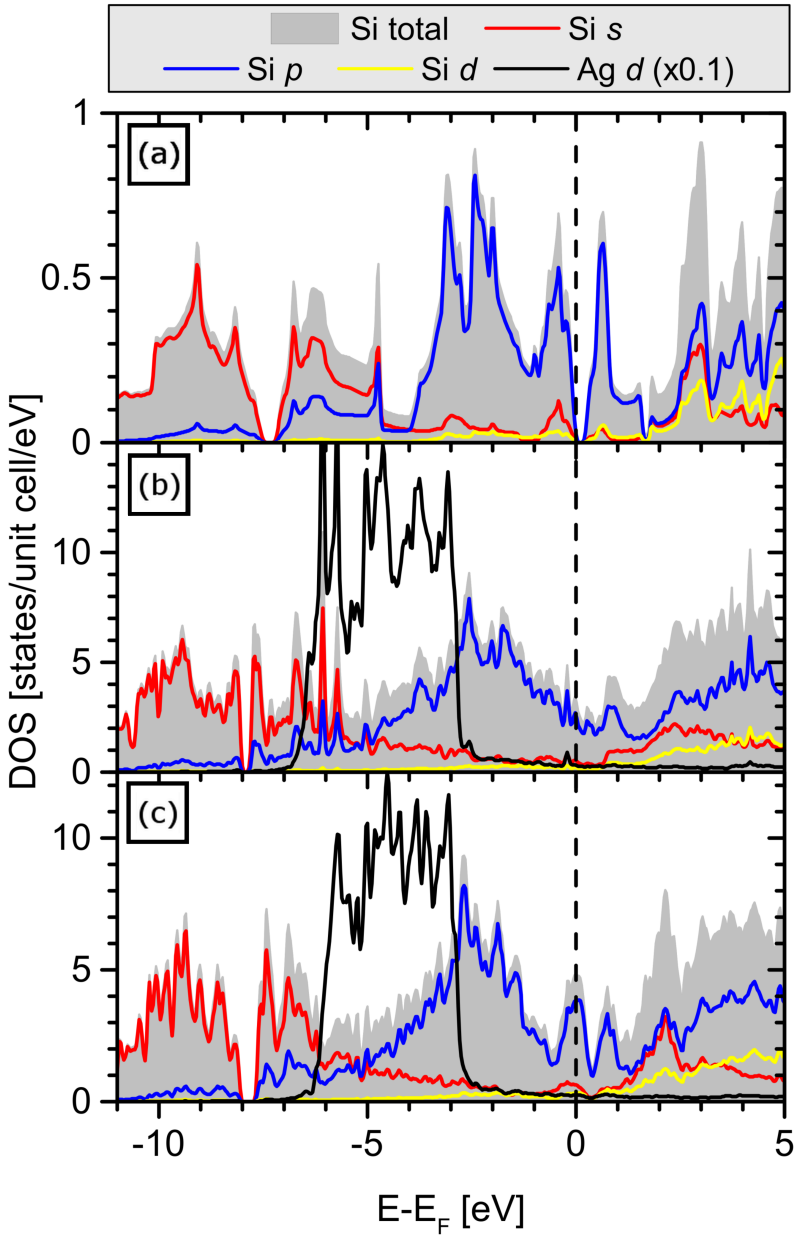

Figure 8.3: The Si and Ag pDOS of (a) a freestanding silicene BL, (b) the (3×3)/(4×4) silicene BL and (c) the $(\sqrt{7}\times\sqrt{7})/(\sqrt{13}\times\sqrt{13})$ BL. The Fermi level is marked with a dashed line.

s and d pDOS. Each show three major peaks, one at 89.5 eV, one at 92 eV and one forming the high-energy shoulder at 98.5 eV. As was the case with the MLs, the BL XAS shows one major feature around 102 eV but is otherwise relatively featureless. Together, the simulated XES and XAS indicate that all three types of BL would be difficult to distinguish from one another, aside perhaps from the downward-shifted valence band maximum in the XES in the freestanding BL, resulting from the 0.22 eV bandgap opening.

Typically when attempting to simulate an XAS measurement, it is important to consider the effect of the core-hole (CH) introduced in the targeted atom during the process of a measurement. This CH can have significant effects on the outcome of the XAS measurement, including a downward shift in the energy of the absorption onset as well as an enhancement of the spectral features near the onset. When the XAS is plotted together with the XES these effects typically manifest themselves as a reduction in the apparent bandgap and an increased spectral weight at the bottom of the XAS.

In our case, with 28 to 36 unique Si sites per unit cell it is not feasible to simulate the effects of a CH in each site. However, we have previously shown [136] that for the metallic epitaxial MLs, which have approximately the same electronic structure as the epitaxial BLs, there is no appreciable CH shift in our XAS measurements, only an enhancement of the spectra at the bottom of the conduction band. It is reasonable to assume that the same will be true of the epitaxial BLs.

8.5 Sample Synthesis

We now turn to experimental characterization of epitaxial multilayers on Ag(111). Our samples for this study are produced in the typical manner of physical vapour deposition of a Si wafer on to a single-crystal disk of Ag(111) held at 500K. Before each deposition, the Ag disk is cleaned with two consecutive cycles of Ar^+ sputtering with an Ar pressure of 10^{-6} Torr and annealing at 500 °C. The depositions take place in an ultra-high vacuum (UHV) chamber with a base pressure of 1×10^{-9} Torr. With our source and sample geometry, we find that a complete ML forms after 1 hr of deposition time, according to the absence of strong $(\sqrt{3} \times \sqrt{3})$R30° points on the LEED pattern (see Figure 8.1(a)). Our 1 hr deposition

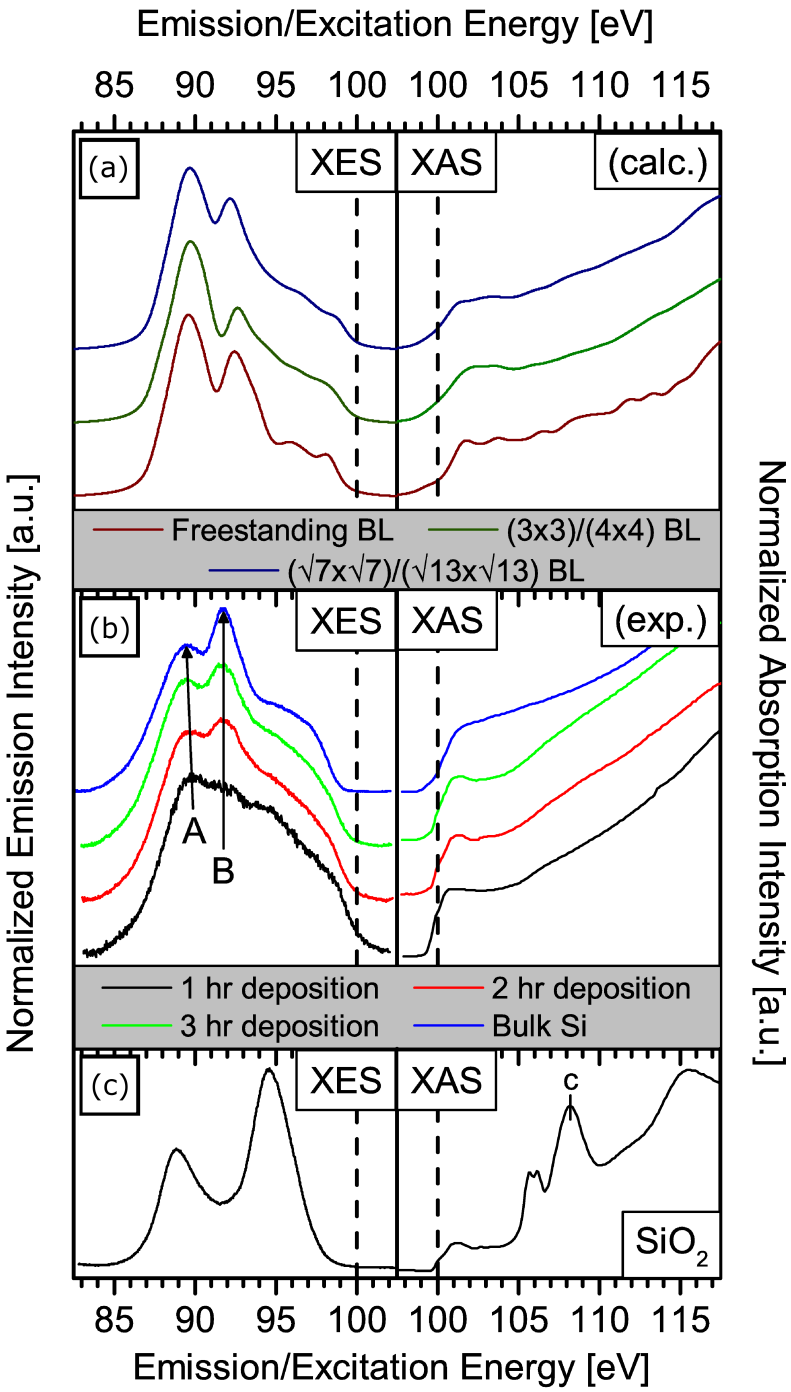

Figure 8.4: (a) The calculated XES and XAS spectra of the silicene BLs investigated in this study. (b) XES and XAS measurements of epitaxial silicene samples ranging from 1 to 3 hrs of deposition, as well as a bulk Si sample. (c) The XES spectrum of SiO_2 and the TEY-mode XAS spectrum of the native oxide on a Si wafer, used for calibration purposes.

parameters resulted in a mixed $(3\times3)/(4\times4)$ and $(\sqrt{7}\times\sqrt{7})/(\sqrt{13}\times\sqrt{13})$ ML, as mentioned previously.

Doubling and tripling the 1 hr deposition time required to form a ML should, if large-scale multilayers of epitaxial silicene exist, roughly form a BL and a trilayer (TL) respectively. Upon depositing more Si, the LEED features associated with the $(3\times3)/(4\times4)$ and $(\sqrt{7}\times\sqrt{7})/(\sqrt{13}\times\sqrt{13})$ ML (blue and red, respectively, in Figure 8.1(d)), begin to fade and the characteristic points arising from a multilayer (green in Figure 8.1(d)) dominate the LEED pattern. Further Si deposition up to 8 hrs is found to simply result in the strengthening of these multilayer LEED features.

After structural characterization via LEED is complete, the samples are transferred into a high-vacuum (HV) transfer cart (base pressure 5×10^{-8} Torr) for approximately 10 to 15 minutes before being loaded into the soft X-ray spectroscopy measurement chamber (base pressure better than 10^{-9} Torr). The expected net exposure of the samples prior to measurement is approximately 90 langmuir.

8.6 Soft X-Ray Spectroscopy

Characterization of the electronic structure of our experimental samples is achieved through soft X-ray emission and absorption spectroscopy (XES and XAS) at the Si $L_{2,3}$-edge. These processes allow us to probe the element- and orbital-specific pDOS the valence and conduction bands, respectively, by directly or indirectly monitoring transitions to and from selected core levels. In our case, we excite the Si $2p$ states, thus probing the Si s and d states in the valence and conduction bands due to the dipole transition selection rules. While it would be preferable to probe the Si p states that dominate the electronic structure near the Fermi level, the large incident X-ray energies required for a Si K-edge measurement (approximately 1.8 keV) render the penetration depth of the photons too large to achieve a useful signal from an atomically thin surface layer of Si atoms. Exciting at an extremely grazing incidence angle will increase the photons path length through the silicene, but it also has the deleterious effect of increasing the beam footprint on the sample and therefore decreasing the resolving power and count rate of the XES measurement.

These soft X-ray spectroscopy measurements were performed at the XES endstation of the REIXS beamline (10-ID2) at the Canadian Light Source at the University of Saskatchewan. The monochromator resolving power ($E/\Delta E$) was 1×10^4 at the Si $L_{2,3}$-edge energy. The emission spectrometer, which uses diffraction gratings in a Rowland circle geometry as dispersive elements and is fitted with a microchannel plate detector, had a resolving power of $(E/\Delta E) = 10^3$ in the same energy region. Oxygen K-edge X-ray absorption spectra were obtained prior to Si $L_{2,3}$-edge measurements to ensure that the sample had not oxidized significantly during the in vacuo transfer from the preparation chamber to the measurement chamber. No significant O K-edge onset was observed. The elliptically polarizing undulator was tuned to produce horizontally polarized photons. All reported measurements were performed with an incidence angle of 70° from the normal, and the XES spectrometer collected photons at 90° from the incident beam. The spot size of the incident X-ray beam was approximately 20 μm $\times$50 μm, which is much larger than the typical continuous silicene domain on the Ag(111) surface. This indicates that our measurements should represent the qualities of the bulk silicene sample and not those of a single domain.

XAS data were calibrated such that the Si–O hybridization feature labelled "c" in Figure 8.4 in the TEY absorption spectrum of the native surface oxide on a Si wafer occurred at 108.1 eV. A series of elastic scattering measurements was used to scale and shift the energy axis of the spectrometer to agree with that of the monochromator, providing a consistent energy calibration between the XES and XAS.

As we reported previously in the first soft X-ray spectroscopy study of ML silicene, [136] the ML XES and XAS spectra are in good agreement with the calculated spectra acquired through DFT. The BL spectra, which from our DFT simulations should resemble that of the ML, instead appear to take on features of the sp^3-hybridized bulk Si spectra (which are shown in blue in Figure 8.4(b)). A peak (labelled "B") appears at 91.5 eV in the BL XES and is more pronounced in the TL XES, coincident with the main feature in the bulk Si emission spectrum. There is also a slight downward shift of the peak at 89.5 eV ("A") in the ML spectrum, indicating that the bulk-like states located slightly lower in energy at 89 eV are beginning to dominate the main emission feature of the ML. The top of the ML valence band, which is marked with a dashed line in Figure 8.4, appears to shift downward with the

addition of Si. This could be taken as evidence of the formation of a BL with a bandgap opening, but it could also be the result of an increased proportion of semiconducting bulk Si to metallic epitaxial Si. The observed XAS could be said to represent a transition to the bulk Si spectrum from the ML XAS due of the emergence of the low-energy shoulder at 100 eV with additional Si layers. However, CH calculations are likely to modify the predicted XAS in this low-energy region, so it is possible that this low-energy shoulder could also be a feature of the BLs we modelled.

Together these soft X-ray spectroscopy measurements indicate that, as the second and third layers of Si are deposited, bulk-like Si begins to dominate the Ag surface. Since epitaxial or freestanding BLs would not be expected to have a bulk-like emission spectrum, our result agrees with the LEEM experiment [152, 228] that reported the progression from Si MLs to bulk-like crystals. However, there is still evidence of some interaction with the Ag surface, which could indicate stable epitaxial multilayer regions among the bulk-like crystals, but could also be a result of the interaction between the substrate and the crystals themselves.

8.7 Conclusion

To summarize, we show that DFT can be used to predict the structures of the most stable BLs on the Ag(111) (4×4) and $(\sqrt{13}\times\sqrt{13})$ supercells, and suggest that the (4×4) supercell hosts an AA-stacked structure that conforms to the $(\sqrt{3}\times\sqrt{3})$R30° topology that has been observed using STM and nc-AFM. We also find that the BL on the $(\sqrt{13}\times\sqrt{13})$ supercell shows evidence of a reduced interaction with the underlying substrate. This BL, however, does not conform to any STM measurements of the Si/Ag(111) surface, which suggests that it does not exist in multilayer silicene samples. In order to explain the absence of this BL in STM data, we propose that the $(\sqrt{7}\times\sqrt{7})/(\sqrt{13}\times\sqrt{13})$ ML domains could act as a seed for bulk Si crystallization, or possibly Ag surface segregation.

Our electronic structure calculations indicate that both BLs should have approximately the same electronic structure as their ML counterparts, namely metallic, strongly interacting with the substrate and without a Dirac cone at the Fermi level. This result conflicts with previous ARPES observations of a Dirac cone-like dispersion in the BL and multilayer

bandstructures [148, 214]. However, it is possible that these observed structures are actually metallic hybridized bands with saddle points, much like those observed in the epitaxial MLs [127, 131].

Through soft X-ray spectroscopy, we conclude that bulk-like Si is predominantly formed on the surface during the deposition of what would be a second and third layer of Si, were large-area silicene multilayers to exist. It would be interesting to determine if bulk Si formation occurred as strongly on a BL deposited on a quasi-pure phase $(3 \times 3)/(4 \times 4)$ ML, which could confirm our suspicion that the $(\sqrt{7} \times \sqrt{7})/(\sqrt{13} \times \sqrt{13})$ ML "seeds" the dewetting process. It is also a distinct possibility that multilayer formation is even more sensitive to deposition conditions like substrate temperature and Si flux than ML formation. The difference between accounts of large-scale silicene multilayer formation and those of Ag-terminated Si or bulk Si crystallization could be the result of minute differences in growth parameters.

8.8 Acknowledgements

The authors gratefully acknowledge the contributions of Prof. Guy Le Lay, Dr. Patrick Vogt, Dr. Paola De Padova and Dr. Andrea Resta for their invaluable experimental guidance. We would also like to acknowledge financial support from the Natural Sciences and Engineering Research Council of Canada (NSERC), the Canada Research Chair Program and the Russian Foundation for Basic Research (Projects 14-02-00006). Calculations utilized Compute Canadas WestGrid HPC consortium. Research was performed at the REIXS beamline of the Canadian Light Source, which is supported by NSERC, the National Research Council (Canada), the Canadian Institutes of Health Research, the Province of Saskatchewan, Western Economic Diversification Canada, and the University of Saskatchewan.

Chapter 9

The Electronic Structure of Lithium Metagallate

Authors: *Neil W. Johnson, John A. McLeod and Alexander Moewes*

Reference: N.W. Johnson, J.A. McLeod and A. Moewes, *Journal of Physics: Condensed Matter* **23**, 445501 (2011). [175]

While this manuscript is not directly related to my studies of epitaxial silicene on Ag(111), it does represent a contribution that I have made to the field of condensed matter physics, and so I have included it in this thesis. It also demonstrates some of the DFT and soft X-ray spectroscopy principles that were alluded to earlier in this thesis that do not appear in the silicene manuscripts, including alternative exchange-correlation functionals and the core-hole effects in XAS.

The experiments on $LiGaO_2$ were some of the first XES and XAS measurements I was involved in, and were carried out in October of 2011 by myself and Dr. John McLeod at the SXF endstation of BL8 at the ALS. Both Dr. McLeod and I performed a portion of the DFT calculations, and we were jointly responsible for interpreting the results and authoring the manuscript, while I handled the submission and peer-review process.

I am licensed to reproduce this manuscript within the pages of this thesis. See Appendix C for more information. The figure numbers, section headings and general formatting have been altered to ensure the consistency of this thesis. No other substantial alterations have been made to the manuscript.

9.1 Introduction

$LiGaO_2$ has been of interest for some time in both academia and industry as a lattice-matched substrate for optoelectronic semiconductors [229]. Large single crystals can be grown by the Czochralski method [230], and high purity single crystals several inches long have been reported [231]. $LiGaO_2$ can cleave to form faces that are lattice-matched to ZnO [232, 233], GaN [229, 231, 234–236], and (found recently) InN [237]. $LiGaO_2$ may be one of the best substrates for growing high purity GaN films [238], and the $LiGaO_2$ crystal face can tune the orientation, and consequently the polarization, of GaN and ZnO films [231, 232].

Early research into the intrinsic properties of $LiGaO_2$ focused on vibrational and optical properties [239, 240], and on possible photoluminescence after doping with transition metals [241, 242]. It has been found that V^{3+}-doped and pure $LiGaO_2$ are both optically active materials [243], and Fe^{3+}-doped $LiGaO_2$ is an efficient emitter of red light when optically pumped [244]. Research on $LiGaO_2$ has also focused on thermal properties [245] and high temperature lattice parameters [246], with the aim of improving the growth of GaN on $LiGaO_2$ [238, 247], and recently atomically flat $LiGaO_2$ surfaces were reported [248].

Since $LiGaO_2$ is such an accommodating substrate for a variety of optoelectronic semiconductors, there has been interest in seeing whether it could also be an active part of an optoelectronic circuit. Early investigations of potential lasing [241] and optical frequency upconversion [249] came back negative, but recent research has shown that $LiGaO_2$ can be alloyed with ZnO [250], creating a material with a tunable direct band gap between 3.3 and 5.6 eV [251]. If wurtzite InN can be alloyed with $LiGaO_2$ in the same manner, the resulting alloy could potentially have a tunable band gap between 0.7 and 5.6 eV [252]. However greater knowledge of the electronic structure of $LiGaO_2$ is necessary to direct research in making $LiGaO_2$ a more functional optoelectronic material.

The electronic structure of $LiGaO_2$ has been studied theoretically [253–255], but despite the academic and industrial interest no experimental investigation beyond the optical range exists. Herein we compare density functional theory (DFT) calculations to O K_α x-ray emission spectroscopy (XES) and K-edge x-ray absorption spectroscopy (XAS) measurements in order to investigate the valence and conduction bands of $LiGaO_2$ in detail.

9.2 X-ray spectroscopy

The oxygen $K_\alpha$soft XES measurements were performed on the SXF endstation of beamline 8.0.1 at the Advanced Light Source (ALS) in Berkeley [192]. The endstation has a Rowland circle geometry x-ray spectrometer and utilizes spherical gratings and an area sensitive multichannel detector. The instrumental resolving power ($E/\Delta E$) was 10^3, and the O K_α XES were energy calibrated using the bismuth germanate (BGO) emission peak at 526.0 eV [256].

The oxygen K-edge soft XAS measurements were performed on the spherical grating monochromator (SGM) beamline at the Canadian Light Source (CLS) in Saskatoon [257,258]. A microchannel plate fluorescence detector was used for the TFY-mode measurements. Both TFY-mode and TEY-mode absorption measurements were normalized by the incident photon flux, which was measured using a highly transparent gold mesh. The instrumental resolving power for the XAS was approximately 5×10^3, and the absorption spectra were calibrated using the BGO absorption peak at 532.7 eV [256].

The sample of $LiGaO_2$ powder (99% purity, Alfa Aesar) and the reference sample of BGO powder (99% purity, Alfa Aesar) were pressed into clean indium foil. These materials were placed under ultrahigh vacuum (5×10^7 torr or better) in each of the two beamline endstations and measured without further treatment.

9.3 Electronic structure calculations

The band structure and density of states (DOS) for $LiGaO_2$ were calculated with DFT methods. The WIEN2k code, an implementation of the full potential linearized augmented plane wave (FP-LAPW) method, was used [177]. The calculation was performed on a $10 \times 8 \times 11$ k-point mesh with a -8 Ryd plane wave cut-off energy, and the crystal structure determined by Marezio was used [259]. When the energy and charge steps in the self-consistent field cycles dropped below 10^4 Ryd/unit cell and 10^3 e/unit cell respectively, the calculation was considered to have converged.

Three exchange-correlation functionals were considered in order to determine which would best predict the observed band gap and Ga 3d valence character. These included the Perdew-

Burke-Ernzerhof generalized gradient approximation functional (PBE-GGA), the local spin density approximation with an added Coulomb repulsion term in the Ga d states (LSDA + U) and the modified Becke-Johnson functional (mBJ) [173, 174]. For calculations with the LSDA + U functional, we initially use a previously reported value of U = 8 eV [260], but find that U = 12 eV is in better agreement with our measurements. As we fine-tune this parameter in such a manner, this approach can no longer be considered strictly *ab initio*. However, this value of Coulomb repulsion is not unreasonable, so all reported results are for the U = 12 eV calculation.

The WIEN2k utility XSPEC, which operates using the formalism described in [213], was used to estimate absorption spectra from the unoccupied DOS. XAS measurement introduces a vacancy into the core of the measured atom, which can cause an energy shift in the measured conduction band. To account for this, one core level electron in the unoccupied DOS calculations was removed and placed as an ambient background charge. Separate calculations were performed for a single core hole per unit cell located at one of the two inequivalent O sites. The calculated XES and XAS spectra were compared to the measured spectra by aligning their main emission features, then shifting the calculated XAS in a way that preserved the theoretically predicted band gap.

9.4 Results and discussion

The band structure and DOS for $LiGaO_2$ calculated with the mBJ functional are shown in figure 9.1. The band structure of $LiGaO_2$ was previously calculated by *ab initio* methods [253]; the structure that we find for each band is essentially the same, but our calculations predict different bandwidths and relative energies. The band gap of $LiGaO_2$ is calculated as 5.658 eV, and is direct and across the Γ point. The top of the valence level is densely packed with rather flat bands, while the bottom of the conduction band has only a few bands with relatively large curvature.

As we might expect, the valence band is dominated by O 2p states. The O 2p character, shown in figure 9.1, is evenly spread across all the energy bands between -3 and 0 eV, while between -5 and -3 eV the O 2p character is somewhat reduced (although still fairly

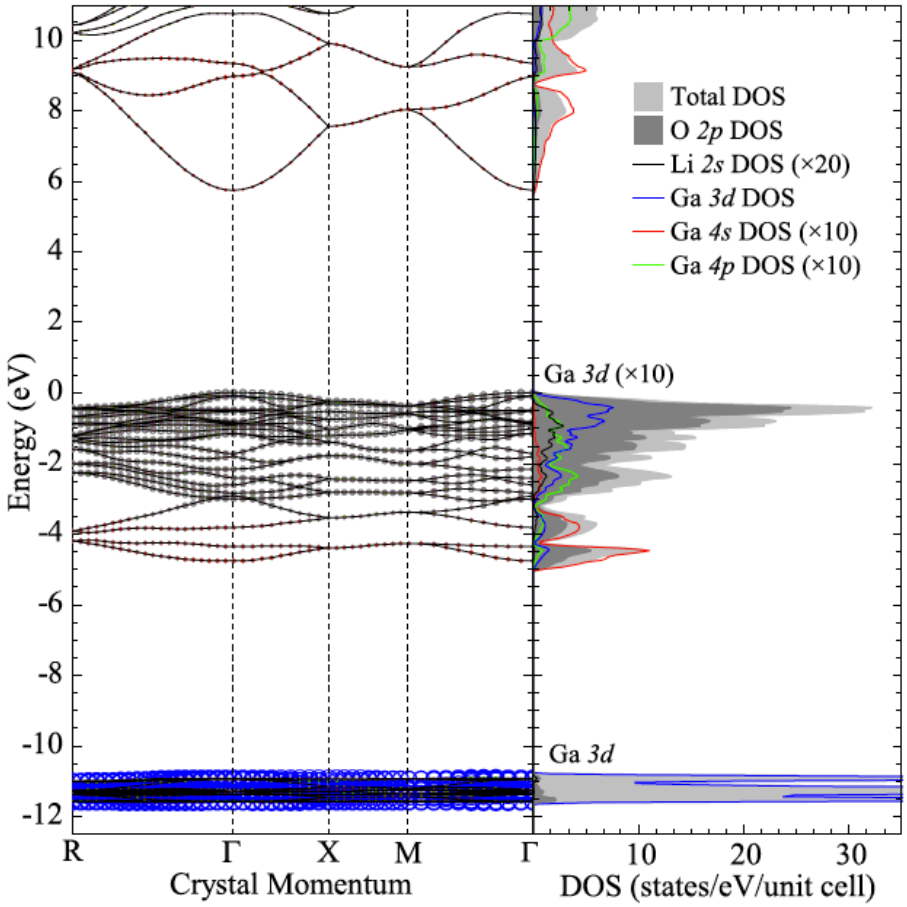

Figure 9.1: The calculated band structure (left panel) and DOS (right panel) for $LiGaO_2$ using the mBJ exchange-correlation functional. In addition to the total DOS, the projected partial DOS for various atomic symmetries is plotted as well. These symmetries are also shown in the band structure; the relative size of the coloured circles indicates the proportional character of that band. The colours for the projected partial states are consistent in the two panels.

constant for all momenta within this region) relative to the amount of Ga and interstitial states. There is a semi-core Ga $3d^{10}$ band weakly hybridized with O 2p states some 11 eV below the top of the valence band, as seen in the projected DOS in figure 9.1. The bottom of the valence band (around -4 eV) shows some hybridization between O 2p and Ga 3s states, the middle of the valence band shows some hybridization between O 2p and Ga 4p states, and the top of the valence band shows some hybridization between O 2p and Ga 3d states. However in all of these cases the Ga contribution to the total DOS is less than 10% of the O 2p contribution (note that the Ga 4s, 4p, and valence level 3d states have been increased by a factor of 10 in figure 9.1), so Ga is close to a complete 3+ ionization state.

The bottom of the conduction band of $LiGaO_2$ (below 9 eV in figure 9.1) is almost evenly hybridized between O 2p and Ga 4s states. Above 9 eV there is roughly even hybridization between O 2p and Ga 4p states. In the valence band, the Li 2s states are weakly present, matching the shape of the O 2p states at roughly 5% of their amplitude. There are almost no Li 2s states in the conduction band below 10 eV, and it is clear that Li only participates in ionic bonding.

While electronic structure calculations can provide detailed insight into the physics of a material, it is important to verify the results of these calculations with empirical measurements. O K_α XES and K-edge XAS spectra provide insight into the valence and conduction O 2p states, respectively. Since the valence band of $LiGaO_2$ is dominated by O 2p states, and since the conduction band contains strong Ga–O 2p hybridized states, these two complementary measurements are useful for verifying the calculated DOS.

The O K_α XES and K-edge XAS spectra are shown in figure 9.2. The non-resonantly excited O K_α XES spectrum has a high-energy satellite (denoted as s in figure 9.2), which we suspect to be a Wentzel–Druyvestyn satellite [261–263]. Resonantly exciting at 545 eV (feature C4 in the XAS; see figure 9.2) suppresses this feature. There is good agreement between the surface sensitive TEY-mode and the bulk sensitive TFY-mode O K-edge XAS spectra, which indicates little surface decomposition and demonstrates that our XAS measurements are not greatly distorted by sample charging (TEY-mode case) or self-absorption (TFY-mode case).

The O K_α XES and K-edge XAS can be used to estimate the band gap of a material without any reliance on *ab initio* calculations.We have previously shown [264–266] that the peak in the second derivative of the XES and XAS spectra can be used to estimate the band gap in a relatively unambiguous manner. In this approach the top of the valence band is identified as the peak in the second derivative of the XES spectrum and the bottom of the conduction band is identified as the peak in the second derivative of the XAS spectrum. This technique suggests that the band gap of $LiGaO_2$ is 5.6 eV, in reasonable agreement with the calculated value of 5.658 eV obtained using the mBJ exchange–correlation functional.

From the DOS we can calculate the theoretical O K_α XES spectrum, as shown in figure 9.2. The calculated XES spectrum shows three distinct features (labelled V1, V2, and V3

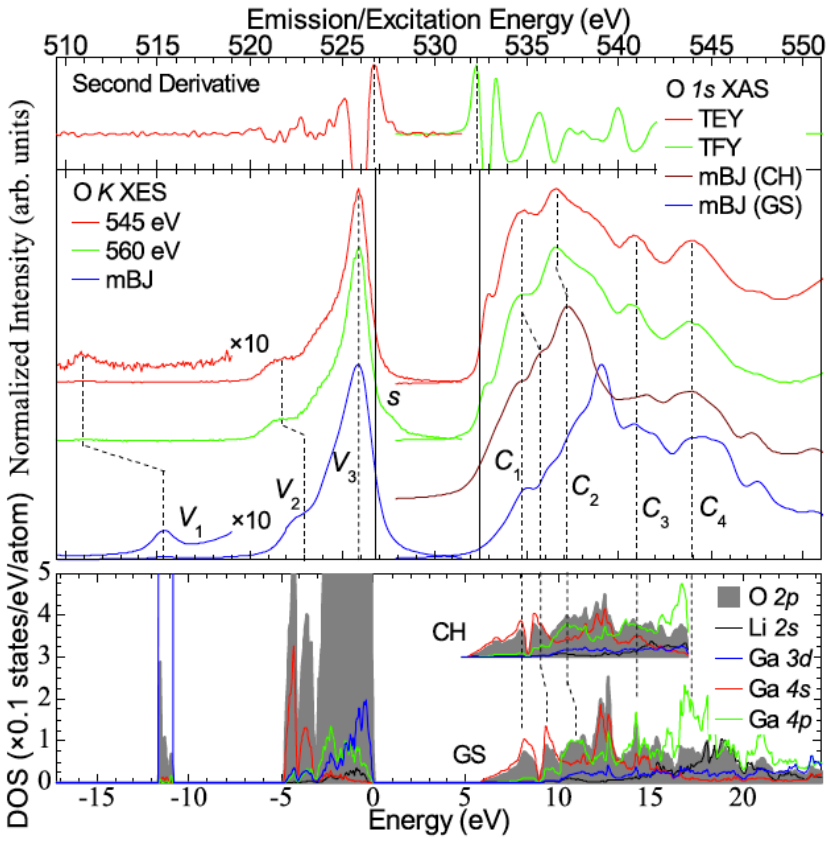

Figure 9.2: The DOS and measured and calculated O K_α XES and K-edge XAS for $LiGaO_2$. The top panel shows the second derivative of the measured O K_α XES and K-edge XAS (TFY-mode) spectra, the centre panel shows the calculated and measured spectra on a common emission/excitation energy scale, and the bottom panel shows the projected partial DOS. For the conduction band both the ground state (GS) and core hole (CH) DOS and calculated O K-edge XAS are shown. The solid vertical lines indicate the valence band maximum and conduction band minimum in the calculated DOS.

in figure 9.2) which are also present in the measured XES. However, the relative energies of these features differ between experiment and calculation. This energy difference is most prominent for feature V1 – the weak O 2p hybridization with the Ga $3d^{10}$ semi-core bands – which is about 4 eV lower in energy in the measured spectrum than in the calculated spectrum (as shown in figure 9.2). This suggests that the interaction between the Ga $3d^{10}$ states and the remainder of the valence states is somewhat overestimated in the calculation.

The O K-edge XAS spectrum can also be calculated from the ground state DOS; the calculated spectrum shown in figure 9.2 is similar to the measured spectrum. The main

differences between the two occur in the first 7–8 eV of the spectra. This is because the actual O K-edge XAS measurement creates a core hole, which in principle can significantly distort XAS spectra from the true ground state conduction band. It has previously been shown that for many oxides the O 1s core hole does not significantly shift the energy of the XAS measurement from the true ground state conduction band [264], and rather simply increases the amplitude of states near the conduction band edge [265]. A calculated XAS spectrum with an explicit O 1s core hole is also shown in figure 9.2, and this spectrum has a higher amplitude near the onset as expected.

Since the crystal structure of $LiGaO_2$ has two distinct oxygen sites, care must be taken when comparing XES and XAS data to the density of states. The XES and XAS measurements are all taken relative to the O 1s binding energy, which may not be the same for atoms at inequivalent sites. However, the calculated energies for core level electrons in $LiGaO_2$ differ by only 0.034 eV between the sites, and are therefore indistinguishable within the resolving power of our measurements.

In the case of the conduction band DOS with an O 1s core hole, the calculations do suggest an energy shift in the conduction band edge from that of the ground state calculation. The magnitude of this shift differs depending on which of the two O sites has the core hole; a core hole in the OI site (to use Marezios notation [259]) is predicted to reduce the band gap by 0.726 eV from the ground state value, while a core hole in the OII site is predicted to reduce the band gap by 0.586 eV. These different shifts mean that caution must be used when attributing features in the measured O K-edge XAS spectrum to specific states in the ground state conduction band. The average core hole perturbed conduction band DOS is shown above the ground state DOS in figure 9.2.

In the XAS measurement, an appreciable core hole effect would cause us to observe a smaller experimental band gap than the true ground state band gap of $LiGaO_2$. Given the good agreement between our measured and calculated band gaps and the value most often quoted in the literature [267], we can say that the core hole effect is probably not significant. However, we cannot verify that no band gap reduction has taken place in our measurements, and so our band gap of 5.6 eV can only be quoted as a lower bound on the experimental value. The conduction band shift of about 0.7 eV that was observed in the core hole calculation

is larger than we would expect to occur in the XAS measurement, as the concentration of core holes in the calculations (one per eight O sites) is significantly higher than that of the measurements (about one per thousand O sites). That being said, we cannot rule out the possibility of the experimental ground state band gap being as high as 6.3 eV, the sum of our experimental band gap and the largest calculated core hole shift.

In any case, the measured O K-edge XAS spectrum possesses four distinct features (labelled C1, C2, C3, and C4 in figure 9.2). These spectral features can be reasonably connected to features in the core hole perturbed and ground state conduction band, as shown in figure 9.2.

The energies of the spectral features labelled in figure 9.2 are presented in table 9.1. In all cases the experimental feature is at the same or a lower energy as compared with the calculated feature. Each feature has also been identified with specific hybridized states or an aspect of the x-ray transition (i.e. the satellite feature). The largest discrepancy, between the location of V1 in the measured and calculated spectra, was discussed above and is attributed to an overestimate of the Ga $3d^{10}$ interaction (although there clearly is some interaction, since the Ga $3d^{10}$ states must hybridize with O 2p states for the feature to appear in an O K_α XES spectrum). The second-largest difference between the measured and calculated spectra is in feature V2; this is possibly due to an underestimate of the O 2p–Ga 4s bonding. The identification of features in the conduction band is somewhat more tentative, given the previously discussed difference in O inequivalent sites and the problems with accurately representing the core hole. However the identification of all the spectral features herein may prove helpful in characterizing the electronic structure of more complicated alloys or heterostructures based on $LiGaO_2$, since performing x-ray spectroscopy measurements may be considerably easier than calculating the electronic properties with *ab initio* methods.

The calculated partial DOS in the semi-core and valence region changes significantly depending on which exchange-correlation functional is used, as illustrated in figure 9.3. The predicted band gaps, valence bandwidths and Ga $3d^{10}$ character are reported in table 9.2, alongside their measured values. While use of the mBJ functional generates the most accurate band gap (see table 9.2 and figure 9.2), it contracts the DOS below the Fermi level, resulting in a narrower valence band and higher-energy Ga $3d^{10}$ band than is observed in the measured

Table 9.1: The energies and identification of spectral features in the calculated ground state and experimental spectra. The difference between the calculated and experimental spectra is also shown (column 'Diff.'). The features are all labelled in figure 9.2.

Feature	Calc. (eV)	Exp. (eV)	Diff. (eV)	Identification
V1	515.3	510.9	4.4	O 2p–Ga 3d
V2	522.8	521.9	0.9	O 2p–Ga 4s
V3	525.9	525.9	0.0	O 2p
s	–	527.5	–	Satellite
C1	534.8	534.8	0.0	O 2p–Ga 4s
C2	537.2	536.5	0.7	O 2p–Ga 4p
C3	540.9	540.9	0.0	O 2p–Ga 4p
C4	544.0	544.0	0.0	O 2p–Ga 4p

O K_α XES spectrum. The other functionals predict a valence bandwidth in better agreement with our measurements (note that the discrepancy between the energy of the measured and calculated V2 emission features in table 9.1 is significantly smaller when calculated with every functional except mBJ), but these functionals significantly underestimate the band gap. Only the LSDA + U calculation predicts a Ga $3d^{10}$ energy in agreement with the value seen in our measurements, but this agreement can be refined to arbitrary accuracy by strategically altering the value of U.

The previous *ab initio* DFT calculation of the electronic structure of $LiGaO_2$ showed the same energy of the Ga $3d^{10}$ states; however the authors predicted that self-energy corrections would cause the Ga $3d^{10}$ states to hybridize with the O 2s states at roughly -15 eV [253]. However, a recent calculation of $LiGaO_2$ using the GW-approximation (which at least partially accounts for self-energy of quasi-particles) predicts the Ga $3d^{10}$ states to rest at only about -13 eV [255]. It is possible that a constrained LSDA + U calculation could provide values for both the energy of the Ga $3d^{10}$ states and the band gap that are in better agreement with experiment, but it is somewhat surprising that no basic DFT functional will provide a band gap, bandwidth, and semi-core Ga $3d^{10}$ state energy that are in better agreement with experiment, especially since one would not think of $LiGaO_2$ as a strongly correlated material.

To summarize, we have calculated electronic structures for $LiGaO_2$ using several different

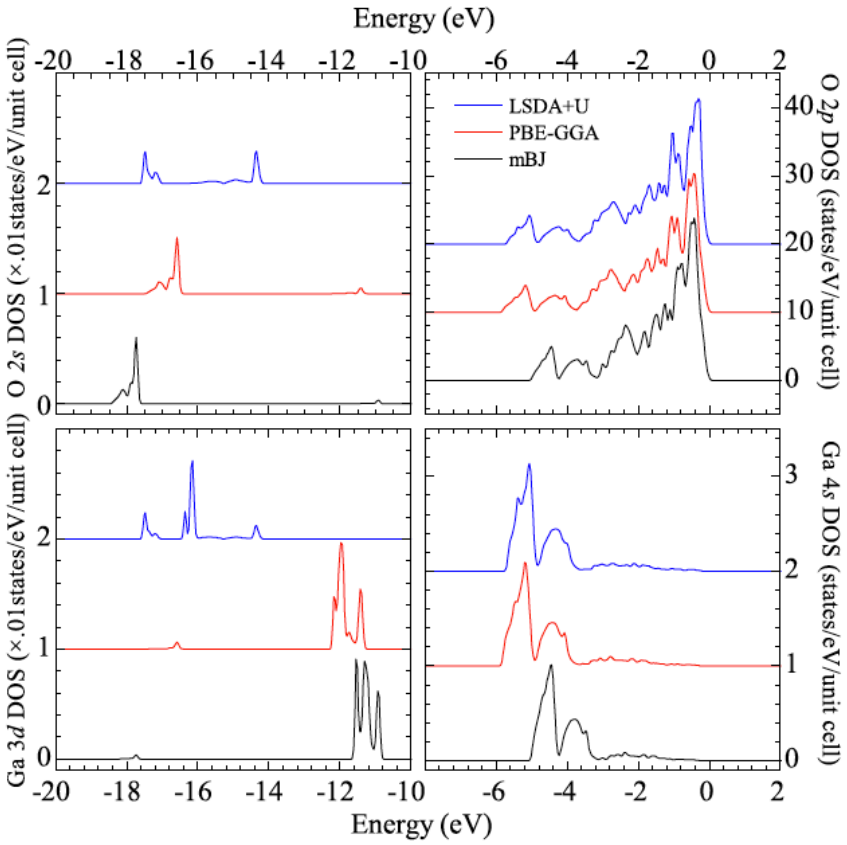

Figure 9.3: Calculated O 2s (top left) and 2p (top right), and Ga 3d (bottom left) and 4s (bottom right) states calculated with each exchange-correlation functional.

Table 9.2: The measured energies for the band gap, valence bandwidth and Ga 3d state centre, as well as values calculated with each exchange-correlation functional.

	Band gap (eV)	Valence band width (eV)	Centre of Ga 3d band (eV)
Measured (±0.1 eV)[a]	5.6	6.2	−15.8[b]
PBE-GGA	3.530	5.987	−11.763
LSDA + U	3.528	5.850	−16.154
mBJ	5.658	5.170	−11.198

[a] Estimated error due to noise in the spectra.
[b]The difference between the centre of the O K_α XES emission feature and the band gap onset.

DFT methods, and tested these calculations against measurements in the soft x-ray regime. Our estimate of the band gap, from O K_α XES and K-edge XAS spectra, is in good agreement with literature values. Additionally, we have closely recreated the observed band gap using DFT with the mBJ exchange-correlation functional, but have shown that none of the *ab initio* calculations are able to accurately predict the energies of the Ga $3d^{10}$ semi-core states; our LSDA + U calculation is shown to place them properly but only with an artificially selected value of U. Since some DFT functionals have been shown to correctly account for the energy of the Zn $3d^{10}$ states in ZnO [266], a soft x-ray spectroscopy analysis of $(LiGa)_{1-x}Zn_{2x}O_2$ might help clarify the chemical activity of the Ga $3d^{10}$ states.

9.5 Acknowledgments

We acknowledge the support of the Natural Sciences and Engineering Research Council of Canada (NSERC), and the Canada Research Chair programme. The Canadian Light Source is supported by NSERC, the National Research Council (NSC) Canada, the Canadian Institutes of Health Research (CIHR), the Province of Saskatchewan, Western Economic Diversification Canada, and the University of Saskatchewan. The Advanced Light Source is supported by the Director, Office of Science, Office of Basic Energy Sciences of the US Department of Energy under Contract No. DE-AC02-05CH11231.

Chapter 10
Conclusions and Future Direction

10.1 Summary of Contributions

Together, the three epitaxial silicene studies included in this thesis represent a significant contribution to the field of silicene research. When the 2014 *Advanced Functional Materials* article was published, there was a fair amount of controversy over the absence or presence of a bandgap in epitaxial silicene on Ag(111). This study added weight to the position that a bandgap does not exist, and provided theoretical and experimental insight into the epilayer-substrate interactions that are responsible. Since its publication, it has been cited by 19 other published works, including two review articles and two book chapters. Further, it represented the first application of core-level spectroscopy to silicene, demonstrating the benefit of using element-specific experimental techniques on epitaxial systems.

Meanwhile, the 2016 *Scientific Reports* study provided disconfirming evidence for an oxygen-induced local bandgap opening that had been suggested by previous authors using DFT calculations and STS measurements. It also demonstrated the extreme sensitivity of silicene to oxidation, and provided evidence that moderate oxidation results in the formation of bulk-like SiO_2 clusters.

Finally, the 2015 *Advanced Functional Materials* article addressed some of the controversies surrounding silicene multilayer growth on Ag(111). Namely, it provided a stable structural model that is able to explain the observed STM and AFM images of the small-scale structure of multilayers, and also confirmed the large-scale observation of dewetting and bulk Si formation during multilayer growth.

As a general conclusion, I would say that these studies indicate that Ag(111) (and perhaps all metallic substrates) should be avoided if the goal is to produce a stable, quasi-freestanding

epitaxial silicene sheet. The epilayer-substrate interaction is strong, multilayer growth does not result in quasi-freestanding sheets passivated by the bottom epilayer, and exposure to air causes the rapid degradation of the sample due to oxygen.

Currently, I have one more silicene study planned for the near future. In exploring alternative corrugation configurations for freestanding silicene (on a (2×2) supercell), I found at least one that also hosts a Dirac cone despite a lack of inversion symmetry. I intend to use WIEN2k to explore the whole family of (2×2) corrugation patterns from a structural and electronic standpoint to determine if silicene's Dirac cone is robust against corrugation defects and to search for equally or perhaps more energetically optimal silicene structures.

10.2 Current State of Silicene Research and Future Directions

Though my research and the majority of the literature to date have outlined several problems inherent in using Ag(111) as a substrate, one fairly recent study mitigated most of them, using silicene grown on Ag(111) to produce the first functioning silicene transistor [219]. One of the major advances in this paper was the development of an oxygen-free etchant to dissolve the Ag substrate after the silicene was deposited without oxidizing the sheet. Also, the authors provided a method for growing an ultra-thin Ag(111) surface so that a crystal worth many thousands of dollars would not have to be sacrificed every time a quasi-freestanding silicene sheet was to be produced. Not only did this study constitute a proof-of-concept for silicene-based electronics, it also marked the first observation of epitaxial silicene removed from its growth substrate. However, given the sample's limited lifetime in air (on the order of a few minutes), there are obviously still many important challenges left to overcome before more complex silicene-based devices can be produced.

A number of alternative substrates for epitaxial silicene have been proposed, some of which have been suggested as suitable candidates for silicene growth on the basis of DFT calculations, while silicene-like sheets have experimentally observed on others. Silicene monolayers on the Ir(111) face [203] were identified only a few months after the first confirmed report of silicene on Ag(111) [127]. These monolayers conform to a $(\sqrt{3} \times \sqrt{3})\mathrm{R}30^\circ/(\sqrt{7} \times \sqrt{7})\mathrm{R}19.1^\circ$

silicene/Ir(111) reconstruction, and have been observed with STM and LEED [203]. However, further analysis showed that there was a strong distortion of the Si hexagonal rings caused by the influence of the Ir(111), and that metallic hybrid bands were introduced into the bandstructure of the silicene as a result [268].

Under certain conditions, when thin layers of ZrB_2 are deposited on to a Si(111) wafer, surface atoms from the Si are prone to segregate from the bulk and rise to the top of the deposited diboride thin film. In 2012, Fleurence *et al.* showed that the surface Si atoms arrange into a silicene-like hexagonal ring structure [204]. The authors used ARPES to probe the VB states and, in comparing the results to DFT calculations, showed that a sizeable direct gap of about 250 meV exists in the silicene. The corrugation pattern and the linear bandstructure expected of freestanding silicene were not present, suggesting that the epitaxial strain of the diboride substrate was significant. I would be interested in applying the same experimental and theoretical treatment presented in this thesis to silicene on ZrB_2, and soft X-ray spectroscopy would be well-suited for verifying the bandgap experimentally.

Silicene grown on insulating substrates may more closely resemble freestanding silicene sheets, as evidenced by Chiappe *et al.*'s study of Si deposited on MoS_2 [225] and Kaloni *et al.*'s theoretical modelling of silicene on hexagonal BN [205]. With an inferred buckling distance of 2 Å , the silicene on MoS_2 closely resembles the metallic HB freestanding silicene structure predicted by Cahangirov *et al.* [99], and the appearance of Si states inside the bandgap of MoS_2 is consistent with this conclusion. Meanwhile, calculations suggest that the silicene sheets on hexagonal BN will more closely resemble their LB structure, including a Dirac cone with a slightly shifted Dirac point and a nearly unaffected Fermi velocity [206]. I have a particularly strong interest in exploring these layered 2D materials as both growth substrates and capping layers for epitaxial silicene, with the potential result of a quasi-freestanding sheet that is both stabilized and passivated by other atomically thin crystals.

Finally, a couple of interesting monoatomic 2D materials have appeared that are not composed of Group 14 elements, namely borophene [269] and phosphorene [270]. While research into these novel members of the 2D material family is still in its infancy, they have already shown promise as a transparent conductor and wide-gap semiconductor, respectively. It would be quite interesting to examine the interaction between borophene and its growth

substrate or to examine how the electronic structure of freestanding phosphorene evolves with thickness using the methods outlined in this thesis.

To close, I believe that soft X-ray spectroscopy has much to offer to the continually expanding field of 2D materials, both freestanding and epitaxial. It is element- and orbital-specific, capable of producing a clear picture of a material's electronic structure even for monolayers and sub-monolayers, and when compared to the predictions of DFT it can be used to validate structural models and verify predicted electronic characteristics. The soft X-ray spectroscopic studies of epitaxial silicene presented here and those of graphene in the literature represent only a small sample of this powerful technique's capabilities, and its role should only continue to grow larger as materials grow smaller.

References

[1] M. M. Waldrop. "More than Moore." *Nature* **530**, (2016) 145.

[2] J. C. Ranuárez; M. Deen; and C.-H. Chen. "A review of gate tunneling current in MOS devices." *Microelectronics Reliability* **46**, (2006) 1939.

[3] A. M. Ionescu and H. Riel. "Tunnel field-effect transistors as energy-efficient electronic switches." *Nature* **479**, (2011) 329.

[4] K. S. Novoselov; A. K. Geim; S. V. Morozov; D. Jiang; Y. Zhang; S. V. Dubonos; I. V. Grigorieva; and A. A. Firsov. "Electric field effect in atomically thin carbon films." *Science* **306**, (2004) 666.

[5] A. K. Geim and A. H. MacDonald. "Graphene: Exploring carbon flatland." *Physics Today* **60**, (2007) 35.

[6] E. P. Randviir; D. A. C. Brownson; and C. E. Banks. "A decade of graphene research: Production, applications and outlook." *Materials Today* **17**, (2014) 426.

[7] P. R. Wallace. "The band theory of graphite." *Physical Review* **71**, (1947) 622.

[8] K. Momma and F. Izumi. "*VESTA3* for three-dimensional visualization of crystal, volumetric and morphology data." *Journal of Applied Crystallography* **44**, (2011) 1272.

[9] R. Peierls. "Quelques propriétés typiques des corps solides." *Annales de l'Institut Henri Poincaré* **5**, (1935) 177.

[10] A. Alastuey and B. Jancovici. "Absence of strict crystalline order in a two-dimensional electron system." *Journal of Statistical Physics* **24**, (1981) 443.

[11] L. Landau and E. Lifshitz. *Statistical Physics: Vol. 5: Course of Theoretical Physics, 2nd Ed.*, (Pergamon Press 1969). ISBN 0750633727.

[12] H. Mermin, N. D.; Wagner. "Absence of ferromagnetism or antiferromagnetism in one- or two-dimensional isotropic Heisenberg models." *Physical Review Letters* **17**, (1966) 1133.

[13] N. D. Mermin. "Crystalline order in two dimensions." *Physical Review* **176**, (1968) 250.

[14] G. W. Semenoff. "Condensed-matter simulation of a three-dimensional anomaly." *Physical Review Letters* **53**, (1984) 2449.

[15] N. W. Ashcroft and N. D. Mermin. *Solid State Physics*, (New York: Holt, Rinehart and Winston 1976). ISBN 0030839939.

[16] K. S. Novoselov; D. Jiang; F. Schedin; T. J. Booth; V. V. Khotkevich; S. V. Morozov; and A. K. Geim. "Two-dimensional atomic crystals." *Proceedings of the National Academy of Sciences of the United States of America* **102**, (2005) 10451.

[17] Y. Zhang; Y. W. Tan; H. L. Stormer; and P. Kim. "Experimental observation of the quantum Hall effect and Berry's phase in graphene." *Nature* **438**, (2005) 201.

[18] L. Landau and E. Lifshitz. *Quantum Mechanics: Vol. 3: Course of Theoretical Physics, 2nd Ed.*, (Pergamon Press 1965). ISBN 0750635398.

[19] S. Pancharatnam. "Generalized theory of interference." *Proceedings of the Indian Academy of Sciences* **XLIV**, (1956) 398.

[20] M. Berry. "Quantal phase factors accompanying adiabatic changes." *Proceedings of the Royal Society A* **392**, (1984) 45.

[21] T. Kariyado and Y. Hatsugai. "Symmetry-protected quantization and bulk-edge correspondence of massless Dirac fermions: Application to the fermionic Shastry-Sutherland model." *Physical Review B* **88**, (2013) 245126.

[22] J. W. McClure. "Diamagnetism of graphite." *Physical Review* **104**, (1956) 666.

[23] A. H. Castro Neto; N. M. R. Peres; K. S. Novoselov; and A. K. Geim. "The electronic properties of graphene." *Reviews of Modern Physics* **81**, (2009) 109.

[24] A. Luican; G. Li; and E. Y. Andrei. "Quantized Landau level spectrum and its density dependence in graphene." *Physical Review B* **83**, (2011) 041405(R).

[25] A. K. Geim. "Graphene prehistory." *Physica Scripta* **T146**, (2012) 014003.

[26] C. Canali; G. Majni; R. Minder; and G. Ottaviani. "Electron and hole drift velocity measurements in silicon and their empirical relation to electric field and temperature." *IEEE Transactions on Electron Devices* **22**, (1975) 1045.

[27] T. Ando; T. Nakanishi; and R. Saito. "Berry's phase and absence of back scattering in carbon nanotubes." *Journal of the Physical Society of Japan* **67**, (1998) 2857.

[28] X. Du; I. Skachko; A. Barker; and E. Y. Andrei. "Approaching ballistic transport in suspended graphene." *Nature Nanotechnology* **3**, (2008) 491.

[29] O. Klein. "Die Reflexion von Elektronen an einem Potentialsprung nach der relativistischen Dynamik von Dirac." *Zeitschrift für Physik* **53**, (1929) 157.

[30] M. I. Katsnelson; K. S. Novoselov; and A. K. Geim. "Chirial tunnelling and the Klein paradox in graphene." *Nature Physics* **2**, (2006) 1986.

[31] X. Du; I. Skachko; F. Duerr; A. Luican; and E. Y. Andrei. "Fractional quantum Hall effect and insulating phase of Dirac electrons in graphene." *Nature* **462**, (2009) 192.

[32] D. Arovas; J. R. Schrieffer; and F. Wilczek. "Fractional statistics and the quantum Hall effect." *Physical Review Letters* **53**, (1984) 722.

[33] R. R. Nair; P. Blake; A. N. Grigorenko; K. S. Novoselov; T. J. Booth; T. Stauber; N. M. R. Peres; and A. K. Geim. "Fine structure constant defines visual transparency of graphene." *Science* **320**, (2008) 1308.

[34] C. Lee; X. Wei; J. W. Kysar; and J. Hone. "Measurement of the elastic properties and intrinsic strength of monolayer graphene." *Science* **321**, (2008) 385.

[35] Y. G. Semenov; K. W. Kim; and J. M. Zavada. "Spin field effect transistor with a graphene channel." *Applied Physics Letters* **91**, (2007) 153105.

[36] D. Pesin and A. H. MacDonald. "Spintronics and pseudospintronics in graphene and topological insulators." *Nature Materials* **11**, (2012) 409.

[37] A. Rycerz; J. Tworzydo; and C. W. J. Beenakker. "Valley filter and valley valve in graphene." *Nature Physics* **3**, (2007) 172.

[38] B. C. Brodie. "On the Atomic Weight of Graphite." *Philosophical Transactions of the Royal Society of London* **149**, (1859) 249.

[39] G. Ruess and F. Vogt. "Hochstlamellarer Kohlenstoff aus Graphitoxyhydroxyd." *Monatshefte für Chemie* **78**, (1948) 222.

[40] B. Kelly. *Physics of Graphite*, (Springer Netherlands 1981). ISBN 0853349606.

[41] M. Noel and R. Santhanam. "Electrochemistry of graphite intercalation compounds." *Journal of Power Sources* **72**, (1998) 53.

[42] M. S. Dresselhaus and G. Dresselhaus. "Intercalation compounds of graphite." *Advances in Physics* **51**, (2002) 1.

[43] G. Yoon; D. H. Seo; K. Ku; J. Kim; S. Jeon; and K. Kang. "Factors affecting the exfoliation of graphite intercalation compounds for graphene synthesis." *Chemistry of Materials* **27**, (2015) 2067.

[44] W. A. de Heer; C. Berger; X. Wu; P. N. First; E. H. Conrad; X. Li; T. Li; M. Sprinkle; J. Hass; M. L. Sadowski; M. Potemski; and G. Martinez. "Epitaxial graphene." *Solid State Communications* **143**, (2007) 92.

[45] T. H. F. Bonaccorso, Z. Sun and A. C. Ferrari. "Graphene photonics and optoelectronics." *Nature Photonics* **4**, (2010) 611.

[46] F. Schwierz. "Graphene transistors." *Nature Nanotechnology* **5**, (2010) 487.

[47] J. C. Meyer; A. K. Geim; M. I. Katsnelson; K. S. Novoselov; T. J. Booth; and S. Roth. "The structure of suspended graphene sheets." *Nature* **446**, (2007) 60.

[48] A. Fasolino; J. H. Los; and M. I. Katsnelson. "Intrinsic ripples in graphene." *Nature Materials* **6**, (2007) 858.

[49] E.-A. Kim and A. H. Castro Neto. "Graphene as an electronic membrane." *EPL* **84**, (2008) 57007.

[50] S. Fratini and F. Guinea. "Substrate-limited electron dynamics in graphene." *Physical Review B* **77**, (2008) 195415.

[51] K. I. Bolotin; K. J. Sikes; Z. Jiang; M. Klima; G. Fudenberg; J. Hone; P. Kim; and H. L. Stormer. "Ultrahigh electron mobility in suspended graphene." *Solid State Communications* **146**, (2008) 351.

[52] S. V. Morozov; K. S. Novoselov; M. I. Katsnelson; F. Schedin; D. C. Elias; J. A. Jaszczak; and A. K. Geim. "Giant intrinsic carrier mobilities in graphene and its bilayer." *Physical Review Letters* **100**, (2008) 11.

[53] A. Blackman, L.C.F.; Ubbelohde. "Stress recrystallization of graphite." *Proceedings of the Royal Society A* **266**, (1962) 20.

[54] S. Bae; H. Kim; Y. Lee; X. Xu; J.-S. Park; Y. Zheng; J. Balakrishnan; T. Lei; H. Ri Kim; Y. I. Song; Y.-J. Kim; K. S. Kim; B. Özyilmaz; J.-H. Ahn; B. H. Hong; and S. Iijima. "Roll-to-roll production of 30-inch graphene films for transparent electrodes." *Nature Nanotechnology* **5**, (2010) 574.

[55] H. Zhou; W. J. Yu; L. Liu; R. Cheng; Y. Chen; X. Huang; Y. Liu; Y. Wang; Y. Huang; and X. Duan. "Chemical vapour deposition growth of large single crystals of monolayer and bilayer graphene." *Nature Communications* **4**, (2013) 2096.

[56] J. Berashevich and T. Chakraborty. "Tunable band gap and magnetic ordering by adsorption of molecules on graphene." *Physical Review B* **80**, (2009) 033404.

[57] F. Yavari; C. Kritzinger; C. Gaire; L. Song; H. Gulapalli; T. Borca-Tasciuc; P. M. Ajayan; and N. Koratkar. "Tunable bandgap in graphene by the controlled adsorption of water molecules." *Small* **6**, (2010) 2535.

[58] M. Papagno; S. Rusponi; P. M. Sheverdyaeva; S. Vlaic; M. Etzkorn; D. Pacilé; P. Moras; C. Carbone; and H. Brune. "Large band gap opening between graphene Dirac cones induced by Na adsorption onto an Ir superlattice." *ACS Nano* **6**, (2012) 199.

[59] C. Cao; M. Wu; J. Jiang; and H. P. Cheng. "Transition metal adatom and dimer adsorbed on graphene: Induced magnetization and electronic structures." *Physical Review B* **81**, (2010) 205424.

[60] I. Pletikosić; M. Kralj; P. Pervan; R. Brako; J. Coraux; A. T. N'Diaye; C. Busse; and T. Michely. "Dirac cones and minigaps for graphene on Ir(111)." *Physical Review Letters* **102**, (2009) 056808.

[61] G. Giovannetti; P. A. Khomyakov; G. Brocks; P. J. Kelly; and J. Van Den Brink. "Substrate-induced band gap in graphene on hexagonal boron nitride: Ab initio density functional calculations." *Physical Review B* **76**, (2007) 073103.

[62] R. Quhe; J. Zheng; G. Luo; Q. Liu; R. Qin; J. Zhou; D. Yu; S. Nagase; W.-N. Mei; Z. Gao; and J. Lu. "Tunable and sizable band gap of single-layer graphene sandwiched between hexagonal boron nitride." *NPG Asia Materials* **4**, (2012) e16.

[63] N. Kharche and S. K. Nayak. "Quasiparticle band gap engineering of graphene and graphone on hexagonal boron nitride substrate." *Nano Letters* **11**, (2011) 5274.

[64] C. R. Dean; a. F. Young; I. Meric; C. Lee; L. Wang; S. Sorgenfrei; K. Watanabe; T. Taniguchi; P. Kim; K. L. Shepard; and J. Hone. "Boron nitride substrates for high-quality graphene electronics." *Nature Nanotechnology* **5**, (2010) 722.

[65] J. M. Xue; J. Sanchez-Yamagishi; D. Bulmash; P. Jacquod; A. Deshpande; K. Watanabe; T. Taniguchi; P. Jarillo-Herrero; and B. J. LeRoy. "Scanning tunnelling microscopy and spectroscopy of ultra-flat graphene on hexagonal boron nitride." *Nature Materials* **10**, (2011) 282.

[66] P. A. Denis. "Band gap opening of monolayer and bilayer graphene doped with aluminium, silicon, phosphorus, and sulfur." *Chemical Physics Letters* **492**, (2010) 251.

[67] L. Pisani; B. Montanari; and N. M. Harrison. "A defective graphene phase predicted to be a room temperature ferromagnetic semiconductor." *New Journal of Physics* **10**.

[68] M. Y. Han; B. Özyilmaz; Y. Zhang; and P. Kim. "Energy band-gap engineering of graphene nanoribbons." *Physical Review Letters* **98**, (2007) 206805.

[69] E. V. Castro; K. S. Novoselov; S. V. Morozov; N. M. R. Peres; J. M. B. L. Dos Santos; J. Nilsson; F. Guinea; A. K. Geim; and A. H. Castro Neto. "Biased bilayer graphene: Semiconductor with a gap tunable by the electric field effect." *Physical Review Letters* **99**, (2007) 8.

[70] J. M. B. Lopes Dos Santos; N. M. R. Peres; and A. H. Castro Neto. "Graphene bilayer with a twist: Electronic structure." *Physical Review Letters* **99**, (2007) 19.

[71] Y. Zhang; T.-T. Tang; C. Girit; Z. Hao; M. C. Martin; A. Zettl; M. F. Crommie; Y. R. Shen; and F. Wang. "Direct observation of a widely tunable bandgap in bilayer graphene." *Nature* **459**, (2009) 820.

[72] M. C. Lemme; T. J. Echtermeyer; M. Baus; and H. Kurz. "A Graphene Field-Effect Device." *IEEE Electron Device Letters* **28**, (2007) 282.

[73] J. Kedzierski; P.-L. Hsu; P. Healey; P. W. Wyatt; C. L. Keast; M. Sprinkle; C. Berger; and W. A. de Heer. "Epitaxial graphene transistors on SiC substrates." *IEEE Transactions on Electron Devices* **55**, (2008) 2078.

[74] I. Meric; A. F. Han; B. O. Young; P. Kim; and K. L. Shepard. "Current saturation in zero-bandgap, top-gated graphene field-effect transistors." *Nature Nanotechnology* **3**, (2008) 654.

[75] Y. Wu; K. A. Jenkins; A. Valdes-Garcia; D. B. Farmer; Y. Zhu; A. A. Bol; C. Dimitrakopoulos; W. Zhu; F. Xia; P. Avouris; and Y.-M. Lin. "State-of-the-art graphene high-frequency electronics." *Nano Letters* **12**, (2012) 3062.

[76] G. Fiori and G. Iannaccone. "Ultralow-voltage bilayer graphene tunnel FET." *IEEE Electron Device Letters* **30**, (2009) 1096.

[77] S. K. Banerjee; L. F. Register; E. Tutuc; D. Reddy; and A. H. MacDonald. "Bilayer pseudospin field-effect transistor (BiSFET): A proposed new logic device." *IEEE Electron Device Letters* **30**, (2009) 158.

[78] E. Gibney. "2D or not 2D?" *Nature* **522**, (2015) 274.

[79] Q. Peng; A. K. Dearden; J. Crean; L. Han; S. Liu; X. Wen; and S. De. "New materials graphyne, graphdiyne, graphone, and graphane: Review of properties, synthesis, and application in nanotechnology." *Nanotechnology, Science and Applications* **7**, (2014) 1.

[80] B. G. Kim and H. J. Choi. "Graphyne: Hexagonal network of carbon with versatile Dirac cones." *Physical Review B* **86**, (2012) 115435.

[81] G. Wang; M. Si; A. Kumar; and R. Pandey. "Strain engineering of Dirac cones in graphyne." *Applied Physics Letters* **104**, (2014) 213107.

[82] D. Malko; C. Neiss; F. Viñes; and A. Görling. "Competition for graphene: Graphynes with direction-dependent Dirac cones." *Physical Review Letters* **108**, (2012) 086804.

[83] M. Long; L. Tang; D. Wang; Y. Li; and Z. Shuai. "Electronic structure and carrier mobility in graphdiyne sheet and nanoribbons: Theoretical predictions." *ACS Nano* **5**, (2011) 2593.

[84] H.-J. Cui; X.-L. Sheng; Q.-B. Yan; Q.-R. Zheng; and G. Su. "Strain-induced Dirac cone-like electronic structures and semiconductor-semimetal transition in graphdiyne." *Physical Chemistry Chemical Physics* **15**, (2013) 8179.

[85] X. Niu; X. Mao; D. Yang; Z. Zhang; M. Si; and D. Xue. "Dirac cone in α-graphdiyne : A first-principles study." *Nanoscale Research Letters* **8**, (2013) 469.

[86] G. Fiori; S. Lebégue; A. Betti; P. Michetti; M. Klintenberg; O. Eriksson; and G. Iannaccone. "Simulation of hydrogenated graphene field-effect transistors through a multiscale approach." *Physical Review B* **82**, (2010) 153404.

[87] A. Thomas; A. Fischer; F. Goettmann; M. Antonietti; J.-O. Müller; R. Schlögl; and J. M. Carlsson. "Graphitic carbon nitride materials: variation of structure and morphology and their use as metal-free catalysts." *Journal of Materials Chemistry* **18**, (2008) 4893.

[88] X. Wang; K. Maeda; A. Thomas; K. Takanabe; G. Xin; J. M. Carlsson; K. Domen; and M. Antonietti. "A metal-free polymeric photocatalyst for hydrogen production from water under visible light." *Nature Materials* **8**, (2009) 76.

[89] A. Du; S. Sanvito; Z. Li; D. Wang; Y. Jiao; T. Liao; Q. Sun; Y. H. Ng; Z. Zhu; R. Amal; and S. C. Smith. "Hybrid graphene and graphitic carbon nitride nanocomposite: Gap opening, electron–hole puddle, interfacial charge transfer, and enhanced visible light response." *Journal of the American Chemical Society* **134**, (2012) 4393.

[90] A. Beal; H. Hughes; and W. Liang. "The reflectivity spectra of some group VA transition metal dichalcogenides." *Journal of Physics C: Solid State Physics* **8**, (1975) 4236.

[91] J. Wilson; F. D. Salvo; and S. Mahajan. "Charge-density waves and superlattices in the metallic layered transition metal dichalcogenides." *Advances in Physics* **24**, (1975) 117.

[92] F. Xia; H. Wang; D. Xiao; M. Dubey; and A. Ramasubramaniam. "Two-dimensional material nanophotonics." *Nature Photonics* **8**, (2014) 899.

[93] H. Yu; G.-B. Liu; P. Gong; X. Xu; and W. Yao. "Dirac cones and Dirac saddle points of bright excitons in monolayer transition metal dichalcogenides." *Nature Communications* **5**, (2014) 3876.

[94] L. Ci; L. Song; C. Jin; D. Jariwala; D. Wu; Y. Li; A. Srivastava; Z. F. Wang; K. Storr; L. Balicas; F. Liu; and P. M. Ajayan. "Atomic layers of hybridized boron nitride and graphene domains." *Nature Materials* **9**, (2010) 430.

[95] K. Takeda and K. Shiraishi. "Theoretical possibility of stage corrugation in Si and Ge analogs of graphite." *Physical Review B* **50**, (1994) 14916.

[96] S. Nagase and M. Aoki. "Hexasilabenzene (Si_6H_6). An ab initio theoretical study of its aromaticity and relative stability." *Journal of the Chemical Society, Chemical Communications* , (1985) 1121.

[97] D. A. Clabo and H. F. Schaefer. "The silicon analog of benzene hexasilabenzene (Si_6H_6)." *The Journal of Chemical Physics* **84**, (1986) 1664.

[98] R. W. G. Wyckoff. *Crystal Structures Vol. 1*, (Interscience New York 1960).

[99] S. Cahangirov; M. Topsakal; E. Aktürk; H. ahin; and S. Ciraci. "Two- and one-dimensional honeycomb structures of silicon and germanium." *Physical Review Letters* **102**, (2009) 236804.

[100] C.-C. Liu; H. Jiang; and Y. Yao. "Low-energy effective Hamiltonian involving spin-orbit coupling in silicene and two-dimensional germanium and tin." *Physical Review B* **84**, (2011) 195430.

[101] H. Nakano; T. Mitsuoka; M. Harada; K. Horibuchi; H. Nozaki; N. Takahashi; T. Nonaka; Y. Seno; and H. Nakamura. "Soft synthesis of single-crystal silicon monolayer sheets." *Angewandte Chemie* **45**, (2006) 6303.

[102] M. R. Tchalala; M. A. Ali; H. Enriquez; A. Kara; A. Lachgar; S. Yagoubi; E. Foy; E. Vega; A. Bendounan; M. G. Silly; F. Sirotti; S. Nitshe; D. Chaudanson; H. Jamgotchian; B. Aufray; A. J. Mayne; G. Dujardin; and H. Oughaddou. "Silicon sheets by redox assisted chemical exfoliation." *Journal of Physics: Condensed Matter* **25**, (2013) 442001.

[103] E. Noguchi; K. Sugawara; R. Yaokawa; T. Hitosugi; H. Nakano; and T. Takahashi. "Direct observation of Dirac cone in multilayer silicene intercalation compound $CaSi_2$." *Advanced Materials* **27**, (2015) 856.

[104] N. D. Drummond; V. Zólyomi; and V. I. Fal'ko. "Electrically tunable band gap in silicene." *Physical Review B* **85**, (2012) 075423.

[105] Z. Ni; Q. Liu; K. Tang; J. Zheng; J. Zhou; R. Qin; Z. Gao; D. Yu; and J. Lu. "Tunable bandgap in silicene and germanene." *Nano Letters* **12**, (2012) 113.

[106] W.-F. Tsai; C.-Y. Huang; T.-R. Chang; H. Lin; H.-T. Jeng; and A. Bansil. "Gated silicene as a tunable source of nearly 100% spin-polarized electrons." *Nature Communications* **4**, (2013) 1500.

[107] C. L. Kane and E. J. Mele. "Quantum spin Hall effect in graphene." *Physical Review Letters* **95**, (2005) 226801.

[108] C.-C. Liu; W. Feng; and Y. Yao. "Quantum spin Hall effect in silicene and two-dimensional germanium." *Physical Review Letters* **107**, (2011) 076802.

[109] X. Lin and J. Ni. "Much stronger binding of metal adatoms to silicene than to graphene: A first-principles study." *Physical Review B* **86**, (2012) 075440.

[110] L. C. Lew Yan Voon; E. Sandberg; R. S. Aga; and A. A. Farajian. "Hydrogen compounds of group-IV nanosheets." *Applied Physics Letters* **97**, (2010) 163114.

[111] V. Zólyomi; J. R. Wallbank; and V. I. Fal'ko. "Silicane and germanane: tight-binding and first-principles studies." *2D Materials* **1**, (2014) 011005.

[112] W.-B. Zhang; Z.-B. Song; and L.-M. Dou. "The tunable electronic structure and mechanical properties of halogenated silicene: A first-principles study." *Journal of Materials Chemistry C* **3**, (2015) 3087.

[113] Y. Ding and Y. Wang. "Electronic structures of silicene fluoride and hydride." *Applied Physics Letters* **100**, (2012) 083102.

[114] X. Wang; H. Liu; and S.-T. Tu. "First-principles study of half-fluorinated silicene sheets." *RSC Advances* **5**, (2015) 6238.

[115] T. H. Osborn and A. A. Farajian. "Stability of lithiated silicene from first principles." *Journal of Physical Chemistry C* **116**, (2012) 22916.

[116] C. Kamal; A. Chakrabarti; A. Banerjee; and S. K. Deb. "Silicene beyond mono-layers–different stacking configurations and their properties." *Journal of Physics: Condensed Matter* **25**, (2013) 085508.

[117] J. Liu and W. Zhang. "Bilayer silicene with an electrically-tunable wide band gap." *RSC Advances* **3**, (2013) 21943.

[118] N. W. Johnson; D. Muir; E. Z. Kurmaev; and A. Moewes. "Stability and electronic characteristics of epitaxial silicene multilayers on Ag(111)." *Advanced Functional Materials* **25**, (2015) 4083.

[119] B. Mohan; A. Kumar; and P. K. Ahluwalia. "A first principle calculation of electronic and dielectric properties of electrically gated low-buckled mono and bilayer silicene." *Physica E: Low-Dimensional Systems and Nanostructures* **53**, (2013) 233.

[120] M. Hansen and K. Anderko. *Metallurgy and Metallurgical Engineering Series: Constitution of Binary Alloys.*, (McGraw-Hill 1958). ISBN 0070260508.

[121] B. Aufray; A. Kara; S. Vizzini; H. Oughaddou; C. Leandri; B. Ealet; and G. Le Lay. "Graphene-like silicon nanoribbons on Ag (110): A possible formation of silicene." *Applied Physics Letters* **96**, (2010) 183102.

[122] B. Lalmi; H. Oughaddou; H. Enriquez; A. Kara; Ś. Vizzini; B. Ealet; and B. Aufray. "Epitaxial growth of a silicene sheet." *Applied Physics Letters* **97**, (2010) 31.

[123] P. De Padova; C. Quaresima; C. Ottaviani; P. M. Sheverdyaeva; P. Moras; C. Carbone; D. Topwal; B. Olivieri; A. Kara; H. Oughaddou *et al.* "Evidence of graphene-like electronic signature in silicene nanoribbons." *Applied Physics Letters* **96**, (2010) 261905.

[124] S. Colonna; G. Serrano; P. Gori; A. Cricenti; and F. Ronci. "Systematic STM and LEED investigation of the Si/Ag(110) surface." *Journal of Physics: Condensed Matter* **25**, (2013) 315301.

[125] G. Le Lay; B. Aufray; C. Léandri; H. Oughaddou; J.-P. Biberian; P. De Padova; M. Dávila; B. Ealet; and A. Kara. "Physics and chemistry of silicene nano-ribbons." *Applied Surface Science* **256**, (2009) 524.

[126] A. Sekiguchi; M. Ichinohe; and R. Kinjo. "The chemistry of disilyne with a genuine Si-Si triple bond: Synthesis, structure, and reactivity." *Bulletin of the Chemical Society of Japan* **79**, (2006) 825.

[127] P. Vogt; P. De Padova; C. Quaresima; J. Avila; E. Frantzeskakis; M. Asensio; A. Resta; B. Ealet; and G. Le Lay. "Silicene: Compelling experimental evidence for graphenelike two-dimensional silicon." *Physical Review Letters* **108**, (2012) 155501.

[128] E. L. Shirley; L. J. Terminello; A. Santoni; and F. J. Himpsel. "Brillouin-zone-selection effects in graphite photoelectron angular distributions." *Physical Review B* **51**, (1995) 13614.

[129] K. R. Knox; S. Wang; A. Morgante; D. Cvetko; A. Locatelli; T. O. Mentes; M. A. Niño; P. Kim; and R. M. Osgood. "Spectromicroscopy of single and multilayer graphene supported by a weakly interacting substrate." *Physical Review B* **78**, (2008) 201408(R).

[130] C.-L. Lin; R. Arafune; K. Kawahara; M. Kanno; N. Tsukahara; E. Minamitani; Y. Kim; M. Kawai; and N. Takagi. "Substrate-induced symmetry breaking in silicene." *Physical Review Letters* **110**, (2013) 076801.

[131] D. Tsoutsou; E. Xenogiannopoulou; E. Golias; P. Tsipas; and A. Dimoulas. "Evidence for hybrid surface metallic band in (4×4) silicene on Ag(111)." *Applied Physics Letters* **103**, (2013) 231604.

[132] S. Cahangirov; M. Audiffred; P. Tang; A. Iacomino; W. Duan; G. Merino; and A. Rubio. "Electronic structure of silicene on Ag(111): Strong hybridization effects." *Physical Review B* **88**, (2013) 035432.

[133] Z.-X. Guo; S. Furuya; J.-I. Iwata; and A. Oshiyama. "Absence and presence of Dirac electrons in silicene on substrates." *Physical Review B* **87**, (2013) 235435.

[134] S. Huang; W. Kang; and L. Yang. "Electronic structure and quasiparticle bandgap of silicene structures." *Applied Physics Letters* **102**, (2013) 133106.

[135] J. Avila; P. D. Padova; S. Cho; I. Colambo; S. Lorcy; C. Quaresima; P. Vogt; A. Resta; G. Le Lay; and M. C. Asensio. "Presence of gapped silicene-derived band in the prototypical (3×3) silicene phase on silver (111) surfaces." *Journal of Physics: Condensed Matter* **25**, (2013) 262001.

[136] N. W. Johnson; P. Vogt; A. Resta; P. De Padova; I. Perez; D. Muir; E. Z. Kurmaev; G. Le Lay; and A. Moewes. "The metallic nature of epitaxial silicene monolayers on Ag(111)." *Advanced Functional Materials* **24**, (2014) 5253.

[137] H. Jamgotchian; Y. Colignon; N. Hamzaoui; B. Ealet; J. Y. Hoarau; B. Aufray; and J. P. Bibérian. "Growth of silicene layers on Ag(111): unexpected effect of the substrate temperature." *Journal of Physics: Condensed Matter* **24**, (2012) 172001.

[138] J. Gao and J. Zhao. "Initial geometries, interaction mechanism and high stability of silicene on Ag(111) surface." *Scientific Reports* **2**, (2012) 861.

[139] R. Arafune; C.-L. Lin; K. Kawahara; N. Tsukahara; E. Minamitani; Y. Kim; N. Takagi; and M. Kawai. "Structural transition of silicene on Ag(111)." *Surface Science* **608**, (2013) 297.

[140] Y. Du; J. Zhuang; H. Liu; X. Xu; S. Eilers; K. Wu; P. Cheng; and J. Zhao. "Tuning the Band Gap in Silicene by Oxidation." *ACS Nano* **8**, (2014) 10019.

[141] X. Xu; J. Zhuang; Y. Du; H. Feng; N. Zhang; C. Liu; T. Lei; J. Wang; M. Spencer; T. Morishita; X. Wang; and S. X. Dou. "Effects of oxygen adsorption on the surface state of epitaxial silicene on Ag(111)." *Scientific Reports* **4**, (2014) 7543.

[142] N. W. Johnson; D. I. Muir; and A. Moewes. "Oxidized monolayers of epitaxial silicene on Ag(111)." *Scientific Reports* **6**, (2016) 22510.

[143] L. Chen; H. Li; B. Feng; Z. Ding; J. Qiu; P. Cheng; K. Wu; and S. Meng. "Spontaneous symmetry breaking and dynamic phase transition in monolayer silicene." *Physical Review Letters* **110**, (2013) 085504.

[144] L. Chen; C.-C. Liu; B. Feng; X. He; P. Cheng; Z. Ding; S. Meng; Y. Yao; and K. Wu. "Evidence for Dirac fermions in a honeycomb lattice based on silicon." *Physical Review Letters* **109**, (2012) 056804.

[145] B. Feng; H. Li; C. C. Liu; T. N. Shao; P. Cheng; Y. Yao; S. Meng; L. Chen; and K. Wu. "Observation of Dirac cone warping and chirality effects in silicene." *ACS Nano* **7**, (2013) 9049.

[146] E. Salomon; R. El Ajjouri; G. L. Lay; and T. Angot. "Growth and structural properties of silicene at multilayer coverage." *Journal of Physics: Condensed Matter* **26**, (2014) 185003.

[147] P. De Padova; O. Kubo; B. Olivieri; C. Quaresima; T. Nakayama; M. Aono; and G. Le Lay. "Multilayer silicene nanoribbons." *Nano Letters* **12**, (2012) 5500.

[148] P. De Padova; J. Avila; A. Resta; I. Razado-Colambo; C. Quaresima; C. Ottaviani; B. Olivieri; T. Bruhn; P. Vogt; M. C. Asensio; and G. Le Lay. "The quasiparticle band dispersion in epitaxial multilayer silicene." *Journal of Physics: Condensed Matter* **25**, (2013) 382202.

[149] P. De Padova; C. Ottaviani; C. Quaresima; B. Olivieri; P. Imperatori; E. Salomon; T. Angot; L. Quagliano; C. Romano; A. Vona; M. Muniz-Miranda; A. Generosi; B. Paci; and G. Le Lay. "24 h stability of thick multilayer silicene in air." *2D Materials* **1**, (2014) 021003.

[150] A. Resta; T. Leoni; C. Barth; A. Ranguis; C. Becker; T. Bruhn; P. Vogt; and G. Le Lay. "Atomic structures of silicene layers grown on Ag(111): scanning tunneling microscopy and noncontact atomic force microscopy observations." *Scientific Reports* **3**, (2013) 2399.

[151] Z.-X. Guo and A. Oshiyama. "Structural tristability and deep Dirac states in bilayer silicene on Ag(111) surfaces." *Physical Review B* **89**, (2014) 155418.

[152] A. Acun; B. Poelsema; H. J. W. Zandvliet; and R. Van Gastel. "The instability of silicene on Ag(111)." *Applied Physics Letters* **103**, (2013) 263119.

[153] T. Shirai; T. Shirasawa; T. Hirahara; N. Fukui; T. Takahashi; and S. Hasegawa. "Structure determination of multilayer silicene grown on Ag(111) films by electron diffraction: Evidence for Ag segregation at the surface." *Physical Review B* **89**, (2014) 241403(R).

[154] A. J. Mannix; B. Kiraly; B. L. Fisher; M. C. Hersam; and N. P. Guisinger. "Silicon growth at the two-dimensional limit on Ag(111)." *ACS Nano* **8**, (2014) 7538.

[155] W. O. Filtvedt; A. Holt; P. A. Ramachandran; and M. C. Melaaen. "Chemical vapor deposition of silicon from silane: Review of growth mechanisms and modeling/scaleup of fluidized bed reactors." *Solar Energy Materials and Solar Cells* **107**, (2012) 188.

[156] T. R. Hogness; T. L. Wilson; and W. C. Johnson. "The thermal decomposition of silane." *Journal of the American Chemical Society* **58**, (1936) 108.

[157] S. P. Walch and C. E. Dateo. "Thermal decomposition pathways and rates for silane, chlorosilane, dichlorosilane, and trichlorosilane." *The Journal of Physical Chemistry A* **105**, (2001) 2015.

[158] M. Laue. "Eine quantitative Prüfung der Theorie für die Interferenzerscheinungen bei Röntgenstrahlen." *Annalen der Physik* **346**, (1913) 989.

[159] S. Nagano and S. Y. Tong. "Multiple-scattering theory of low-energy electron diffraction for a nonspherical scattering potential." *Physical Review B* **32**, (1985) 6562.

[160] F. J. Giessibl. "Advances in atomic force microscopy." *Reviews of Modern Physics* **75**, (2003) 949.

[161] J. Tersoff and D. R. Hamann. "Theory of the scanning tunneling microscope." *Physical Review B* **31**, (1985) 805.

[162] D. Kaltsas; L. Tsetseris; and A. Dimoulas. "Silicene on metal substrates: A first-principles study on the emergence of a hierarchy of honeycomb structures." *Applied Surface Science* **291**, (2014) 93.

[163] D. Ceperley. *Recent Progress in Many-Body Theories, Volume 4*, (Springer US 1995). ISBN 1461519379.

[164] P. Hohenberg and W. Kohn. "Inhomogeneous Electron Gas." *Phys. Rev.* **136**, (1964) B864.

[165] M. Levy. "Universal variational functionals of electron densities, first-order density matrices, and natural spin-orbitals and solution of the v-representability problem." *Proceedings of the National Academy of Sciences* **76**, (1979) 6062.

[166] L. H. Thomas. "The calculation of atomic fields." *Mathematical Proceedings of the Cambridge Philosophical Society* **23**, (1927) 542.

[167] E. Fermi. "Un metodo statistico per la determinazione di alcune priorieta dellatome." *Rendiconti Accademia Nazionale Lincei* **6**, (1927) 32.

[168] T. Koopmans. "Über die Zuordnung von Wellenfunktionen und Eigenwerten zu den Einzelnen Elektronen Eines Atoms." *Physica* **1**, (1934) 104.

[169] M. F. Bloch. "Bemerkung zur Elektronentheorie des Ferromagnetismus und der elektrischen Leitfähigkeit." *Zeitschrift für Physik* **57**, (1929) 545.

[170] D. M. Ceperley and B. J. Alder. "Ground state of the electron gas by a stochastic method." *Physical Review Letters* **45**, (1980) 566.

[171] J. P. Perdew; K. Burke; and M. Ernzerhof. "Generalized Gradient Approximation Made Simple." *Physical Review Letters* **77**, (1996) 3865.

[172] J. P. Perdew. "Density functional theory and the band gap problem." *International Journal of Quantum Chemistry* **28**, (1985) 497.

[173] A. D. Becke and E. R. Johnson. "A simple effective potential for exchange." *The Journal of Chemical Physics* **124**, 221101.

[174] F. Tran and P. Blaha. "Accurate band gaps of semiconductors and insulators with a semilocal exchange-correlation potential." *Physical Review Letters* **102**, (2009) 226401.

[175] N. W. Johnson; J. A. McLeod; and A. Moewes. "The electronic structure of lithium metagallate." *Journal of Physics: Condensed Matter* **23**, (2011) 445501.

[176] F. Hintze; N. W. Johnson; M. Seibald; D. Muir; A. Moewes; and W. Schnick. "Magnesium double nitride Mg_3GaN_3 as new host lattice for Eu^{2+} doping: synthesis, structural studies, luminescence, and band-gap determination." *Chemistry of Materials* **25**, (2013) 4044.

[177] P. Blaha; K. Schwarz; G. K. H. Madsen; D. Kvasnicka; and J. Luitz. *WIEN2k, An Augmented Plane Wave + Local Orbitals Program for Calculating Crystal Properties*, (Karlheinz Schwarz, Techn. Universitat Wien, Austria 2001). ISBN 3950103112.

[178] L. Pollack and J. P. Perdew. "Evaluating density functional performance for the quasi-two-dimensional electron gas." *Journal Of Physics: Condensed Matter* **12**, (2000) 1239.

[179] H. J. Monkhorst and J. D. Pack. "Special points for Brillouin-zone integrations." *Physical Review B* **13**, (1976) 5188.

[180] H. Hellmann. *Einführung in die Quantenchemie*, (Leipzig und Wien : F. Deuticke 1937).

[181] R. P. Feynman. "Forces in molecules." *Phys. Rev.* **56**, (1939) 340.

[182] B. Kohler; S. Wilke; M. Scheffler; R. Kouba; and C. Ambrosch-Draxl. "Force calculation and atomic-structure optimization for the full-potential linearized augmented plane-wave code WIEN." *Computer Physics Communications* **94**, (1996) 31.

[183] R. Yu; D. Singh; and H. Krakauer. "All-electron and pseudopotential force calculations using the linearized-augmented-plane-wave method." *Physical Review B* **43**, (1991) 6411.

[184] G. Madsen; P. Blaha; K. Schwarz; E. Sjöstedt; and L. Nordström. "Efficient linearization of the augmented plane-wave method." *Physical Review B* **64**, (2001) 195134.

[185] K.-J. Kim. "Characteristics of synchrotron radiation." *AIP Conference Proceedings* **184**, (1989) 565.

[186] G. B. Rybicki and A. P. Lightman. *Radiative Processes in Astrophysics*, (John Wiley & Sons 2008).

[187] K. Halbach. "Permanent magnet undulators." *Le Journal de Physique Colloques* **44**, (1983) C1.

[188] G. Brown; K. Halbach; J. Harris; and H. Winick. "Wiggler and undulator magnets - A review." *Nuclear Instruments and Methods in Physics Research* **208**, (1983) 65.

[189] H. Winick; G. Brown; K. Halbach; and J. Harris. "Wiggler and undulator magnets." *Physics Today* **34**, (1981) 50.

[190] "REIXS website." `http://www.lightsource.ca/beamlines/reixs.php`. Accessed: 2016-01-30.

[191] "Beamline 8.0.1 website." `https://www-als.lbl.gov/index.php/ring-leaders/115-801.html`. Accessed: 2016-01-30.

[192] J. J. Jia; T. A. Callcott; J. Yurkas; A. W. Ellis; F. J. Himpsel; M. G. Samant; J. Stöhr; D. L. Ederer; J. A. Carlisle; E. A. Hudson; L. J. Terminello; D. K. Shuh; and R. C. C. Perera. "First experimental results from IBM/TENN/TULANE/LLNL/LBL undulator beamline at the advanced light source." *Review of Scientific Instruments* **66**, (1995) 1394.

[193] A. J. Achkar. "Inverse partial fluorescence yield spectroscopy." (M.Sc. Thesis, 2011).

[194] A. J. Achkar; T. Z. Regier; H. Wadati; Y. J. Kim; H. Zhang; and D. G. Hawthorn. "Bulk sensitive x-ray absorption spectroscopy free of self-absorption effects." *Physical Review B* **83**, (2011) 081106(R).

[195] G. P. Williams. *X-ray Data Booklet: Electron Binding Energies*, (Lawrence Berkeley National Laboratory 2009).

[196] S. Dick and G. Oehlinger. "Crystal structure of calciumdisilicide, 3R-$CaSi_2$." *Zeitschrift für Kristallographie-New Crystal Structures* **213**, (1998) 246.

[197] B. L. Henke; E. M. Gullikson; and J. C. Davis. "X-ray interactions: photoabsorption, scattering, transmission, and reflection at E= 50-30,000 eV, Z= 1-92." *Atomic Data and Nuclear Data Tables* **54**, (1993) 181.

[198] M. O. Krause and J. Oliver. "Natural widths of atomic K and L levels, Kα X-ray lines and several KLL Auger lines." *Journal of Physical and Chemical Reference Data* **8**, (1979) 329.

[199] D. A. Goodings and R. Harris. "Calculations of the X-ray emission bands of copper using augmented plane wave Bloch functions." *Journal of Physics C: Solid State Physics* **2**, (1969) 1808.

[200] G. G. Guzmán-Verri and L. C. Lew Yan Voon. "Electronic structure of silicon-based nanostructures." *Physical Review B* **76**, (2007) 075131.

[201] Q. Tang and Z. Zhou. "Graphene-analogous low-dimensional materials." *Progress in Materials Science* **58**, (2013) 1244.

[202] D. Chiappe; C. Grazianetti; G. Tallarida; M. Fanciulli; and A. Molle. "Local electronic properties of corrugated silicene phases." *Advanced Materials* **24**, (2012) 5088.

[203] L. Meng; Y. Wang; L. Zhang; S. Du; R. Wu; L. Li; Y. Zhang; G. Li; H. Zhou; W. A. Hofer; and H.-J. Gao. "Buckled silicene formation on Ir(111)." *Nano Letters* **13**, (2013) 685.

[204] A. Fleurence; R. Friedlein; T. Ozaki; H. Kawai; Y. Wang; and Y. Yamada-Takamura. "Experimental evidence for epitaxial silicene on diboride thin films." *Physical Review Letters* **108**, (2012) 245501.

[205] T. P. Kaloni; M. Tahir; and U. Schwingenschlögl. "Quasi free-standing silicene in a superlattice with hexagonal boron nitride." *Scientific Reports* **3**, (2013) 3192.

[206] L. Li; X. Wang; X. Zhao; and M. Zhao. "Moiré superstructures of silicene on hexagonal boron nitride: A first-principles study." *Physics Letters A* **377**, (2013) 2628.

[207] B. Kiraly; E. V. Iski; A. J. Mannix; B. L. Fisher; M. C. Hersam; and N. P. Guisinger. "Solid-source growth and atomic-scale characterization of graphene on Ag (111)." *Nature Communications* **4**, (2013) 2804.

[208] B. Feng; Z. Ding; S. Meng; Y. Yao; X. He; P. Cheng; L. Chen; and K. Wu. "Evidence of silicene in honeycomb structures of silicon on Ag (111)." *Nano Letters* **12**, (2012) 3507.

[209] H. Enriquez; A. Kara; B. Lalmi; H. Oughaddou *et al.* "Silicene structures on silver surfaces." *Journal of Physics: Condensed Matter* **24**, (2012) 314211.

[210] D. Kaltsas; L. Tsetseris; and A. Dimoulas. "Structural evolution of single-layer films during deposition of silicon on silver: a first-principles study." *Journal of Physics: Condensed Matter* **24**, (2012) 442001.

[211] E. Cinquanta; E. Scalise; D. Chiappe; C. Grazianetti; B. van den Broek; M. Houssa; M. Fanciulli; and A. Molle. "Getting through the nature of silicene: An sp^2–sp^3 two-dimensional silicon nanosheet." *The Journal of Physical Chemistry C* **117**, (2013) 16719.

[212] A. Moewes; E. Z. Kurmaev; J. S. Tse; M. Geshi; M. J. Ferguson; V. A. Trofimova; and Y. M. Yarmoshenko. "Electronic structure of alkali-metal-doped M_8Si_{46} ($M = \mathrm{Na}, \mathrm{K}$) clathrates." *Physical Review B* **65**, (2002) 153106.

[213] K. Schwarz; A. Neckel; and J. Nordgren. "On the X-ray emission spectra from FeAl." *Journal of Physics F: Metal Physics* **9**, (1979) 2509.

[214] P. De Padova; P. Vogt; A. Resta; J. Avila; I. Razado-Colambo; C. Quaresima; C. Ottaviani; B. Olivieri; T. Bruhn; T. Hirahara; T. Shirai; S. Hasegawa; M. Carmen Asensio; and G. Le Lay. "Evidence of Dirac fermions in multilayer silicene." *Applied Physics Letters* **102**, 163106.

[215] P. Vogt; P. Capiod; M. Berthe; A. Resta; P. De Padova; T. Bruhn; G. Le Lay; and B. Grandidier. "Synthesis and electrical conductivity of multilayer silicene." *Applied Physics Letters* **104**, (2014) 021602.

[216] A. Kara; H. Enriquez; A. P. Seitsonen; L. L. Y. Voon; S. Vizzini; B. Aufray; and H. Oughaddou. "A review on silicene – new candidate for electronics." *Surface Science Reports* **67**, (2012) 1.

[217] A. Podsiadły-Paszkowska and M. Krawiec. "Dirac fermions in silicene on Pb (111) surface." *Physical Chemistry Chemical Physics* **17**, (2015) 2246.

[218] Y. Yuan; R. Quhe; J. Zheng; Y. Wang; Z. Ni; J. Shi; and J. Lu. "Strong band hybridization between silicene and Ag (111) substrate." *Physica E: Low-dimensional Systems and Nanostructures* **58**, (2014) 38.

[219] L. Tao; E. Cinquanta; D. Chiappe; C. Grazianetti; M. Fanciulli; M. Dubey; A. Molle; and D. Akinwande. "Silicene field-effect transistors operating at room temperature." *Nature Nanotechnology* **10**, (2015) 227.

[220] R. Wang; X. Pi; Z. Ni; Y. Liu; S. Lin; M. Xu; and D. Yang. "Silicene oxides: formation, structures and electronic properties." *Scientific Reports* **3**, (2013) 03507.

[221] G. Liu; X. Lei; M. Wu; B. Xu; and C. Ouyang. "Comparison of the stability of free-standing silicene and hydrogenated silicene in oxygen: a first principles investigation." *Journal of Physics: Condensed Matter* **26**, (2014) 355007.

[222] R. Mozzi and B. Warren. "The structure of vitreous silica." *Journal of Applied Crystallography* **2**, (1969) 164.

[223] L. A. Garvie; P. Rez; J. R. Alvarez; P. R. Buseck; A. J. Craven; and R. Brydson. "Bonding in alpha-quartz (SiO_2): A view of the unoccupied states." *American Mineralogist* **85**, (2000) 732.

[224] D. Li; G. Bancroft; M. Kasrai; M. Fleet; R. Secco; X. Feng; K. Tan; and B. Yang. "X-ray absorption spectroscopy of silicon dioxide (SiO_2) polymorphs; the structural characterization of opal." *American Mineralogist* **79**, (1994) 622.

[225] D. Chiappe; E. Scalise; E. Cinquanta; C. Grazianetti; B. Van Den Broek; M. Fanciulli; M. Houssa; and A. Molle. "Two-dimensional Si nanosheets with local hexagonal structure on a MoS_2 surface." *Advanced Materials* **26**, (2014) 2096.

[226] H. Liu; J. Gao; and J. Zhao. "Silicene on substrates: a way to preserve or tune its electronic properties." *The Journal of Physical Chemistry C* **117**, (2013) 10353.

[227] R. Stephan; M.-C. Hanf; and P. Sonnet. "Spatial analysis of interactions at the silicene/Ag interface: first principles study." *Journal of Physics: Condensed Matter* **27**, (2014) 015002.

[228] P. Moras; T. Mentes; P. Sheverdyaeva; A. Locatelli; and C. Carbone. "Coexistence of multiple silicene phases in silicon grown on Ag (111)." *Journal of Physics: Condensed Matter* **26**, (2014) 185001.

[229] W. A. Doolittle; S. Kang; T. J. Kropewnicki; S. Stock; P. A. Kohl; and A. S. Brown. "MBE growth of high quality GaN on $LiGaO_2$." *Journal of Electronic Materials* **27**, (1998) L58.

[230] K. Xu; P. Deng; J. Xu; G. Zhou; W. Liu; and Y. Tian. "Growth and characterization of $LiGaO_2$ substrate crystal for GaN epitaxy." *Journal of Crystal Growth* **216**, (2000) 343.

[231] M. M. Chou; C. Chen; D. Hang; and W.-T. Yang. "Growth of nonpolar m-plane GaN epitaxial film on a lattice-matched (100) β-$LiGaO_2$ substrate by chemical vapor deposition." *Thin Solid Films* **519**, (2011) 5066.

[232] M. M. Chou; D.-R. Hang; C. Chen; and Y.-H. Liao. "Epitaxial growth of nonpolar m-plane ZnO (10–10) on large-size $LiGaO_2$ (100) substrates." *Thin Solid Films* **519**, (2011) 3627.

[233] S. Liu; S. Zhou; Y. Wang; X. Zhang; X. Li; C. Xia; Y. Hang; and J. Xu. "Epitaxial growth of ZnO thin films on $LiGaO_2$ substrates by pulsed-laser deposition." *Journal of Crystal Growth* **292**, (2006) 125.

[234] S. Duan; X. Teng; P. Han; and D.-C. Lu. "Growth and characterization of GaN on $LiGaO_2$." *Journal of Crystal Growth* **195**, (1998) 304.

[235] O. Kryliouk; M. Reed; T. Dann; T. Anderson; and B. Chai. "Growth of GaN single crystal substrates." *Materials Science and Engineering: B* **59**, (1999) 6.

[236] W. A. Doolittle; S. Kang; and A. Brown. "{MBE} growth of high quality GaN on $LiGaO_2$ for high frequency, high power electronic applications." *Solid-State Electronics* **44**, (2000) 229.

[237] G. Li; S. Mu; and S.-J. Shih. "Achieving atomically flat surfaces for $LiGaO_2$ substrates for epitaxial growth of GaN films." *Materials Science and Engineering: B* **170**, (2010) 9.

[238] R. J. Matyi; W. A. Doolittle; and A. S. Brown. "High resolution x-ray diffraction analyses of GaN/$LiGaO_2$." *Journal of Physics D: Applied Physics* **32**, (1999) A61.

[239] P. Knoll and H. Kuzmany. "Nonlinear-optical properties and signs of the Raman tensor for $LiGaO_2$." *Physical Review B* **29**, (1984) 2221.

[240] H. Neumann. "Vibrational Properties of $LiGaO_2$ (II). Theoretical Model Considerations." *Crystal Research and Technology* **21**, (1986) 1361.

[241] S. Kammoun. "Crystal-Field Analysis of the $V3^+$ Excitation Spectrum in $LiGaO_2$ and $LiAlO_2$ Oxide Crystals." *physica status solidi (b)* **232**, (2002) 306.

[242] S. Kück and S. Hartung. "Comparative study of the spectroscopic properties of $Cr4^+$-doped $LiAlO_2$ and $LiGaO_2$." *Chemical Physics* **240**, (1999) 387.

[243] G. M. Kuz'micheva; V. B. Rybakov; A. V. Gaister; and E. V. Zharikov. "Structure and Properties of $LiGaO_2$ Crystals." *Inorganic Materials* **37**, (2001) 281.

[244] G. J. Dirksen; A. N. J. M. Hoffman; T. P. van de Bout; M. P. G. Laudy; and G. Blasse. "Luminescence spectra of pure and doped $GaBO_3$ and $LiGaO_2$." *Journal of Materials Chemistry* **1**, (1991) 1001.

[245] S. Weise and H. Neumann. "Thermal Analysis of $LiGaO_2$ and $NaGaO_2$." *Crystal Research and Technology* **31**, (1996) 659.

[246] C. Rawn and J. Chaudhuri. "High temperature X-ray diffraction study of $LiGaO_2$." *Journal of Crystal Growth* **225**, (2001) 214.

[247] C.-H. Shih; I. Lo; W.-Y. Pang; Y.-C. Wang; and M. M. Chou. "Characterization of M-plane GaN film grown on β-$LiGaO_2$ (100) by plasma-assisted molecular beam epitaxy." *Thin Solid Films* **519**, (2011) 3569.

[248] G. Li and H. Yang. "Epitaxial growth of high quality nonpolar InN films on $LiGaO_2$ substrates." *Crystal Growth & Design* **11**, (2011) 664.

[249] S. N. Rashkeev; S. Limpijumnong; and W. R. L. Lambrecht. "Theoretical evaluation of $LiGaO_2$ for frequency upconversion to ultraviolet." *Journal of the Optical Society of America B* **16**, (1999) 2217.

[250] T. Omata; K. Tanaka; A. Tazuke; K. Nose; and S. Otsuka-Yao-Matsuo. "Wide band gap semiconductor alloy: $x(LiGaO_2)_{1/2}$–$(1–x)$ZnO." *Journal of Applied Physics* **103**, 083706.

[251] T. Omata; K. Tanaka; A. Tazuke; K. Nose; and S. Otsuka-Yao-Matsuo. "Novel wide band gap alloyed semiconductors, $x(LiGaO_2)_{1/2}$–$(1–x)$ZnO, and fabrication of their thin films." *Science in China Series E: Technological Sciences* **52**, (2009) 111.

[252] P.-T. Chen; J. Downes; A. Fernandes; K. Butcher; M. Wintrebert-Fouquet; R. Wuhrer; and M. Phillips. "Effects of crystallinity and chemical variation on apparent band-gap shift in polycrystalline indium nitride." *Thin Solid Films* **519**, (2011) 1831.

[253] S. B. Limpijumnong S, Lambrecht W R L and K. K. *Materials Research Society Symposium Proceedings (San Francisco)*, volume 449, (Pittsburgh: Materials Research Society 1997).

[254] A. Boonchun and W. R. L. Lambrecht. "First-principles study of the elasticity, piezoelectricity, and vibrational modes in $LiGaO_2$ compared with ZnO and GaN." *Physical Review B* **81**, (2010) 235214.

[255] A. Boonchun and W. R. L. Lambrecht. "Achieving atomically flat surfaces for $LiGaO_2$ substrates for epitaxial growth of GaN films." *Proceedings of SPIE* **7940**, (2011) 79400N.

[256] J. Denlinger (2011). ALS beamline scientist, private communication.

[257] T. Regier; J. Krochak; T. Sham; Y. Hu; J. Thompson; and R. Blyth. "Performance and capabilities of the Canadian Dragon: The SGM beamline at the Canadian Light Source." *Nuclear Instruments and Methods in Physics Research Section A: Accelerators, Spectrometers, Detectors and Associated Equipment* **582**, (2007) 93.

[258] T. Regier; J. Paulsen; G. Wright; I. Coulthard; K. Tan; T. Sham; and R. Blyth. "Commissioning of the spherical grating monochromator soft X-ray spectroscopy beamline at the Canadian Light Source." *AIP Conference Proceedings* **879**, (2007) 473.

[259] M. Marezio. "The crystal structure of $LiGaO_2$." *Acta Crystallographica* **18**, (1965) 481.

[260] G. Giorgi and K. Yamashita. "Amphoteric behavior of Ge in GaAs: an LDA analysis." *Modelling and Simulation in Materials Science and Engineering* **19**, (2011) 035001.

[261] G. Wentzel. "Excitation potential of $K\alpha_{3,4}$ satellite lines: A case for astronomy." *Annalen der Physik (Leipzig)* **66**, (1921) 437.

[262] M. J. Druyvesteyn. "Das Röntgenspektrum zweiter Art." *Zeitschrift für Physik* **43**, (1927) 707.

[263] J. Valjakka; J. Utriainen; T. Åberg; and J. Tulkki. "Direction-dependent initial-state relaxation in oxygen K x-ray emission." *Physical Review B* **32**, (1985) 6892.

[264] E. Z. Kurmaev; R. G. Wilks; A. Moewes; L. D. Finkelstein; S. N. Shamin; and J. Kuneš. "Oxygen x-ray emission and absorption spectra as a probe of the electronic structure of strongly correlated oxides." *Physical Review B* **77**, (2008) 165127.

[265] J. A. McLeod; R. G. Wilks; N. A. Skorikov; L. D. Finkelstein; M. Abu-Samak; E. Z. Kurmaev; and A. Moewes. "Band gaps and electronic structure of alkaline-earth and post-transition-metal oxides." *Physical Review B* **81**, (2010) 245123.

[266] J. McLeod; R. Green; A. Moewes; N. A. Skorikov; L. D. Finkelstein; E. Z. Kurmaev; and M. Abu-Samak. "A valence structure of alkaline and post-transition metal oxides." *Proceedings of SPIE* **7940**, (2011) 79400R.

[267] J. T. Wolan and G. B. Hoflund. "Chemical alteration of the native oxide layer on $LiGaO_2(001)$ by exposure to hyperthermal atomic hydrogen." *Journal of Vacuum Science & Technology A* **16**, (1998) 3414.

[268] W. Wei; Y. Dai; B. Huang; M. H. Whangbo; and T. Jacob. "Loss of linear band dispersion and trigonal structure in silicene on Ir(111)." *Journal of Physical Chemistry Letters* **6**, (2015) 1065.

[269] A. J. Mannix; X.-F. Zhou; B. Kiraly; J. D. Wood; D. Alducin; B. D. Myers; X. Liu; B. L. Fisher; U. Santiago; J. R. Guest; M. J. Yacaman; A. Ponce; A. R. Oganov; M. C. Hersam; and N. P. Guisinger. "Synthesis of borophenes: Anisotropic, two-dimensional boron polymorphs." *Science* **350**, (2015) 1513.

[270] H. Liu; A. T. Neal; Z. Zhu; Z. Luo; X. Xu; D. Tomnek; and P. D. Ye. "Phosphorene: An unexplored 2D semiconductor with a high hole mobility." *ACS Nano* **8**, (2014) 4033. PMID: 24655084.

[271] S. Reich; J. Maultzsch; C. Thomsen; and P. Ordejón. "Tight-binding description of graphene." *Physical Review B* **66**, (2002) 035412.

[272] U. von Barth and G. Grossmann. "The effect of the core hole on X-ray emission spectra in simple metals." *Solid State Communications* **32**, (1979) 645.

[273] U. von Barth and G. Grossmann. "Dynamical effects in x-ray spectra and the final-state rule." *Physical Review B* **25**, (1982) 5150.

Appendix A

Tight-Binding Calculation for Graphene and the Dirac Cone

In this appendix, I will derive the Dirac cone electronic structure of graphene and silicene within the TB approximation and show that DFT calculations result in the same low-energy bandstructure. The TB derivation for graphene will for the most part follow the steps of Wallace [7]. However, the *nnn* interaction will be ignored for the sake of simplicity as its inclusion only results in an electron-hole asymmetry and a slight trigonal warping, but otherwise does not affect the low-energy dispersion in a significant way.

I will first begin with a basic description of the graphene unit cell, which is shown in Figure A.1(a). There are two equivalent C atoms per cell, commonly referred to as the A and B sites. These sites generate two equivalent triangular sublattices, the A and B sublattices, when taken over the whole of the crystal. The unit cell as shown is spanned by two basis vectors

$$\vec{a}_1 = \frac{d}{2}(3, \sqrt{3}) \qquad \vec{a}_2 = \frac{d}{2}(3, -\sqrt{3}) \tag{A.1}$$

where d defines the C-C *nn* distance, about 1.42 Å. Typically, the unit cell is defined such that the A site is located at the origin and the B site is located at the coordinates (2/3, 2/3), as in Figure A.1(a). The vectors joining the *nn* atoms to the A site at the origin of the unit cell are given by

$$\vec{\delta}_1 = \frac{d}{2}(1, \sqrt{3}) \qquad \vec{\delta}_2 = \frac{d}{2}(1, -\sqrt{3}) \qquad \vec{\delta}_3 = -d(1, 0) \tag{A.2}$$

By calculating the reciprocals of the direct lattice vectors, one can derive the triangular reciprocal lattice shown in Figure A.1(b), which has the basis vectors

$$\vec{b}_1 = \frac{2\pi}{3d}(1, \sqrt{3}) \qquad \vec{b}_2 = \frac{2\pi}{3d}(1, -\sqrt{3}) \tag{A.3}$$

Following the usual method of connecting an arbitrary reciprocal lattice point to all its nearest neighbours and bisecting them with perpendicular lines, the Brillouin zone is found to be hexagonal, also shown in Figure A.1(b). The notable high-symmetry k-points in this Brillouin zone are labelled. Taking into account that any two points which can be connected by a sum of integer multiples of $\vec{b}_1$ and $\vec{b}_2$ are equivalent, there are two unique Brillouin zone corners (K and K') that will become important later in this derivation and have coordinates of

$$K = \frac{2\pi}{3d}(1, \frac{1}{\sqrt{3}}) \qquad K' = \frac{2\pi}{3d}(1, -\frac{1}{\sqrt{3}}). \tag{A.4}$$

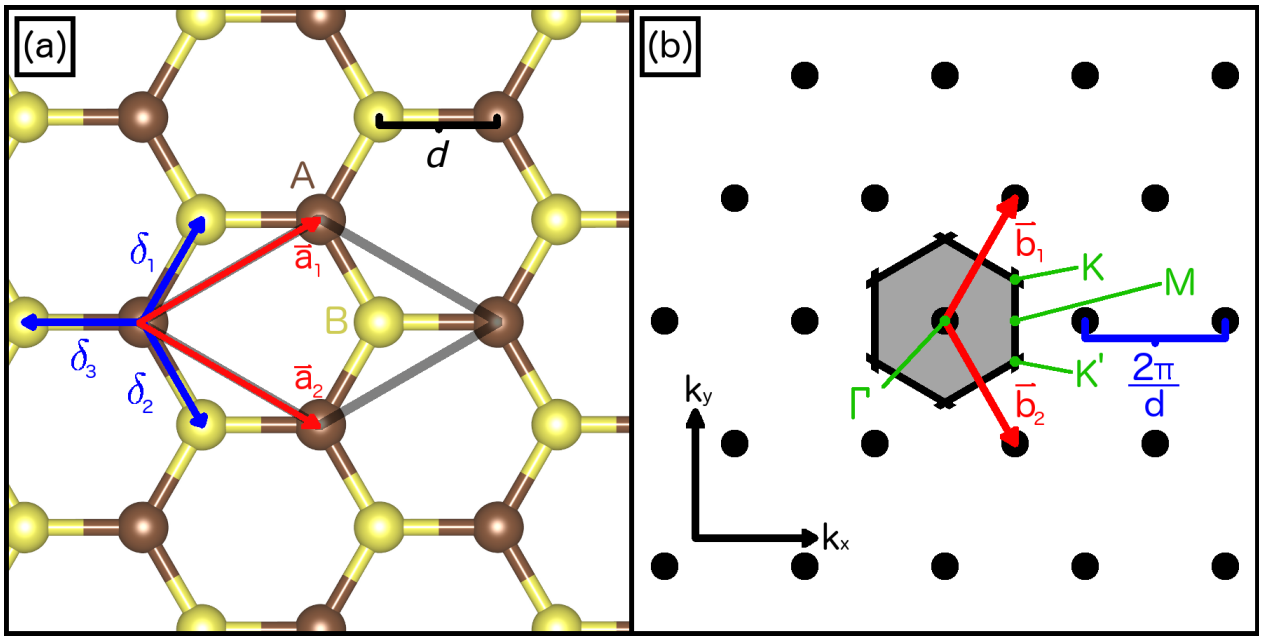

Figure A.1: (a) Top view of the crystal structure of graphene, showing the A and B sublattices, the direct lattice vectors $\vec{a}_i$ and the *nn* vectors δ_i. The C-C distance d is about 1.42 Å. Visualization created with the VESTA software package [8]. (b) The reciprocal lattice of graphene, and its lattice vectors $\vec{b}_i$. The first Brillouin zone is shaded in grey and the special lattice points Γ, M, K and K' are labelled.

A C atom has four valence electrons, two of which are in the $2s$ orbitals and two in the $2p$ orbitals. In graphene they conform to the well-known sp^2 hybridization scheme, in which the two s orbitals and one p orbital hybridize to form an in-plane σ bond with each of the three *nn* atoms. The remaining orbital has p_z character and is responsible for the conductivity of graphene, so it is the state that is of interest to the TB approximation. Each C site in the unit cell each contributes a $2p_z$ electron, so the trial wavefunction takes the following form:

$$\psi(\vec{r})_k = \psi(\vec{r})_k^A + \lambda\psi(\vec{r})_k^B \tag{A.5}$$

where λ is a complex coefficient and $\psi(\vec{r})_k^A$ and $\psi(\vec{r})_k^B$ are related to p_z-like atomic orbitals centred at sites A and B, respectively. Since p_z-like atomic orbitals themselves do not satisfy the periodicity of the system (i.e. they are not Bloch functions), we construct $\psi(\vec{r})_k^A$ and $\psi(\vec{r})_k^B$ as follows:

$$\psi(\vec{r})_k^A = \frac{1}{\sqrt{N}}\sum_{\vec{R}_A} e^{i\vec{k}\cdot\vec{R}_A}\phi^A(\vec{r}-\vec{R}_A) \qquad \psi(\vec{r})_k^B = \frac{1}{\sqrt{N}}\sum_{\vec{R}_B} e^{i\vec{k}\cdot\vec{R}_B}\phi^B(\vec{r}-\vec{R}_B) \tag{A.6}$$

where $\vec{R}_A$ and $\vec{R}_B$ are the locations of all of the A and B sites, respectively. N is the number of cells in the crystal being considered, and is included such that the wavefunctions are normalized to N A and N B electrons when integrated over the whole crystal. The LCAO wavefunction can now be inserted into the Schrödinger equation

$$\hat{H}\psi(\vec{r})_k = E(\vec{k})\psi(\vec{r})_k, \tag{A.7}$$

and integrated over the entirety of the crystal (after left-multiplying by $\psi(\vec{r})_k^{A*}$ or $\psi(\vec{r})_k^{B*}$) to obtain the system of equations

$$\int \psi_k^{A*}\hat{H}\psi_k^A dV + \lambda \int \psi_k^{A*}\hat{H}\psi_k^B dV = E(\vec{k})\left(\psi_k^{A*}\psi_k^A dV + \lambda \int \psi_k^{A*}\psi_k^B dV\right) \tag{A.8}$$

$$\int \psi_k^{B*}\hat{H}\psi_k^A dV + \lambda \int \psi_k^{B*}\hat{H}\psi_k^B dV = E(\vec{k})\left(\lambda\psi_k^{B*}\psi_k^B dV + \int \psi_k^{B*}\psi_k^A dV\right). \tag{A.9}$$

In Wallace's treatment of the system, the final terms were neglected as the overlap between adjacent atoms was assumed to be small. Calling the first integral in Equation A.8 $H_{AA}(\vec{k})$, the second $H_{AB}(\vec{k})$, the third $S_{AA}(\vec{k})$ and the fourth $S_{AB}(\vec{k}) = 0$ and likewise the first integral in Equation A.9 $H_{BA}(\vec{k})$, the second $H_{BB}(\vec{k})$ and the third $S_{BB}(\vec{k})$ and the fourth $S_{BA}(\vec{k}) = 0$, the system of equations shortens to:

$$H_{AA}(\vec{k}) + \lambda H_{AB}(\vec{k}) = E(\vec{k})S_{AA}(\vec{k}) \tag{A.10}$$

$$H_{BA}(\vec{k}) + \lambda H_{BB}(\vec{k}) = E(\vec{k})\lambda S_{BB}(\vec{k}). \tag{A.11}$$

Since $S_{AA}(\vec{k})$ and $S_{BB}(\vec{k})$ simply count the number of electrons resulting from each site, they can be replaced by N, the number of unit cells in the crystal being examined. Algebraically eliminating λ from the equations, they can be rewritten in determinant form:

$$\begin{vmatrix} H_{AA}(\vec{k})N - E(\vec{k}) & H_{BA}(\vec{k}) \\ H_{AB}(\vec{k}) & H_{AA}(\vec{k})N - E(\vec{k}) \end{vmatrix} = 0, \tag{A.12}$$

where the equality $H_{AA}(\vec{k}) = H_{BB}(\vec{k})$ stemming from the equivalence between the two sites has been used. This expression is known as the *secular equation*, and it will take this particular form for any TB approximation that considers two single-electron sites per unit cell. Solving for $E(\vec{k})$ results in a quadratic equation with the solution

$$E(\vec{k}) = H_{AA}(\vec{k}) \pm \sqrt{H_{AB}(\vec{k})H_{BA}(\vec{k})} = H_{AA}(\vec{k}) \pm \left|H_{AB}(\vec{k})\right|, \tag{A.13}$$

since $H_{AB}(\vec{k})$ and $H_{BA}(\vec{k})$ can only differ in terms of phase. The two solutions correspond to the occupied π and unoccupied π^* bands, with the two C electrons occupying opposite spin states in the valence band in the ground state. Already it is apparent that these bands will be symmetric about the value $H_{AA}(\vec{k})$, which is a consequence of not including the overlap integrals $S_{AB}(\vec{k})$ and $S_{BA}(\vec{k})$.

The simplest solution to a TB problem is the *nn* approximation, in which any interaction between atoms that are not immediately adjacent are not considered. Under this treatment, $H_{AA}(\vec{k})$ simplifies to a constant corresponding to the energy of a $2p_z$ orbital in an isolated atom, as there are no A sites in the *nn* shell. The term $H_{AB}(\vec{k})$ is evaluated as

$$H_{AB} = \frac{1}{N} \int \sum_{\vec{R}_A} e^{-i\vec{k}\cdot\vec{R}_A} \phi^{A*}(\vec{r} - \vec{R}_A) \hat{H} \sum_{\vec{R}_B} e^{i\vec{k}\cdot\vec{R}_B} \phi^{B}(\vec{r} - \vec{R}_B) dV. \tag{A.14}$$

The exponential factors can collect together and the summations can be rearranged to produce

$$H_{AB} = \frac{1}{N} \int \sum_{\vec{R}_A} \sum_{\vec{R}_B} e^{i\vec{k}\cdot(\vec{R}_B - \vec{R}_A)} \phi^{A*}(\vec{r} - \vec{R}_A) \hat{H} \phi^{B}(\vec{r} - \vec{R}_B) dV. \tag{A.15}$$

Since $\vec{\delta_1}, \vec{\delta_2}$ and $\vec{\delta_3}$ are the vectors connecting an A site to its three nn B sites (as in Figure A.1(a)), once can collect the energy of an A-B interaction into a single term γ_0 and write

$$H_{AB} = \gamma_0 \left(e^{i\vec{k}\cdot\vec{\delta_1}} + e^{i\vec{k}\cdot\vec{\delta_2}} + e^{i\vec{k}\cdot\vec{\delta_3}} \right). \tag{A.16}$$

Substituting in the values for the A-B separation vectors,

$$H_{AB} = \gamma_0 \exp[-idk_x] \left(1 + 2\exp\left(i\frac{3d}{2}k_x \right) \cos\left(\frac{\sqrt{3}d}{2}k_y \right) \right) \tag{A.17}$$

which means that

$$|H_{AB}| = \gamma_0 \left(1 + 4\cos\left(\frac{3d}{2}k_x \right) \cos\left(\frac{\sqrt{3}d}{2}k_y \right) + 4\cos^2\left(\frac{\sqrt{3}d}{2}k_y \right) \right)^{1/2}. \tag{A.18}$$

This function is plotted on a typical k-path for a hexagonal Brillouin zone ($\Gamma - M - K - \Gamma$) in Figure A.2(a), and over the whole first Brillouin zone in Figure A.2(b). At the points $\vec{K}$ and $\vec{K}'$ mentioned above, H_{AB} vanishes, implying a degeneracy between the π and π^* bands at these momenta. Taking a first-order Taylor series expansion of equation function near the K point, with $\vec{q} = (q_x, q_y)$ representing a small displacement in momentum space,

$$H_{AB}(\vec{q}) \approx H_{AB}(\vec{K}) + \vec{q}\cdot\vec{\nabla} H_{AB}(\vec{K}) = \vec{q}\cdot\vec{\nabla} H_{AB}(\vec{K}) \tag{A.19}$$

$$H_{AB}(\vec{q}) \approx \frac{3\gamma_0 d}{4} \left(i(1 + \sqrt{3}i)q_x - (1 + \sqrt{3}i)q_y \right) \tag{A.20}$$

which, if the proper phase is absorbed into the definition of the wavefunction, can be rewritten as

$$\hat{H}'_K(\vec{q}) = \frac{3\gamma_0 d}{2} \begin{pmatrix} 0 & q_x - iq_y \\ q_x + iq_y & 0 \end{pmatrix}. \tag{A.21}$$

A similar relationship can be derived near the K' point, except that the x-momenta are flipped in sign:

$$\hat{H}'_{K'}(\vec{q}) = \frac{3\gamma_0 d}{2} \begin{pmatrix} 0 & -q_x - iq_y \\ -q_x + iq_y & 0 \end{pmatrix}. \tag{A.22}$$

The energy dispersion expanded about the points K and K' is then

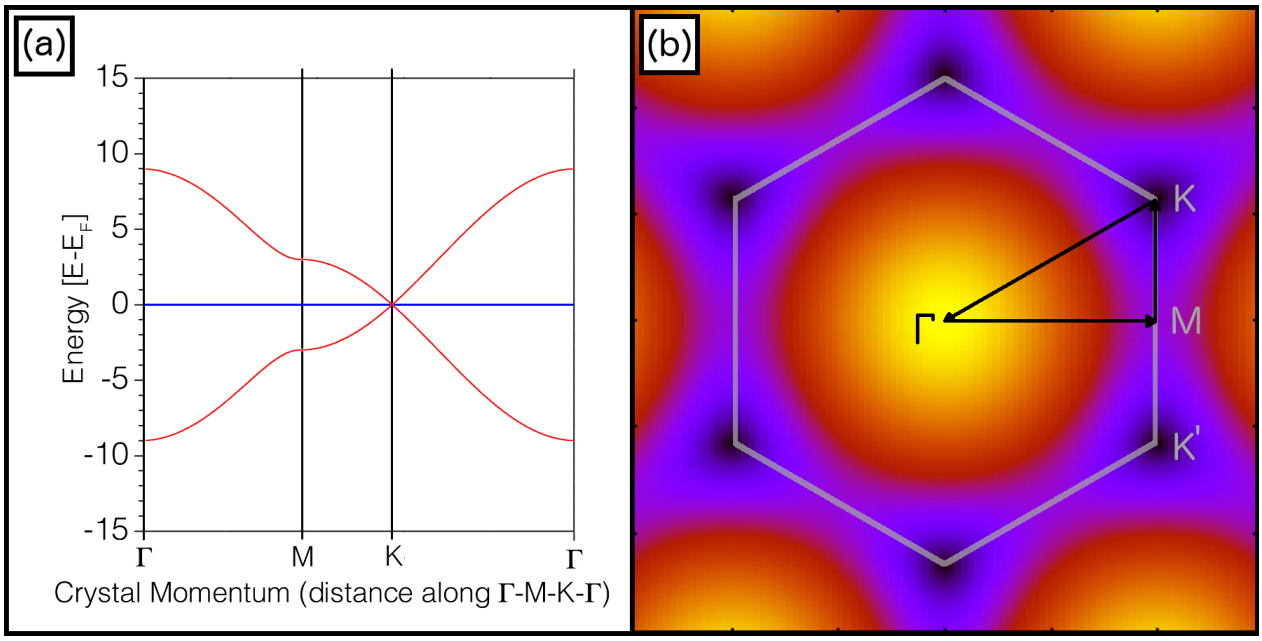

Figure A.2: (a) The TB bandstructure of graphene plotted along the typical ($\Gamma - M - K - \Gamma$) path for hexagonal lattices. The degenerate band crossing at the K-point is evident. (b) The the TB solution plotted over the first Brillouin zone of graphene (grey hexagon). The colours indicate the energy of the π and π^* bands relative to the Fermi level, with yellow being the maximum and black representing zero.

$$E(\vec{q}) = \frac{3\gamma_0 d}{2} |\vec{q}| \,. \tag{A.23}$$

This relation indicates that the energy bands are linear in the vicinity of the degenerate point, and that the curves of constant energy in this region are circular. That is, the bands in 3D energy-momentum space look like two symmetric cones placed tip-to-tip at the degeneracy point. This can be clearly seen in Figure A.3(a), where the TB solution is plotted in 3D energy-momentum space near the point K. The leading coefficient in the conical region can be collected into a term with units of velocity (after converting the crystal momentum to momentum through the relation $\vec{p} = \hbar\vec{k}$), and is called the Fermi velocity (v_F). The value of γ_0 for graphene has been estimated through DFT calculations to be approximately 3 eV [271], resulting in a Fermi velocity of $\sim 1 \times 10^6$ m s^{-1}, or about 0.3% the speed of light in a vacuum.

To show that the conical bandstructure is not just an artefact of the TB approximation, I have included the results of *ab initio* DFT calculations in Figure A.3(b). This bandstructure was obtained with the WIEN2k program suite on a single unit cell of graphene with 15 Å of vacuum separating the sheets, using a $(15 \times 15 \times 1)$ k-point mesh, a cutoff energy of -7 Ry and an RK_{max} of 6 (see Chapter 4 for an explanation of these parameters and a description of the application of DFT to 2D crystals). In this (non spin-polarized) DFT calculation, the linear band crossing remains, and the best agreement between the TB and DFT calculations is in the vicinity of the degenerate point, with the agreement deteriorating further away from the Fermi energy. Notably, the electron-hole asymmetry that the overlap-free TB calculations miss is apparent in the DFT bandstructure, but it is negligible at low energies. Both methods

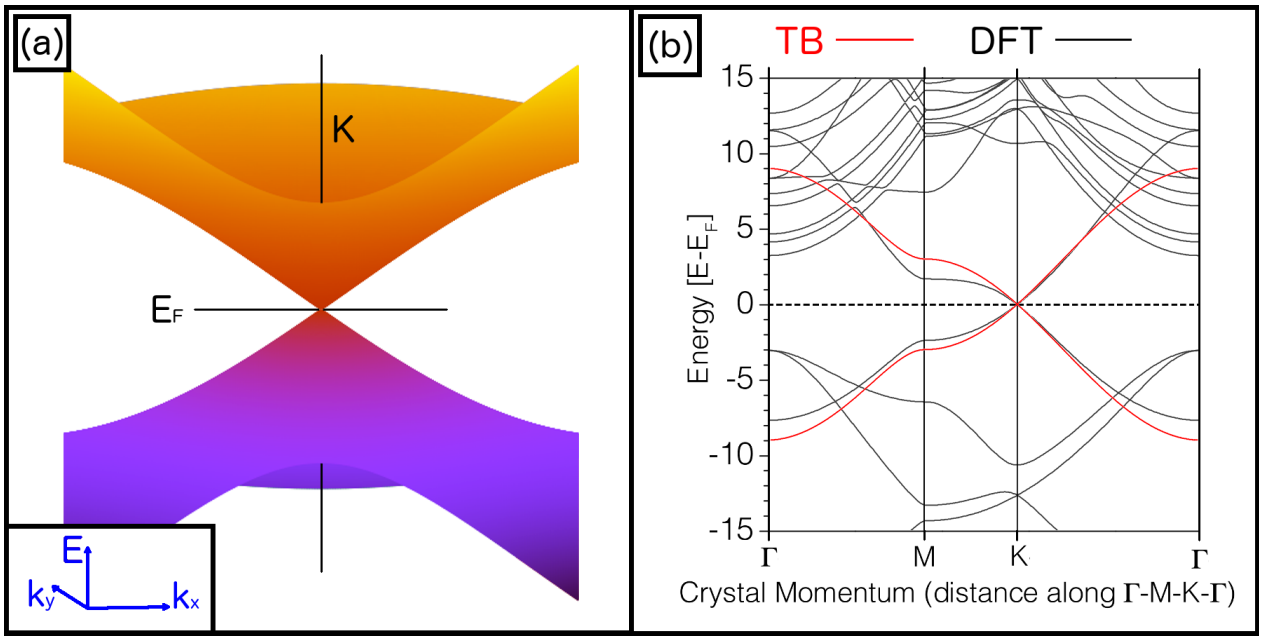

Figure A.3: (a) A close-up of the degenerate point and conical bandstructure in 3D energy-momentum space for the TB calculation. (b) A DFT calculation of the bandstructure of graphene plotted with the TB calculation for comparison.

produce approximately the same cone slope corresponding to a Fermi velocity of 10^6 ms^{-1}.

Carrier spin was neglected in the construction of the Hamiltonian. When incorporated, a SOC term is introduced into the Hamiltonian in such a way that it opens a gap between the π and π^* bands, removing the Dirac point without significantly altering the linearity of the bands in this region. The magnitude of this SOC-induced gap is negligibly small for graphene, usually somewhere between 1 and 100 μeV for TB approximations or spin-polarized DFT calculations.

While the derivation up to this point has specifically considered the case of graphene, its results are generalizable to other systems provided that a few conditions are met: a hexagonal honeycomb atomic structure, inversion symmetry (the equivalence of the A and B sublattices) and the sp^2 hybridization scheme with p_z valence orbitals. As discussed in Chapter 2, graphene is not the only material that can satisfy these criteria. Such a conical bandstructure would therefore be possible in a number of monoatomic 2D materials, though the existence and stability of such materials are not guaranteed.

Appendix B

Core-Level Transitions

Core-level spectroscopic techniques are based around electronic transitions between tightly bound core-level states and delocalized states of interest in the VB and CB. In both XES and XAS, these transitions are mediated by single photons (one incident photon causes the excitation in XAS, and one photon is emitted during the fluorescent decay process in XES). Fermi's Golden Rule gives the rate W of such transitions as

$$W = \frac{2\pi}{\hbar} \left|\langle \Psi_f | T_1 | \Psi_i \rangle\right|^2 \delta(E_f - E_i - \hbar\omega), \tag{B.1}$$

where Ψ_i and Ψ_f are the net electronic wavefunctions prior to and after the transition, respectively, with their associated energies E_i and E_f, while $\hbar\omega$ gives the energy of the incident/emitted photon. T_1 is the single-photon transition operator, which is known from time-dependent perturbation theory:

$$T_1 = -\frac{e}{mc} \exp\left(i\vec{k}\cdot\vec{r}\right) \vec{p}\cdot\vec{A}. \tag{B.2}$$

Here, $\vec{k}\cdot\vec{r}$ is a projection of the photon's wavevector onto the electron's position $\vec{r}$, and $\vec{p}\cdot\vec{A}$ is the projection of the electron's momentum $\vec{p}$ on to the vector potential of the photon $\vec{A}$. Relating the photon's wavevector and energy, and applying the delta function in Equation B.1:

$$T_1 = -\frac{e}{mc} \exp\left(i\frac{E_f - E_i}{\hbar c}\hat{n}\cdot\vec{r}\right) \vec{p}\cdot\vec{A}, \tag{B.3}$$

where $\hat{n}$ denotes the direction of the photon's propagation.

The quantity $\hbar c$ has a value of about 197 eV nm, while the quantity $(E_f - E_i)\hat{n}\cdot\vec{r}$ varies with the energy of the photon, its geometric relationship to the electron and the electron's orbital radius. However, in soft X-ray spectroscopy the photon energies involved are usually on the order of a few hundred eV (and no more than 2 keV) and the radii of the electronic states range from less than 1 Å (for core-states) to no more than a few Å (for the emitting VB states in XES). The argument of the exponential is therefore less than unity, so it can be replaced with the Maclaurin series

$$\exp\left(i\frac{E_f - E_i}{\hbar c}\hat{n}\cdot\vec{r}\right) \approx 1 + i\frac{E_f - E_i}{\hbar c}\hat{n}\cdot\vec{r} - \left(\frac{E_f - E_i}{\hbar c}\hat{n}\cdot\vec{r}\right)^2 + ... \tag{B.4}$$

The first term of this expression is the dominant one, especially for low energy core-level transitions like the ones in Si $2p$ spectroscopy. If we exclude all others, the transition operator becomes

$$T_1 = -\frac{e}{mc}\vec{p}\cdot\vec{A}, \tag{B.5}$$

or, if $\vec{A} = A\hat{e}$, where $\hat{e}$ is the polarization vector of the incident/emitted photon,

$$T_1 = -\frac{Ae}{mc}\vec{p}\cdot\hat{e}. \tag{B.6}$$

The electron's momentum $\vec{p}$ can be related to the commutator of the electron's ground-state Hamiltonian $\hat{H}_0$ and its position $\vec{r}$,

$$[\vec{r}, \hat{H}_0] = \frac{i\hbar}{m}\vec{p}, \tag{B.7}$$

which results in the transition operator

$$T_1 = -\frac{eA}{i\hbar c}[\vec{r}, \hat{H}_0]\cdot\hat{e}. \tag{B.8}$$

When this is inserted into the transition rate calculation in Equation B.1:

$$W = \frac{2\pi e^2 A^2}{\hbar^3 c^2}\left|\langle\Psi_f|[\vec{r}, \hat{H}_0]\cdot\hat{e}|\Psi_i\rangle\right|^2 \delta(E_f - E_i - \hbar\omega), \tag{B.9}$$

but since $[\vec{r}, \hat{H}_0] = \vec{r}\hat{H}_0 - \hat{H}_0\vec{r}$,

$$W = \frac{2\pi e^2 A^2}{\hbar^3 c^2}(E_f - E_i)^2\left|\langle\Psi_f|\vec{r}\cdot\hat{e}|\Psi_i\rangle\right|^2 \delta(E_f - E_i - \hbar\omega). \tag{B.10}$$

The transition operator has now become that of an electric dipole, and thus the dipole selection rules ($\Delta\ell = \pm 1$) apply. That is, core-level transitions from an s state will predominantly be to or from the p states in the VB and CB, while core-level transitions from a p state will predominantly be to or from the s and d VB and CB states (the "forbidden" quadrupole transitions resulting from the second term in the Maclaurin expansion are allowed, but largely suppressed).

In and XES or XAS measurement, the observed signal as a function of emitted or incident energy, $I(\hbar\omega)$, will be the product of the transition matrix element W and the number of initial and final states available for the transition. The core-level states are highly localized in energy, so their contribution is basically just a scaling factor applied to the observed signal (though the situation is slightly more complicated when there are split core-levels from SOC, as discussed in (see Chapter 5 for Si $2p$ core-level spectroscopy). The states of interest in the VB or CB are distributed in energy, and are therefore often represented as an energetic density of states (DOS), which is equal to the material's bandstructure integrated across all crystal momenta. Because of the dipole selection rules, the transition operator breaks this DOS down by angular momentum into the partial (projected) DOS, or pDOS. The emitted or absorbed signal is therefore given by

$$I(\hbar\omega) \propto \omega^2\left|\langle\Psi_f|\vec{r}\cdot\hat{e}|\Psi_i\rangle\right|^2 \cdot pDOS(\hbar\omega), \tag{B.11}$$

neglecting the effects of instrumental and lifetime broadening.

The final-state rule [272,273] states that the observed transition energies will be primarily determined by the final state Ψ_f of the atom. For an XES measurement, the final state of the atom after the transition of interest includes completely full core-levels and a hole in the VB. This VB hole has little to no effect on the energy spectrum of the rest of the VB electrons,

so an XES measurement essentially probes the ground-state VB structure. In XAS, the final state resulting from the transition includes a core-level vacancy, which reduces the nuclear screening and can significantly rearrange the measured CB states (see Chapter 5 for a brief discussion of these effects). XAS is therefore *not* a measure of the ground-state CB structure, though on occasion the effects of the core-level vacancy end up being negligible.

In WIEN2k, the core-level states are represented as a combination of spherical harmonics and the radial solutions to the Schrödinger equations (see Chapter 4), while the interstitial density can be projected on to the angular momentum operators once the calculation has been converged using the command "lapw2 -qtl", converting the DOS to the pDOS. After selecting a specific core-level state, the transition rate can be calculated for each projection of the VB/CB states as a function of energy. When these functions are multiplied by the appropriate projection of the pDOS, the result is the tw-pDOS which should correspond to the measured spectrum, again neglecting any broadening effects.

As an illustration of this concept, Figure B.1 shows the pDOS for an isolated LB silicene sheet, including its $3s$, $3p$ and $3d$ states. The tw-pDOS are plotted for a $2p$ core-level transition and a $1s$ core-level transition, corresponding to K- and $L_{2,3}$-edge spectroscopy. The dipole selection rules are evident, as the tw-pDOS strongly resembles the $3p$ states for a $1s$ core-level transition and the sum of the $3s$ and $3d$ states for a $2p$ core-level transition.

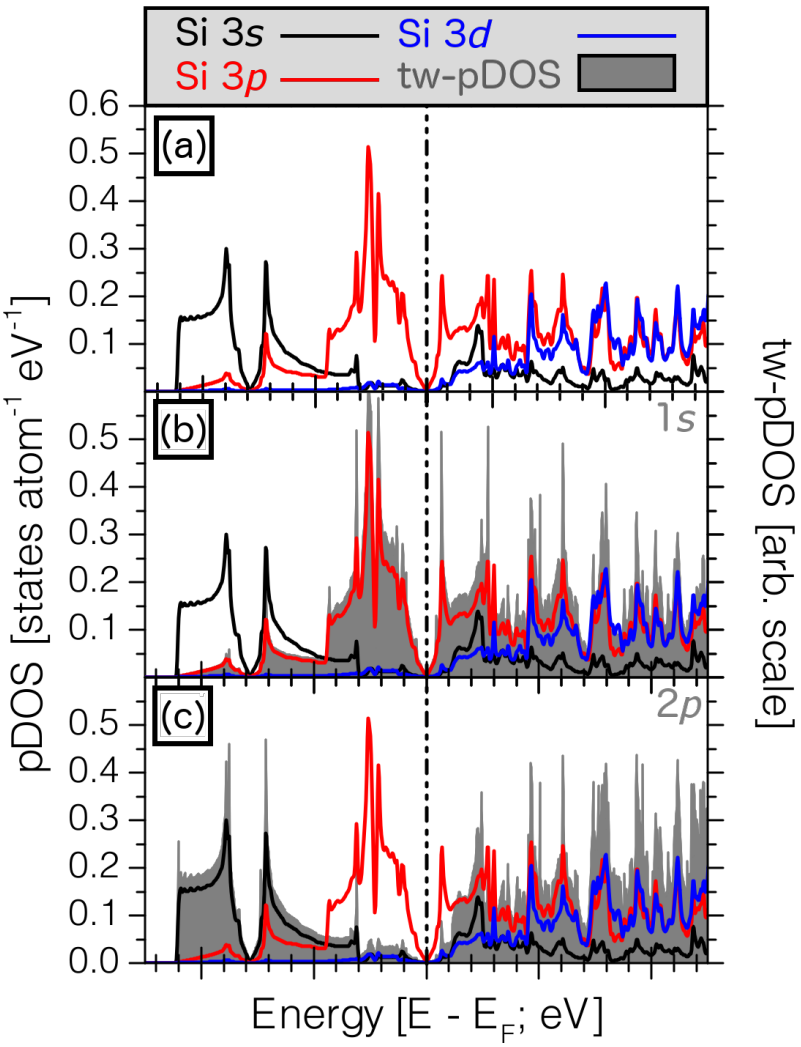

Figure B.1: (a) The pDOS for freestanding LB silicene, projected into $3s$, $3p$ and $3d$ orbitals. (b) The pDOS plotted alongside the tw-pDOS for a $1s$ Si core-level, showing the strong sensitivity to the $3p$ states. The increase in W with energy can also be observed. (c) The pDOS plotted alongside the tw-pDOS for a $1s$ Si core-level, showing the strong sensitivity to the $3s$ and $3d$ states.

Appendix C

Copyright Information

This appendix details copyright information regarding the previously published figures and full articles that have been reproduced within the pages of this manuscript. Text that is quoted from the copyright agreements will appear in italics.

C.1 Copyright Agreements for Reproduced Articles

C.1.1 Advanced Functional Materials and physica status solidi (a) Copyright Transfer Agreement

The full articles reproduced in Chapters 6 and 8 (References 136 and 118) were both originally published in *Advanced Functional Materials*, and the full article published in Chapter 9 (Reference 175 was originally published in physica status solidi (a), journals published by "Wiley-VCH Verlag GmbH & Co. KGaA" (hereafter Wiley). Wiley's transfer of copyright agreement, which was signed by the authors for both articles, includes the following clause:

3. Final Published Version. *Wiley-VCH hereby licenses back to the Contributor the following rights with respect to the final published version of the Contribution:*

b. Re-use in other publications. *The right to re-use the final Contribution or parts thereof for any publication authored or edited by the Contributor (excluding journal articles) where such re-used material constitutes less than half of the total material in such publication. In such case, any modifications should be accurately noted.*

As first author of all three articles, I qualify as a Contributor, and this manuscript qualifies as a publication I have authored. Chapters 6, 8 and 9 together constitute less than half of this manuscript, and therefore reproduction of these articles is acceptable without written permission from Wiley.

Wiley's full Copyright Transfer Agreement can be found here: `http://www.wiley-vch.de/util/cta/PS_Global.pdf`

C.1.2 Scientific Reports

The full article reproduced in Chapter 7 (Reference 142) was originally published in *Scientific Reports*, an open-access journal published by the Nature Publishing Group. Material published in *Scientific Reports* is subject to the Creative Commons Attribution 4.0 International License, which grants any person, regardless of their involvement or non-involvement with the publication:

Section 2 – Scope.

a. License grant.

1. Subject to the terms and conditions of this Public License, the Licensor hereby grants You a worldwide, royalty-free, non-sublicensable, non-exclusive, irrevocable license to exercise the Licensed Rights in the Licensed Material to:

A. reproduce and Share the Licensed Material, in whole or in part;

where "Share" is defined as:

Section 1 – Definitions.

Share means to provide material to the public by any means or process that requires permission under the Licensed Rights, such as reproduction, public display, public performance, distribution, dissemination, communication, or importation, and to make material available to the public including in ways that members of the public may access the material from a place and at a time individually chosen by them.

As this article is licensed under the Creative Commons Attribution 4.0 International License, there is no copyright holder.

The *Scientific Reports* License Agreement can be found here: `http://www.nature.com/srep/journal-policies/editorial-policies#license-agreement`, and the Creative Commons Attribution 4.0 International License can be found here: `http://creativecommons.org/licenses/by/4.0/legalcode`.

C.2 Permissions to Reproduce Figures

Some figures (Figures 2.4, 2.5, 2.9, 2.10 and 4.4) in this manuscript are entirely or partly reproduced from publications by other authors (References [5], [30], [127], [131], and [136], respectively). Permissions have been obtained for the use of all of these figures in this manuscript through the Copyright Clearance Center. The relevant license numbers are 3827451188954, 3827400180052, 3827401456544, 3827410517866, and 3827931454892 respectively.